DISSERTATION

PROTEIN ENGINEERING THERAPEUTIC STRATEGIES AND TOOLS

Submitted by

Angeline Ngoc Ta

Department of Chemistry

In partial fulfillment of the requirements

For the Degree of Doctor of Philosophy

Colorado State University

Fort Collins, Colorado

Spring 2019

Doctoral Committee:

Advisor: Christopher Snow

Chuck Henry
Alan Kennan
Tim Stasevich

ABSTRACT

PROTEIN ENGINEERING THERAPEUTIC STRATEGIES AND TOOLS

Proteins have become an important tool for research development and therapeutics. Proteins complement the use of small molecules as well as overcome challenges that small molecules cannot. The contrasting difference of their diverse functional and structural properties allows for complex processes like molecular recognition and catalysis. Through loops, turns, helixes, and sheets, these structural motifs provide a protein with shape and electrostatics to achieve a particular function. Overall, I describe here two examples of functional proteins where the protein's complex structure plays an important role in the development of new strategies and tools for therapeutics. The first part of this dissertation shows the effects of increased antibody recruitment on targeted cell death through the use of an immunotherapeutic cocktail of cell surface HER2 receptor binding proteins. The second part of this dissertation describes the use of a protein's chiral environment to develop a new artificial metalloenzyme that selectively catalyses synthesis of the most common N-heterocycle found in FDA approved pharmaceuticals.

ACKNOWLEDGEMENTS

I would like to thank my former research advisor, Dr. Brian McNaughton. He has facilitated in my development as a researcher, presenter, figure maker, and scientist. I am grateful for the guidance, patience, confidence, and skills to adapt and overcome.

I would also like to thank my current advisor, Prof. Chris Snow for adopting me into his group. He went from being my out of area committee member, to not being on my committee, to being my advisor. I appreciate your flexibility and the care provided me as I finished up. Thank you to the Snow lab members for your willingness to help and making me feel included.

Thank you to my committee members, Prof. Chuck Henry, Prof. Alan Kennan, and Prof. Tim Stesavich. I appreciate your time, feedback, and understanding.

Thanks to all my collaborators. Research knows no distance. With a little help from e-mail and Skype I've been able to learn a great deal from each of you. Without your expertise, my projects would not have been possible.

Thank you to my lab mates. You don't realize what you have until it is gone. Your constant feedback and willingness to talk science and experiments has helped me progress through my research. I am grateful to have had lab mates who help you celebrate the wins and support you through the losses.

A very special thank you to my friends and family. Your outside perspective and encouragement was more appreciated than I can express. Finally, I am extremely grateful for my fiancé, Jangir, for being my support. You helped keep me grounded and was there for me every step of the way. I am indebted to your willingness to help and provide me with a different perspective on my research and experiences. I cannot put down in words how much I appreciate your patience and understanding over the years.

TABLE OF CONTENTS

LIST OF TABLES

LIST OF FIGURES

Chapter 1

Minimalist Antibodies and Mimetics: An Update and Recent Applications

Adapted from:

Bruce, V.J.*; Ta, A.N.*; McNaughton, B.R., ChemBioChem, 2017, 17, 1892.

I co-authored this review article with Virginia Bruce. Our individual research projects involve the use of minimalist antibody scaffolds, providing us the knowledge to collaborate on a review concerning antibody alternatives.

1.1 Introduction

Over half of the top selling drugs of 2018 are biologics. The use of proteins in therapeutics has helped expand the scope of what is druggable through cell surface interactions with the use of antibodies. The immune system utilizes antibodies to recognize foreign or disease-relevant receptors, initiating an immune response to destroy unwelcomed guests. Because researchers can evolve antibodies to bind virtually any target, it is perhaps unsurprising that these reagents, and their small-molecule conjugates, are used extensively in clinical and basic research environments. However, virtues of antibodies are countered by significant challenges. Foremost among these is the need for expression in mammalian cells (largely due to often necessary post-translational modifications). In response to these challenges, researchers have developed an array of minimalist antibodies and mimetics, which are smaller, more stable, simpler to express in *Escherichia coli*, and amendable to laboratory evolution and protein engineering. Here, we describe these scaffolds, and discuss recent applications of minimalist antibodies and mimetics.

1.2 Antibodies: Structure, Function, Virtues, and Challenges

The most predominant antibody type is the immunoglobulin of isotype G (IgG), which weighs approximately 150 kDa. [1] Members of this antibody class each consist of two distinct regions: the fragment antigen-binding (Fab) and fragment crystallizable (Fc, Figure 1.1a). The Fab fragment consists of a constant light-chain domain (C_L) and a variable light-chain domain (V_L) (Figure 1.1a, green), linked to the constant (CH1) and the variable (V_H) heavy-chain domains (Figure 1.1a, gray). When folded properly, six solvent-exposed loops from V_L and V_H domains are presented. Collectively these loops are referred to as the complementary determining regions (CDRs, Figure 1.1b), and this is where the antigen is bound. Both the V_L and V_H domains display three CDRs, with loops having an average length of ten amino acids.

In contrast to the CDRs, the Fc region has high sequence homology. The Fcs of IgG1 and IgG4 each consist of two domains of the heavy chain (CH2 and CH3) connected to one another through two disulfide bonds in the hinge region [2] (Figure 1.1a; all disulfide bonds are highlighted in red). Multiple regions within the Fc are critical to antibody function, and endow unique properties. For example, the in vivo half-life of an IgG (ca. 21 days [3]) is much longer than those of most proteins. [3] This is achieved through an epitope on the surface of the Fc that interacts with the neonatal Fc receptor, FcRn. FcRn mediates a salvaging pathway by binding and transporting IgG into and across cells, dramatically slowing its degradation. [4, 5] FcRn binds to the CH2–CH3 hinge region of IgG (Figure 1.1c) with high affinity under the acidic conditions typically found within endosomes (pH<6.5) and with virtually no affinity in environments outside endosomes (typically pH≈7.4). [6, 7] This pH dependent binding mediates the FcRn–IgG interaction after uptake into acidic endosomes, allows IgG to piggyback with FcRn back to the plasma membrane and the complex to dissociate once returned to the circulatory system. This sequestration/transport mechanism saves antibodies from degradation through the endosome/lysosome pathway. Regions of Fc also mediate immune system stimulation, such as antibody-dependent cellular cytotoxicity (ADCC) [8,9] or complement-dependent cytotoxicity (CDC). [10,11] Fc gamma receptors (FcγRs) on the surfaces of immune effector cells such as natural killer (NK) cells and macrophages

recognize the Fc regions of antibodies bound to a target cell (Figure 1.1d). [12, 13] Upon binding, the immunoreceptor tyrosine-based activation motif (ITAM) is phosphorylated; this then triggers the activation of the effector cell and the release of perforin, lytic enzymes, tumor necrosis factor (TNF), and/or granzymes for cell destruction through ADCC. In CDC, C1q of complex C1 binds to the Fc region and triggers the complement cascade activation and eventual formation of membrane attack complex (MAC) at the surfaces of the target cells, leading to cell lysis.

In addition to the proteinogenic amino acids that make up antibodies, extensive post-translational modifications (disulfide- bond formation and glycosylation) are required to deliver a mature immunoglobulin. As a result of the large size and molecular complexity of an antibody, challenges arise in their production—fully modified antibodies must be prepared in mammalian cells. [14, 15] This form of production is relatively costly, slow, and low-yielding in comparison with expression of many recombinant proteins in *Escherichia coli*.

Challenges in the preparation and manipulation of antibodies motivated researchers to develop minimalist forms and mimetics with improved expression in *E. coli* and stability. Over the past few decades, researchers have developed a number of protein scaffolds that are amenable to extensive mutagenesis and laboratory evolution to achieve new recognition and unique function with relative ease.

Many new protein–protein interactions are achieved (through high-throughput screening or in laboratory evolution) by resurfacing helix or β-strand structural features. Excellent papers and reviews on common scaffolds exist. [16–20] Here, however, we focus on minimalist forms of antibodies, and their mimetics, which, like antibodies, rely on maturation of loops to achieve recognition. Modern applications and protein engineering efforts to generate new properties and function are discussed throughout.

1.3 Antibody Fragments

Immunoglobulins have a modular architecture, and each module has a unique biological function. This modular architecture allows researchers to minimalize components, thus generating new

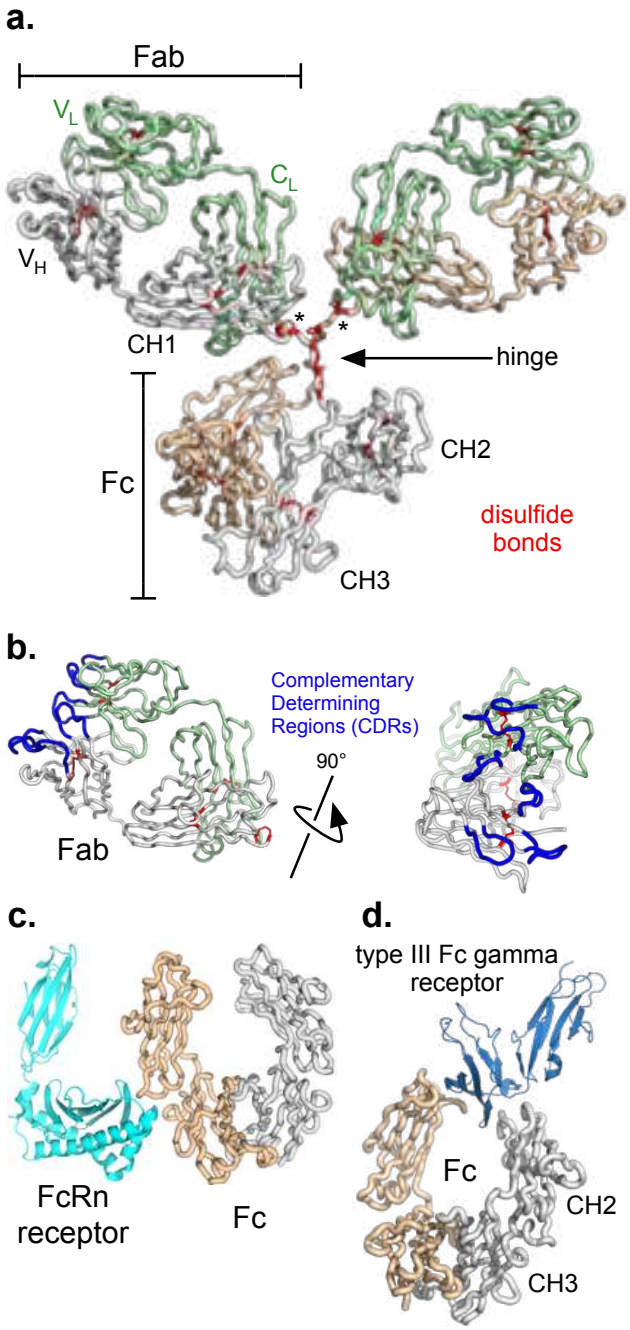

Figure 1.1: (a) IgG1 and 4 consist of two heavy chains (gray and brown) and two light chains (green). The heavy chains contain the fragment crystallizable (Fc), the constant region (CH1), and the variable region (V_H). The light chain is made up of a constant region (C_L) and variable region (V_L), and is covalently attached to V_H/C_H through a single disulfide bond (denoted by *). Collectively, the V_L/C_L-CH1/V_H region is called the Fab fragment, and is where antigen binding occurs (PDB ID: 1IGY). (b) CDRs (blue) from a Fab fragment (PDB ID: 1IGY). (c) Interaction between CH3 and CH2 of Fc and the neonatal Fc receptor (FcRn) (PDB ID: 1I1A). (d) ADCC is initiated by the type III Fcγ receptor binding to CH3 domains from the A and B chain of Fc (PDB ID: 1T89).

proteins that retain certain properties, but lose others. For example, because the Fab fragment is solely responsible for antigen binding, this domain—and variations on the structural theme—have been used for recognition in clinical and basic research settings, as well as targeted delivery of cargo.

1.3.1 Fab fragments

Cartoon depictions of IgG and antibody fragments discussed in this Chapter are shown in Figure 1.2. Full-length Fab fragments contain both CH1/V_H and C_L/V_L fusions, connected by a single disulfide bond (denoted by asterisks in Figure 1.1). These minimalist antibodies have some advantages and disadvantages over immunoglobulins. For example, Fab fragments retain target recognition, but lose properties encoded within the Fc domain, such as immune response stimulation and long in vivo half-life. Because these fragments have a relatively short existence in plasma, in comparison with antibodies, antibody fragments might be of particular value in applications that favor or require shorter biological lifetime (such as imaging). Moreover, their small size endows deeper tumor penetration [21–23], and simpler expression in *E. coli*, and manipulation in the laboratory.

Fab fragments can be produced through chemical or protease digestion of full-length immunoglobulins. [24] However, more commonly these fragments are produced by recombinant expression in bacteria. [25] Fab fragments have been used as therapeutics, as well as in diagnosis, detection, imaging, and crystallography applications. [21, 24, 26, 27]

At present, a number of Fab fragments are in clinical trials. For example, citatuzumab bogatox (VB6-845) is a recombinant immunotoxin for use as a treatment for ovarian cancer and other solid tumors. [28] In this drug lead, deBouganin—a de-immunized plant toxin—is fused to a humanized Fab fragment that targets epithelial cell adhesion molecules (EpCAMs). In addition, naptumomab estafenato (ABR-217620) is a fusion protein therapeutic for advanced renal cell carcinoma and other solid tumors. [29] The fusion consists of a Fab fragment that binds 5T4 (a cell-surface tumor antigen), and superantigen staphylococcal enterotoxin A (a protein that binds to major histocompatibility complex class II molecules and activates T lymphocytes).

Fab fragments are also routinely used as tools for imaging and detection. ThromboView is a radiolabeled Fab fragment that targets the D dimer region of crosslinked fibrin for deepvein thrombosis imaging. [30] In basic research applications, Fab fragments have been used for imaging inside mammalian cells. For example, Stasevich, Morisaki, and co-workers have utilized Fabs to study translation in living cells. Using a Fab fragment that recognizes the FLAG tag (DYKDDDK) they perform nascent chain tracking (NCT). [31] mRNA encoding a 10x FLAG-tagged protein and 24x MS2 tag in the 3'-untranslated region is produced in cells. Fluorescently labeled MS2 coat protein recognizes the mRNA, thus detecting its presence in a mammalian cell. By use of an orthogonally labeled FLAG binding Fab, translation of the encoded protein is detected, following translation of the FLAG tag from the ribosome. Collectively, these two fluorescently labeled components provide a glimpse into translational dynamics in living mammalian cells.

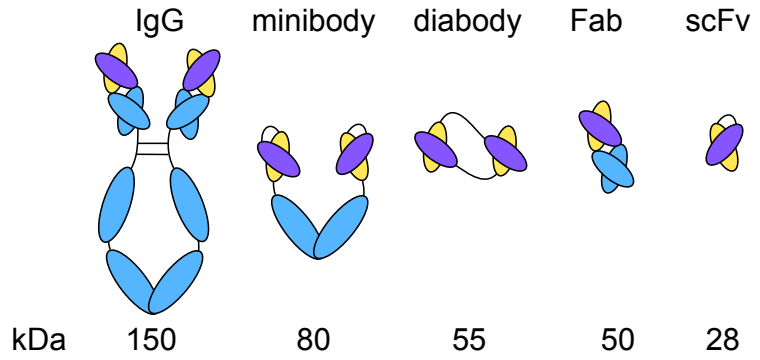

Figure 1.2: Cartoon depiction of IgG and fragments discussed in this Chapter.

1.3.2 Single-chain variable fragments (scFv)

Single-chain fragment variable antibodies (scFvs) were first reported in 1988 as minimalist forms of Fab fragments. [32] These ≈28 kDa fragments result from the genetic linkage of V_H to V_C, typically with a flexible 10-to-25-residue linker. [21] Whereas antibodies can contain up to 25 disulfide bonds and Fab fragments can require five disulfide bonds, scFv typically only contain two, thus simplifying their recombinant expression and stability in reducing environments (such

as the cytosol of bacteria). New strains of *E. coli* with enzymes to facilitate disulfide formation further simplify the recombinant production of scFvs. [33]

Similarly to other Fab-based antibody fragments, scFvs do not participate in immune response stimulation, and removal of the FcRn receptor results in substantially decreased in vivo half-lives. However, their small size and easy expression make scFvs relatively simple minimalist antibodies to prepare and manipulate in the laboratory. Clinically, scFvs display better tumor penetration, more rapid blood clearance, lower retention times in nontarget tissue, and reduced immunogenicity. [34]

Because functional scFvs can be expressed in the reducing environment of the cytosol, these reagents can be generated inside a cell for use in certain applications. For example, Kimura, Sato, and co-workers utilized a scFv specific for histone H3 lysine 9 acetylation (H3K9ac), fused with green fluorescent protein (GFP) to identify post-translational histone modifications in living cells. [35] This approach enables tracking of the spatiotemporal dynamics of endogenous histone modifications in a genetically encoded format.

Recently, scFv-based technology called SunTag has been used for real-time detection of proteins in living cells and to amplify transcription. [36] In the context of protein detection, cells are made to express a protein that displays many copies of a short peptide epitope. The cells also express a scFv that recognizes the epitope, fused to a fluorescent protein such as GFP. When concomitantly expressed, the scFv-GFP fusion selectively recognizes the epitope-tagged protein, resulting in the illumination of that protein in a living cell (Figure 1.3a). Additionally, SunTag has been used to enhance transcription. Vale, Tanenbaum, and co-workers made cells express a nuclease-inactive form of Cas9 (dCas9) fused to multiple peptide epitopes, as well as a scFv that binds the epitope while fused to VP64, a transcriptional activator. Complex formation between the peptide epitopes on dCas9 and the scFv-VP64 fusion led to recruitment of many copies of the transcriptional activator to transcriptional machinery on DNA—resulting in increased transcription (Figure 1.3b).

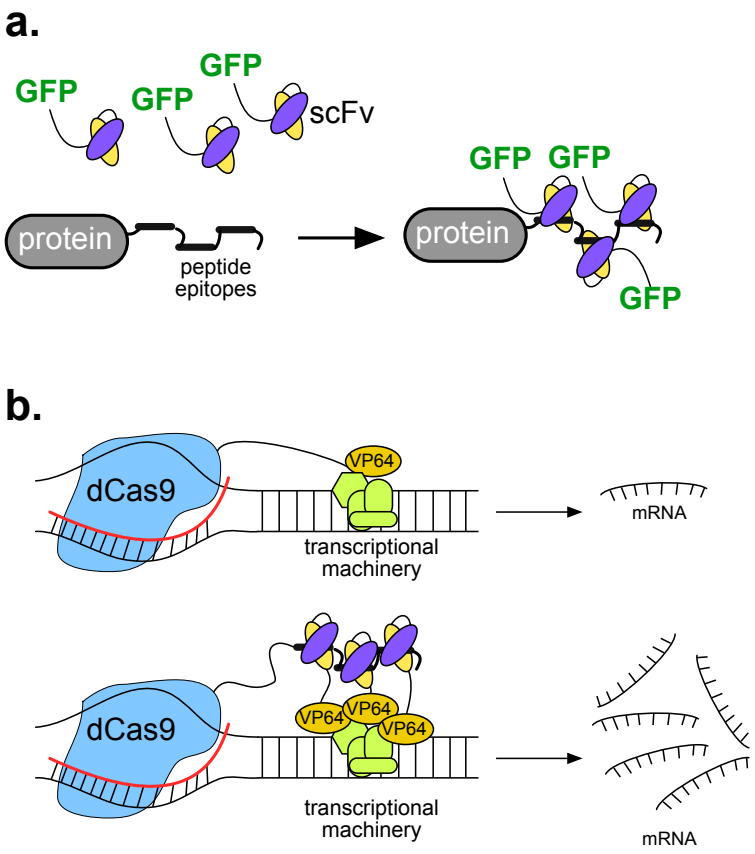

Figure 1.3: SunTag technology utilizes scFv fusions and has been used to: (a) illuminate and track proteins in living cells, and (b) recruit a transcriptional activator (VP64), resulting in increased transcription of a gene in a cell.

1.3.3 Minibodies

Minibodies are a single polypeptide consisting of scFv-CH3-CH3-scFv; functional minibodies can be expressed recombinantly in *E. coli*. [37] The principal benefit of including CH3 is an appreciable increase in biological half-life relative to scFv. Variants that contain the hinge region (flex minibodies) and variants that do not contain the hinge region (LD minibodies) have both been reported—with the flex minibodies showing higher tumor uptake and slower clearance times. [37] Similarly to their scFv cousins, minibodies retain target affinity, but lose immune response stimulation.

However, conjugates of minibodies have been used for targeted delivery of toxic proteins or small-molecule compounds. [37] Additionally, because a minibody consists of a single polypep-

tide, scFv domains with different target recognition can be encoded, and bispecific binding (concomitant recognition of two different targets) can be achieved. [38]

Recently, the Wu lab developed an immunoPET (positron emission tomography) radiotracer for imaging of prostate cancer by targeting prostate stem cell antigens through affinity maturation of the previously developed hu1G8 minibody modified with ^{124}I and ^{98}Zr radiolabels. [39, 40] Marasco, Han, and coworkers reported a minibody as a potential therapy for cutaneous T-cell lymphoma (CTCL) that targets the CC chemokine receptor 4 (CCR4). [41] In a creative modern application, Park, Lee, and co-workers prepared a polypeptide consisting of polyarginine (Arg_9) and an anti-JL1 minibody. When this was noncovalently complexed with siRNA, through charge complementation, and then applied to mammalian cells, siRNA delivery was achieved specifically in leukemic cells. [42]

In another innovative application, Marasco, Abdel-Motal, and co-workers examined the utility of an anti-gp120 minibody in protecting against sexual transmission of HIV-1. [43] Through the use of an adeno-associated viral (AAV) vector, anti-HIV-1 gp120 minibody was introduced into cervico-vaginal epithelial cells. After secretion to the cell surface, the minibody binds HIV-1 gp120, resulting in sequestration of the virus and decreased infection.

1.3.4 Diabodies

A diabody is a complex consisting of two unconjugated singlechain fragment variables. [44,45] Although scFvs can be engineered to be multivalent with the addition of either chemical or genetic cross-links, it was found that reducing the scFv linker allowed for multimerization and stability. As in the case of minibodies, because scFv domains with differing targets can be mixed, bispecific recognition can be achieved.

Similarly to their larger minibody relatives, diabodies have relatively short in vivo half-lives, and thus could be better suited for imaging, because they can illuminate their targets and then be degraded and cleared. Additionally, the smaller size of diabodies, in relation to IgG and larger fragments, endows improved accumulation and penetration of tumors expressing relevant anti-

gens. [46, 47] With these characteristics in mind, most therapeutically relevant applications of diabodies have revolved around PET imaging. At present, diabody conjugates to PET labels have been validated for pancreatic cancer (anti-CAI9-9), anti-leukocyte cell-adhesion molecule (ALCAM/CD166), and breast cancer (anti-HER2). [48–50]

Diabody conjugates for imaging applications that involve binding of the extra domain-B (EDB) of fibronectin (a biomarker for angiogenesis/atherosclerotic plaque), carcinoembryonic antigen (CEA, a validated marker for gastrointestinal cancers), and Her2/Neu (a biomarker for both ovarian and breast cancers) have also been reported. [51–53]

1.4 Nanobodies: A camelid-derived scaffold

Heavy-chain IgGs (hcIgGs) produced in camelids differ from IgGs produced in other mammals. [54, 55] Although hcIgG is also a homodimer of two disulfide-linked heavy chains, with familiar CH2, CH3, and variable domains, it lacks a light chain. Binding between antigen and hcIgG, as for their IgG cousins, relies entirely on amino acids residing in loops (complementarity-determining regions, CDRs) of the single variable domain (referred to as V_HH in hcIgG, Figure 1.4a). Separating the CDR loops are four relatively sequence-homologous β-strands, which makeup the "framework region". [54] When separated from hcIgG, the V_HH domain is called a "nanobody" (Figure 1.4b), and an excellent review on their discovery and structure has been published. [56]

Nanobodies have many properties that make them particularly well suited as scaffolds for the directed evolution of new recognition in the laboratory. [57] These proteins are small (ca. 15 kDa), can be expressed in a folded and stable form with or without disulfide bonds in *E. coli*, and are easy to manipulate in the laboratory. An obvious difference between the variable regions of IgG and hcIgG is that binding is generated from amino acids in three loops in the hcIgG variant and in six loops in IgG (from heavy and light variable domains). However, hcIgG can compensate for this smaller apparent binding surface by expansion of CDR loops. For example, in comparison with IgG, nanobodies typically have longer CDR3 loops (ranging from eight to 24 residues) than

those found in mouse or human antibodies (nine and 12 residues, respectively). [58] The expanded CDR3 can dramatically increase the size of the paratope (the part of the protein that recognizes the epitope). This extended display architecture is generally credited with allowing nanobodies to bind surfaces that challenge or evade IgG, such as deep clefts within enzymes. [58, 59]

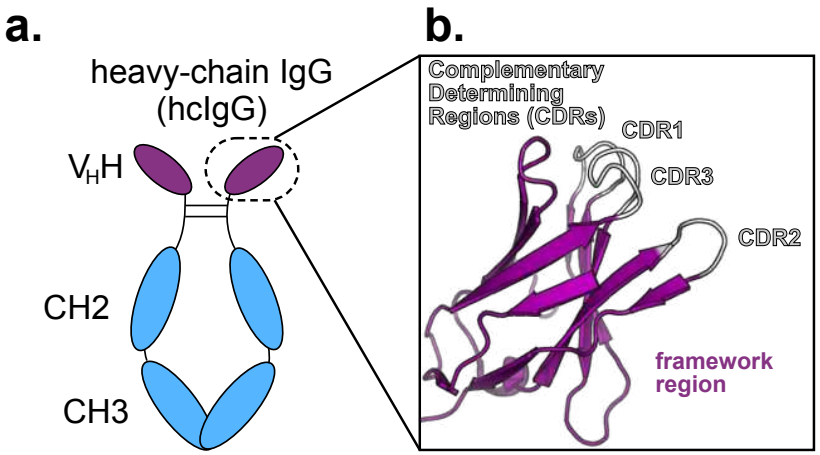

Figure 1.4: (a) The architecture of a heavy-chain IgG (hcIgG), which consist of two heavy chains (CH3, CH2, and V_HH), connected by disulfide bonds in the hinge region. (b) Nanobodies (a) GFP-binding nanobody is shown as an example, (PDB: 3OGO) are the V_HH domain of hcIgG, and consist of a framework region (purple) and complementary determining regions (CDRs, grey), where antigen recognition occurs.

1.4.1 Recent applications of nanobodies

Like their Fab fragment counterparts, nanobodies do not contain FcRn receptors and thus have relatively short in vivo half-lives. As a result, nanobodies can be used in situations such as bioimaging, in which relatively short half-lives and clearances are favored. Of course, this requires selective recognition of a disease-relevant cell surface biomarker. Probably one of the most widely studied and utilized biomarkers is the human epidermal growth factor receptor type 2 (HER2), which is overexpressed in ≈20–30% of breast and ovarian carcinomas. [60, 61] This tyrosine kinase receptor is responsible for cell proliferation, reduction in apoptosis, and enhanced cell mobility, making it an ideal extracellular model protein. A nanobody for the HER2 receptor has been developed (termed 5F7, K_D ≈0.1 nm) and used extensively for imaging and proof-of-concept nanobody technologies. [62, 63]

With no receptors to recruit NK cells or other immune system components present in the Fc region, nanobodies cannot illicit immune responses such as ADCC or CDC. One approach would be to fuse a nanobody to an Fc dimer. However, post-translational glycosylation of Fc is necessary to induce ADCC or CDC, and this requires expression in mammalian cells, thus complicating its preparation in the lab. To overcome this obstacle, our lab has prepared conjugates of small-molecule compounds and nanobodies that bind a target cell biomarker and recruit an antibody to the cell surface, resulting in ADCC (Figure 1.5a). [64] Specifically, using a combination of lipoic acid ligase bioconjugation and reactivity between a hydrazine and a protein-bound aldehyde, we coupled dinitrophenyl (DNP) to a previously reported [65] HER2-binding nanobody. As a result of human exposure to DNP, likely from DNP-containing dyes, preservatives, and/or pesticides, it is estimated that $\approx$1% of IgGs and IgMs recognize DNP, [66,67] and can thus recruit endogenous antibodies to a targeted cell. [68,69] Satisfyingly, when HER2- positive breast cancer cells (SK-BR-3) were treated with the nanobody activation immunotherapeutic, anti-DNP antibody and peripheral blood mononuclear cells (PBMCs) were recruited, triggering appreciable ADCC. Conversely, the nanobody activation immunotherapeutic did not induce ADCC for MB-MDA-231 breast cells that express low levels of HER2. Similarly, when either cell line was treated under conditions in which a component (the nanobody activation immunotherapeutic, anti-DNP antibody, or PBMC) was absent, no appreciable ADCC was detected (Figure 1.5b). [64]

Like most proteins, including antibodies, their fragments, and mimetics, nanobodies do not appreciably penetrate mammalian cells. This limits their recognition to cell-surface or excreted proteins. However, because of the robust nature of nanobodies, several intracellularly active nanobodies have been identified and remain functional in reducing environments, [70] such as the interior of a mammalian cell. In an effort to prepare nanobodies that actively penetrate mammalian cells, our laboratory recently performed polycationic resurfacing (mutation of solvent-exposed residues either to lysine or to arginine) on three separate nanobody frameworks (a resurfaced GFP-binding nanobody [71, 72] is shown as an example in Figure 1.5c). [73] Polycationic resurfacing does not appreciably alter expression in *E. coli*, folding, stability, or function (target recognition). However,

polycationic resurfaced nanobodies potently penetrate mammalian cells and reside in the cytosol. Thus, these new nanobody scaffolds likely represent a general solution for intracellular delivery of nanobodies that bind and modulate disease-relevant receptors that reside inside a cell.

Whereas nanobodies have largely been used to recognize large conformational regions on proteins, they can also be subjected to directed evolution to recognize small unfolded peptide epitopes. Recently, Rothbauer, Braun, and co-workers generated a nanobody called BC2-nb that recognizes a short linear epitope corresponding to residues 16–27 of β-catenin (BC2T). [74] The structure of this complex was solved by X-ray crystallography, revealing complete encapsulation of the epitope by an extended CDR3 loop (Figure 1.5d). This nanobody has shown utility as a reagent for capture and detection of BC2T-tagged proteins.

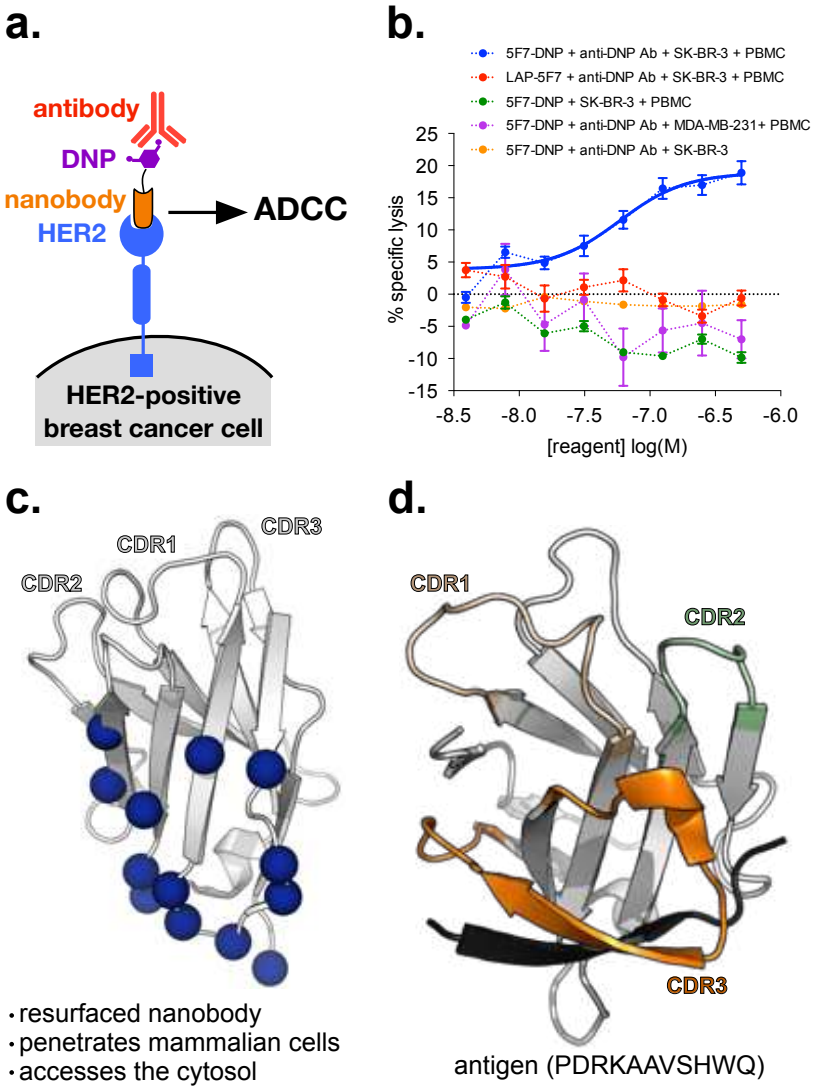

Figure 1.5: (a) Concept of a nanobody activation immunotherapeutic. A HER2-binding nanobody (orange) is chemically conjugated to DNP (purple), which is recognized by endogenous antibodies in human serum (red). Recruitment of antibodies to the surface of HER2-positive breast cancer cells leads to ADCC. (b) ADCC of high HER2-expressing SK-BR-3 cells (blue), but not of low HER2-expressing MB-MDA-231 cells (purple), triggered by the nanobody activation immunotherapeutic DNP-5F7. The unconjugated nanobody (LAP-5F7) is not toxic to SK-BR-3 cells (red). DNP-5F7 in the absence of anti-DNP antibodies (green) or PMBCs (orange) also does not trigger ADCC. Error bars represent standard error from three independent experiments. (c) Polycationic resurfacing of the nanobody framework region results in potent cell penetration and access to the cytosol. Residues highlighted with a blue sphere were mutated to either arginine or lysine (PDB ID: 3OGO). (d) Structure of a recently reported nanobody with an expanded CDR3 that is able to bind a small peptide antigen. (PDB ID: 5IVO)

1.5 Monobodies: A fibronectin-derived scaffold

All of the above examples (variations on the theme of Fab fragments and nanobodies) are derived from immunoglobulins (either IgGs or hcIgGs). These are contrasted with monobodies—scaffolds from the human-derived 10th fibronectin type III domain (FNfn10). With the aid of the FNfn10 scaffold, protein binding interactions can be fashioned to particular targets through loop interactions or side-and-loop interactions. Loops can be mutated and elongated with minimal stability loss, allowing for a large diversity of binding faces. Because they do not start from the usual protein scaffolds involved in adaptive immunity, monobodies can be made to bind to a variety of targets to serve many different functions while still being inherently nontoxic and immunogenic. First reported by the Koide lab in 1998, monobodies are essentially structurally simplified mimetics of a heavy-chain fragment variable, in that both present three binding loops for antigen recognition (Figure 1.6). [75] Monobodies do not contain disulfide bonds, are small (ca. 10 kDa) and generally stable, express well as soluble proteins in *E. coli*, and, due to the nature of the fibronectin type III structure from which monobodies are derived, can be used as a binding protein that mimics IgG V_H (Figure 1.6). Similarly to Fab fragments and nanobodies, monobodies are useful in binding to a specific target, but do not contain an Fc region, which would dramatically increase their serum stability. This results in monobodies generally being used as diagnostic tools to identify cell-surface biomarkers (where relatively quick clearance might be beneficial), and more recently as modulators of enzyme function and selectivity.

1.5.1 Recent applications of monobodies

Monobodies have been used as proteinaceous reagents to bind various disease-relevant macromolecules, resulting in the modulation, study, and characterization of complex cellular processes. For example, researchers have used monobodies that bind Fluc-type F^- channels to validate its unique mechanism of action for controlling intracellular levels of fluoride ion. [76–78] Monobody drug leads that bind structurally diverse disease-relevant targets have also been reported. For example, Kuhlman, Guntas, and co-workers used computational loop grafting of the BC and FG loops,

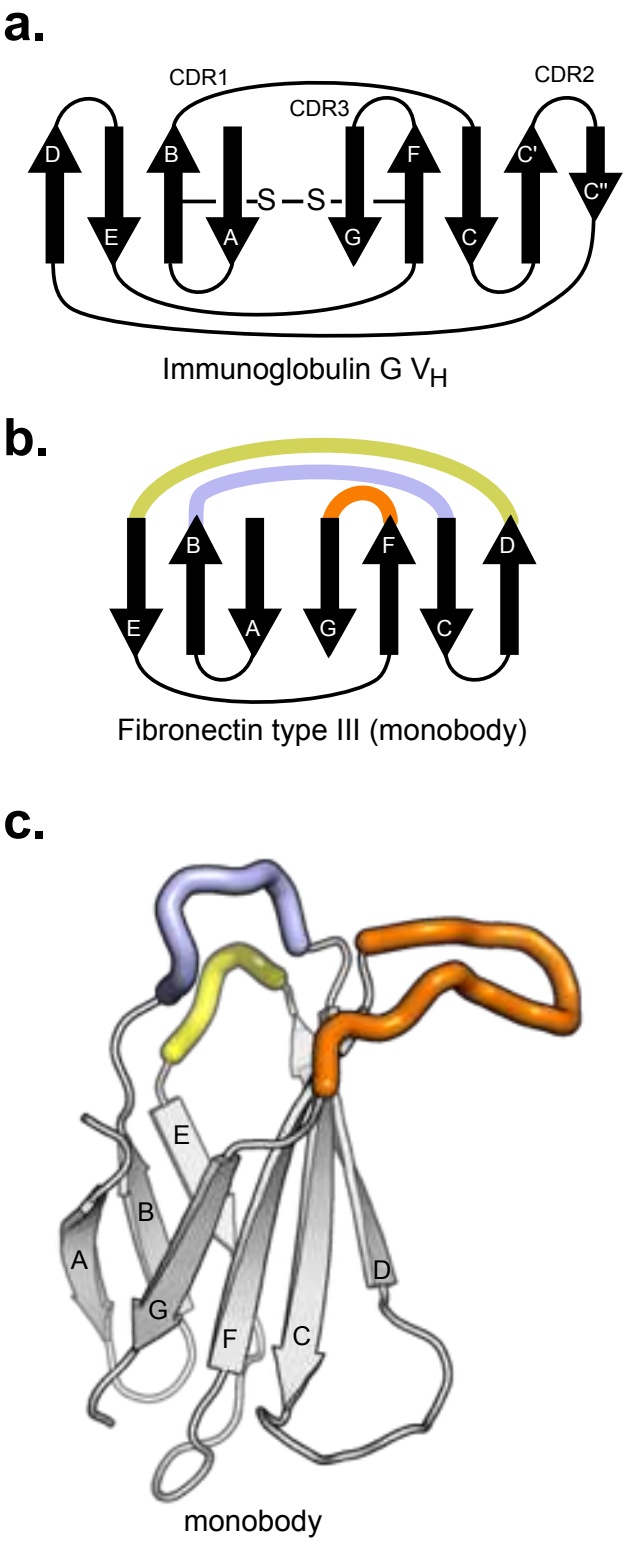

Figure 1.6: (a) Structural architecture of IgG V_H. (b) Structural architecture of the tenth fibronectin type III (monobody). (c) Structure of a monobody. Antigen binding loops are colored (PDB ID: 1FNF).

together with phage display, to engineer a monobody (R1) that binds to Kelch-like ECH-associated protein 1 (KEAP1) with a K_D of 300 pm. This monobody inhibits the interaction between KEAP1 and nuclear factor erythroid 2-related factor 2 (NRF2), resulting in activation of NRF2 [79]—a key regulator of cellular oxidative environments and an interaction associated with several disease states.

Monobodies have also been used as diagnostic reagents. For example, Hong, Park, and co-workers developed a monobody that binds to human EphA2 (hEphA2), an early marker for various tumors. [80] Whereas monobodies have largely been used to recognize and/or modulate the biological activation of specific proteins, they have more recently been applied to more diverse functions such as altered enzyme activity and biotechnology validation. In recent work, Koide, Tanaka, and co-workers showed that a monobody can alter an enzyme's specificity for its target, without modifying the amino acid sequence of the enzyme. [81] In particular, they found monobodies that were able to restrict β-galactosidase transgalactosylation yields of galacto-oligosaccharides (GOSs) to specific lengths rather than mixtures.

Very recently, in the context of extending phage-assisted continuous evolution [82] (PACE) to protein–protein interaction discovery, Liu, Badran, and co-workers re-evolved a monobody to bind the SH2 domain of ABL1. Beginning with a previously characterized mutant monobody (Tyr87Ala), which binds the SH2 domain target with dramatically lower affinity (100–1000- fold), continuous evolution through PACE was used to regain tight binding. [83]

1.6 Summary and Outlook

Proteins are increasingly being used in basic research and clinical settings to modulate disease-relevant receptors and to control cell function and fate. At present, half of the top 20 selling drugs are biologics, and many of these are antibodies and their conjugates. Relative challenges associated with the expression of full-length and chemically mature (post-translationally modified) antibodies in mammalian cell culture have motivated researchers to develop an array of minimalist antibody forms and mimetics. In this Chapter we have highlighted various forms of IgG fragments (Fab,

scFv, minibodies, diabodies), hcIgG-derived nanobodies, and fibronectin-derived monobodies as alternatives to full-length IgGs.

Specifically, scFvs, nanobodies, and monobodies are structurally simpler (lack disulfide bonds), easier to express in *E. coli*, and can be simpler to engineer and use in directed evolution than IgGs and IgG-derived counterparts. Moreover, the relatively small sizes of scFvs, nanobodies, and monobodies often correlate with greater tumor penetration, and thus, in some cases, this virtue could be used to improve the efficacy of tumor-targeted therapies (although challenges with relatively short in vivo lifetimes would remain an issue). Because long in vivo lifetimes are a key advantage of IgGs and derivatives that retain Fc, many applications of IgG derivatives lacking Fc, or of nonimmunoglobulin- derived proteins such as nanobodies and monobodies, include diagnostic and bioanalytical applications. However, smaller IgG-derived proteins that lack Fc, as well as nanobodies and monobodies, are particularly well suited for some medically relevant applications, such as bioimaging, because rapid clearance is not a major issue, or is even beneficial. Historically, full-length antibodies have been used as bioanalytical tools—western blot being an obvious example. However, relative challenges in the expression of these molecular Winnebagos opens the door for smaller and simpler proteins, and nanobodies have recently been used in this context. [74]

Full-length antibodies continue to enjoy application in immunotherapy and as conjugates to small-molecule therapeutics and imaging reagents, in which their primary job is to delivery these cargos selectively to diseased cells. [84] Owing to their simpler expression and ability to evolve in the laboratory, truncated structural forms of antibodies, and non-immunoglobulin mimetics play an increasingly important role in human health, the creative use of these proteins will continue to represent a growing area of protein science, biologics research, and therapeutic discovery. Use as an immunotherapeutic has sparked interest and much research has gone towards the developement of these engineered antibody mimetics.

Chapter 2

Antibody Mimetic Immunotherapeutics and Insight into the Effects of Multi-domain Antibody Recruitment

Adapted from:

Ta, A.N.; McNaughton, B.R., Future Medicinal Chemistry, 2017, 9, 1301.

Ta, A.N.; McNaughton, B.R., ChemBioChem, in preparation.

2.1 What are immunotherapeutics?

Immunotherapy is an approach to treating disease that relies on controlling the immune system. Immunotherapeutics are classified as either suppression immunotherapeutics, which reduce the immune response, or activation immunotherapeutics, which elicit the immune system to seek out and destroy diseased cells. Immunotherapy emerged as a field and therapeutic strategy with the development and administration of immune system suppressing small-molecule drugs (e.g., azathioprine, FK506, cyclosporin A and rapamycin). As immune system suppressants, these drugs have been used to treat inflammatory and autoimmune diseases, as well as to suppress rejection following organ transplant. Today, immunotherapeutics continue to be used to treat a multitude of inflammatory and autoimmune diseases. Over the last two decades, however, immunotherapeutics have also been developed to elicit immune system components to seek out and destroy numerous cancers.

Rarely has a therapeutic approach been the focus of so much attention, generated so much enthusiasm (inside and outside of the laboratory), and developed so rapidly – both within the global pharmaceutical industry and academic laboratories. It is difficult to overstate the impact immunotherapeutics have on human health, and their place in modern pharmaceuticals. Of the top

ten selling drugs in 2015 [85], six are characterized, at least in part, as having an immunotherapeutic mechanism of action (Humira™, Enbrel™,Remicade™, Rituxan™, Herceptin™ and Revlimid™).

2.2 Biologics as immunotherapeutics

In addition to witnessing an explosion of immunotherapeutics into the market, the past two decades have also witnessed the age of biologics – principally protein drugs. Historically, disease has been treated with small-molecule drugs. However, in contrast to their small-molecule counterparts, the size and complexity of proteins often result in surfaces capable of recognizing disease relevant receptors that challenge or evade small molecules. Additionally, proteins can be evolved (either *in vivo* or in the laboratory) to selectively and potently bind virtually any disease-relevant receptor. This initial discovery process is often much simpler, and less expensive, than the analogous small-molecule centered approach. By virtue of these facts, it is perhaps unsurprising that advances in immunotherapy and biologics have dovetailed – and this relationship has led to new immunotherapeutics and drug leads.

2.3 Antibody immunotherapeutics

Principally, biological immunotherapeutics are full length immunoglobulins of the isotype G (IgG, referred to herein as antibodies). These include topselling drugs Humira, Remicade, Rituxan and Herceptin. Antibodies are large (≈150 kDa) multi-domain proteins [2]. In the context of immunotherapeutic activity and pharmacology, antibodies have two important regions. Recognition of a binding partner occurs within the fragment antigen-binding (Fab) region, which consists of heavy- and light-chain domains. Specifically, binding interactions are the result of sequence optimization of loops, so-called complimentary determining regions (CDRs) within the variable light-chain and variable heavy-chain domains (V_L and V_H, respectively) [86]. Some antibodies can act as suppression immunotherapeutics by binding to, and thus sequestering, immune-stimulating polypeptides. For example, Humira is a full-length monoclonal antibody that binds to TNF-α,

which in the absence of Humira forms a complex with TNF-α receptors [87] and activates an inflammatory response. Given the ability of this drug to inhibit the TNF-α/TNF-α receptor complex, Humira is an effective treatment for autoimmune and inflammatory diseases, including rheumatoid arthritis, psoriatic arthritis, ankylosing spondylitis, Crohn's disease, plaque psoriasis, ulcerative colitis, chronic psoriasis, hidradenitis suppurativa, juvenile idiopathic arthritis and noninfection uveitis. Similarly, Remicade is a TNF-α binding antibody, and thus an effective treatment for many autoimmune and inflammatory diseases [88].

The *in vivo* half-life of antibodies (ca. $\approx$21 days) is much longer than most proteins [86]. This virtue is endowed by an epitope in the fragment crystallizable region (Fc), which binds the neonatal Fc receptor, FcRn, in a pH-dependent manner. Formation of the Fc/FcRn complex leads to a complicated process that continuously shuttles the antibody from the circulatory system to the cell interior (within endosomes) and back again. As a result of this biological shell game, antibodies evade degradation by serum and lysosomal proteases [4, 5]. A region found within Fc is also necessary to induce activation immunotherapeutic mechanisms, such as antibody-dependent cellular cytotoxicity (ADCC) [8,9] or complement-dependent cytotoxicity (CDC) [10, 11]. Specifically, Fc γ-receptors on the surface of immune effector cells, such as natural killer cells and macrophages, recognize Fc in antibodies that are bound to disease-relevant receptors on the surface of targeted cells (via interactions involving CDRs within the Fab fragment). Following Fc–Fc γ-receptor complex formation, the immunoreceptor tyrosine-based activation motif is phosphorylated, triggering activation of the effector cell and release of perforin, lytic enzymes, TNF and/or granzymes for cell destruction through ADCC. In CDC, C1q of complex C1 binds to the Fc region and triggers the complement cascade activation and eventual formation of membrane attack complex at the surface of the target cells. Ultimately, this leads to lysis of the antibody-bound cell.

Current activation immunotherapeutics include Herceptin, a monoclonal antibody that binds to an extracellular domain of HER2, a biomarker that is overexpressed on the surface of approximately 20–30% of breast cancers and gastric cancers [89]. In addition to other therapeutic mechanisms, experiments on laboratory animals show that Herceptin recruits immune system compo-

nents to HER2-positive cells, resulting in cell-selective ADCC. In a similar vein, Rituxan is a monoclonal antibody that binds CD20 on the surface of normal and malignant B cells, leading to, among other outcomes, ADCC and CDC [90]. As an activation immunotherapeutic that facilitates selective destruction of B cells, Rituxan principally finds use in fighting cancers of the blood, such as non-Hodgkin's lymphoma and chronic lymphocytic leukemia. However, the story is more complex: Rituxan can also act as a suppression immunotherapeutic. Since Rituxan leads to destruction of B cells – a critical component of the immune system – this drug suppresses the immune response. As a result, Rituxan is also an effective therapeutic for a number of autoimmune diseases such as rheumatoid arthritis.

2.4 Antibody mimetic immunotherapeutics

While regions within full-length antibodies enable tailored recognition, long serum stability and activation immunotherapeutic activity, the complex structure and post-translational modifications of these molecular behemoths complicate their production and manipulation. In response, researchers have developed minimalist antibodies and antibody mimetics. A number of small (<20 kDa) proteins that mimic CDR display within antibody Fab fragments have been reported. Evolution of these CDR loop mimics, using methods like phage display, often leads to new proteins with tailored recognition – including recognition of disease-relevant cell surface biomarkers. Popular examples include monobodies [75] – a fibronectin type III-derived protein scaffold – and affimers [91] – a phytocystatin-derived protein scaffold. In addition to these non-antibody scaffolds, researchers have relied on nanobodies [56] – the fragment antigen-binding region in camelid-derived heavy-chain IgG (which lacks a light chain). In contrast to antibodies, these proteins often have a relatively small number of disulfide bonds (or none at all), are not post-translationally glycosylated, express well in bacteria or yeast and are relatively stable. Collectively, these features simplify their production and manipulation. In addition, their small size, relative to full-length antibodies, can result in improved tumor penetration [21].

Antibody mimetics are often simpler to prepare and manipulate, but lack Fc. As a result, these proteins experience relatively short lifetimes *in vivo*, and do not induce or activate the immune system. Recently, however, protein engineers have used techniques such as sequence-selective chemical conjugation and/or genetic fusion as a means to generate nonantibody proteins with dramatically improved *in vivo* stability, and potent activation immunotherapeutic activity.

One approach to turning on activation immunotherapeutic activity is to incorporate a component (such as a small molecule) that recruits an endogenous antibody (which contains Fc and thus can recruit immune effector cells). Fortunately, a number of small molecules have been reported that bind endogenous antibodies. For example, researchers have shown that antibodies recognizing dinitrophenyl (DNP) constitute approximately 1% of circulating IgM and approximately 0.8% of circulating IgG, likely due to exposure to DNP-containing dyes, preservatives and/or pesticides. Recently, we showed that sequence-selective bioconjugation of a DNP containing molecule to a HER2-binding nanobody led to a new immunotherapeutic that potently and selectively destroys HER2-positive breast cancer cells in culture, via ADCC [64].

Of course, since nanobodies lack Fc, these therapeutic leads undoubtedly have relatively short *in vivo* stability compared with IgG antibodies. However, a number of strategies have been reported that dramatically improve the *in vivo* stability of nonantibody proteins. These include chemical conjugation to PEG (PEGylation), fusion to Fc or genetic fusion to human serum albumin (HSA)-binding peptides or proteins [92]. The development of nanobody-based immunotherapeutics with improved serum stability is a major focus of many pharmaceutical companies. For example, recently Ablynx reported nanobody-based immunosuppressant drug leads, which are now in clinical trials. Since nanobodies are amenable to extensive mutagenesis and manipulation, scientists have been able to genetically link them to proteins that endow properties, such as long *in vivo* stability, and multivalent recognition. For example, Vobarilizumab™ consists of an IL-6R-binding nanobody that is genetically fused to an HSA-binding nanobody [93]. Recognition of IL-6R blocks the IL-6R/IL-6 interaction, leading to a blockage of the inflammatory response. In concert, the HSA-binding nanobody component allows the drug to find residence on HSA, an abundant (35–50

g/l) protein in blood. As a result, the HSA-bound drug essentially hides from serum proteases and enjoys a relatively long lifetime *in vivo*. Similarly, Ablynx has also reported a nanobody-based immunotherapeutic that targets two different diseaserelevant receptors. ALX-0761 (M1095) is an anti-IL-17A/F nanobody designed to treat autoimmune disorders such as psoriasis [94]. This nanobody-based fusion protein consists of an anti-IL-17F nanobody, anti-HSA nanobody and anti-IL-17A/F nanobody – resulting in a 40-kDa trivalent suppression immunotherapeutic that neutralizes proinflammatory cytokines, IL-17A and IL-17F. While optimization of nanobody-based fusions, such as overcoming sequestration of smaller proteins (MW <40 kDa) by the kidneys, is certainly necessary, this new frontier in immunotherapeutic design and discovery will undoubtedly lead to new therapies.

2.5 An Immunotherapeutic Cocktail of Biologics

Decades ago, a handful of small-molecule drugs capable of suppressing the immune system ignited the field of immunotherapy. As molecular and cellular biology techniques rapidly evolved, enabling cloning and large-scale production of proteins, recombinant antibody drugs joined the effort. As a result, immunotherapeutics represent a significant – and growing – sector of the global pharmaceutical industry. Most recently, researchers with expertise in protein engineering and bioconjugation are developing new antibody mimetics with long serum stability and/or activation immunotherapeutic activity. These biologics represent a new class of suppression or activation immunotherapeutics, and will undoubtedly have a significant impact on the future of human health.

However, a challenge with developing immunotherapeutic biologics is potency and efficiency. We attempted to address this issue by developing a non-antibody activation immunotherapeutic cocktail of biologics. The cocktail allows for the use of proteins that recognize different domains of extracellular HER2. Multi-domain binding provides an increase in antibody recruitment. However, the increased effect of antibody recruitment does not correlate to effector cell recruitment for targeted cell death. This may be due to the locations of antibody recruitment to HER2 and the steric interferences of effector cell recruitment.

Half of the top 10 selling drugs of 2017 are biologics. [95] Principally, biological immunotherapeutics are full-length immunoglobulins of isotype G. One of which is Herceptin (Trastuzumab) that binds to human epidermal growth factor receptor 2 (HER2), an overexpressed receptor in ≈20-30% of breast cancers. [89]

Antibodies are large (≈150 kDa) multi-domain proteins that have three important areas in the context of therapeutics. Recognition of a binding partner occurs within the fragment antigen-binding (Fab) region specifically from loops known as complimentary determining regions (CDRs). In vivo half-life (≈21 days) is achieved by an epitope in the fragment crystallizable (Fc) region that binds the neonatal Fc receptor (FcRn). Another region found within Fc is necessary for an immunotherapeutic response through mechanisms such as antibody-dependent cellular cytotoxicity (ADCC) and compliment-dependent cytotoxicity (CDC). [86]

Fc is recognized by Fc gamma receptors (FcγR) on effector cells such as Natural Killer (NK) cells. Upon binding, immunoreceptor tyrosine-based activation motif (ITAM) is phosphorylated which then triggers activation of the effector cell and release of perforins, lytic enzymes, tumor necrosis factor (TNF), and/or granzymes for cell destruction through ADCC. [86] Effector cells cannot be activated by the binding of one antibody to a single FcR, but rather a particular threshold must be met. [96]

Though full-length antibodies provide specific recognition, long in vivo half-life, and immunotherapeutic activity, the multi-domain structure and post-translational modifications makes production and manipulation challenging.

In response, researchers have been developing and optimizing minimalist antibodies and antibody mimics. These smaller proteins are evolved to contain specific recognition, mimicking the Fab region. However, due to the lack of Fc, they have relatively short lifetimes in vivo and do not have immunotherapeutic activity. These functions can be engineered in through chemical conjugations and/or genetic fusions. An important aspect of installing immunotherapeutic activity for non-antibody proteins is ensuring potency and efficiency. For antibodies, this has been done by

improving therapeutic benefits through enhancing ADCC. The main strategy has been to modify the Fc portion of antibodies to increase binding affinity to activating effector cell receptors. [97]

But recently, Herceptin has been paired with Perjeta (Pertuzumab) and been shown to improve survival in women diagnosed with early stage HER2-postive breast cancer. It has also been shown to improve survival in women diagnosed with HER2-positive metastatic breast cancer. Herceptin inhibits HER2 dimerization and Perjeta inhibits HER2 heterodimerization with other HER family receptors, blocking the enhanced growth rate due to increase in cellular signaling as a result of overexpressed HER2. [98, 99] Herceptin and Perjeta bind to different domains on the extracellular portion of HER2 and both induce ADCC. It has been shown that the use of both antibodies provides a minimal increase in ADCC over the use of one. [100, 101] This combination therapeutic has shown the possibility of improved potency and efficiency of ADCC through multi-domain binding to HER2.

With the slight improvement in ADCC with the use of two antibodies, we were interested in seeing the effects of three antibodies. To gain insight into this strategy we used easily expressible and purifiable antibody mimics. We have developed an activation immunotherapeutic cocktail of antibody mimics with multivalent recognition. Each protein binds to different domains on HER2 and recruits antibodies, leading to effector cell recruitment and targeted cell death. However, although multi-domain binding allows for more efficient recruitment of antibodies, this does not directly correlate to more potent and efficient cell death.

2.6 Results and Discussion

2.6.1 An immunotherapeutic cocktail that targets spatially distinct regions on extracellular HER2 leads to an increase in antibody recruitment to HER2-positive breast cancer cells.

The extracellular portion of HER2 consists of four domains. We used two nanobodies (5F7 and 2Rs15d) and one affibody (ZHER2). Each bind to HER2 at a different domain with excel-

lent affinity (K_D ≈510 pM, ≈7 nM, and ≈20 pM respectively) [65, 102–104]. To each of these HER2 binding proteins there is an antibody recruiting component that could ultimately recruit effector cells. To ensure functionality of a multi-domain binding system, a His6 tag was used as the antibody recruiting component (Figure 2.1a).

When fused to a His6 tag, each protein fusion recruits His6 binding antibody (Figure 2.1b) and can recruit FITC-labeled His6 antibody to the surface of HER2-positive breast cancer cells (Figure 2.1c). We see a hook effect [105], which is typically observed in immuno- and related assays which are 3 body systems. Each protein fusion bound HER2-positive breast cancer SK-BR-3 cells with a half maximal effective concentration (EC50) of ≈7 nM. MDA-MB-231 cells low in HER2 were not recognized by anti-His6 antibody.

We observed high levels of SK-BR-3 cell fluorescence following incubation with ≈30 nM His6 fusion proteins and anti-His6-FITC antibodies. In contrast, when SK-BR-3 cells were first treated with HER2-targeting siRNA, leading to decreased cellular levels of HER2, we observed decreased levels of cellular fluorescence, indicating the decrease in HER2 prevents protein recruitment and ensure the specificity of our proteins for HER2 (Figure 2.1d).

Importantly, we observe increased anti-His6-FITC recruitment for cells treated with one, two, or all three of the HER2 binding His6 fusion proteins. The hook begins ≈30 nM for each protein individually, however with the use of protein mixtures you not only see an increase in antibody recruitment at the same total concentrations (ref. SI), but this allows for higher total concentrations of proteins to be used without seeing the decrease in affect. Specifically, for an individual protein at 30 nM you see a mean fluorescence of ≈200. Using two proteins at a total of 30 nM (15 nM each protein), you see a mean fluorescence ≈350. Using two proteins at 30 nM each (60 nM total protein), you see a mean fluorescence ≈400, whereas one protein at 60 nM you see a mean fluorescence ≈200. The use of 3 proteins allows for an even greater increase in recruited antibodies. This suggests that each protein is able to recruit anti-His6-FITC when used as a cocktail, resulting in a high effective concentration of recruited antibodies to the cell surface. Cells low in HER2 are shown to not recruit antibodies to the cell surface (Figure 2.1e).

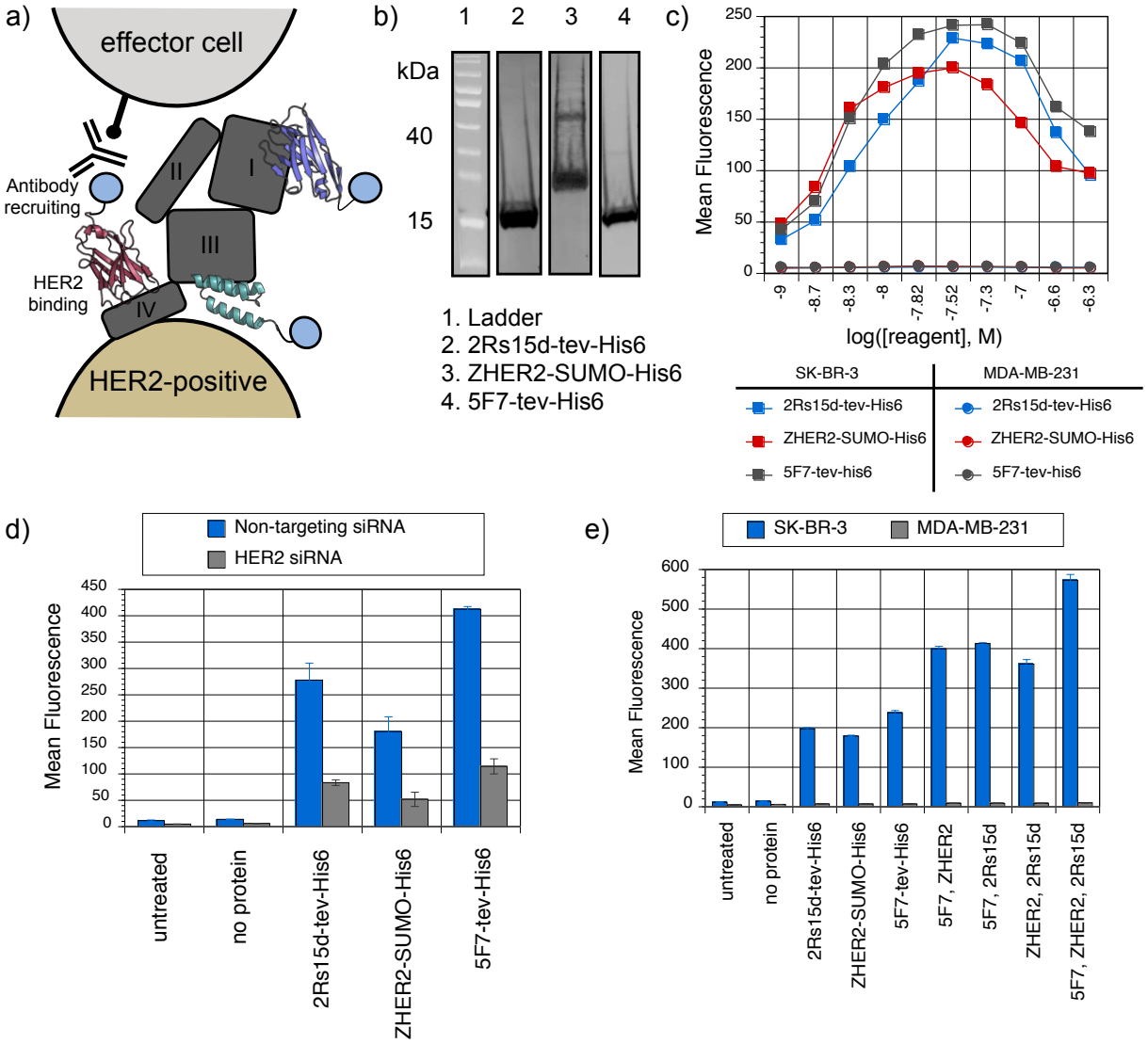

Figure 2.1: An immunotherapeutic cocktail that leads to an increase in antibody recruitment. (a) Representative figure of two nanobodies (5F7 PDB : 3OGO*, 2Rs15d PDB : 5MY6) and an affibody (ZHER2 PDB : 3MZW) binding to HER2. Each protein has a high affinity for separate domains on HER2 (5F7 with domain IV, $K_D \approx$510 pM; 2Rs15d with domain I, $K_D \approx$5 nM; ZHER2 with domain III, $K_D \approx$22 pM). Each protein contains a His6 tag as an antibody recruiting component that can ultimately recruit effector cells to target cell. (b) Recognition of proteins on western blot using a commercial anti-His6 antibody. (c) Determination of the half maximal effective concentration (EC50) of recruitment of FITC labeled anti-His6 antibodies to the surface of HER2 positive SK-BR-3 cells by flow cytometry (d) Selective recruitment of FITC labeled anti-His6 antibodies to HER2 overexpressing SK-BR-3 cells. (e) $\approx$3x increase in antibody recruitment when proteins are used in combination versus individually. *GFP nanobody PDB used

2.6.2 Increase in antibody recruitment through multi-domain binding to the cell surface does not have a direct correlation to effector cell recruitment and activation for targeted cell death.

The use of an immunotherapeutic cocktail consisting of three proteins each binding to a separate domain on HER2 allows for an increase in antibody recruitment, but not effector cell recruitment to HER2-positive breast cancer cells. With an ADCC reporter bioassay we actually observe a decrease in effector cell activation using the mixture of 3 proteins. The combination of 5F7 and ZHER2 shows a slight increase in effector cell activation as compared to an individual protein. (Figure 2.2)

Antibody properties such as FcγR affinity [106], binding level [107, 108], and location [109] have studied effects on effector cell mechanism and efficiency and can help explain the results of the protein fusion cocktail. Location of the recruited antibody can have an important influence in cell death. Proximity to the cell surface is crucial for ADCC. [109] 5F7 binds to the same domain as Herceptin and is more proximal to the membrane. This possibly allows for more efficient ADCC than the other 2 HER2 binding proteins. ZHER2's location appears to be proximal to the membrane as well, but with the addition of the SUMO tag for purification purposes this may affect the ADCC efficiency. The lower activation signal may also be caused by the steric hinderance of the location of domain III and the ability to recruit effector cells effectively to that location. Sterics may also be a factor [110, 111] influencing effector cell activation. SK-BR-3 cells have $\approx$1.6x10^6 HER2/cell. [112] Each HER2 with the cocktail can have 3 antibodies recruited to it (as shown with flow cytometry data), but sterically this may not in tern recruit three effector cells to HER2. In order to activate effector cells, there is a threshold antibody binding that must occur. In theory, the more antibodies bound allows for more effector cell binding options, however, the increase in antibodies bound to target cells may actually be preventing or blocking effector cell binding. Another option is due to 2Rs15d being furthest from the membrane effector cells are binding most to the antibody recruited to domain I. Due to location being important for ADCC, effector cells recruited to domain I would decrease the efficiency of effector cell activation for ADCC. This

would also explain why without the use of 2Rs15d in the combination of 5F7 and ZHER2 we see a slight increase in ADCC activation.

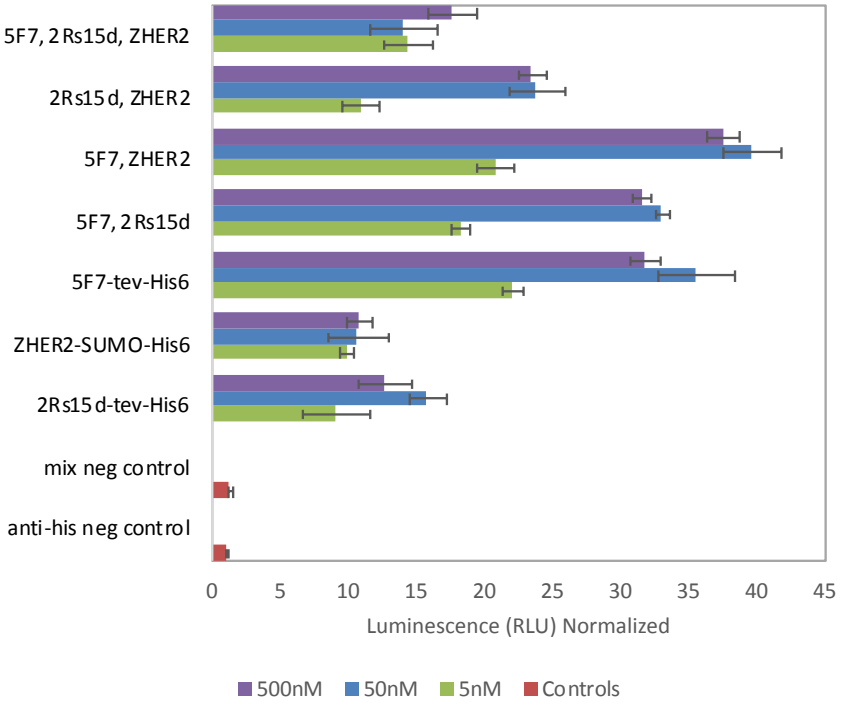

Figure 2.2: ADCC assay using the immunotherapeutic cocktail showing that increase in antibody recruitment does not correlate to effector cell recruitment and activation for cell death. Results were normalized to anti-his negative control and done in triplicate.

2.7 Conclusion

We have developed an immunotherapeutic cocktail with multivalent recognition of HER2 and antibodies. The multi-domain binding cocktail shows that although there is an increase in antibody recruitment, location and sterics prevent the same affects for effector cell recruitment and targeted cell death. The therapeutic strategy of increasing antibodies for more cell death may still be a good approach, however, a better understanding of the system is necessary. The combination effect of Herceptin and Perjeta were minimal for ADCC [100, 101] and benefits in the combination is due to more factors such as prevention of HER2 dimerization. The idea of therapeutic cocktails can

still be beneficial, but alternative approaches keeping in mind location, sterics, and mechanism will be required moving forward. An understanding for what improves or weakens this mechanism is important for the development of more effective and potent immunotherapeutics.

2.8 Experimental Details

2.8.1 Protein Expression and Purification

Proteins were expressed in *E. coli*. Bacteria was grown in lysogeny broth (LB, 1L) containing carbenicillin (1mL of 0.1g/mL) to an OD_{600} ≈0.5 and induced with Isopropyl β-D-1-thiogalactopyranoside (IPTG, 1mM) at 20 °C overnight. Cells were collected by centrifugation, resuspended in phosphate buffer containing a protease inhibitor tablet. Cell suspension was subjected to a freeze-thaw cycle at -20 °C and sonicated. Lysate was cleared by centrifugation and the supernatant was incubated with Ni-NTA agarose resin. Resin was collected and washed with phosphate buffer containing imidazole (25mM and 50mM) then eluted with buffer containing 400mM imidazole. Proteins were then dialyzed and analyzed for purity.

2.8.2 Flow cytometry

Mammalian cells were grown in T-75 flasks at 37 °C with appropriate CO_2 levels. Cells were washed with DPBS then detached using Trypsin. Cells were pelleted and resuspended in flow cytometry buffer (DPBS + 2% BSA) at 60,000 cells per 50μL. Cell solution was added to 100μL of protein solution, immediately followed by addition of anti-6X His tag FITC antibody (1:150). Mixture was incubated over ice for 30 minutes then washed with flow cytometry buffer prior to flow cytometry analysis.

2.8.3 Antibody-Dependent Cellular Cytotoxicity

Measured according to Promega's ADCC Reporter Bioassays, V Variant kit protocol. High-HER2-expressing breast cancer cells were plated 15,000 cells per well in 100μL media volume (McCoys 5a 10% FBS) 20-24 hours before assay. Cells were incubated with protein cocktail at a

variety of concentrations and 15μg/mL Anti-His-Tag Chimeric antibody for 1 hour at 37 °C 5% CO_2. Effector cells were then added at a 5:1 ratio of E:T cells and incubated for 6 hours at 37 °C 5% CO_2. Bio-Glow Luciferase was added prior to measuring on plate reader.

2.9 Supporting Information

2.9.1 Materials

SK-BR-3 cells, American Type Culture Collection (ATCC, Cat. No. HTB-30)

MDA-MB-231 cells, ATCC (Cat. No. HTB-26)

McCoy's 5A modified medium, Corning (10-050-CV)

L-15 Leibovitz Media, HyClone (SH30525-01)

RPMI 1640 w/ Hepes, Gln, Corning (10-041-CV)

HyPure Cell Culture grade water, HyClone (SH3052902)

Dulbecco's Phosphate Buffered Saline Solution, HyClone (SH3002802), Corning (21-031-CV)

Phosphate-Buffered Saline, 1X, Corning (21-040-CV)

Trypsin 0.25%, HyClone (SH3004201)

Fetal Select Bovine Serum, Atlas Biologicals (FS-0500-AD)

iBlot Transfer Stack, PVDF, mini, Life Technologies (IB4010-02)

96-Well Microplates, Tissue Culture-Treated with Lid, White with Clear Bottom, Sterile, Individually Wrapped, Corning (3610)

96-Well Microplates, Tissue Culture-Treated with Lid, Clear with Flat Bottom, Sterile, Individually Wrapped, costar (3596)

6-Well Clear plates, costar (3516)

ADCC Reporter Bioassays, V Variant Complete and Core kit, Promega (G7014, G7010, provided by Promega)

ON-TARGETplus human ERBB2 siRNA, Dharmacon

ON-TARGETplus non-targeting control siRNA #1, Dharmacon

5X siRNA Bufer, Dharmacon

Dharmafect 2 siRNA transfection reagent, Dharmacon

Anti-6X His tag antibody (FITC), Abcam (ab1206)

Anti-6X His tag antibody [HIS.H8], Abcam (ab18184)

Anti-His-Tag Chimeric antibody, Human monoclonal (SAB5600096 Sigma)

Donkey Anti-Mouse IgG H&L (Alexa Fluor® 790), Abcam (ab186699)

Goat Anti-Human IgG (Fab')2 (HRP), Abcam (ab87422)

Herceptin (provided by Melissa Gray)

Bovine serum albumin (BSA), RPI (A30075)

LB Miller Broth, Fisher (BP9723-5)

Agar, Fisher (BP1423-2)

Restriction Enzymes, NEB

Oligonucleotides, IDT

G-Blocks, IDT

Carbenicillin, GoldBio Technology

Isopropyl-b-D-1-thiogalactopyranoside (IPTG), GoldBio Technology

Snakeskin Dialysis Tubing 10K MWCO, Thermo Scientific

HisPur Ni-NTA Resin, Thermo-Scientific Pierce

Quick Ligation Kit, NEB

Miniprep Kit, OMEGA

PageRuler Prestained Protein Ladder, Thermo Scientific

12% Ready Gel precast gels, Biorad

SHuffle T7 Express Competent E. coli, NEB

5-α chemically competent E. coli, NEB

BL21 (DE3) chemically competent E. coli, NEB

Sodium Chloride

Sodium Phosphate Dibasic

Sodium Phosphate Monobasic

Imidazole

Odessey Blocking Buffer, Li-Cor

Non-fat instant dry milk

Trypan Blue

2.9.2 Instrumentation

CyAn ADP Flow Cytometer, Beckman Coulter

FlowJo, LLC 10.4.2 software

Synergy 2 Microplate Reader, Biotek Inc.

Avanti centrifuge, Beckman Coulter

Allegra x-15R Centrifuge, Beckman Coulter

Microfuge 18 Centrifuge, Beckman Coulter

MJ mini gradient thermal cycler, Biorad

Clinical 200 Centrifuge, VWR

Centrifuge 5418, Eppendorf

VistaVision Microscope, VWR

Q125 Qsonica sonicator

Molecular imager gel doc XR+ system, Biorad

Innova 42 incubator shakers, New Brunswick Scientific

Excella E25R incubator shakers, New Brunswick Scientific

TC20 Automated Cell Counter, BioRad

NanoDrop 2000 UV-Vis Spectrophotometer, Thermo Scientific

Odyssey CLx near IR Scanner, Li-Cor

iBlot gel transfer station, Invitrogen

symphony B10P pH meter, VWR

2.9.3 Western Blot

2Rs15d-tev-His6, ZHER2-SUMO-His6, and 5F7-tev-His6 were run on a 12% protein gel, then transferred to a PVDF membrane using Invitrogen's iBlot gel transfer station. The membrane was blocked with instant nonfat dry milk in PBS (2g/10mL) for 45 minutes shaking at room temperature. The membrane was then incubated with 4μL anti-6X His tag antibody in 8mL Odyssey Li-Cor blocking buffer overnight shaking at 4 °C. Membrane was then washed with PBS, PBS + 0.1% Tween-20 three time with shaking for 5 minutes each time, and PBS. The membrane was next incubated with 1μL donkey anti-mouse Alexa Fluor 790 in 10mL Odyssey Li-Cor blocking buffer for 1 hour shaking at room temperature, followed by the washing steps and imaging on an Odyssey near-IR scanner.

2.9.4 Flow Cytometry (EC50, siRNA knockdown, Cocktail mixture)

General procedure:

Cells (SK-BR-3 or MDA-MB-231) were cultured in T-75 flasks at 37 °C and appropriate CO_2 levels (5% for SK-BR-3, 0% for MDA-MB-231) until about 90% confluency. Cells washed with DPBS (1 x 5mL), detached with Trypsin (5mL) for 5-10 minutes at 37 °C, pelleted (1000g for 5min), and resuspended in 1mL of flow cytometry buffer (DPBS + 2% BSA). Cells were counted in the presence of Trypan Blue using the T20 Automated Cell Counter then diluted to achieve 60,000 cell per 50μL. 50μL cell solution was added to 100μL of protein solution in flow cytometry buffer, immediately followed by the addition of anti-6X His tag FITC antibody (1:150). Mixture was incubated over ice for 30 minutes. Cells were then washed by the addition of 850μL flow cytometry buffer, pelleted, resuspended in 300μL, and pelleted. Samples were stored on ice as pellets and resuspended in 200μL flow cytometry buffer right before analysis on a CyAn ADP flow cytometer.

Half maximal effective concentration (EC50):

Protein concentrations used were 500nM, 250nM, 100nM, 50nM, 30nM, 15nM, 10nM, 5nM, 2nM, and 1nM.

siRNA knockdown:

HER2 expression on SK-BR-3 cells was siRNA knocked down according to Dharmacon's protocol. SK-BR-3 cells were plated into 6-well clear plates at $2x10^5$ cells/well with a volume total of 2mL. Cells were incubated at 37 °C 5% CO_2 for 12h to allow to adhere to the plate. siRNAs (ON-TARGETplus human ERBB2 and ON-TARGETplus non-targeting control) were transfected at a final concentration of 25nM in 6-well plates containing the cells and incubated at 37 °C 5% CO_2. Media was changed after 24 hours and incubated for an additional 72 hours. Cells were analyzed for HER2 expression by flow cytometry using 30nM of proteins.

Cocktail mixture:

Each protein concentration was at 30nM. Cocktail mixtures included each individual protein at 30nM.

2.9.5 Antibody-Dependent Cellular Cytotoxicity Assay

Cell death by antibody-dependent cellular cytotoxicity was measured using Promega's ADCC Reporter Bioassays, V Variant kits. Protocol according to Promega. SK-BR-3 cells were plated to 96-Well, White with Clear Bottom Microplates at 15,000 cells per well in 100uL media volume (McCoys 5a 10% FBS) 20-24 hours before assay. Cells were incubated with 5nM, 50nM, or 500nM of protein(s) in 25μL volume with 25μL of 15μg/mL Anti-His-Tag Chimeric antibody for 1 hour at 37 °C 5% CO_2. Effector cells were added at a 5:1 ratio of E:T cells in 25μL volume and incubated for 6 hours at 37 °C 5% CO_2. Bio-Glow Luciferase was added and incubated at RT for $\approx$20 minutes before measuring on plate reader at an integration time of 0.5sec/well.

2.9.6 Protein sequences

5F7-tev-His6:

GEVQLVESGGGLVQAGGSLRLSCAASGITFSINTMGWYRQAPGKQRELVALISSIGDTYYA
DSVKGRFTISRDNAKNTVYLQMNSLKPEDTAVYYCKRFRTAAQGTDYWGQGTQVTVSSE
NLYFQGHHHHHH

2Rs15d-tev-His6:

GQVQLQESGGGSVQAGGSLKLTCAASGYIFNSCGMGWYRQSPGRERELVSRISGDGDTW
HKESVKGRFTISQDNVKKTLYLQMNSLKPEDTAVYFCAVCYNLETYWGQGTQVTVSS EN
LYFQGHHHHHH

ZHER2-SUMO-His6:

GVDNKFNKEMRNAYWEIALLPNLNNQQKRAFIRSLYDDPSQSANLLAEAKKLNDAQAPK
GGSGGSSDSEVNQEAKPEVKPEVKPETHINLKVSDGSSEIFFKIKKTTPLRRLMEAF AKRQ
GKEMDSLRFLYDGIRIQADQTPEDLDMEDNDIIEAHREQIGGATYGSHHHHHH

2.9.7 Protein expression and purification

All amplicons were cloned into a pETDuet-1 plasmid using restriction enzymes NcoI and KpnI. DNA sequences were confirmed by QuintaraBio. 5F7 and 2Rs15d containing DNA were transformed into SHuffle T7 (ST7) *E. coli* for protein production. ZHER2 containing DNA was transformed into BL21 (DE3) *E. coli* for protein production. Overnight starter cultures were grown in LB containing carbenicillin and placed at the appropriate temperature (30 °C for ST7, 37 °C for BL21) shaking at 200 RPM. Overnight starter cultures were used to inoculate 1 L of LB containing carbenicillin (1mL of 0.1g/mL) at 30 °C/37 °C shaking at 200 RPM to an OD_{600} of ≈0.5. Cultures were then induced with IPTG (final concentration of 1 mM) and brought to 20 °C shaking at 200 RPM overnight. Cells were harvested by centrifugation (5000 RPM for 10 min at 4 °C) and resuspended in phosphate buffer (10 mL, 25 mM sodium phosphate, 100 mM sodium chloride, pH 7.4) with a protease inhibitor tablet (1/2 tablet, Roche cOmplete ULTRA Tables, Mini, EDTA free, EASYpack). Cell suspension was subject to one freeze-thaw cycle at -20 °C followed by sonication (2 min cycle, 50% amplitude, over ice). Cell lysate was cleared by centrifugation (9000 RPM for 15 min at 4 °C) and the supernatant was incubated with Ni-NTA agarose resin (1 mL) rotating at 4 °C for 30 minutes. The resin was collected by centrifugation (4750 RPM for 10 min at 4 °C) and washed with phosphate wash buffer (25 mL, 25 mM sodium phosphate, 100 mM sodium chloride, 25 mM imidazole, pH 7.4 and 25mL with 50 mM imidazole). Proteins were then eluted with phosphate elution buffer (6 mL, 25 mM sodium phosphate, 100 mM sodium chloride, 400

mM imidazole, pH 7.4) and dialyzed in phosphate buffer (2 L, 25 mM sodium acetate, 100 mM sodium chloride, pH 7.4) overnight. Second dialysis was done for ≈6-8 hours. Purified protein was then observed by SDS-PAGE.

2.9.8 Protein gel

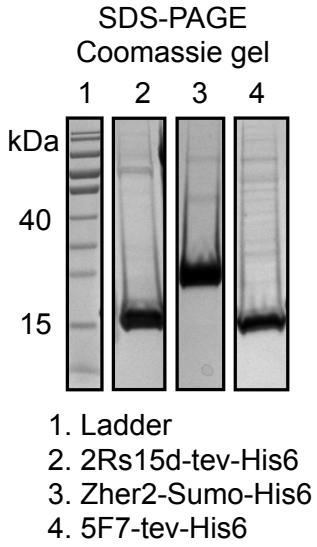

Figure 2.3: SDS-PAGE coomassie stained gel of proteins.

2.9.9 Flow Cytometry of mixtures at different concentrations

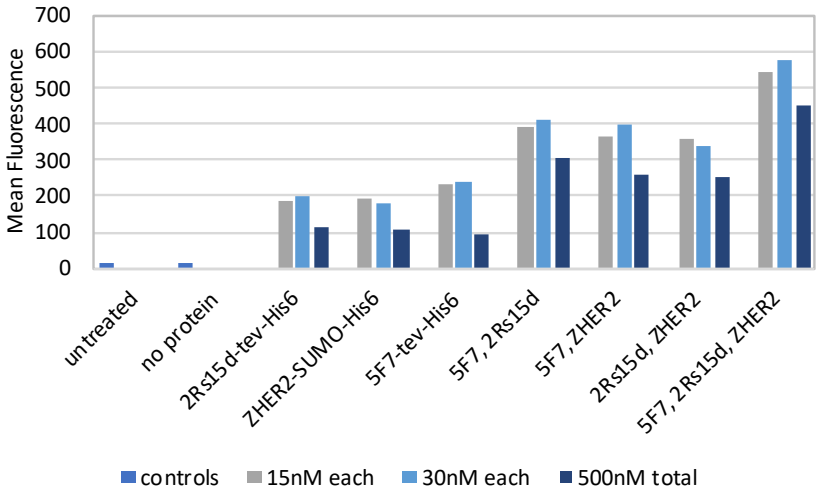

Figure 2.4: Flow Cytometry results for individual proteins and mixtures of at 15nM each, 30nM each, and 500nM total showing that mixtures allow for higher effective recruitment of antibodies to the cell surface.

2.9.10 ADCC Herceptin positive control

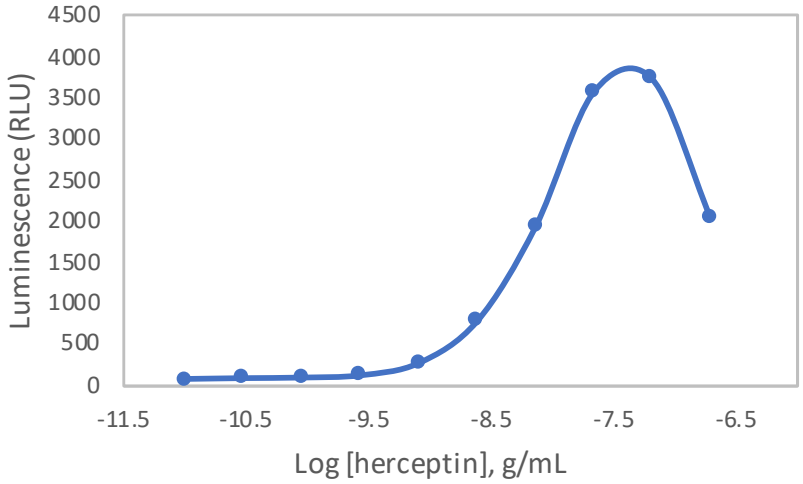

Figure 2.5: ADCC assay with Herceptin for a positive control. Using 15,000 target cells with a 5:1 E:T cell ratio and 30μg/mL 3-fold dilutions of Herceptin.

Chapter 3

Artificial Metalloenzymes

Artificial metalloenzymes (ArMs) have emerged as a promising approach to combine the attractive properties of transition metal catalysis and biocatalysis. The idea is to combine the best of both worlds in homogenous catalysis to achieve high reactivity and selectivity under mild conditions. [113] In the 1970s, Yamamura and Kaiser, and Wilson and Whitesides, introduced the concept of artificial metalloenzyme catalysis. [114, 115] However, it wasn't until the recent advances in protein engineering and organometallic synthesis that the development of ArMs has significantly progressed. Transition metals provide catalysis of a broad range of reactions while proteins provide a well defined surface to catalyze reactions in a chiral environment. The combination of these two factors make ArMs a promising catalyst for new and difficult syntheses. [116] ArMs have been shown to catalyze a variety of reactions and have been addressed in a number of recent reviews. [113, 117–122]

The strategy used to achieve enantioselectivity is to force the incoming reactant to approach selectively from one side of the substrate by sterically blocking the other side. In transition metal catalysis, this is controlled by the first coordination sphere of the metal ligand. Enzymatic catalysis takes this a step further by providing a second coordination sphere that includes the biomolecular scaffold (hydrogen bonds, hydrophobic interactions, charges) (Figure 3.1). [113] The second coordination sphere can compliment the transition state to catalyze reactivity and/or direct chemical reactants to one side for selectivity. ArMs aim to catalyze through the cohesive effects of the transition metal with the protein scaffold.

Taking advantage of a protein's diverse functional and structural properties in chemical syntheses has allowed for a second coordination sphere to interact with the metal catalyst, substrates, and intermediates for optimal reaction conditions. The greatest virtue of a protein scaffold is the ability to easily improve or adjust ArM performance through mutagenesis and directed evolution. Common methods used to anchor metals into proteins are through supramolecular non-covalent

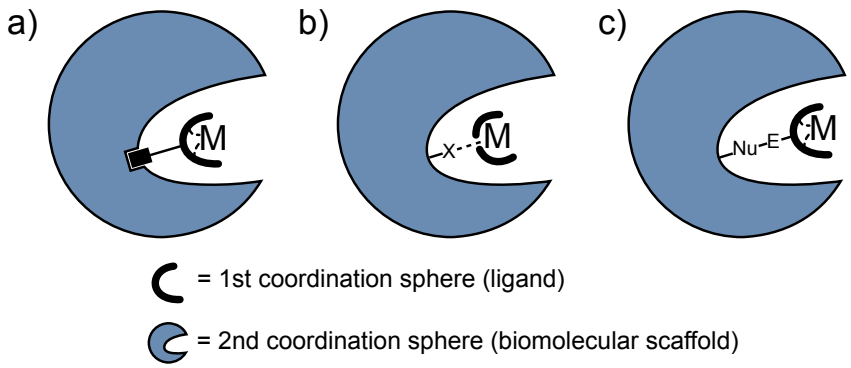

Figure 3.1: Representation of artificial metalloenzyme anchoring schemes and coordination spheres. Metal ligand is the first coordination sphere and biomolecular scaffold is the second coordination sphere that influences catalytic activitiy. (a) supramolecular non-covalent anchoring of metal into protein scaffold. (b) dative anchoring of metal into protein scaffold. (c) covalent anchoring of metal into protein scaffold.

interactions, dative interactions, and covalent interactions (Figure 3.1). Supramolecular anchoring uses the high affinity that a protein has for a particular ligand. Dative anchoring uses nucleophilic amino acid residues (Cys, Ser, His, Glu, Asp, etc.) to coordinate with the metal center. Covalent anchoring uses nucleophilic attack on an electrophilic moiety containing a metal. With these anchoring methods, three common strategies can be used in the development of ArMs: (1) repurposing natural metalloenzymes, (2) redesigning metalloenzymes, and (3) creating new metalloenzymes. (Figure 3.2) [113, 119, 121–123]

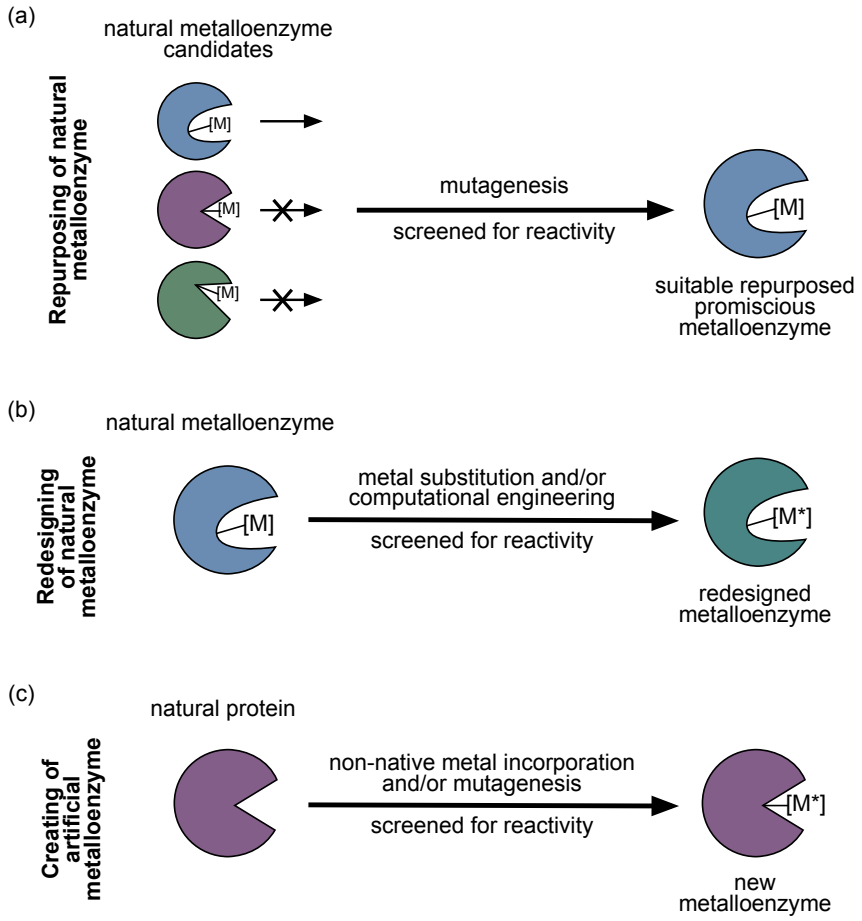

Figure 3.2: Strategies for the development of artificial metalloenzymes. (a) repurposing natural metalloenzymes. (b) redesigning metalloenzymes. (c) creating new metalloenzymes. M* = non-native metal

3.1 Repurposing natural metalloenzymes

Repurposing of natural metalloenzymes to catalyze new reactions relies on the promiscuity of the enzyme (Figure 3.2a). Proteins are seen to catalyze a number of chemical reactions in nature, with half of the enzymes requiring the presence of a metal to function. Despite the availability of a number of natural metalloenzymes, a select few have been extensively studied and used for transformations not observed in nature. The repurposing of natural metalloenzymes in the development of ArMs was pioneered by Francis Arnold in 2013. Most common are iron catalysis with heme proteins such as cytochrome P450 that has been used for reactions such as cyclopropanation [124,125], olefin aziridination [126], nitrene insertion [126–131], and carbene insertion [132–134]. Cy-

tochrome P450 has attracted chemists due to the enzyme's redox capabilities. [135] Other heme proteins have been used such as myoglobin for cyclopropanation [124, 125, 136], carbene insertion [133, 134], and C-H amination. [126]

A recent study from the Arnold lab repurposed cytochrome c from *Rhodothermus marinus* to catalyze carbon-silicon bond formation, a transformation unknown in nature. [137] They found that heme proteins catalyze the formations of organosilicon compounds under physiological conditions through a carbene insertion into silicon-hydrogen bonds with high chemo- and enantioselectivity. Cytochrome P450 and myoglobin variants showed product formation with higher turnover, but cytochrome c also provided enantioinduction with an enantiomeric excess of 97%. To improve the carbon-silicon bond forming catalyst, a variant library from site-saturation mutagenesis of M100 was tested. M100 was believed to be displaced upon iron-carbenoid formation and thus mutating could facilitate in active site formation. V75 and M103 were later also mutated as they were close to the iron heme center. Directed evolution provided a mutant cytochrome c that catalyzed carbon-silicon bond formation (<30-fold improved from wild type) with a variety of Si variants. With just a few mutations cytochrome c was repurposed to form a chemical bond not naturally formed by enzymes (Figure 3.3). This work from Arnold, as well as many others, shows that a number of natural metalloenzymes are highly evolvable and fit to be repurposed for transformations not observed in nature.

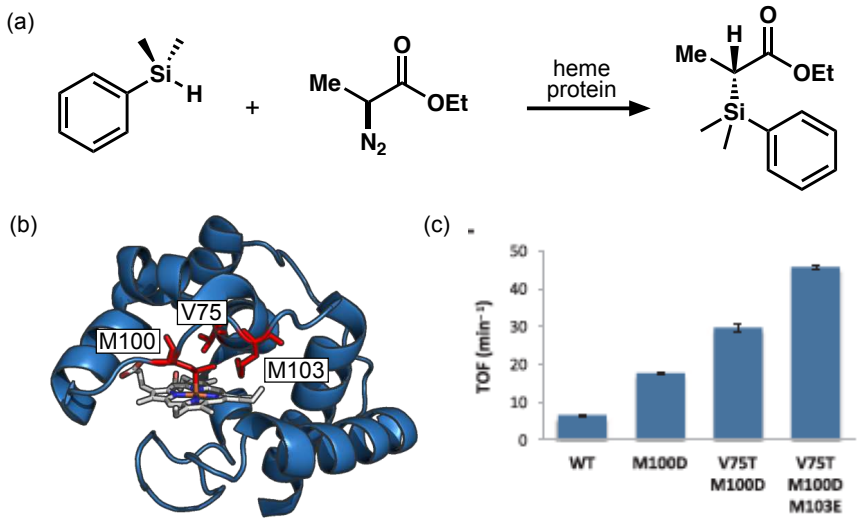

Figure 3.3: Evolved cytochrome c catalyses carbon-silicon bond formation. (a) Formation of carbon–silicon bond catalyzed by cytochrome c from *Rhodothermus marinus*. (b) Structure of Cytochrome c (PDB: 3CP5) . Amino acid residues M100, V75, and M103 close to the heme iron were mutated. (c) Carbon-silicon bond forming rates. Chart figure from Ref [137].

A novel approach from Shoji and Watanabe, repurposed cytochrome P450 by the addition of "decoy molecules" to enable catalytic oxidation of nonnative substrates. [138] Although Cytochrome P450 has been used for a variety of reactions, it has very high substrate specificities and generally very low catalytic activity for nonnative substrates. To use P450 for nonnative substrate oxidation, altering substrate specificity is necessary so binding of the substrate to the active site is not needed for catalysis. Common approach has been to make mutations in the protein, but Shoji and Watanabe instead found that by adding an inert substrate similar to the natural substrates, the binding pocket could be made to accommodate nonnative substrates (Figure 3.4). The catalytic activity, enantioselectivity, and regioselectivity is dependent on the decoy molecule used and has been shown to oxidize a wide variety of nonnative substrates. The system has been used for epoxidation of styrenes, C-H bond hydroxylation, sulfoxidation, and aromatic ring hydroxylation where without the decoy molecule oxidation did not proceed. This new approach to repurposing metalloenzymes could be used in combination with protein mutagenesis to expand the scope of reactivity using natural metalloenzymes.

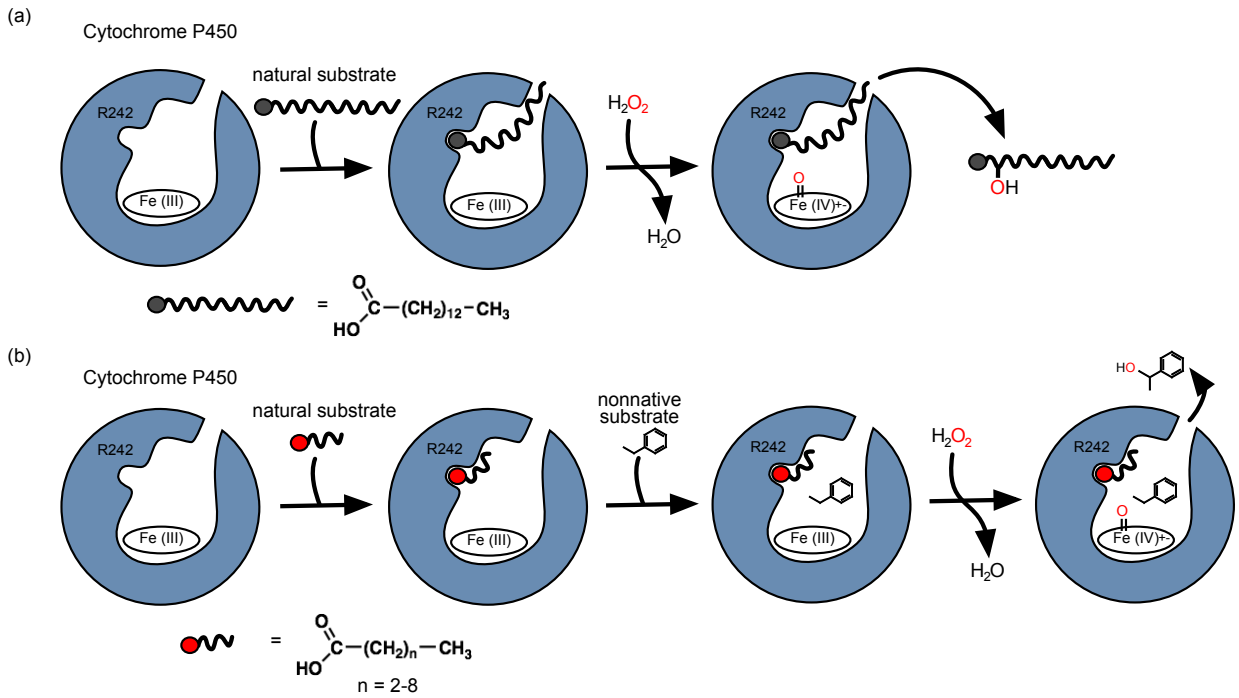

Figure 3.4: A schematic representation of cytochrome P450 reaction mechanism. (a) natural (b) with decoy molecule

3.2 Redesigning metalloenzymes

Redesigning of metalloenzymes is often necessary to achieve new and desired chemical transformations (Figure 3.2b). Repurposing of natural metalloenzymes is limited to what is provided in nature and the level of promiscuity. The ability to redesign metalloenzymes based on natural metalloenzymes provides an additional degree of added promiscuity and diversity for new reactivity. By taking a natural metalloenzyme scaffold, the second coordination sphere is essentially already setup, and thus, potentially has a lower starting activation barrier before introducing a new active metal center and engineering the second coordination sphere to expand the reactivity scope. Heme proteins have been redesigned to have alternative metals such as Mn for C-H amination [126] and hydroxylation [139], Co for C-H amination [126], and Ir for C-H amination [140], carbene insertion [141, 142], and cyclopropanation [141].

In a more extensive redesign of a metalloenzyme, Baker and coworkers used computational design and directed evolution to develop a highly active organophosphate hydrolase starting from

a functionally diverse set of mononuclear zinc-containing metalloenzyme scaffolds [143]. Zinc-containing enzymes have a diverse mechanistic role, is redox stable, and is already seen as a catalyst in many natural hydrolases, making it a good starting template. On the basis of an adenosine deaminase and extracted set of mononuclear zinc enzyme scaffolds with at least one open coordination site on the zinc atom from the Protein Data Bank (PDB), a computationally engineered organophosphate hydrolase was developed (Figure 3.4). Through an understanding of the reaction mechanism, models were constructed of the reaction transition state in order to redesign the mononuclear zinc-containing active site in an adenosine deaminase. Mutations to adenosine deaminase provided shape complementarity to the transition state and directed evolution provided more mutations necessary for activity. The redesigned metalloenzyme efficiently catalyzes the hydrolysis of the R_p isomer of a coumarinyl analog of the nerve agent cyclosarin. Redesign of metalloenzymes through metal substitution, computational engineering, and directed evolution offers new catalytic potential for novel transformations.

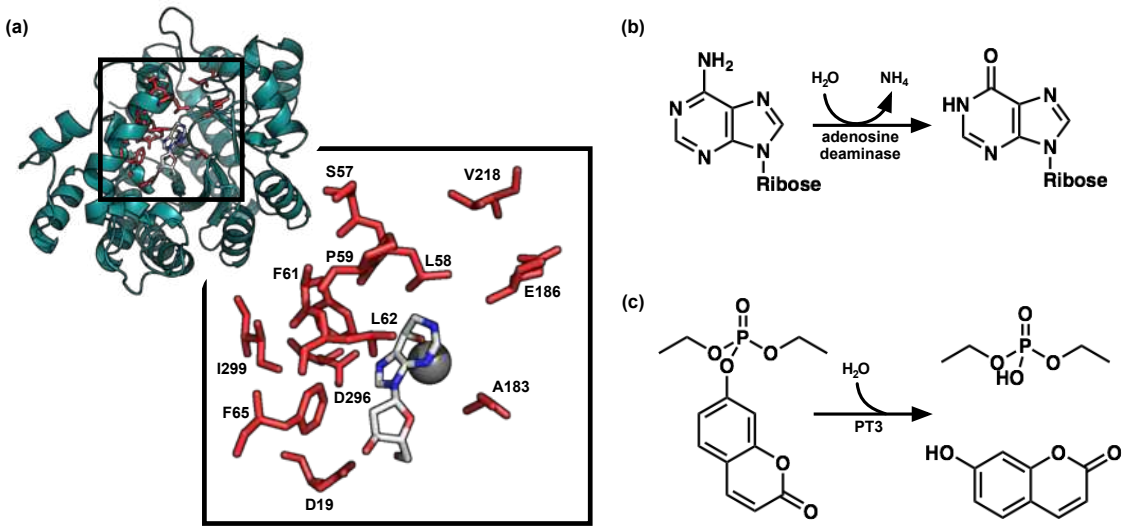

Figure 3.5: Computational active site redesign. (a) Structure of adenosine deaminase (PDB: 1A4L). Residues highlighted in red were mutated based on findings from modeling transition state geometries in a set of mononuclear zinc metalloenzyme active sites and directed evolution. (b) Wild-type adenosine deaminase reaction (c) The organophosphate hydrolysis reaction with the redesigned adenosine deaminase (PT3).

3.3 Creating new metalloenzymes

Creating metalloenzymes through the incorporation of a metal cofactor to any protein expands the realm of possible new reactivity even further by not limiting the starting scaffold to natural metalloenzymes (Figure 3.2c). Metal cofactors can be anchored to proteins via covalent or non-covalent interactions (Figure 3.1). However, the protein scaffold used is limited by the binding pocket and its ability to house the metal catalyst and substrates. While synthesis of metal cofactors and having to optimize the first and second coordination spheres may be a challenge. The combination of chemical and biomolecular variability expands the diversity of an artificial metalloenzyme. A variety of proteins have been used such as a tHisF and oligopeptidase with dirhodium for cyclopropanation [144, 145], papain with ruthenium and rhodium for transfer hydrogenation of aryl ketones [146, 147], chymotrypsin with ruthenium for ring closing metathesis [148], and lipases with ruthenium for olefin metathesis [149], rhodium for chemoselective hydrogenation of olefins over ketones [150], and palladium for immobolized Heck reaction [151].

Most notably, following the pioneering work of Whitesides, many ArMs have been developed using the biotin-(strep)avidin technology. [152, 153] Streptavidin is a tetrameric protein known for its extremely high affinity for biotin ($K_D \approx 10^{-14}$M). This allows for supramolecular anchoring of a metal cofactor. Each monomer of Streptavidin can have biotin bound deep within the pocket. Designed biotinylated metal cofactors typically project the metal complex to be solvent exposed and proximity and location affects the selectivity. Expanded upon by Ward, he has developed a library of streptavidin artificial metalloenzymes with biotinylated metal cofactors that were able to catalyze reactions including Suzuki cross coupling [154], allylic alkylation [155], sulfoxidation [156, 157], hydrogenation [158–161], transfer hydrogenation [162–171], and olefin metathesis [172].

An important study from Hyster and company discovered an artificial metalloenzyme that efficiently and selectively catalyzes benzannulation reactions. [173] Benzannulation reaction (aka Wulff-Dötz reaction) is a chemical reaction used to generate highly substituted phenols in a single step through C-H bond activation using a transition metal. This reaction is used in a variety of phar-

maceuticals and natural products where stereoselectivity is important. Hyster and company made an artificial metalloenzyme using streptavidin and a biotin rhodium complex. Streptavidin binds to biotin non-covalently within a well defined cleft that allows for the rhodium to be positioned in a particular location to selectively catalyze the benzannulation reaction. Point mutations were made and found that the addition of a carboxylate residue (K121E) and an aromatic residue (S112Y) helped improve activity and selectivity. With the addition of well positioned tyrosine and glutamic acid that act in concert with the rhodium metal, the reaction achieved up to an 86% enantiomeric excess (ee) and 92 fold acceleration compared to the rhodium complex alone (Figure 3.6). By taking a general protein scaffold with the capability of incorporating a metal cofactor, new ArMs have been developed not based on natural metalloenzymes and have been shown to successfully expand the scope of possibly chemistry.

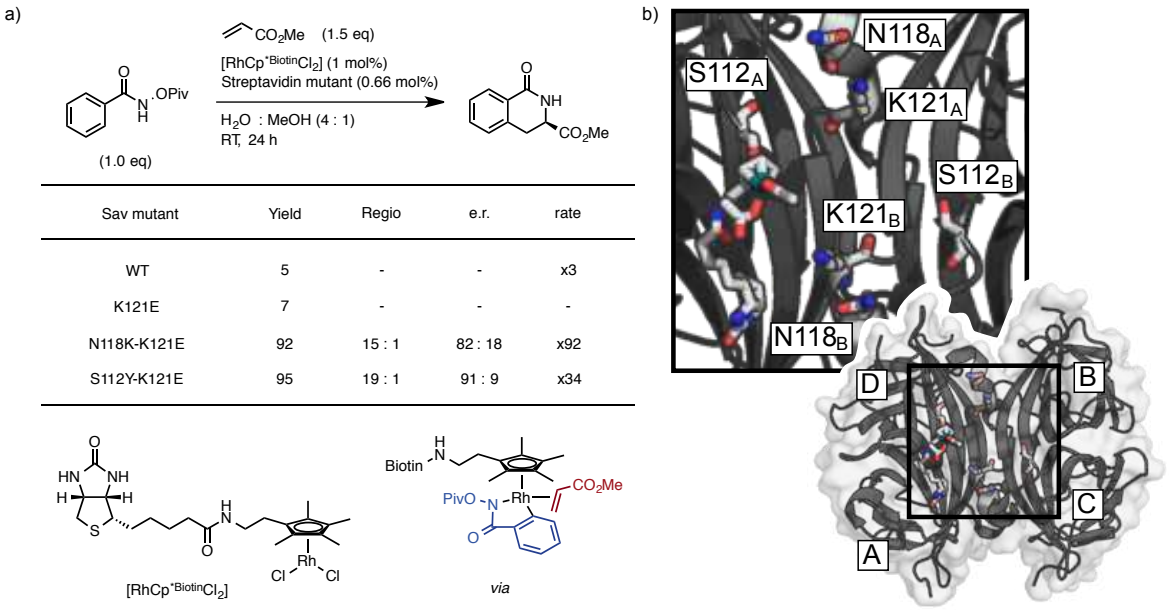

Sav mutant	Yield	Regio	e.r.	rate
WT	5	-	-	x3
K121E	7	-	-	-
N118K-K121E	92	15 : 1	82 : 18	x92
S112Y-K121E	95	19 : 1	91 : 9	x34

Figure 3.6: Biotinylated Rh(III) species complexed to an engineered tetrameric streptavidin (tSav) for accelerated asymmetric C-H activation. (a) tSav was engineered to couple benzamides and alkenes to get dihydroisoquinolones with excellent stereoselectivity (rr = 19:1 and er = 91:9) and rate acceleration (92-fold) compared to the activity of the non-protein bound Rh complex via a concerted metalation-deprotonation (CMD) mechanism. (b) AutoDock of tSav (PDB: 3RY1) with biotinylated Rh(III) complex rendered in PyMOL with key residues highlighted.

3.4 Summary

Artificial metalloenzymes have been proven to be successful at creating a cohesive effect between the first coordination sphere of the transition metal and the second coordination sphere of the protein scaffold for high reactivity and selectivity of existing and new chemistry. Either through repurposing natural metalloenzymes, redesigning metalloenzymes, or creating new metalloenzymes, the diversity of components and methods has facilitated in expanding the realm of possible transformations. Despite recent advances, ArMs are still underdeveloped. A better understanding of the intricacies and complexities of the metal, substrate, and protein interactions are necessary to improve our ability to design and evolve ArMs. The future development of ArMs requires collaborative efforts in not only transition metal catalysis and biocatalysis, but also in computational protein engineering. Insight into the molecular dictates that occur during ArM catalysis through computational analysis will further assist in engineering proteins for this designer function.

Chapter 4

Asymmetric δ-Lactam Synthesis with a Monomeric Streptavidin Artificial Metalloenzyme

Adapted from:

Hassan, I.S.*; Ta, A.N.*; Danneman, M.W.*; Semakul, N.; Burns, M.; Basch, C.H.; Dippon, V.N.; McNaughton, B.R.; Rovis, T., JACS, submitted 2019

I co-first authored this manuscript with Michael Danneman and Isra Hassan. Michael and Isra focused on the chemical synthetic side and I focused on the protein side. With each of our research expertise we equally contributed to this collaborative project.

4.1 Introduction

Reliable design of artificial metalloenzymes (ArMs) that—like natural enzymes—accelerate and control reactivity, but catalyse transformations not observed in Nature, remains an unsolved and important challenge. We report that a monomeric streptavidin (mSav) Rh(III) ArM permits asymmetric synthesis of α,β-unsaturated-δ-lactams via a novel tandem C-H activation and [4+2] annulation reaction. These products are readily derivatized to enantioenriched piperidines – the most common N-heterocycle found in FDA approved pharmaceuticals. mSav ArM, but not the more commonly used tetrameric form (tSav), couples substituted N-pivaloyloxy acrylamides with diverse styrenes under mild conditions. Desired δ-lactams are achieved in yields as high as 99% and enantiomeric excess of 97%. Studies show that Rh(III) catalysis in the mSav protein scaffold can give up to a 168-fold rate acceleration relative to the isolated biotinylated Rh(III) cofactor.

Mutagenesis and screening of naturally occuring enzymes is often used—with varied success—to repurpose and redesign ArMs that enable new chemical transformations [137, 142, 145, 174–180]. An alternative approach to access non-natural reactivity in enzymes is to use a generic protein scaffold and a synthetic metal co-factor to create an artificial metalloenzyme (ArM) [115,

122, 152, 160, 173, 181, 182]. In these cases, the bound metal co-factor facilitates a mode of chemical reactivity not observed in the native protein.

The most common ArM platform developed to date is the biotin-tetrameric (strept)avidin (biotin-tSav) system, pioneered by Whitesides [115] and Ward [122] (Figure 4.1b). These ArMs utilize high affinity ($K_D \approx 10^{-14}$M) interactions between tSav and biotin-metal conjugates. A representative example of such a conjugate (1), used in this work, is shown in Figure 4.1a. tSav-based ArMs have been utilized in an increasing number of transition-metal mediated transformations.

In order to improve the synthetic utility of artificial metalloenzymes, we sought to develop a conceptually rapid and attractive approach to assemble a precursor to piperidines – the most common N-heterocycle found in FDA approved pharmaceuticals (Figure 4.1d) [183, 184]. Strategies for efficient and selective piperidine synthesis often rely on preassembly of an acyclic precursor and subsequent cyclization. The transformation we targeted is the union of N-pivaloyloxy acrylamides and styrenes. The styrene coupling partner is commercially available, while the N-pivaloyloxy acrylamides are accessible in a single step. Extensive precedent exists for the coupling of N-oxy benzamides and alpha olefins [173, 185, 186], but the corresponding reaction of N-oxy acrylamide and alkenes is unknown.

We reasoned that if monomeric streptavidin (mSav, Figure 4.1c), could serve as a competent ArM template, it might simplify ArM tuning and analysis. Like tSav, biotin is bound tightly by mSav (K_D 2 nM [187–191]) but has been engineered to resist tetramerization [187–189] by replacing hydrophobic amino-acid residues at the barrel-barrel interface with charged ones.

4.2 Results and Discussion

Evaluation began with the coupling of acrylamide (2a) and *para*-methoxystyrene (3a) to provide the desired δ-lactam (4aa). The use of Cp*$RhCl_2$, (where Cp* is pentamethylcyclopentadienyl) provides the desired product in modest yield (25%, Table 4.1, entry 1). Similar results were observed with the biotinylated form (1, $Cp^{*biotin}RhCl_2$), which provides the desired δ-lactam (4aa) in 15% yield, (Table 4.1, entry 2). We previously showed that when complexed

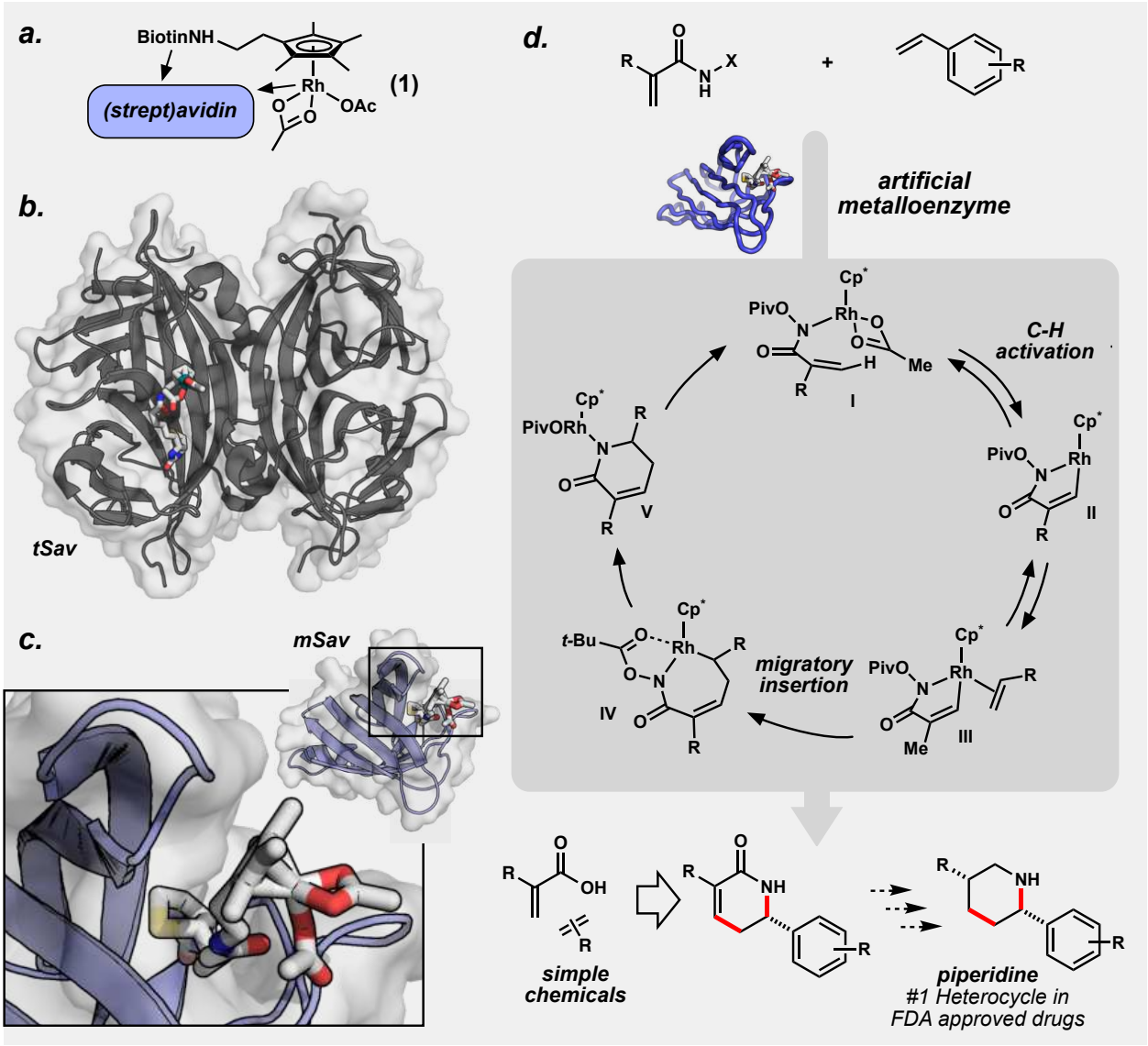

Figure 4.1: (a) Biotin binds (strept)avidin, thus providing a chiral environment for a conjugated metal, which can coordinate to, or be influenced by, proteinaceous components. (b) tetrameric streptavidin (tSav) artificial metalloenzyme (ArM). (c) monomeric streptavidin (mSav) ArM. For (b) and (c) tSav (PDB: 3RY1) and mSav (PDB: 4JNJ) were complexed with the biotin cofactor in AutoDock and rendered in PyMOL. (d) Acrylamide and alkene coupling envisioned by mSav-based ArM (shown as ribbon diagram), along with proposed mechanism. ArM depictions were rendered in PyMOL.

with Cp*^{biotin}RhCl$_2$, wt-tSav-derived ArMs catalyze a reaction between pivaloyl-protected benzhydroxamic acid and methyl acrylate to afford a dihydroisoquinolone [173]. However, in the union of styrene and acrylamide, tSav-based ArMs afford the desired δ-lactam (4aa) in 9% yield and poor stereocontrol (-26% ee, Table 4.1, entry 3). Similarly, a mutant tSav (N118K/K121E) that proved to be a highly reactive ArM in our previous work [173] did not provide the desired δ-lactam (4aa) in appreciable yield (Table 4.1, entry 4).

Table 4.1: Evaluation of organometallic catalysts and artificial metalloenzymes for a tandem C-H activation and [4+2] annulation reaction between acrylamide (2a) and *para*-methoxystyrene (3a) to provide the desired δ-lactam (4aa).

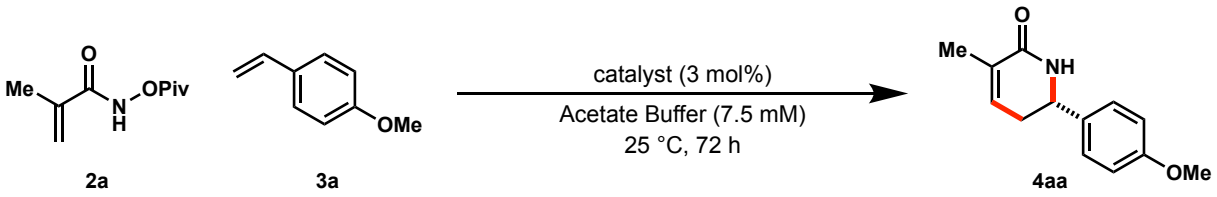

entry	catalyst	yield (%)[a]	enantiomeric excess (%)[b]
1	Cp*RhCl$_2$	25	0
2	Cp*^{biotin}RhCl$_2$	15	0
3	wt-tSav:Cp*^{biotin}RhCl$_2$	9	-26
4	N118K-K121E-tSav:Cp*^{biotin}RhCl$_2$	3	0
5[c]	wt-mSav:Cp*^{biotin}RhCl$_2$	44	92
6	**wt-mSav:Cp*^{biotin}RhCl$_2$**	**99**	**91**
7[d]	wt-mSav:Cp*^{biotin}RhCl$_2$	58	82

2a (3.0μmol), **3a** (1.5μmol), catalyst, in 200μL of acetate buffer (62.5 mM NaOAc, 100 mM NaCl, pH 7.4) with 3 μL MeOH. [a]Conversion and yield determined by ^{1}H NMR analysis relative to a trimethyl(phenyl)silane internal standard. [b]Enantiomeric excess determined by HPLC analysis. [c]1 mol% catalyst. [d]200μL of NaCl buffer (100 mM NaCl, pH 7.4) used.

In an effort to improve the reaction, we turned our attention to mSav artificial metalloenzyme. Satisfyingly, 1 mol% wt-mSav:Cp*^{biotin}RhCl$_2$ ArM, enables the coupling of acrylamide (2a) and *para*-methoxystyrene (3a) to provide the desired δ-lactam (4aa) in 44% yield and 92% enantiomeric excess (ee) (Table 4.1, entry 5). A modest increase in metalloenzyme catalyst loading results in substantially higher yield and virtually identical selectivity, delivering the desired

δ-lactam (4aa) in 99% yield and 91% ee (Table 4.1, entry 6). Interestingly, the tSav ArM delivers the opposite enantiomer to that of the mSav catalyzed reaction, underscoring the large difference in active site geometry between the two systems.

A plausible catalytic cycle for this reaction, supported by prior work from our lab [192], is proposed in Figure 4.1d. Metalation of the amide by rhodium generates intermediate I. C-H activation occurs, presumably via a concerted-metalation deprotonation (CMD) mechanism, providing five-membered rhodacycle II. Subsequent alkene coordination and migratory insertion would give seven-membered rhodacycle IV. N-O bond cleavage and reductive elimination then occurs to form transient Rh(III) intermediate V. Protodemetallation regenerates the Rh(III) catalyst and closes the catalytic cycle.

The wt-mSav:Cp$^{*\mathrm{biotin}}$RhCl$_2$ catalyzed reaction proved broadly tolerant to the coupling partners employed (Figure 4.2a). With respect to the styrene partner, enantioselectivities were best with *para*-substituted styrenes, regardless of electronic character. Meta-substituted styrenes are also tolerated, affording good to high enantioselectivities, while a single ortho-substituted styrene led to somewhat decreased selectivity. Styrene itself was a poor substrate, proceeding in modest selectivity and yield (4ab). Importantly, all substrates give the desired δ-lactam products as single regioisomers. Substitution on the acrylamide is well tolerated regardless of steric demand affording product with enantioselectivities that match the corresponding methacrylamide system (Figure 4.2b). However, aryland alkoxy- substitution results in diminished yields (4ca, 4ea and 4ed).

In order to derivatize the resulting δ-lactam products into piperidines the coupling of 2a and 3a to provide 4aa was performed at a .15 mmol scale providing identical results to the reaction performed on a 1.5 μmol scale (99% yield, 91% ee). Hydrogenation of 4aa affords the reduced lactam 6aa in 99% yield and 10:1 dr. Subsequent reduction of 6aa with LiAlH$_4$ furnishes the desired piperidine 5aa in 81% yield and 7:1 dr (Figure 4.2c).

Indeed, the derivatization can proceed under exceedingly mild reduction conditions. Treatment of a range of δ-lactams (6) formed in high diastereoselectivity following hydrogenation with

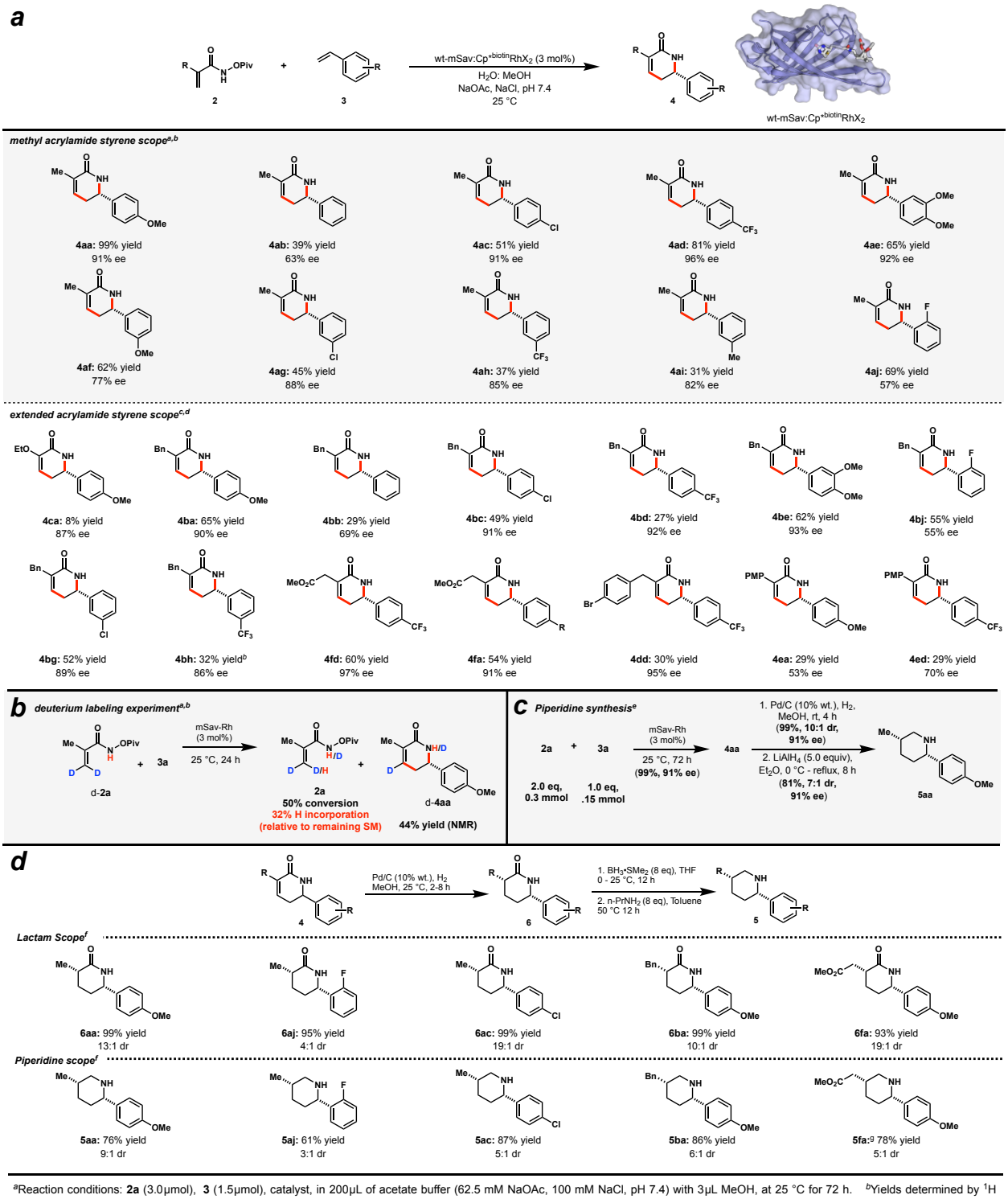

[a]Reaction conditions: **2a** (3.0μmol), **3** (1.5μmol), catalyst, in 200μL of acetate buffer (62.5 mM NaOAc, 100 mM NaCl, pH 7.4) with 3μL MeOH, at 25 °C for 72 h. [b]Yields determined by ^{1}H NMR analysis relative to a trimethyl(phenyl)silane internal standard. Enantiomeric excess determined by HPLC analysis. [c]Reaction conditions: **2** (1.5μmol), **3** (3.0μmol), catalyst, in 100μL of acetate buffer (25 mM NaOAc, 100 mM NaCl, pH 7.4) with 1.5μL MeOH, at 25 °C for 48 h. [d]Yields determined by HPLC analysis relative to a 1,3,5-trimethoxybenzene internal standard. Enantiomeric excess determined by HPLC analysis. [e]Reactions conducted at a .15 mmol scale. Yields determined by ^{1}H NMR analysis relative to a trimethyl(phenyl)silane internal standard. Enantiomeric excess and dr determined by HPLC analysis. [f]Diastereoselectivity determined by ^{1}H NMR. [g]Reaction conducted with 5 eq. BH_3•SMe_2 and 5 eq. n-$PrNH_2$.

Figure 4.2: (a) Reaction Scope. (b) Deuterium labeling experiment. (c) Piperidine synthesis. (d) Piperidine scope.

$BH_3{\cdot}SMe_2$ provides the corresponding piperidines in good yield and comparable diastereoselectivity to the $LiAlH_4$ reduction (Figure 4.2d). Notably, these reduction conditions are tolerant of ester functionalities (5fa).

While the $Cp^{*biotin}RhCl_2$ cofactor alone delivers the desired δ-lactam (4aa) with no appreciable selectivity (0% ee, Table 4.1, entry 2), its significantly reduced reactivity was a surprise (25% yield with 3 mol% catalyst loading, compared to 99% yield with an equivalent of the mSav artificial metalloenzyme). To interrogate the relative reactivity of mSav:$Cp^{*biotin}RhCl_2$ versus $Cp^{*biotin}RhCl_2$, we conducted a head-to-head competition experiment, adapting conditions established for tSav reactivity [173]. The addition of equimolar $Cp^{*biotin}RhCl_2$ to mSav:$Cp^{*biotin}RhCl_2$ results in a modest decrease in selectivity. Further addition of the cofactor to the metalloenzyme reaction results in further decreases, but the observed selectivity is far in excess of what one would predict if the Rh catalyst were equally reactive inside and out of the protein environment. Indeed, even in the presence of 10-fold excess of "achiral" cofactor Rh(III), the reaction still proceeds in 60% ee, commensurate with an 80-fold faster reaction inside the metalloenzyme (see section 4.4). Interestingly, wt-tSav:$Cp^{*biotin}RhCl_2$ was found to be much less reactive (k_{rel} = 30), than its mSav-based counterpart.

While benzannulation chemistry with tSav was also noted to proceed some 90-fold faster, relative to the cofactor, those experiments were conducted in a system starved of carboxylate base (a requisite component for the C-H activation step), and the acceleration in rate was attributed to a carboxylate residue that we had engineered into the tSav active site. In stark contrast, the current reaction is conducted in the presence of a large excess of carboxylate base (63 mmol in NaOAc). Furthermore, a deuterium labeling experiment illustrates that the C-H activation step is reversible, suggesting that the concerted metalation/deprotonation (CMD) is not the turnover limiting step (Figure 4.2b). Thus, we were interested in determining the residues responsible for the increased reactivity of the mSav system.

To begin to evaluate the molecular dictates of reactivity and stereocontrol, a preliminary set of mSav mutants was expressed, targeting specific residues that we felt may impact the reaction. We

began with mutation of tyrosine 112 (Y112), which neighbors the putative Cp*^{biotin}Rh pocket. In comparison to the ArM featuring wtmSav (k_{rel} = 78, compared to the cofactor alone), the Y112A mutant provides the desired product in modest yield and enantiomeric excess (37% and 61%, respectively), with an order of magnitude slower reactivity (k_{rel} = 10, Figure 4.3). This observation is consistent with its likely role as a rigidifying element through π-stacking to the Cp framework on the catalyst [173]. Despite significant decreases in reactivity and selectivity, Y112A maintains affinity for biotin (see section 4.4).

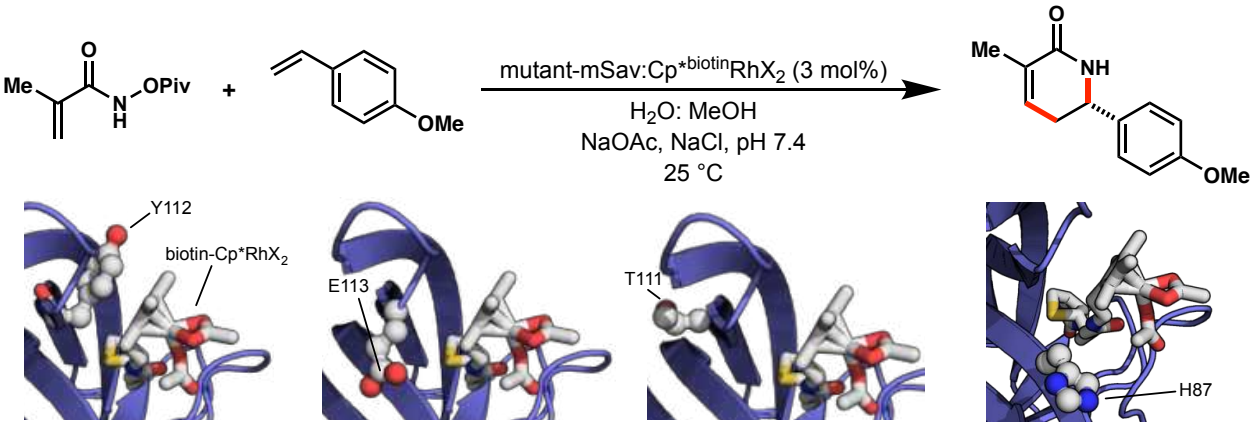

mSav (Y112A)			mSav (E113A)			mSav (T111E)			mSav (H87A)		
yield (%)[a]	relative rate (k_{rel})	enantiomeric excess (%)[b]	yield (%)[a]	relative rate (k_{rel})	enantiomeric excess (%)[b]	yield (%)[a]	relative rate (k_{rel})	enantiomeric excess (%)[b]	yield (%)[a]	relative rate (k_{rel})	enantiomeric excess (%)[b]
37	10	61	67	18	94	96	168	92	99	127	94

Figure 4.3: Mutational effects on yield, relative rate, and enantiomeric excess. [a]Yield determined by ^{1}H NMR analysis relative to a trimethyl(phenyl)silane internal standard. [b]Enantiomeric excess determined by HPLC analysis. mSav depictions were rendered in PyMOL using PDB access code 4JNJ with docked Cp*^{biotin}RhCl$_2$.

Several other nearby mutations proved enlightening (Figure 4.3). Mutation of a glutamate residue at position 113 (E113A) significantly decreased reactivity (k_{rel} =18), without impacting selectivity (ee = 94%). On the other hand, mutation of H87 to alanine (H87A) increases reactivity (k_{rel} = 127) and retains excellent stereocontrol (ee = 94%). While one may argue that a basic histidine proximal to the Rh active site may be inhibiting Rh reactivity, it would be implausible that the wt-mSav, bearing the putative inhibitory histidine at 87, is faster than the cofactor alone (k_{rel} = 78). Thus, the H87A mutation likely suggests a different role for the histidine, which we

posit is to partially stabilize the charge at 113. In support of the role of charge in that part of the protein backbone, we examined a T111E mutation. The T111E-based artificial metalloenzyme maintains good selectivity (ee = 92%), but is 168 times more active than the cofactor alone. This suggests that mutations outside the coordination sphere of rhodium can influence reactivity.

4.3 Conclusion

In conclusion, we have developed an artificial metalloenzyme that efficiently catalyzes an enantioselective tandem C-H activation and [4+2] annulation reaction to afford δ-substituted lactams. This metalloenzyme accepts a diverse array of acrylamide and styrene coupling partners, which is not often seen in artificial metalloenzyme constructs. The mSav metalloenzyme platform demonstrates superior reactivity relative to its tSav counterpart and the free cofactor alone. Importantly, reactivity can be accelerated by mutagenesis of residues neighboring, and away from, the putative $Cp^{*biotin}Rh$ pocket. We hypothesize that this can be attributed to mSav-Rh's ability to considerably stabilize Rh containing transition states, most likely the migratory insertion event. Further computational analysis is currently being done to understand the molecular dictates of the reaction.

4.4 Supporting Information

4.4.1 General methods

Flash column chromatography was performed on SiliCycle Inc.® silica gel 60 (230-400 mesh). Thin Layer chromatography was performed on SiliCycle Inc.® 0.25 mm silica gel 60-F plates. Visualization was accomplished with UV light (254 nm) or $KMnO_4$ staining.

^{1}H-NMR and ^{13}C-NMR spectra were recorded on Bruker 300, 400 or 500 MHz spectrometers at ambient temperature. ^{1}H-NMR data are reported as the following: chemical shift in parts per million (δ, ppm) from chloroform ($CDCl_3$) taken as 7.26 ppm, integration, multiplicity (s=singlet, d=doublet, t=triplet, q=quartet, m=multiplet, dd=doublet of doublets) and coupling constant (J in Hz unit). ^{13}C-NMR is reported as the following: chemical shifts are reported in ppm from $CDCl_3$ taken as 77.0 ppm.

Low-resolution mass spectra (LSMS) were obtained on ACQUITY Waters UPLC/mass spectrometer equipped with electrospray ionization.

Infrared spectra (IR) were recored on a Perkin Elmer Paragon 1000 FT-IR spectrometer.

4.4.2 Preparation of starting materials

2-substituted acrylic acids for 2b and 2d were prepared according to the procedure. [193]

2-ethoxy acrylic acid for 2c was prepared according the procedure. [194]

2-aryl acrylic acid for 2e was prepared according to the procedure. [195]

Partial esterification of itaconic acid for 2f was prepared according to the literature procedure. [196]

All alkenes in this study were purchased from commercial sources and used without further purification.

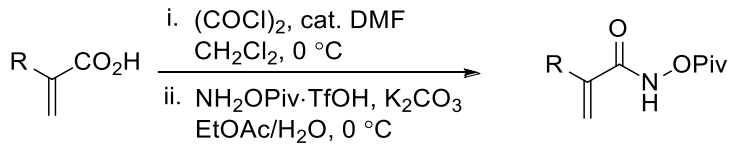

Figure 4.4: N-(pivaloyloxy) α-substituted acrylamides.

i. To a solution of 2-substituted acrylic acid (1 equiv) in dry CH_2Cl_2 (0.17 M) at 0°C (ice bath) under N_2 was added dropwise oxalyl chloride (1.1 equiv) and a few drops of DMF. The reaction was then stirred at 0 °C to room temperature (typically 2-3 h). The volatiles were removed under reduced pressure to give a crude acid chloride.

ii. To the solution of $NH_2OPiv{\cdot}TfOH$ (1.1 equiv), K_2CO_3 (2.0 equiv) and EtOAc/H_2O (2/1 by v/v, 0.1M) at 0 °C (ice bath), the crude acid chloride was added dropwise (while a small amount of EtOAc can be used as a solvent). The mixture was stirred at the same temperature for 0.75 - 1 h (prolonged reaction time led to the decomposition of the N-pivaloyloxy acrylamide). Upon the completion (monitored by TLC), saturated $NaHCO_3$ was added. The aqueous layer was extracted with EtOAc (x3), washed with brine, dried with $MgSO_4$, and filtered. The solvent was

removed under reduced pressure to give a crude N-(pivaloyloxy) α-substituted acrylamide, which was purified by a flash column chromatography (5% to 25% EtOAc/hexane). [1]

Table 4.2: N-(Pivaloyloxy)methacrylamide (2a) characterization.

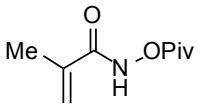

2a

^{1}H NMR (500 MHz, $CDCl_3$)δ 9.22 (s, NH), 5.84 (s, 1H), 5.50 – 5.47 (m, 1H), 1.99 (t, J = 1.3 Hz, 3H), 1.34 (s, 9H).

^{13}C NMR (126 MHz, $CDCl_3$)δ 176.90, 167.26, 136.91, 121.97, 38.39, 26.98, 18.29

IR (neat, cm^{-1}) 3225, 2977, 1782, 1671, 1629, 1481, 1055, 1033, 1015.

LRMS (ESI) m/z calcd for $C_9H_{15}NO_3$ $[M+H]^+$: 186.1, found: 186.2.

Table 4.3: 2-Benzyl-N-(pivaloyloxy)acrylamide (2b) characterization.

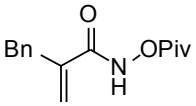

2b

^{1}H NMR (500 MHz, $CDCl_3$)δ 8.97 (s, NH), 7.35 (t, J = 7.4 Hz, 2H), 7.26 (m, 2H), 5.96 (s, 1H), 5.39 (t, J = 1.3 Hz, 1H), 3.69 (s, 2H), 1.33 (s, 9H).

^{13}C NMR (126 MHz, $CDCl_3$) δ 176.73, 166.93, 141.07, 137.47, 129.00, 128.75, 126.82, 122.52, 38.39, 38.10, 26.99.

IR (neat, cm^{-1}) 3217, 2981, 1780, 1668, 1080.

LRMS (ESI) m/z calcd for $C_{15}H_{19}NO_3$ $[M+H]^+$: 262.1, found: 262.2.

Table 4.4: 2-Ethoxy-N-(pivaloyloxy)acrylamide (2c) characterization.

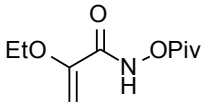

2c

^{1}H NMR (500 MHz, $CDCl_3$)δ 9.70 (s, 1H), 5.36 (s, 59H), 4.49 (s, 1H), 3.84 (q, J = 6.8 Hz, 3H), 1.35 (t, J = 7.0 Hz, 5H), 1.31 (s, 9H).

^{13}C NMR (126 MHz, $CDCl_3$)δ 176.18, 160.01, 151.78, 91.76, 64.25, 38.35, 26.95, 14.18.

IR (neat, cm^{-1}) 3245, 2979, 2937, 1782, 1693, 1628, 1479, 1300, 1059, 1081.

LRMS (ESI) m/z calcd for $C_{10}H_{17}NO_4$ $[M+H]^+$: 216.1, found: 216.2.

4.4.3 General procedures for dihydropyridone synthesis (racemic)

Substituted N-(pivaloyloxy) acrylamide (0.1 mmol, 1 eq), $[Cp^*RhCl_2]^2$ (0.0025 mmol, 2.5 mol%), CsOAc (0.025 mmol, 0.25 equiv) and alkene (0.11 mmol, 1.1 equiv) were added to a dram vial charged with a stir bar. Trifluoroethanol (TFE) (0.33 mL, 0.3 M) was added and the

[1]The protected hydroxylamine triflic acid salt (NH2OPiv·TfOH) [also commercially available from CarboSynth, UK] can be synthesized in gram quantities via a simple two step synthetic sequence from commercially available starting material. Commercially available acid chlorides or carboxylic acids (converted to their corresponding acid chlorides *in situ*) are treated with NH2OPiv·TfOH to afford the desired library of acrylamides in very efficient reaction times (0.75 - 4 h).

Table 4.5: 2-(4-Bromobenzyl)-N-(pivaloyloxy)acrylamide (2d) characterization.

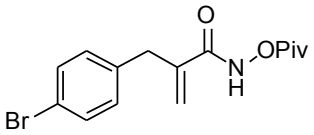

2d

^{1}H NMR (500 MHz, $CDCl_3$)δ 9.03 (s, NH), 7.45 (d, J = 8.4 Hz, 2H), 7.11 (d, J = 8.4 Hz, 2H), 5.91 (s, 1H), 5.39 (t, J = 1.4 Hz, 1H), 3.63 (s, 2H), 1.33 (s, 9H).

^{13}C NMR (126 MHz, $CDCl_3$)δ 176.77, 166.75, 140.84, 136.60, 131.78, 130.74, 122.28, 120.69, 38.39, 37.57, 26.98.

IR (neat, cm^{-1}) 3221, 29675, 1779, 1668, 1624, 1487, 1073, 1032, 1012.

LRMS (ESI) m/z calcd for $C_{15}H_{18}BrNO_3$ $[M+H]^+$: 340.1, 342.1, found: 340.0, 342.0.

Table 4.6: 2-(4-methoxyphenyl)-N-(pivaloyloxy)acrylamide (2e) characterization.

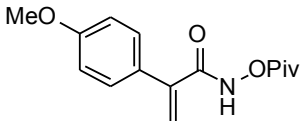

2e

^{1}H NMR (500 MHz, $CDCl_3$)δ 9.23 (s, NH), 7.38 (d, J = 8.7 Hz, 2H), 6.88 (d, J = 8.6 Hz, 2H), 5.97 (s, 1H), 5.66 (s, 1H), 3.79 (s, 3H), 1.32 (s, 9H).

^{13}C NMR (126 MHz, $CDCl_3$) δ 176.60, 166.48, 160.04, 141.04, 129.00, 127.96, 121.19, 114.11, 55.29, 38.34, 26.99.

IR (neat, cm^{-1}) 3229, 2973, 1780, 1670, 1608, 1513, 1252, 1181, 1076, 1033, 837.

LRMS (ESI) m/z calcd for $C_{15}H_{19}NO_4$ $[M+H]^+$, $[M+Na]^+$: 278.1, found: 278.1.

Table 4.7: Methyl 3-((pivaloyloxy)carbamoyl)but-3-enoate (2f) characterization.

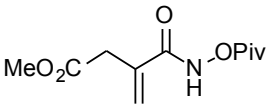

2f

^{1}H NMR (500 MHz, $CDCl_3$)δ 9.77 (s, NH), 6.07 (s, 1H), 5.63 (s, 1H), 3.74 (s, 3H), 3.42 (s, 2H), 1.34 (s, 9H).

^{13}C NMR (126 MHz, $CDCl_3$)δ 176.49, 171.40, 166.39, 134.56, 125.32, 52.48, 38.39, 37.77, 27.02.

IR (neat, cm^{-1}) 2972, 1741, 1055, 1033, 1013.

LRMS (ESI) m/z calcd for $C_{11}H_{17}NO_5$ $[M+H]^+$, $[M+Na]^+$: 244.1, found: 244.1, 266.1.

mixture was stirred at room temperature until the starting material was consumed (monitoring by TLC). The reaction was quenched with saturated $NaHCO_3$ and extracted 3 times with EtOAc. The organic layer was washed with brine, dried over $MgSO_4$, filtered, and solvent was evaporated to obtain crude product. The crude product was purified by column chromatography using gradient 10% to 50% EtOAc/hexane containing 1% Et_3N as an eluent to obtain the product.

4.4.4 Product characterizations (racemic)

Table 4.8: 6-(4-Methoxyphenyl)-3-methyl-5,6-dihydropyridin-2(1H)-one (4aa) characterization.

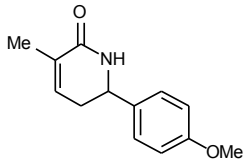

4aa

Off-white solid (17.8 mg, 82% yield)

^{1}H NMR (500 MHz, $CDCl_3$) δ 7.26 (d, *J* = 8.7 Hz, 2H), 6.89 (d, *J* = 8.6 Hz, 2H), 6.34 (ddd, *J* = 5.0, 3.7, 1.7 Hz, 1H), 5.56 (s, 1H), 4.64 (dd, *J* = 9.9, 7.6 Hz, 1H), 3.80 (s, 3H), 2.45 (ddd, *J* = 8.1, 4.0, 1.8 Hz, 2H), 1.92 (d, *J* = 1.9 Hz, 3H).

^{13}C NMR ($CDCl_3$, 126 MHz) δ 167.75, 159.48, 134.45, 133.32, 130.86, 127.62, 114.22, 55.71, 55.33, 33.47, 16.61.

IR (neat, cm^{-1}) 3204, 2923, 1673, 1627, 1512, 1244, 1176, 1033, 826.

LRMS (ESI) m/z calcd for $C_{13}H_{15}NO_2$ $[M+H]^+$: 218.1, found: 218.2.

Table 4.9: 3-Methyl-6-phenyl-5,6-dihydropyridin-2(1H)-one (4ab) characterization.

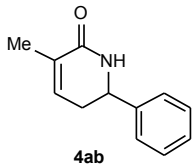

4ab

Off-white solid (13.1 mg, 70% yield).

^{1}H NMR (500 MHz, $CDCl_3$) δ 7.39-7.26 (m, 5H), 6.34 (m, 1H), 5.66 (s, NH), 4.70 (dd, *J* = 10.5, 6.7 Hz, 1H), 2.50 (m, 2H), 1.93 (s, 3H).

^{13}C NMR ($CDCl_3$, 126 MHz) δ 167.73, 141.35, 134.27, 130.92, 128.90, 128.23, 126.39, 56.21, 33.37, 16.61. IR (neat, cm^{-1}) 3214, 3063, 2923, 2886, 1676, 1633, 699.

LRMS (ESI) m/z calcd for $C_{12}H_{13}NO$ $[M+H]^+$: 188.1, found: 188.2.

Table 4.10: 6-(4-Chlorophenyl)-3-methyl-5,6-dihydropyridin-2(1H)-one (4ac) characterization.

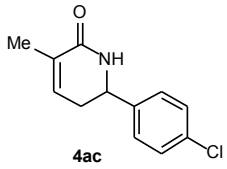

4ac

Light-orange solid (28.1 mg, 63%).

^{1}H NMR (500 MHz, $CDCl_3$) δ 7.34 (d, *J* = 8.5 Hz, 2H), 7.28 (d, *J* = 8.5 Hz, 2H), 6.33 (ddd, *J* = 5.2, 3.2, 1.6 Hz, 1H), 5.65 (s, 1H), 4.68 (dd, *J* = 11.2, 5.8 Hz, 1H), 2.71 – 2.28 (m, 3H), 2.16 – 1.67 (m, 3H).

^{13}C NMR (126 MHz, $CDCl_3$) δ 167.61, 139.83, 134.05, 134.00, 130.99, 129.06, 127.73, 55.53, 33.23, 16.53.

IR (neat, cm^{-1}) 3194, 3062, 2976, 2950, 2920, 2807, 1675, 1631, 1578, 1494, 1495, 1421, 1408, 1374, 1345, 1286, 1246, 1179.

HRMS (ASAP) m/z calcd for $C_{12}H_{13}ClNO$ $[M+H]^+$: 222.0686, found: 222.0687.

Table 4.11: 3-Methyl-6-(4-(trifluoromethyl)phenyl)-5,6-dihydropyridin-2(1H)-one (4ad) characterization.

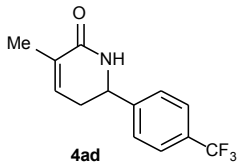

4ad

Off-white solid (18.1 mg, 71% yield)

^{1}H NMR (500 MHz, $CDCl_3$) δ 7.63 (d, *J* = 8.1 Hz, 2H), 7.47 (d, *J* = 8.0 Hz, 2H), 6.32 (dt, *J* = 3.5, 1.7 Hz, 1H), 5.87 (s, 1H), 4.78 (dd, *J* = 10.9, 5.8 Hz, 1H), 2.70 – 2.36 (m, 2H), 1.91 (d, *J* = 1.9 Hz, 3H).

^{13}C NMR ($CDCl_3$, 126 MHz)δ 167.65, 145.42, 133.81, 131.12, 130.61, 130.35, 126.75, 125.93, 125.90, 125.87, 125.84, 124.98, 55.63, 33.08, 16.56.

^{19}F NMR ($CDCl_3$, 282 MHz) δ -61.78.

IR (neat, cm^{-1}) 3194, 2924, 1673, 1630, 1324, 1109, 1068, 906, 730.

LRMS (ESI) m/z calcd for $C_{13}H_{12}F_3NO$ $[M+H]^+$: 256.1, found: 256.1.

Table 4.12: 6-(3,4-Dimethoxyphenyl)-3-methyl-5,6-dihydropyridin-2(1H)-one (4ae) characterization.

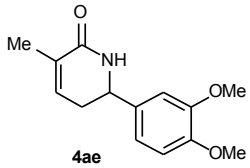

4ae

Reaction run on a 0.200 mmol scale.

Light-orange solid (32.5 mg, 66%).

^{1}H NMR (500 MHz, $CDCl_3$) δ 7.07 – 6.62 (m, 3H), 6.35 (tt, *J* = 3.6, 1.9 Hz, 1H), 5.62 (s, 1H), 4.63 (dd, *J* = 10.2, 7.5 Hz, 1H), 3.87 (d, *J* = 3.1 Hz, 6H), 2.59 – 2.25 (m, 2H), 1.92 (d, *J* = 2.3 Hz, 3H).

^{13}C NMR (126 MHz, $CDCl_3$)δ 167.75, 149.22, 148.87, 134.45, 133.73, 130.78, 118.71, 111.13, 109.18, 56.04, 55.91, 55.89, 33.53, 16.55.

IR (neat, cm^{-1}) 3249, 3223, 3066, 3001, 2935, 2833, 1673, 1629, 1516, 1458, 1421, 1261, 1253.

HRMS (ASAP) m/z calcd for $C_{14}H_{18}NO_3$ $[M+H]^+$: 248.1287, found: 248.1284.

Table 4.13: 6-(3-Methoxyphenyl)-3-methyl-5,6-dihydropyridin-2(1H)-one (4af) characterization.

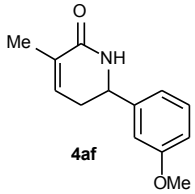

4af

Reaction run on a 0.200 mmol scale.

Light-orange solid (32.8 mg, 75%).

^{1}H NMR (500 MHz, $CDCl_3$) δ 7.28 (t, *J* = 7.9 Hz, 1H), 7.00 – 6.71 (m, 3H), 6.35 (ddd, *J* = 5.2, 3.5, 1.6 Hz, 1H), 5.63 (s, 1H), 4.67 (dd, *J* = 10.2, 7.1 Hz, 1H), 3.81 (s, 3H), 2.74 – 2.35 (m, 2H), 1.92 (q, *J* = 1.7 Hz, 3H).

^{13}C NMR (126 MHz, $CDCl_3$)δ 167.66, 159.96, 142.93, 134.30, 130.86, 129.95, 118.59, 113.58, 111.95, 56.18, 55.26, 33.32, 16.56.

IR (neat, cm^{-1}) 3209, 3052, 2946, 2920, 2840, 1677, 1633, 1600, 1487, 1454, 1429.

HRMS (ASAP) m/z calcd for $C_{13}H_{16}NO_2$ $[M+H]^+$: 218.1181, found: 218.1180.

Table 4.14: 6-(3-Chlorophenyl)-3-methyl-5,6-dihydropyridin-2(1H)-one (4ag) characterization.

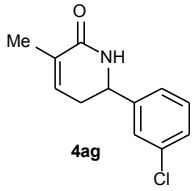

4ag

Reaction run on a 0.200 mmol scale.

Orange solid (26.8 mg, 61%).

^{1}H NMR (500 MHz, $CDCl_3$) δ 7.37 – 7.27 (m, 3H), 7.22 (ddd, *J* = 6.0, 3.2, 1.8 Hz, 1H), 6.32 (ddd, *J* = 5.1, 3.2, 1.6 Hz, 1H), 5.74 (s, 1H), 4.67 (dd, *J* = 11.1, 5.8 Hz, 1H), 2.91 – 2.27 (m, 2H), 2.16 (s, 0H), 2.06 – 1.69 (m, 2H).

^{13}C NMR (126 MHz, $CDCl_3$)δ 167.54, 143.44, 134.74, 133.88, 131.01, 130.16, 128.34, 126.63, 124.48, 55.59, 33.09, 16.52.

IR (neat, cm^{-1}) 3256, 3216, 3070, 2953, 2920, 2880, 2844, 1677, 1629, 1600, 1575, 1454, 1425.

HRMS (ASAP) m/z calcd for $C_{12}H_{13}ClNO$ $[M+H]^+$: 222.0686, found: 222.0680.

Table 4.15: 3-Methyl-6-(3-(trifluoromethyl)phenyl)-5,6-dihydropyridin-2(1H)-one (4ah) characterization.

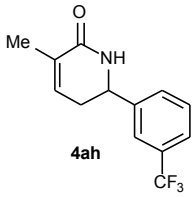

4ah

Reaction run on a 0.200 mmol scale.

Light-orange solid (24.7 mg, 48%).

^{1}H NMR (500 MHz, $CDCl_3$) δ 7.63 – 7.53 (m, 3H), 7.50 (t, *J* = 7.7 Hz, 1H), 6.34 (ddd, *J* = 5.1, 3.2, 1.6 Hz, 1H), 5.84 (s, 1H), 4.78 (dd, *J* = 11.2, 5.7 Hz, 1H), 2.76 – 2.37 (m, 2H), 2.00 – 1.80 (m, 2H).

^{13}C NMR (126 MHz, $CDCl_3$)δ 167.64, 142.43, 133.85, 131.30 (q, *J* = 32.4 Hz), 131.11, 129.72, 129.44, 125.07 (q, *J* = 3.8 Hz), 123.83 (q, *J* = 270.5 Hz), 123.25 (q, *J* = 3.8 Hz), 55.75, 33.18, 16.51.

^{19}F NMR (470 MHz, $CDCl_3$)δ -61.79.

IR (neat, cm^{-1}) 3216, 3070, 2979, 2953, 2924, 2888, 1677, 1633, 1451, 1429, 1326.

HRMS (ASAP) m/z calcd for $C_{13}H_{13}F_3NO$ $[M+H]^+$: 256.0949, found: 256.0945.

Table 4.16: 3-Methyl-6-(m-tolyl)-5,6-dihydropyridin-2(1H)-one (4ai) characterization.

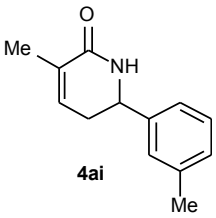

4ai

Reaction run on a 0.200 mmol scale.

Light-brown oil (25.6 mg, 64%).

^{1}H NMR (500 MHz, $CDCl_3$) δ 7.28 – 7.21 (m, 1H), 7.19 – 7.09 (m, 3H), 6.33 (ddd, *J* = 5.3, 3.6, 1.7 Hz, 1H), 5.64 (s, 1H), 4.65 (dd, *J* = 9.8, 7.6 Hz, 1H), 2.47 (ddt, *J* = 7.8, 3.7, 2.1 Hz, 2H), 2.35 (s, 3H), 1.92 (d, *J* = 1.9 Hz, 2H).

^{13}C NMR (126 MHz, $CDCl_3$)δ 167.65, 141.27, 138.59, 134.26, 130.82, 128.88, 128.72, 127.01, 123.37, 56.10, 33.32, 21.37, 16.54.

IR (neat, cm^{-1}) 3212, 3052, 3030, 2950, 2920, 2884, 1673, 1629, 1491, 1454, 1429.

HRMS (ASAP) m/z calcd for $C_{13}H_{16}NO$ $[M+H]^+$: 202.1232, found: 202.1230.

Table 4.17: 6-(2-Fluorophenyl)-3-methyl-5,6-dihydropyridin-2(1H)-one (4aj) characterization.

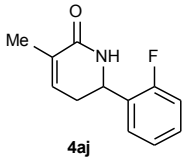

4aj

Reaction run on a 0.200 mmol scale.

Off-white solid (13.3 mg, 32%).

^{1}H NMR (500 MHz, $CDCl_3$) δ 7.40 (td, J = 7.6, 1.8 Hz, 1H), 7.34 – 7.24 (m, 1H), 7.20 – 7.12 (m, 1H), 7.05 (ddd, J = 10.6, 8.2, 1.2 Hz, 1H), 6.31 (tt, J = 3.6, 1.7 Hz, 1H), 5.79 (s, 1H), 5.06 (ddd, J = 10.0, 5.9, 1.6 Hz, 1H), 2.91 – 2.19 (m, 2H), 1.91 (d, J = 1.9 Hz, 3H).

^{13}C NMR (126 MHz, $CDCl_3$) δ 167.84, 159.95 (d, $J_{C\text{-}F}$ = 246.9 Hz), 134.04, 130.86, 129.52 (d, $J_{C\text{-}F}$ = 8.2 Hz), 128.44 (d, $J_{C\text{-}F}$ = 12.8 Hz), 127.39 (d, $J_{C\text{-}F}$ = 3.7 Hz), 124.52 (d, $J_{C\text{-}F}$ = 3.6 Hz), 115.69 (d, $J_{C\text{-}F}$ = 21.7 Hz), 48.95 (d, $J_{C\text{-}F}$ = 3.6 Hz), 31.25, 16.56.

^{19}F NMR (470 MHz, $CDCl_3$)δ -118.24.

IR (neat, cm^{-1}) 3260, 3194, 3143, 3063, 2957, 2924, 2891, 1677, 1629, 1585, 1483, 1451, 1429.

HRMS (ASAP) m/z calcd for $C_{12}H_{13}FNO$ $[M+H]^+$: 206.0981, found: 206.0982.

Table 4.18: 3-Benzyl-6-(4-methoxyphenyl)-5,6-dihydropyridin-2(1H)-one (4ba) characterization.

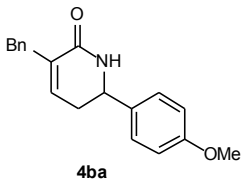

4ba

Off-white solid (26.0 mg, 89% yield).

^{1}H NMR (500 MHz, $CDCl_3$) δ 7.31 (t, J = 7.5 Hz, 2H), 7.28 – 7.15 (m, 4H), 6.88 (d, J = 8.7 Hz, 2H), 6.14 (ddd, J = 4.6, 3.0, 1.7 Hz, 1H), 5.68 (s, 1H), 4.62 (t, J = 8.6 Hz, 1H), 3.80 (s, 3H), 3.66 (t, J = 2.1 Hz, 2H), 2.46 (ddt, J = 9.5, 4.0, 1.9 Hz, 2H).

^{13}C NMR ($CDCl_3$, 126 MHz)δ 167.02, 159.50, 139.33, 135.16, 134.95, 133.18, 129.34, 128.41, 127.67, 126.19, 114.22, 55.38, 55.34, 36.05, 33.50.

IR (neat, cm^{-1}) 3207, 3060, 3027, 2932, 2836, 1672, 1629, 1512, 1247, 1032, 826, 700.

LRMS (ESI) m/z calcd for $C_{19}H_{19}NO_2$ $[M+H]^+$, $[M+Na]^+$: 294.1, 316.1, found: 294.1, 316.1.

Table 4.19: 3-Benzyl-6-phenyl-5,6-dihydropyridin-2(1H)-one (4bb) characterization.

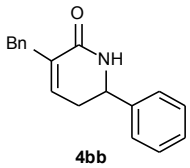

4bb

Off-white solid (22.2 mg, 85% yield).

^{1}H NMR (500 MHz, $CDCl_3$) δ 7.42 – 7.28 (m, 8H), 7.28 – 7.19 (m, 4H), 6.14 (td, J = 3.6, 1.8 Hz, 1H), 5.68 (s, 1H), 4.90 – 4.26 (m, 1H), 3.67 (s, 1H), 2.69 – 2.35 (m, 2H).

^{13}C NMR (126 MHz, $CDCl_3$)δ 166.96, 141.20, 139.29, 135.01, 134.99, 129.35, 128.91, 128.42, 128.27, 126.45, 126.21, 55.91, 36.06, 33.41.

IR (neat, cm^{-1}) 3206, 3061, 3027, 2917, 1673, 1630, 1494, 1453, 1424, 1290, 698.

LRMS (ESI) m/z calcd for $C_{18}H_{17}NO$ $[M+H]^+$: 265.1, found: 265.1.

Table 4.20: 3-Benzyl-6-(4-chlorophenyl)-5,6-dihydropyridin-2(1H)-one (4bc) characterization.

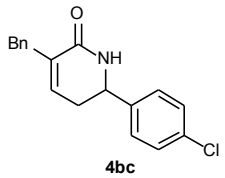

4bc

Off-white solid (21.2 mg, 71% yield).

^{1}H NMR (500 MHz, $CDCl_3$)δ 7.30 -7.28 (m, 4H), 7.24-7.19 (m, 5H), 6.10 (m, 1H), 5.88 (s, NH), 4.65 (dd, *J* = 5.0, 10.0 Hz, 1H), 3.62 (s, 2H), 2.53-2.49 (m, 1H), 2.44-2.38 (m, 1H).

^{13}C NMR ($CDCl_3$, 126 MHz)δ 166.94, 139.74, 139.17, 135.12, 134.68, 133.98, 129.31, 129.04, 128.43, 127.82, 126.25, 55.15, 36.06, 33.25.

IR (neat, cm^{-1}) 3207, 3061, 3028, 2921, 1674, 1631, 1492, 1092, 1014, 822, 699.

LRMS (ESI) m/z calcd for $C_{18}H_{16}ClNO$ $[M+H]^+$: 298.1, found: 298.1.

Table 4.21: 3-Benzyl-6-(4-(trifluoromethyl)phenyl)-5,6-dihydropyridin-2(1H)-one (4bd) characterization.

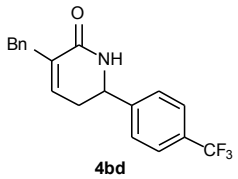

4bd

Off-white solid (15.3 mg, 46% yield).

^{1}H NMR (500 MHz, $CDCl_3$)δ 7.63 (d, *J* = 8.1 Hz, 2H), 7.45 (d, *J* = 8.0 Hz, 2H), 7.32 (m, 2H), 7.25 (m, 3H), 6.16 (m, 1H), 5.93 (s, NH), 4.78 (dd, *J* = 10.7, 5.7 Hz, 1H), 3.68 (s, 2H), 2.84-2.56 (m, 1H), 2.55-2.38 (m, 1H).

^{13}C NMR ($CDCl_3$, 126 MHz)δ 166.87, 145.23, 139.07, 135.23, 134.49, 130.49, 129.28, 128.44, 126.79, 126.29, 125.88, 55.30, 36.07, 33.12.

IR (neat, cm^{-1}) 3212, 3064, 2922, 1675, 1630, 1324, 1164, 1121, 1068, 826, 700.

LRMS (ESI) m/z calcd for $C_{19}H_{16}F_3NO$ $[M+H]^+$: 332.1, found: 332.1.

Table 4.22: 3-Benzyl-6-(3,4-dimethoxyphenyl)-5,6-dihydropyridin-2(1H)-one (4be) characterization.

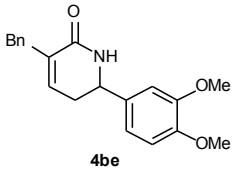

4be

Reaction run on a 0.200 mmol scale.

Light-orange oil (49.1 mg, 76%). **^{1}H NMR** (500 MHz, $CDCl_3$) δ 7.35 – 7.26 (m, 2H), 7.27 – 7.18 (m, 3H), 6.88 – 6.79 (m, 3H), 6.16 (td, *J* = 3.8, 2.2 Hz, 1H), 5.65 (s, 1H), 4.62 (dd, *J* = 9.5, 7.9 Hz, 1H), 3.86 (d, *J* = 11.6 Hz, 6H), 3.65 (s, 1H), 2.48 (ddt, *J* = 7.8, 4.0, 1.7 Hz, 2H).

^{13}C NMR (126 MHz, $CDCl_3$)δ 166.95, 149.23, 148.89, 139.25, 135.18, 134.86, 133.62, 129.25, 128.37, 126.16, 118.75, 111.15, 109.20, 55.92, 55.87, 55.71, 36.01, 33.53.

IR (neat, cm^{-1}) 3092, 3070, 3033, 1961, 1819, 1677, 1629, 1516, 1476, 1454, 1418, 1264, 1235, 1137, 1031, 670.

HRMS (ESI) m/z calcd for $C_{20}H_{22}NO_3$ $[M+H]^+$: 324.1600, found: 324.1608.

Table 4.23: 3-Benzyl-6-(3-chlorophenyl)-5,6-dihydropyridin-2(1H)-one (4bg) characterization.

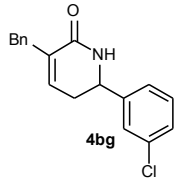

4bg

Off-white solid (17.4 mg, 58% yield).

^{1}H NMR (500 MHz, $CDCl_3$)δ 7.33 -7.28 (m, 5H), 7.23-7.18 (m, 4H), 6.13 (m, 1H), 5.82 (s, NH), 4.67 (dd, *J* = 10.0, 5.0 Hz, 1H), 3.55 (s, 2H), 2.58-2.53 (m, 1H), 2.49-2.43 (m, 1H).

^{13}C NMR ($CDCl_3$, 126 MHz)δ 166.84, 143.33, 139.13, 135.11, 134.78, 134.64, 130.20, 129.29, 128.45, 128.41, 126.69, 126.25, 124.57, 55.29, 36.04, 33.16.

IR (neat, cm^{-1}) 3204, 2897, 1674, 1630, 1422, 696.

LRMS (ESI) m/z calcd for $C_{18}H_{16}ClNO$ $[M+H]^+$: 298.1, found: 298.1.

Table 4.24: 3-Benzyl-6-(3-(trifluoromethyl)phenyl)-5,6-dihydropyridin-2(1H)-one (4bh) characterization.

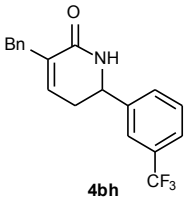

4bh

Off-white solid (14.5 mg, 44% yield).

^{1}H NMR (500 MHz, $CDCl_3$)δ 7.62 (s, 1H), 7.61 (d, *J* = 10.0 Hz, 1H), 7.54-7.48 (m, 2H), 7.36-7.31 (m, 2H), 7.26-7.23 (m, 3H), 6.17 (m, 1H), 5.90 (s, NH), 4.79 (dd, *J* = 10.0, 5.0 Hz, 1H), 3.69 (s, 2H), 2.64-2.59 (m, 1H), 2.54-2.47 (m, 1H).

^{13}C NMR ($CDCl_3$, 126 MHz) δ 166.90, 142.3 1, 139.07, 135.20, 134.58, 131.46, 131.20, 130.94, 129.80, 129.46, 129.28, 128.46, 126.28, 125.11, 123.27, 55.43, 36.02, 33.21.

^{19}F NMR ($CDCl_3$, 282 MHz)δ -61.82.

IR (neat, cm^{-1}) 2939, 1676, 1631, 1328, 700.

LRMS (ESI) m/z calcd for $C_{19}H_{16}F_3NO$ $[M+H]^+$: 332.1, found: 332.1.

Table 4.25: 3-Benzyl-6-(3-fluorophenyl)-5,6-dihydropyridin-2(1H)-one (4bj) characterization.

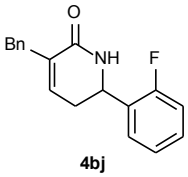

4bj

Yellow oil (19.9 mg, 71% yield).

^{1}H NMR (500 MHz, $CDCl_3$)δ 7.34 -7.29 (m, 3H), 7.23-7.20 (m, 3H), 7.09 (d, *J* = 7.8, Hz, 1H), 7.06-6.97 (m, 2H), 6.13 (m, 1H), 5.80 (s, NH), 4.68 (dd, *J* = 11.0, 5.7 Hz, 1H), 3.65 (s, 2H), 2.58-2.52 (m, 1H), 2.49-2.42 (m, 1H).

^{13}C NMR ($CDCl_3$, 126 MHz)δ 166.85, 163.94, 161.98, 143.87, 143.82, 139.14, 135.09, 134.68, 130.54, 130.48, 129.31, 128.44, 126.25, 122.04, 122.01, 115.25, 115.08, 113.58, 113.40, 55.33, 36.04, 33.18.

IR (neat, cm^{-1}) 3208, 3062, 3028, 2920, 1674, 1631, 784, 699.

LRMS (ESI) m/z calcd for $C_{18}H_{16}FNO$ $[M+H]^+$: 282.1, found: 282.1.

Table 4.26: 3-Ethoxy-6-(4-methoxyphenyl)-5,6-dihydropyridin-2(1H)-one (4ca) characterization.

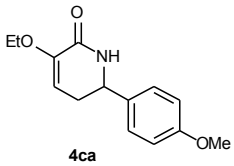

4ca

Off-white solid (12.6 mg, 51% yield)

^{1}H NMR (500 MHz, $CDCl_3$) δ 7.33 – 7.27 (m, *J* = 8.7 Hz, 2H), 6.91 (d, *J* = 8.7 Hz, 2H), 5.70 (s, 1H), 5.41 (s, 1H), 4.66 (dd, *J* = 11.8, 5.5 Hz, 1H), 3.88 – 3.83 (m, 2H), 3.83 (s, 3H), 2.69 – 2.44 (m, 2H), 1.44 (t, *J* = 7.0 Hz, 3H). **^{13}C NMR** ($CDCl_3$, 126 MHz)δ 163.49, 159.54, 146.86, 132.82, 127.60, 114.24, 104.68, 63.56, 55.55, 55.33, 32.00, 14.34.

IR (neat, cm^{-1}) 3227, 1680, 1633, 1513, 1247, 1177, 912.

LRMS (ESI) m/z calcd for $C_{14}H_{17}NO_3$ $[M+H]^+$: 248.1, found: 248.2, 270.1.

Table 4.27: 3-(4-Bromobenzyl)-6-(4-(trifluoromethyl)phenyl)-5,6-dihydropyridin-2(1H)-one (4dd) characterization.

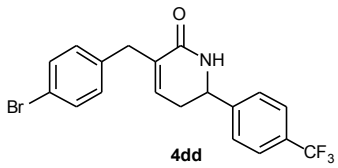

4dd

Off-white solid (24.2 mg, 59% yield)

^{1}H NMR (500 MHz, $CDCl_3$) δ 7.63 (d, *J* = 8.1 Hz, 2H), 7.43 (dd, *J* = 10.2, 8.1 Hz, 4H), 7.11 (d, *J* = 8.3 Hz, 2H), 6.20 (ddt, *J* = 5.0, 3.2, 1.5 Hz, 1H), 6.04 (s, NH), 4.77 (dd, *J* = 10.8, 5.7 Hz, 1H), 3.61 (d, *J* = 2.1 Hz, 2H), 2.77 – 2.58 (m, 1H), 2.50 (dddt, *J* = 17.8, 10.7, 3.6, 2.1 Hz, 1H). **^{13}C NMR** ($CDCl_3$, 126 MHz) δ 166.66, 145.08, 138.16, 134.78, 134.73, 131.49, 130.97, 130.67, 130.41, 126.78, 125.94, 125.91, 125.88, 125.85, 124.96, 122.79, 120.16, 55.25, 35.64, 33.08.

^{19}F NMR ($CDCl_3$, 282 MHz) δ -61.76.

IR (neat, cm^{-1}) 4210, 2923, 1674, 1629, 1323, 1162, 1120, 1067.

LRMS (ESI) m/z calcd for $C_{19}H_{15}BrF_3NO$ $[M+H]^+$: 410.0, found: 410.1.

Table 4.28: 3,6-Bis(4-methoxyphenyl)-5,6-dihydropyridin-2(1H)-one (4ea) characterization.

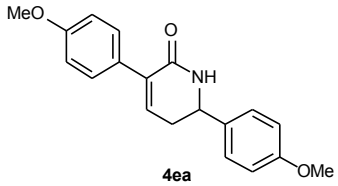

4ea

Off-white solid (16.4 mg, 53% yield)

^{1}H NMR (500 MHz, $CDCl_3$) δ 7.43 (d, *J* = 8.7 Hz, 2H), 7.32 (d, *J* = 8.7 Hz, 2H), 6.91 (t, *J* = 8.8 Hz, 3H), 6.64 (t, *J* = 4.5 Hz, 1H), 5.77 (s, 1H), 4.75 (t, *J* = 8.6 Hz, 1H), 3.82 (d, *J* = 1.2 Hz, 6H), 2.65 (dd, *J* = 8.8, 4.3 Hz, 2H).

^{13}C NMR ($CDCl_3$, 126 MHz)δ 166.34, 159.57, 159.33, 135.50, 135.01, 133.04, 129.74, 128.83, 127.72, 114.30, 113.53, 55.36, 55.31, 33.80.

IR (neat, cm^{-1}) 3184, 1665, 1610, 1510, 1300, 1247, 1181, 1033, 825.

LRMS (ESI) m/z calcd for $C_{19}H_{19}NO_3$ $[M+H]^+$: 310.1, found: 310.1, 332.1.

Table 4.29: 3-(4-Methoxyphenyl)-6-(4-(trifluoromethyl)phenyl)-5,6-dihydropyridin-2(1H)-one (4ed) characterization.

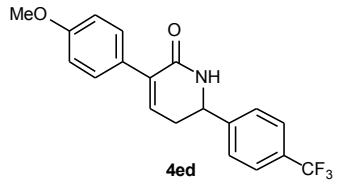

4ed

Off-white solid (5.6 mg, 16% yield)

^{1}H NMR (500 MHz, $CDCl_3$) δ 7.69 (d, *J* = 8.1 Hz, 2H), 7.56 (d, *J* = 8.0 Hz, 2H), 7.44 (d, *J* = 8.7 Hz, 2H), 6.93 (d, *J* = 8.7 Hz, 2H), 6.65 (dd, *J* = 5.5, 3.4 Hz, 1H), 5.97 (s, NH), 4.97 – 4.82 (m, 1H), 3.84 (s, 3H), 2.81 (dtd, *J* = 17.6, 5.6, 1.1 Hz, 1H), 2.68 (ddd, *J* = 17.6, 10.7, 3.5 Hz, 1H). **^{13}C NMR** ($CDCl_3$, 126 MHz)δ 166.26, 159.47, 145.11, 135.19, 134.77, 129.73, 128.45, 126.83, 126.00, 125.97, 125.94, 113.58, 55.36, 55.32, 33.47, 29.71.

^{19}F NMR ($CDCl_3$, 282 MHz) δ -61.77.

IR (neat, cm^{-1}) 3195, 3060, 2922, 1667, 1609, 1511, 1324, 1118, 827.

LRMS (ESI) m/z calcd for $C_{19}H_{16}F_3NO_2$ $[M+H]^+$: 348.1, found: 348.2.

Table 4.30: Methyl 2-(6-(4-methoxyphenyl)-2-oxo-1,2,5,6-tetrahydropyridin-3-yl)acetate (4fa) characterization.

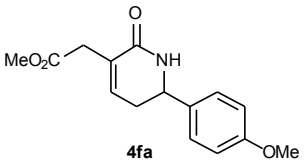

4fa

Off-white solid (20.4 mg, 74% yield)

^{1}H NMR (500 MHz, $CDCl_3$) δ 7.28 (d, *J* = 8.7 Hz, 2H), 6.89 (d, *J* = 8.6 Hz, 2H), 6.52 – 6.46 (m, 1H), 5.64 (s, 1H), 4.71 (dd, *J* = 9.7, 7.5 Hz, 1H), 3.80 (s, 3H), 3.70 (s, 3H), 3.34 (ddd, *J* = 66.8, 16.5, 1.4 Hz, 2H), 2.62 – 2.49 (m, 2H).

^{13}C NMR ($CDCl_3$, 126 MHz)δ 171.76, 166.20, 159.56, 137.58, 132.99, 128.65, 127.70, 114.26, 55.37, 55.34, 52.02, 35.62, 33.44.

IR (neat, cm^{-1}) 3210, 2961, 2837, 1734, 1677, 1513, 1246, 1159, 1029, 830.

LRMS (ESI) m/z calcd for $C_{15}H_{17}NO_4$ $[M+H]^+$: 276.1, found: 276.1, 298.1.

Table 4.31: Methyl 2-(2-oxo-6-(4-(trifluoromethyl)phenyl)-1,2,5,6-tetrahydropyridin-3-yl)acetate (4fd) characterization.

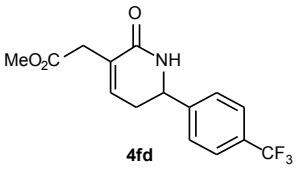

4fd

Off-white solid (23.2 mg, 74% yield)

^{1}H NMR (500 MHz, $CDCl_3$) δ 7.66 (d, *J* = 8.1 Hz, 2H), 7.53 (d, *J* = 8.1 Hz, 2H), 6.48 (dd, *J* = 5.1, 3.5 Hz, 1H), 6.14 (s, NH), 4.87 (ddd, *J* = 10.5, 5.8, 1.6 Hz, 1H), 3.71 (s, 3H), 3.38 – 3.29 (m, 2H), 2.73 (dt, *J* = 17.7, 5.6 Hz, 1H), 2.61 – 2.46 (m, 1H). **^{13}C NMR** ($CDCl_3$, 126 MHz)δ 171.60, 166.14, 145.14, 136.85, 130.63, 130.37, 128.93, 126.86, 125.92, 125.89, 125.86, 125.84, 124.99, 122.82, 55.16, 52.01, 35.59, 32.98, 29.70.

^{19}F NMR ($CDCl_3$, 282 MHz) δ -61.77.

IR (neat, cm^{-1}) 3203, 1722, 1685, 1639, 1330, 1154, 1114, 1070.

LRMS (ESI) m/z calcd for $C_{15}H_{14}F_3NO_3$ $[M+H]^+$: 314.1, found: 314.1, 336.0.

4.4.5 Copies of NMR spectra

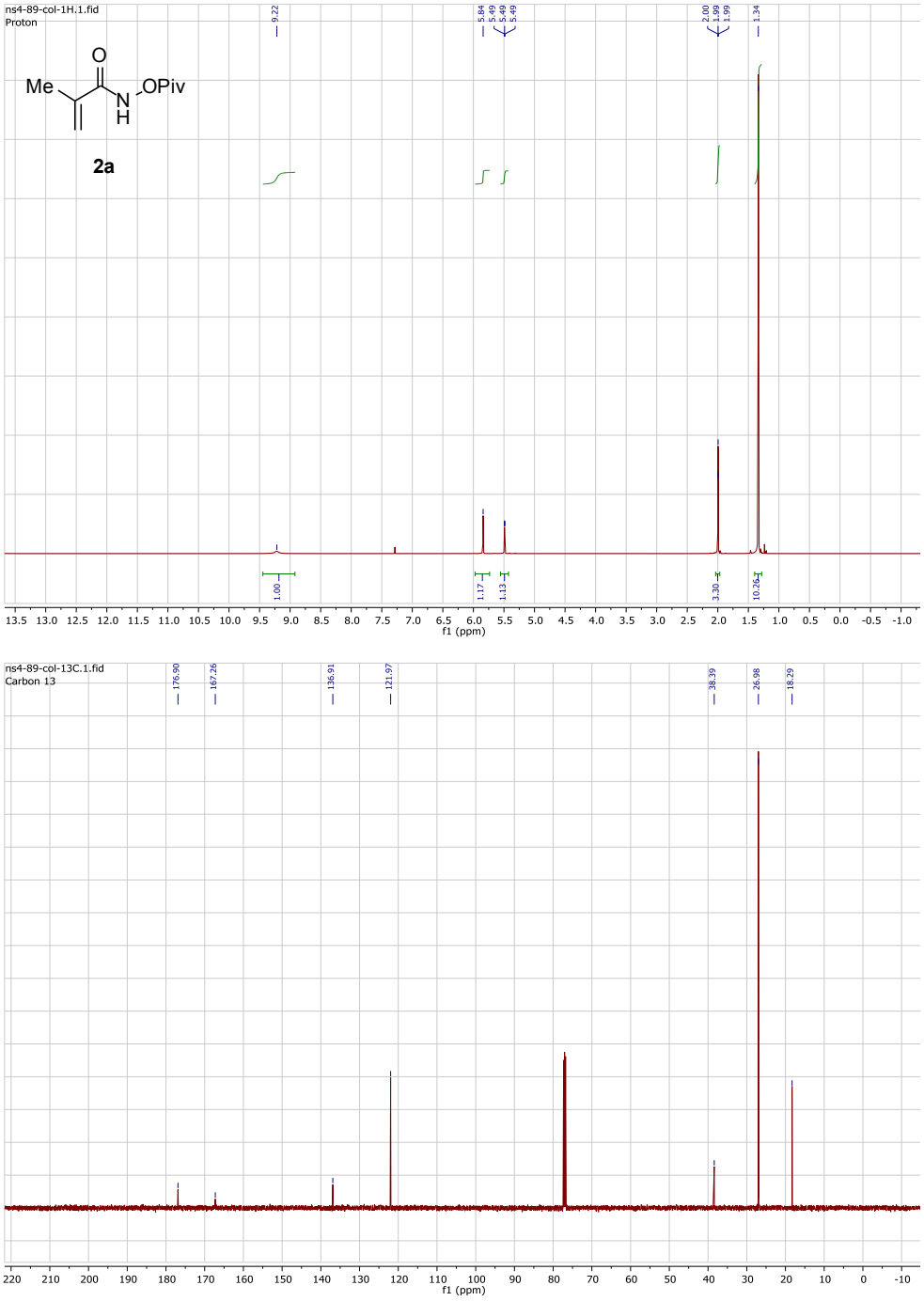

Figure 4.5: N-(Pivaloyloxy)methacrylamide (2a) NMR.

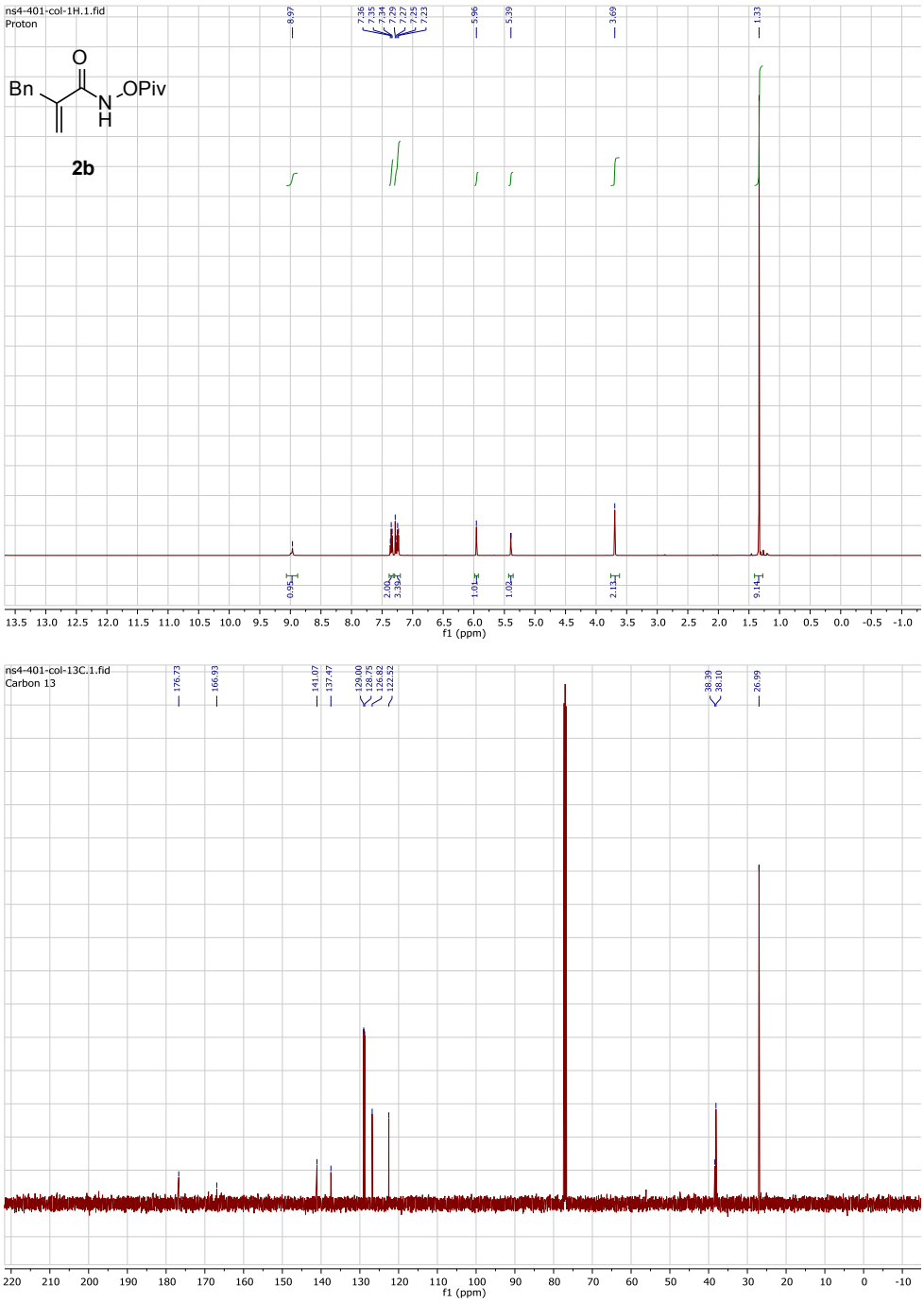

Figure 4.6: 2-Benzyl-N-(pivaloyloxy)acrylamide (2b) NMR.

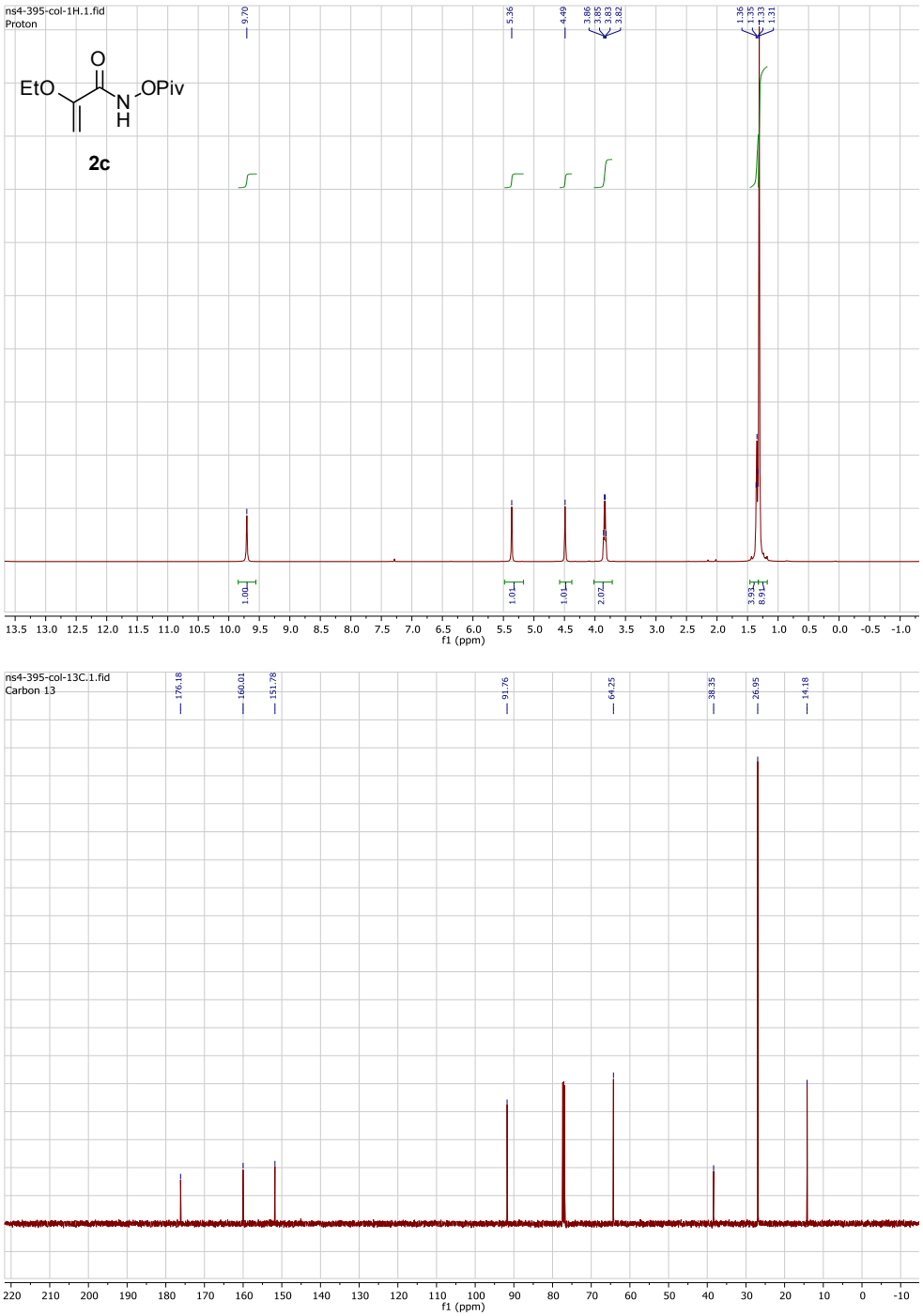

Figure 4.7: 2-Ethoxy-N-(pivaloyloxy)acrylamide (2c) NMR.

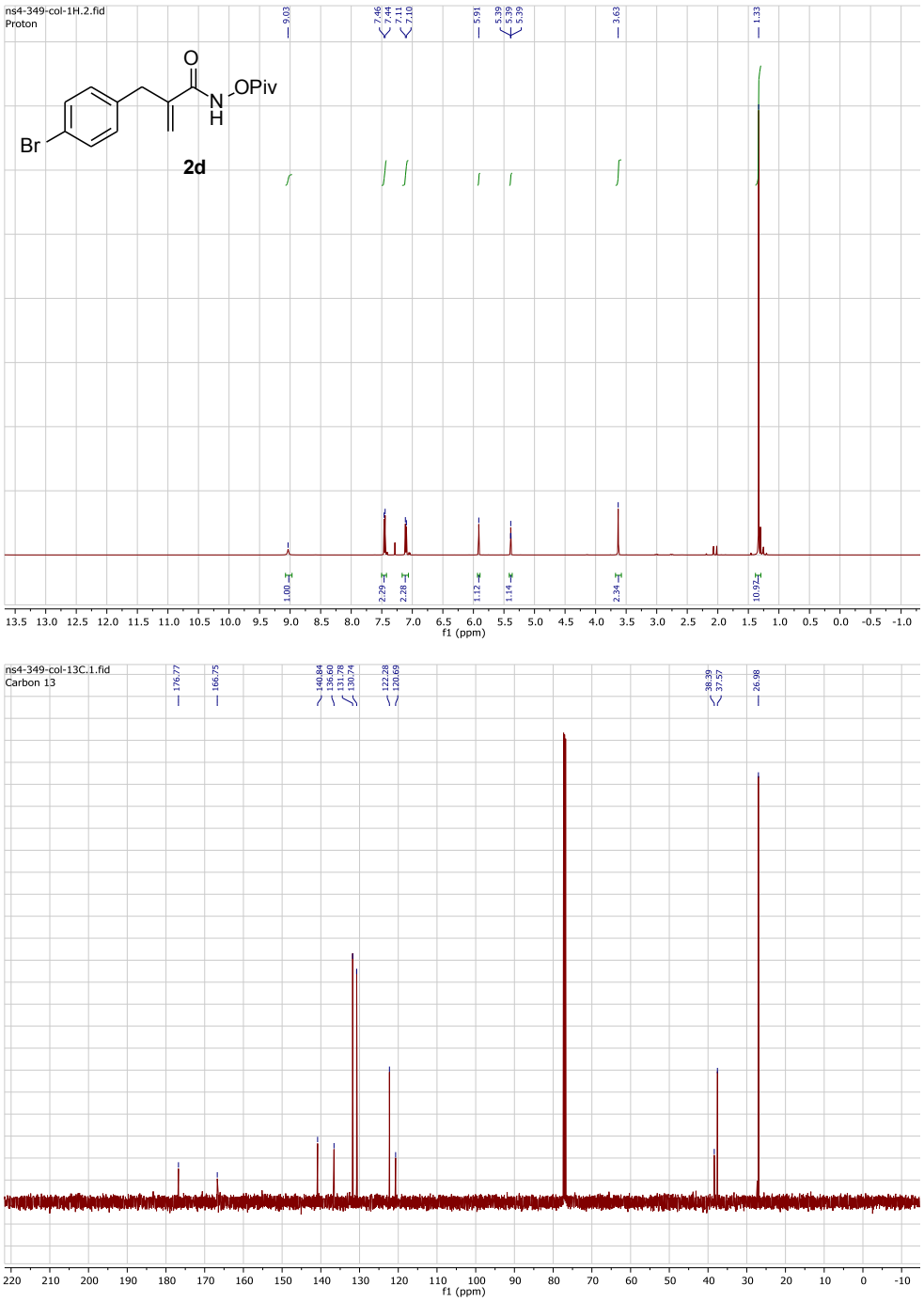

Figure 4.8: 2-(4-Bromobenzyl)-N-(pivaloyloxy)acrylamide (2d) NMR.

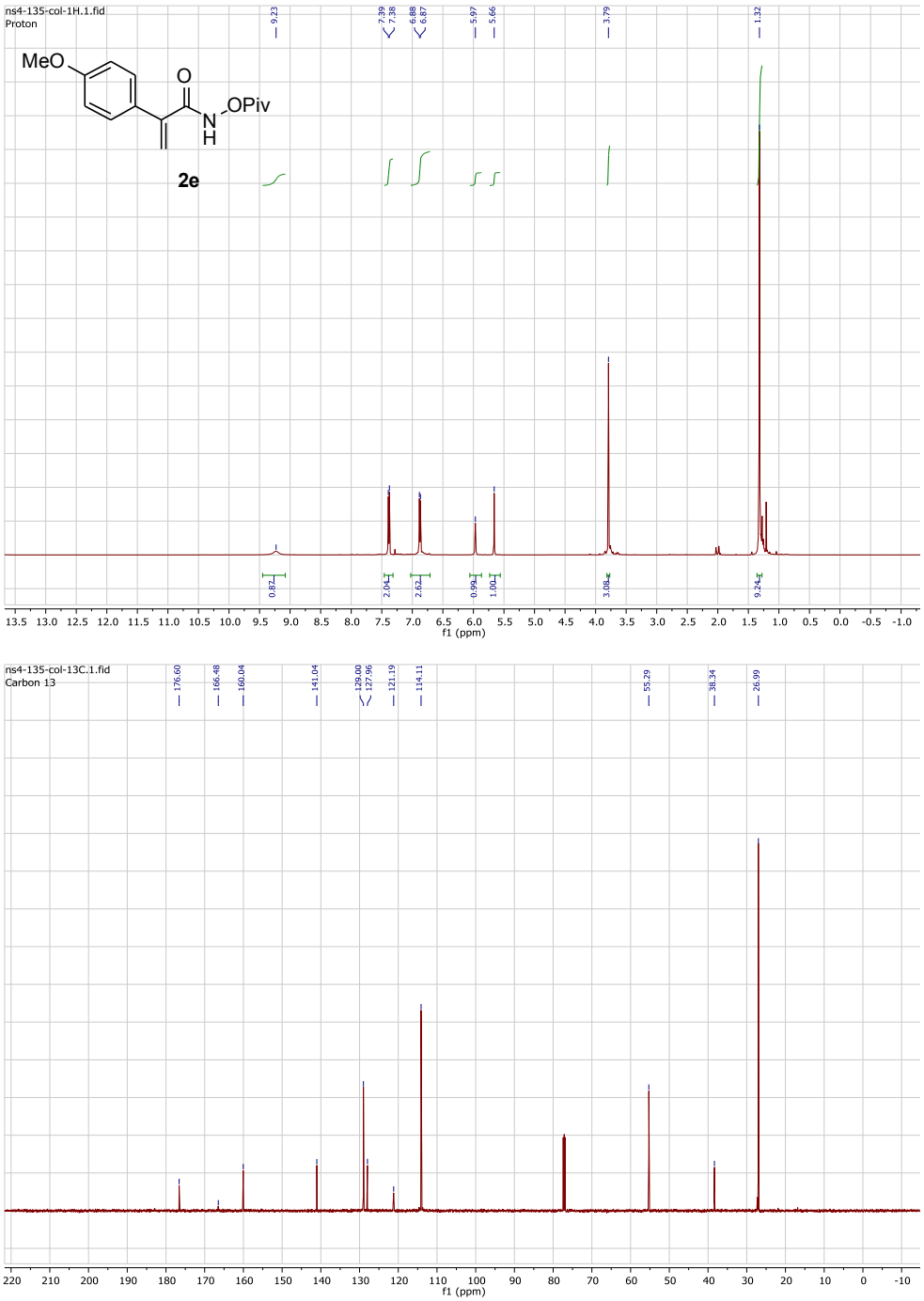

Figure 4.9: 2-(4-methoxyphenyl)-N-(pivaloyloxy)acrylamide (2e) NMR.

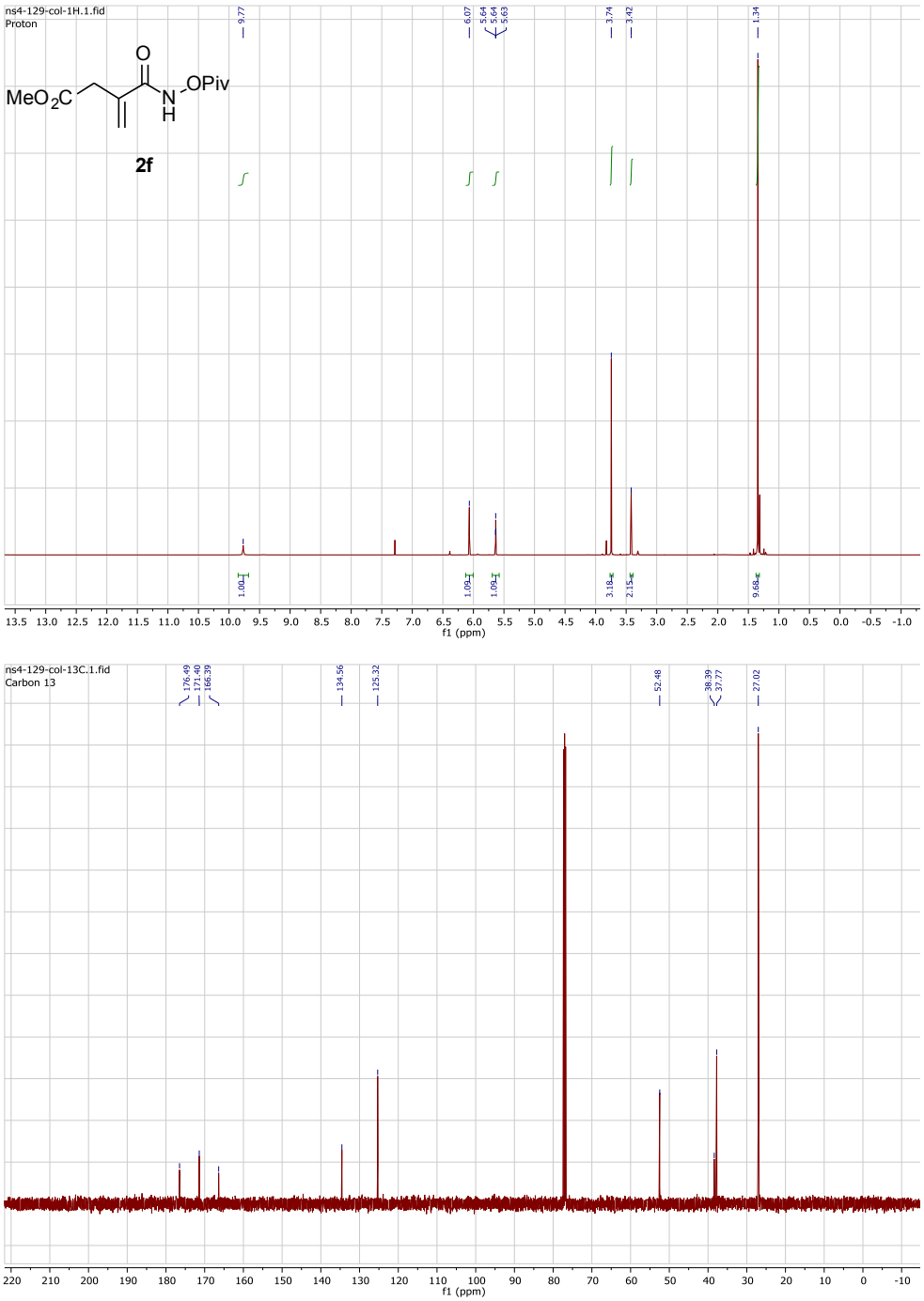

Figure 4.10: Methyl 3-((pivaloyloxy)carbamoyl)but-3-enoate (2f) NMR.

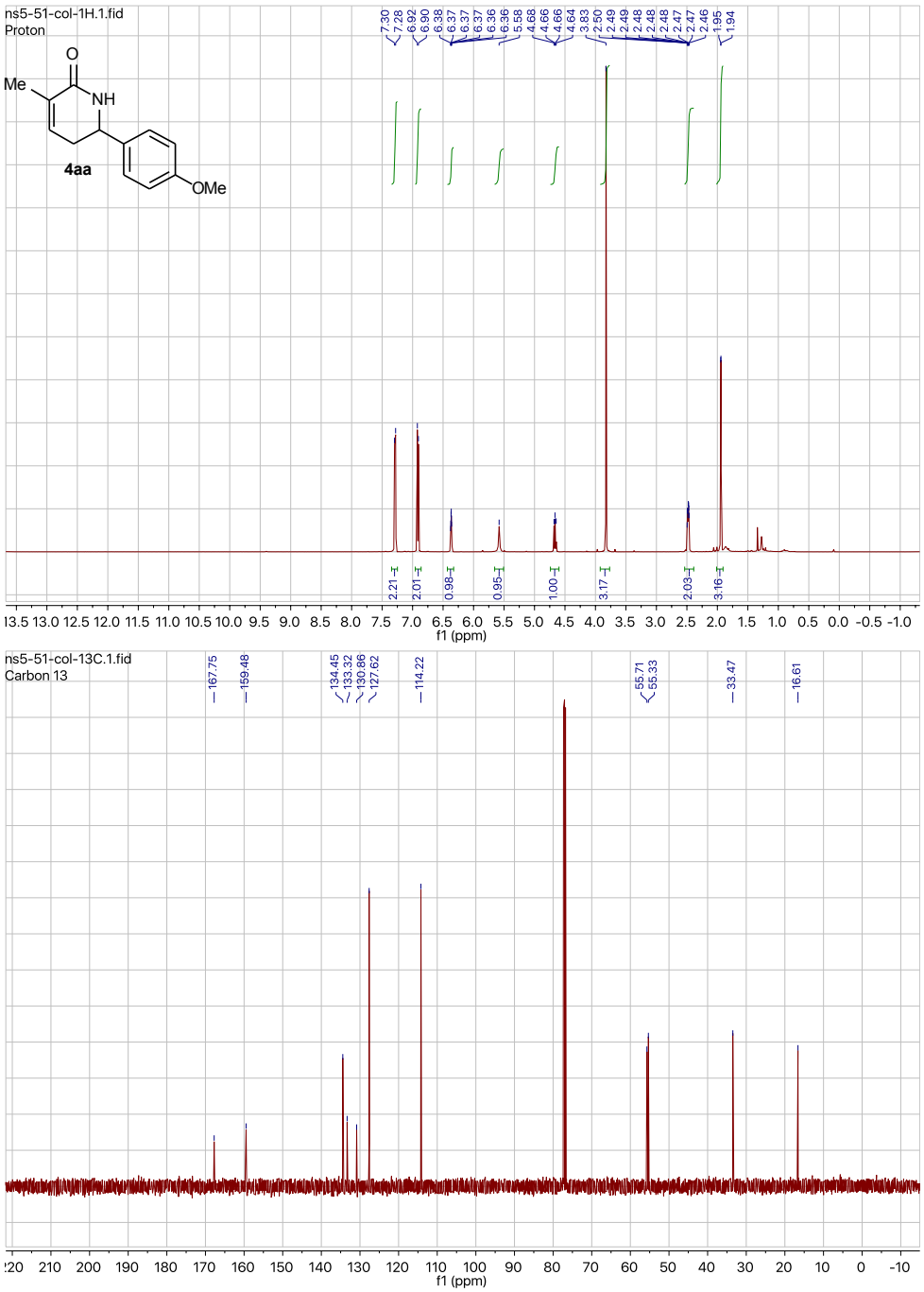

Figure 4.11: 6-(4-Methoxyphenyl)-3-methyl-5,6-dihydropyridin-2(1H)-one (4aa) NMR.

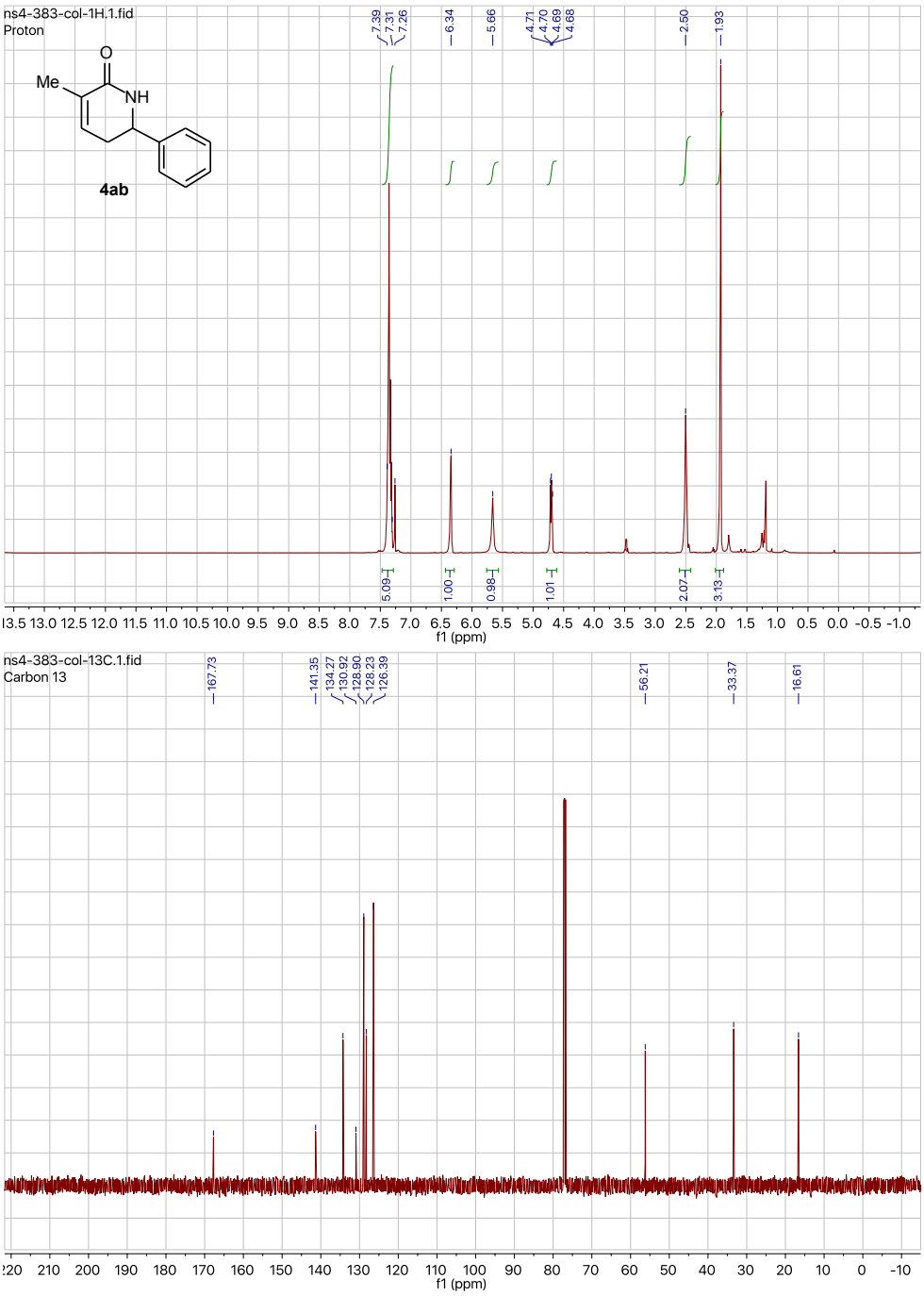

Figure 4.12: 3-Methyl-6-phenyl-5,6-dihydropyridin-2(1H)-one (4ab) NMR.

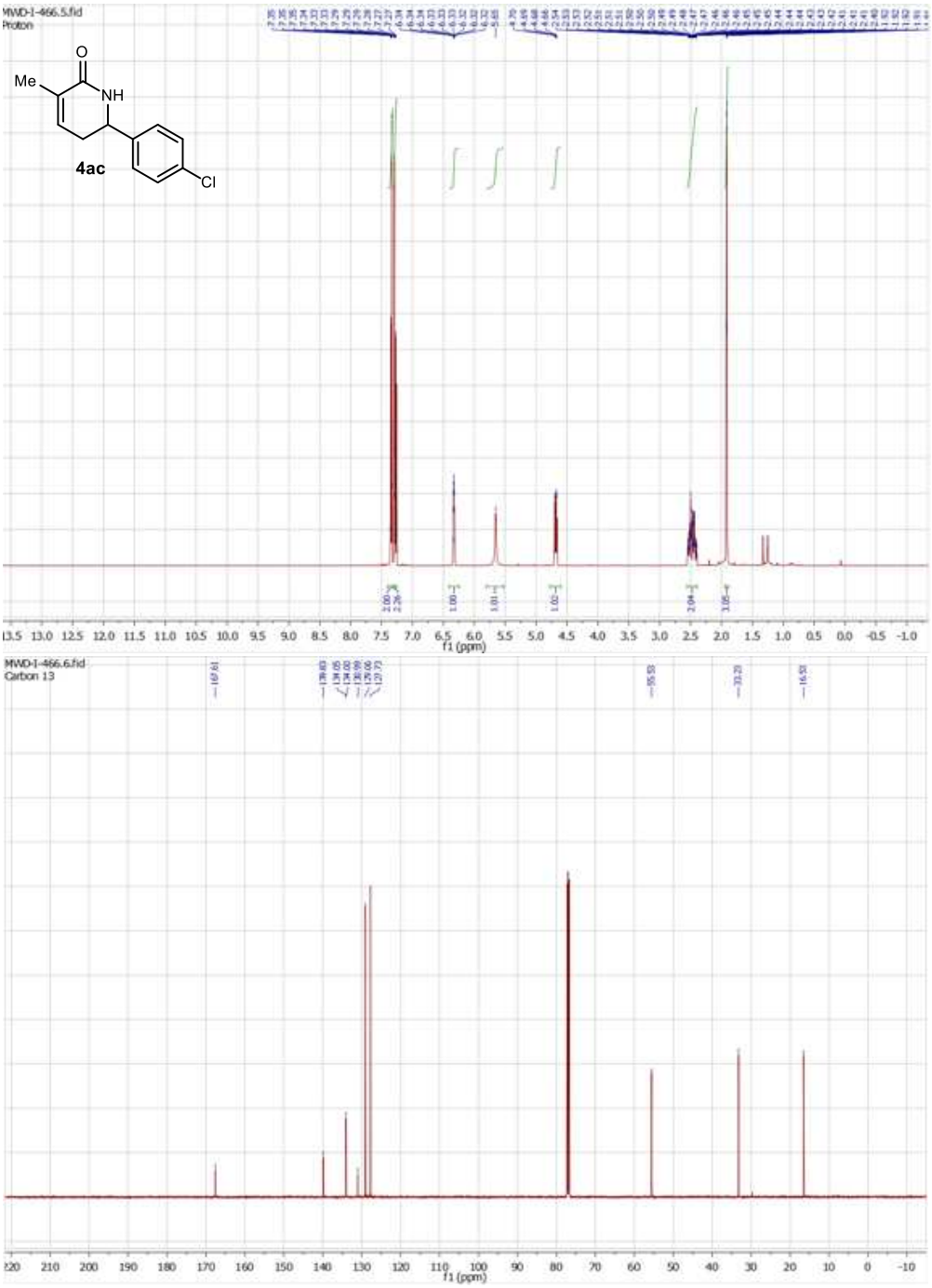

Figure 4.13: 6-(4-Chlorophenyl)-3-methyl-5,6-dihydropyridin-2(1H)-one (4ac) NMR.

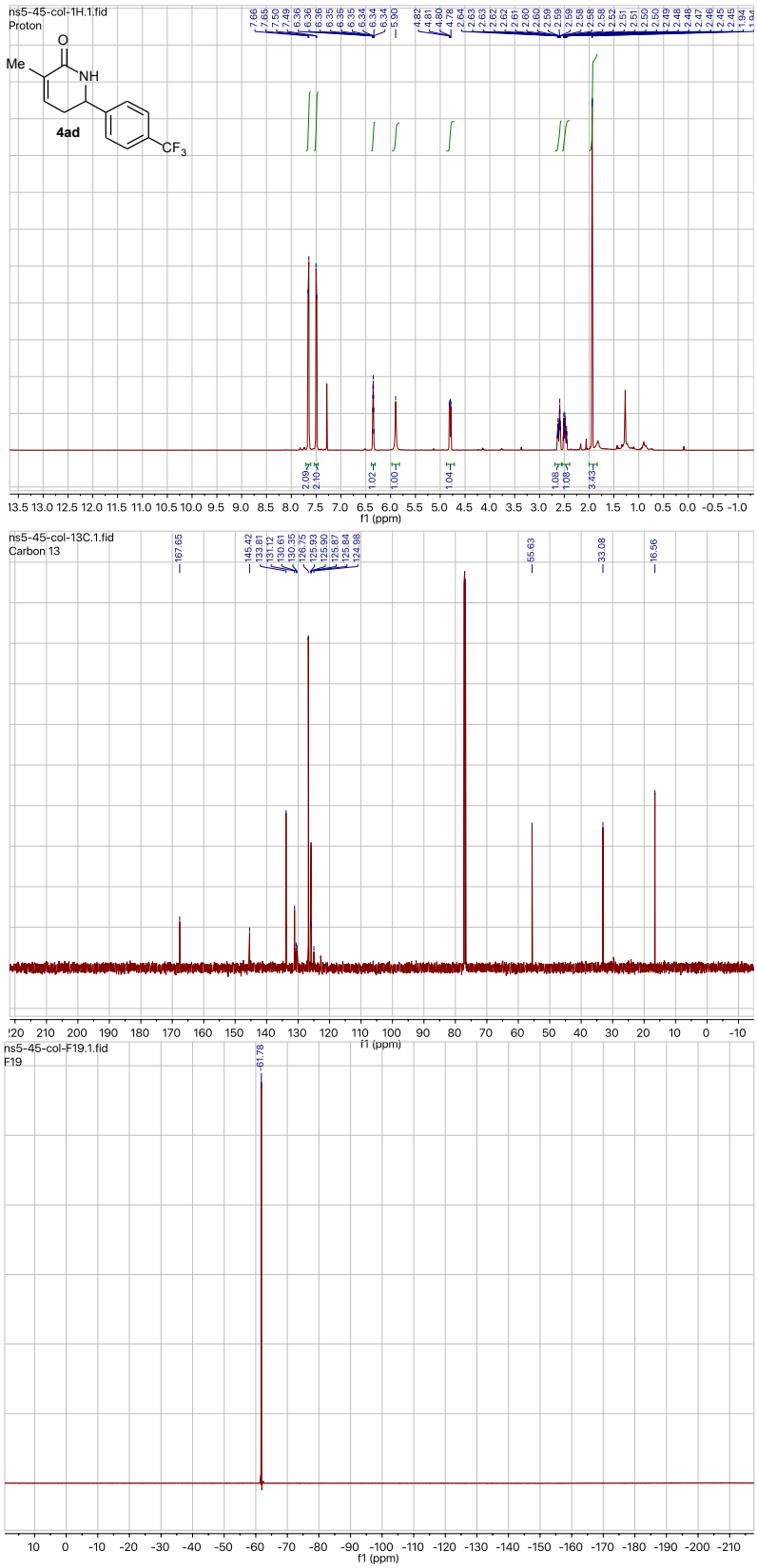

Figure 4.14: 3-Methyl-6-(4-(trifluoromethyl)phenyl)-5,6-dihydropyridin-2(1H)-one (4ad) NMR.

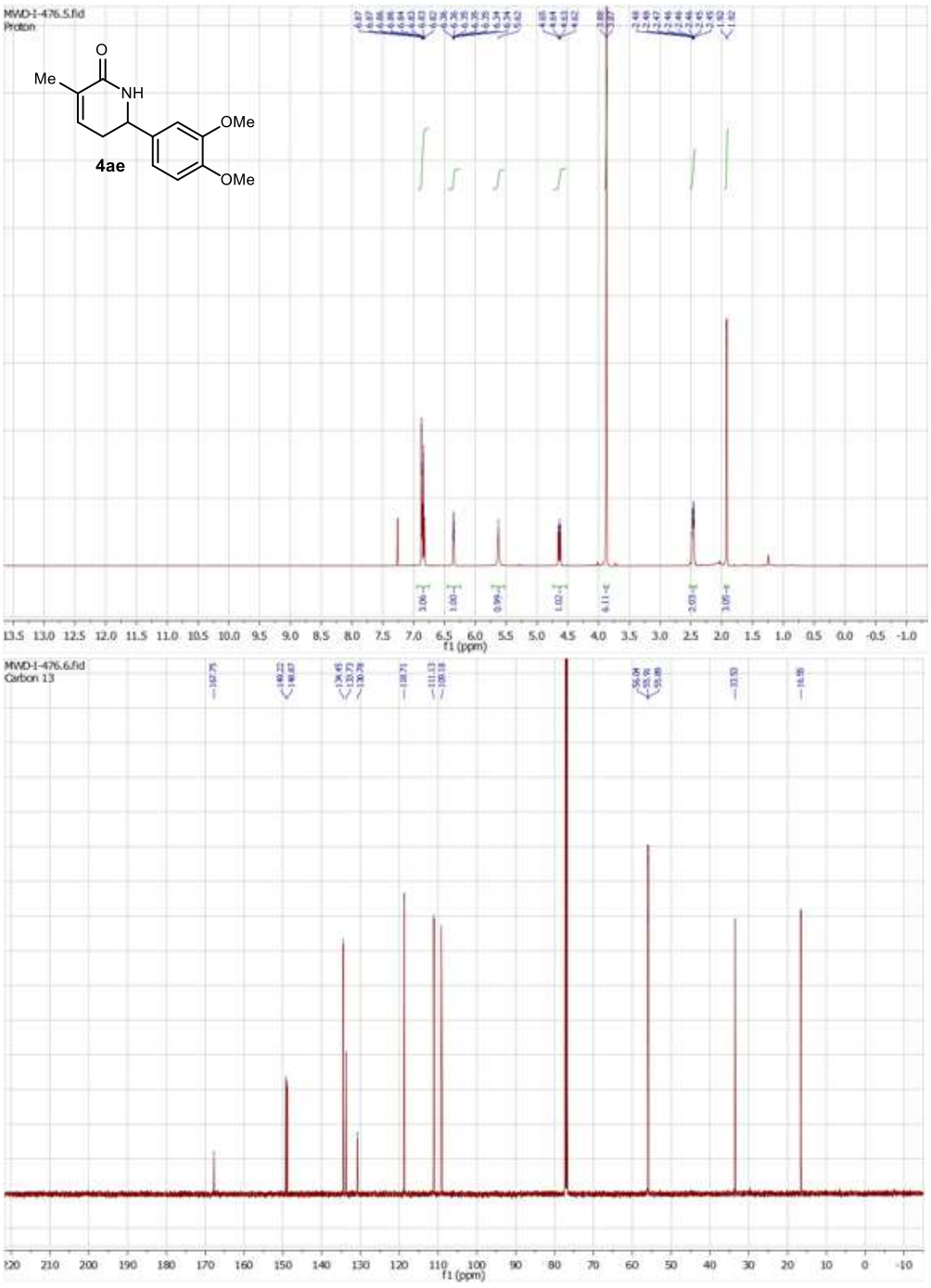

Figure 4.15: 6-(3,4-Dimethoxyphenyl)-3-methyl-5,6-dihydropyridin-2(1H)-one (4ae) NMR.

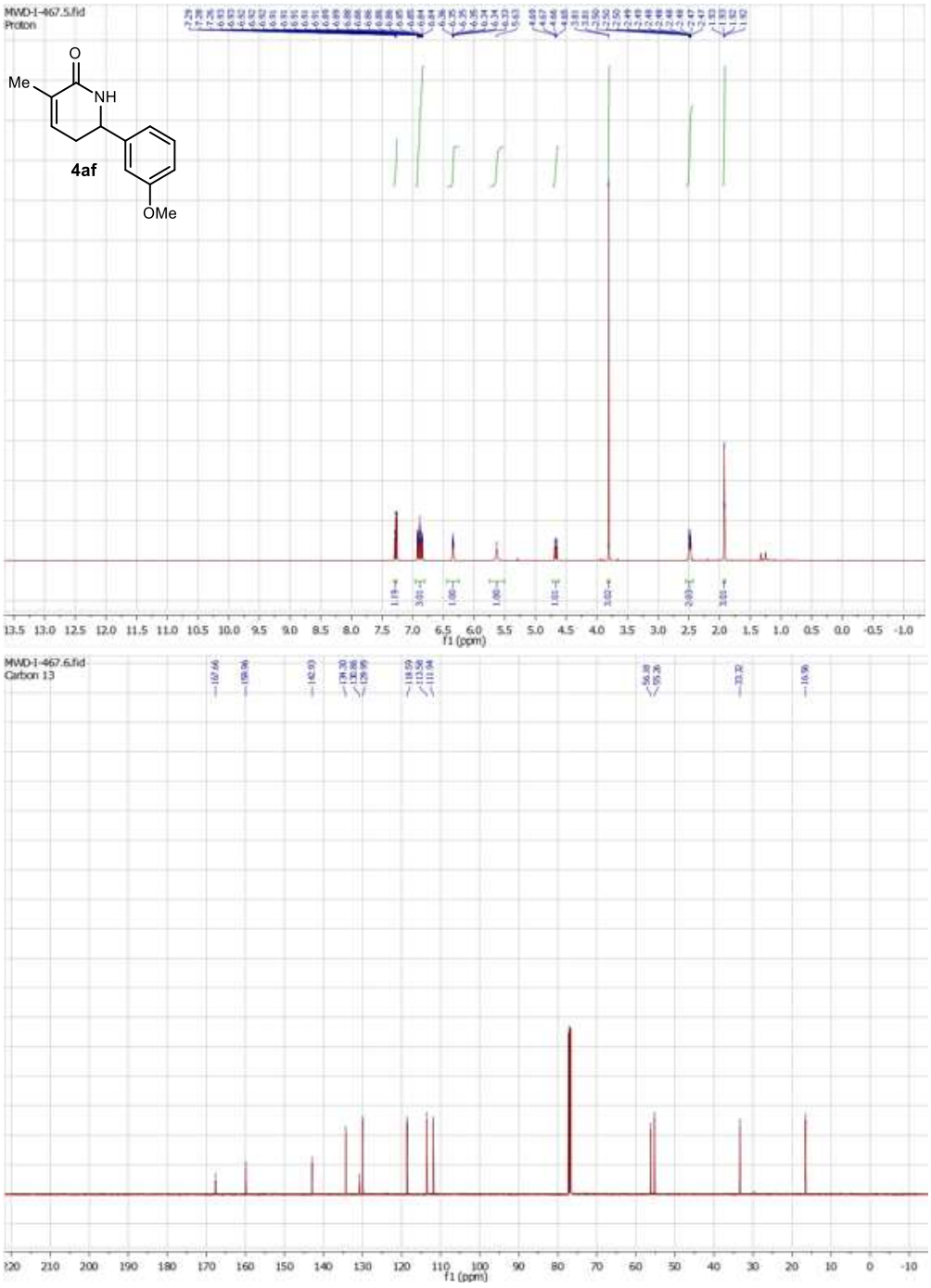

Figure 4.16: 6-(3-Methoxyphenyl)-3-methyl-5,6-dihydropyridin-2(1H)-one (4af) NMR.

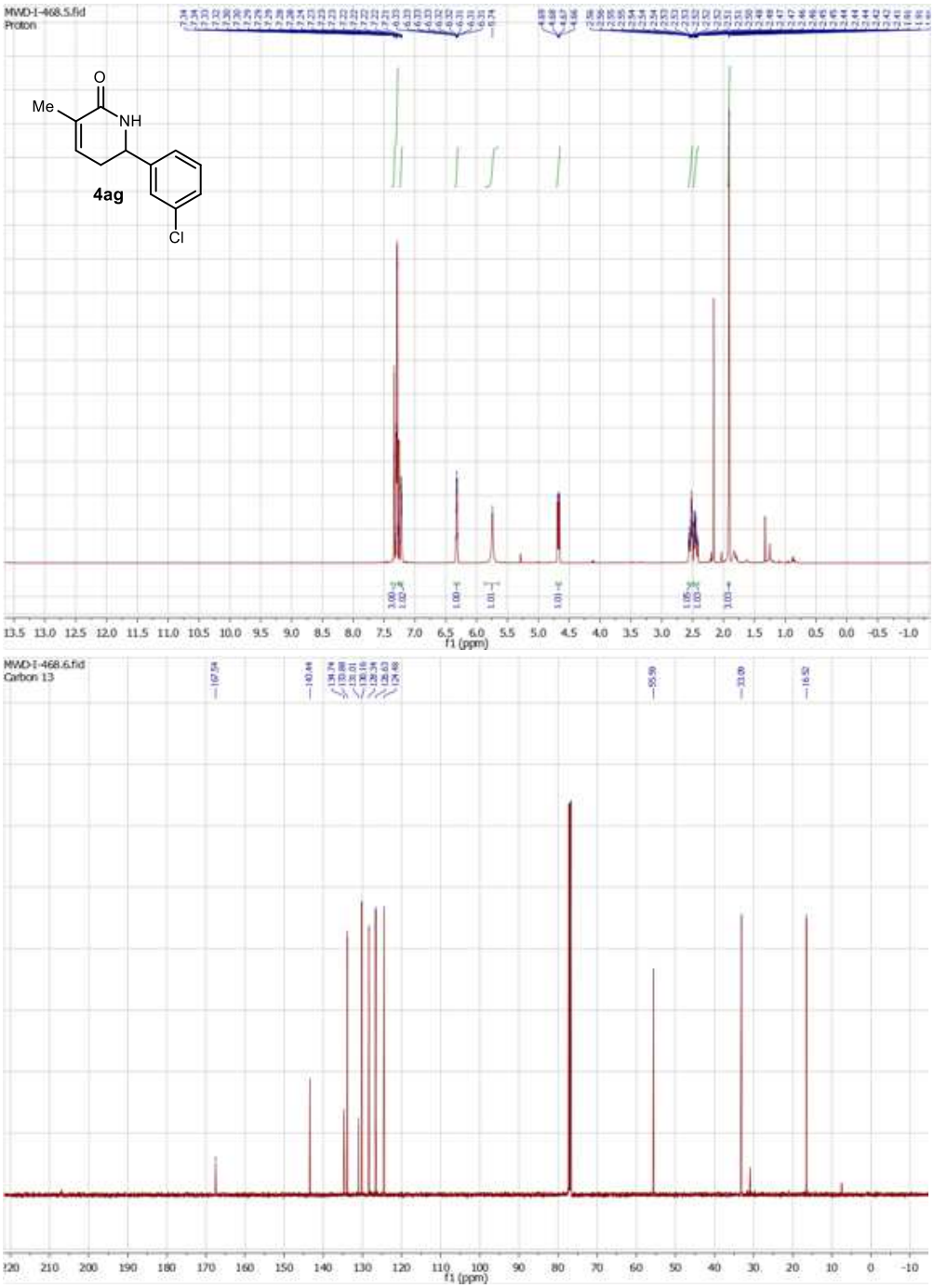

Figure 4.17: 6-(3-Chlorophenyl)-3-methyl-5,6-dihydropyridin-2(1H)-one (4ag) NMR.

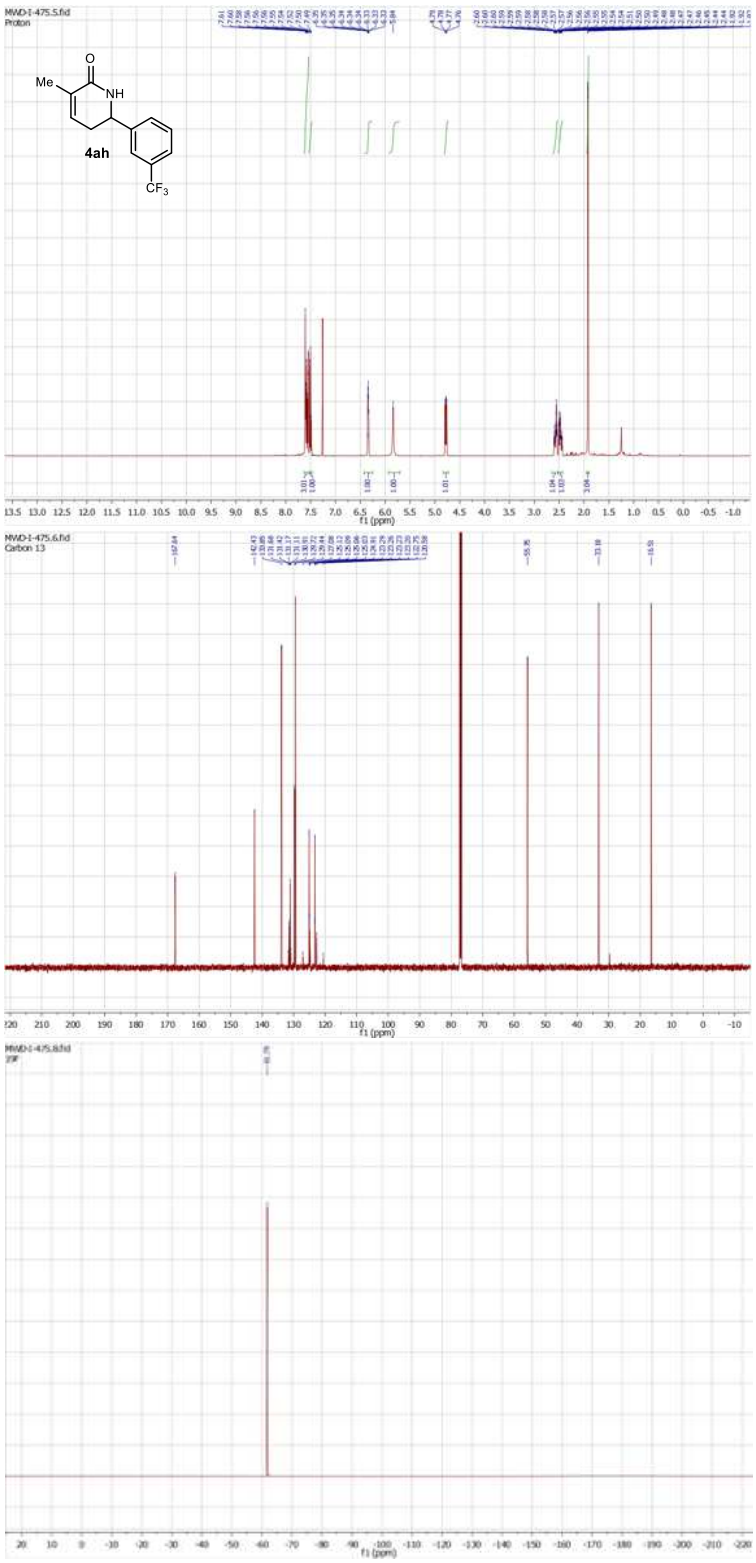

Figure 4.18: 3-Methyl-6-(3-(trifluoromethyl)phenyl)-5,6-dihydropyridin-2(1H)-one (4ah) NMR.

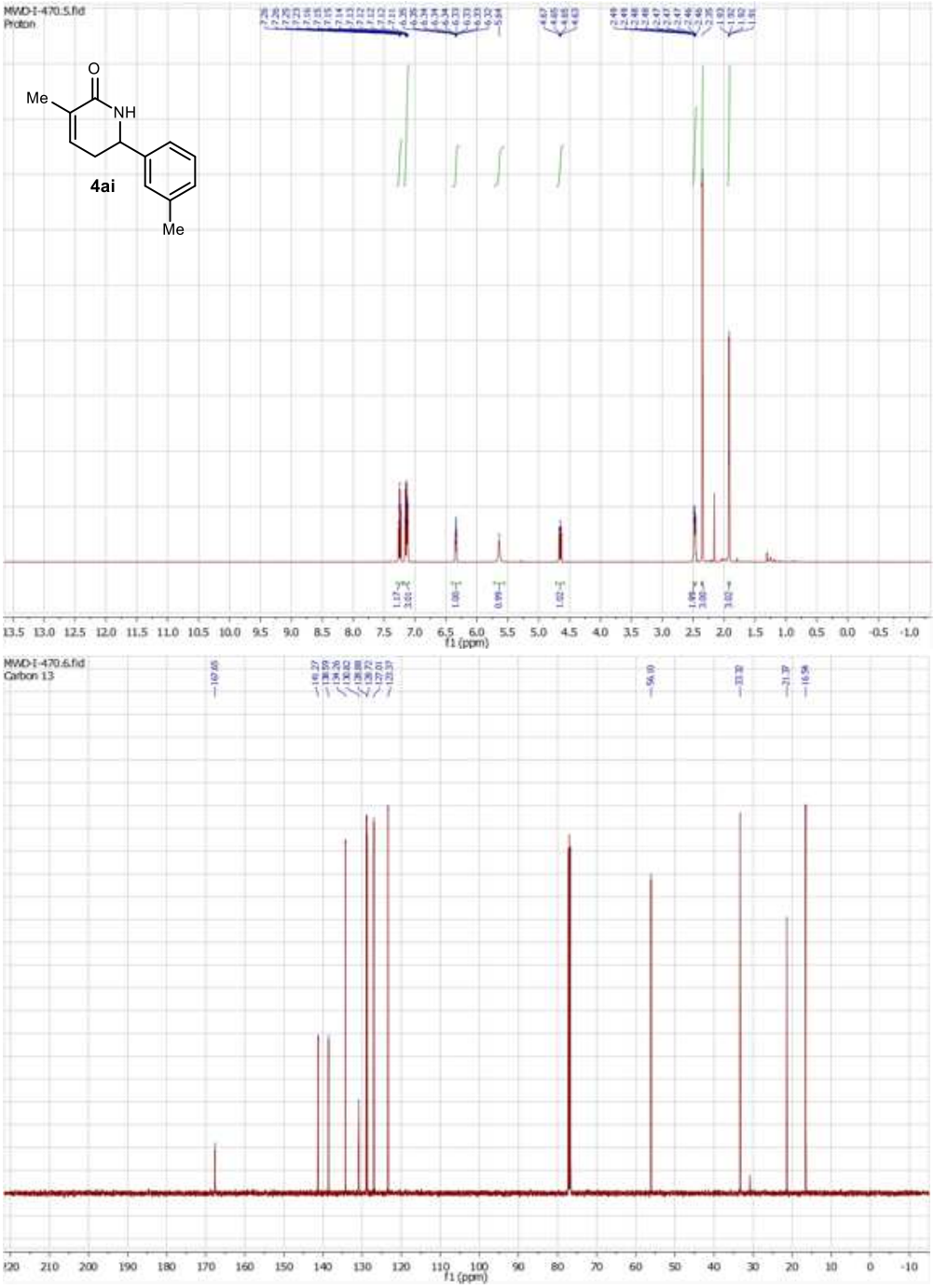

Figure 4.19: 3-Methyl-6-(m-tolyl)-5,6-dihydropyridin-2(1H)-one (4ai) NMR.

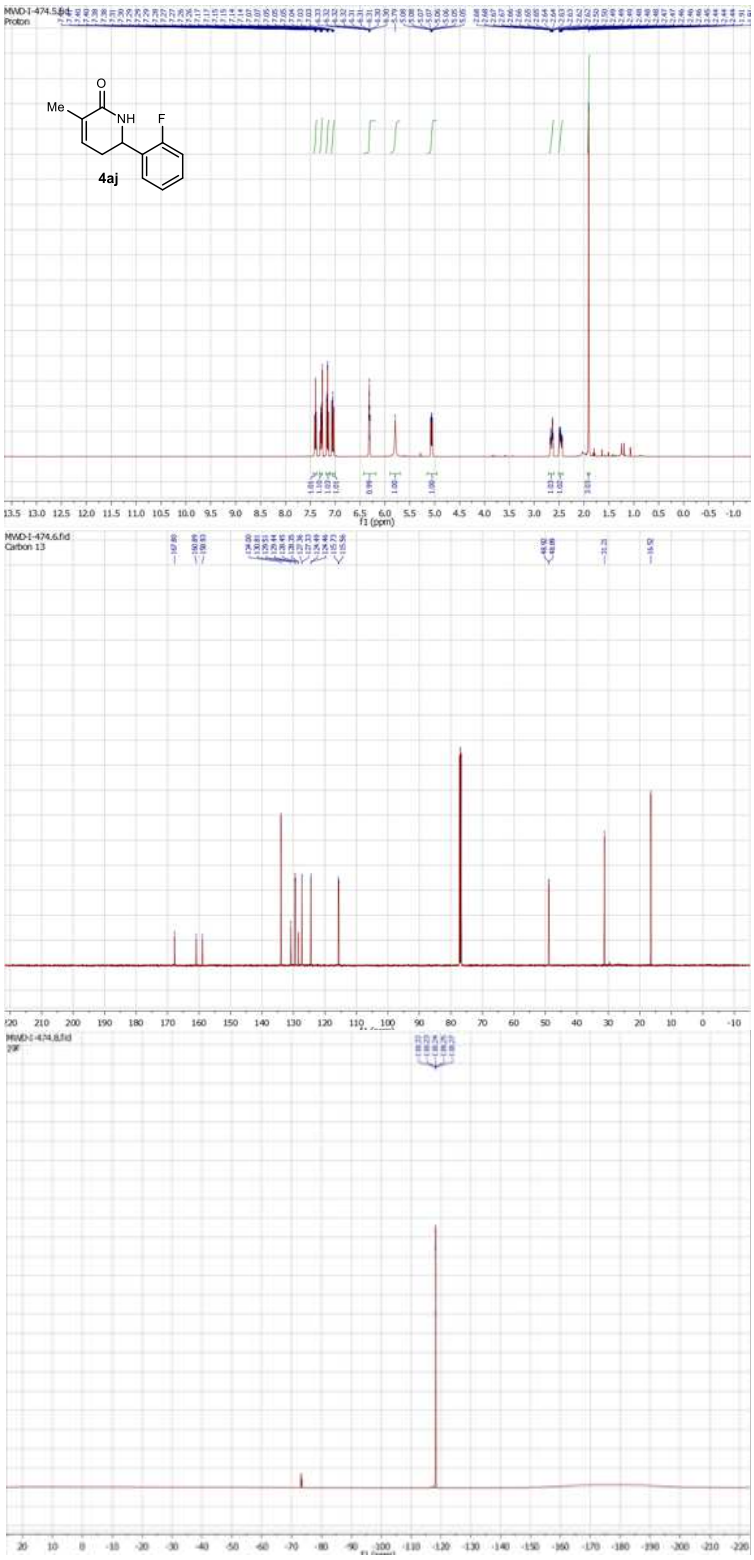

Figure 4.20: 6-(2-Fluorophenyl)-3-methyl-5,6-dihydropyridin-2(1H)-one (4aj) NMR.

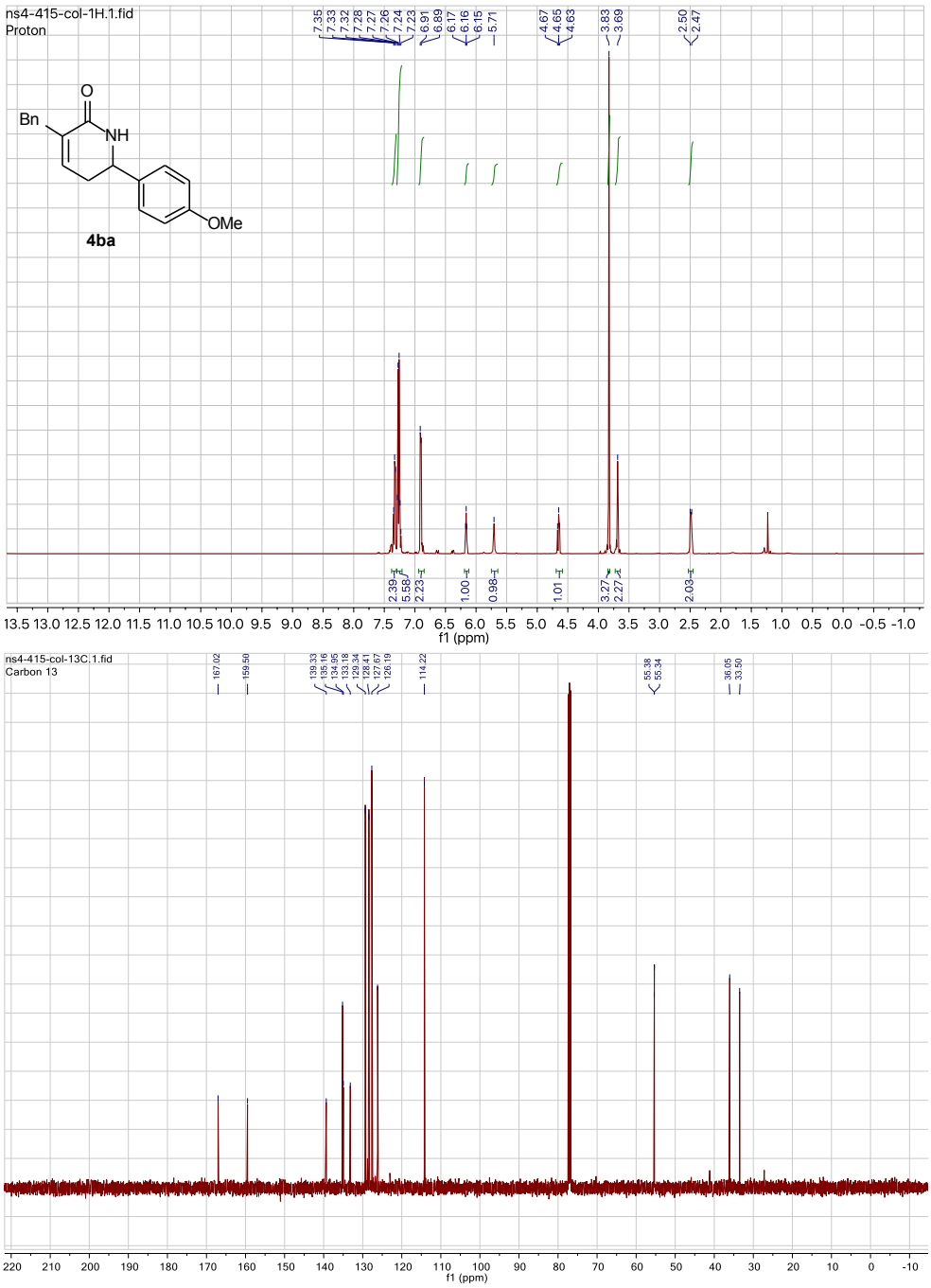

Figure 4.21: 3-Benzyl-6-(4-methoxyphenyl)-5,6-dihydropyridin-2(1H)-one (4ba) NMR.

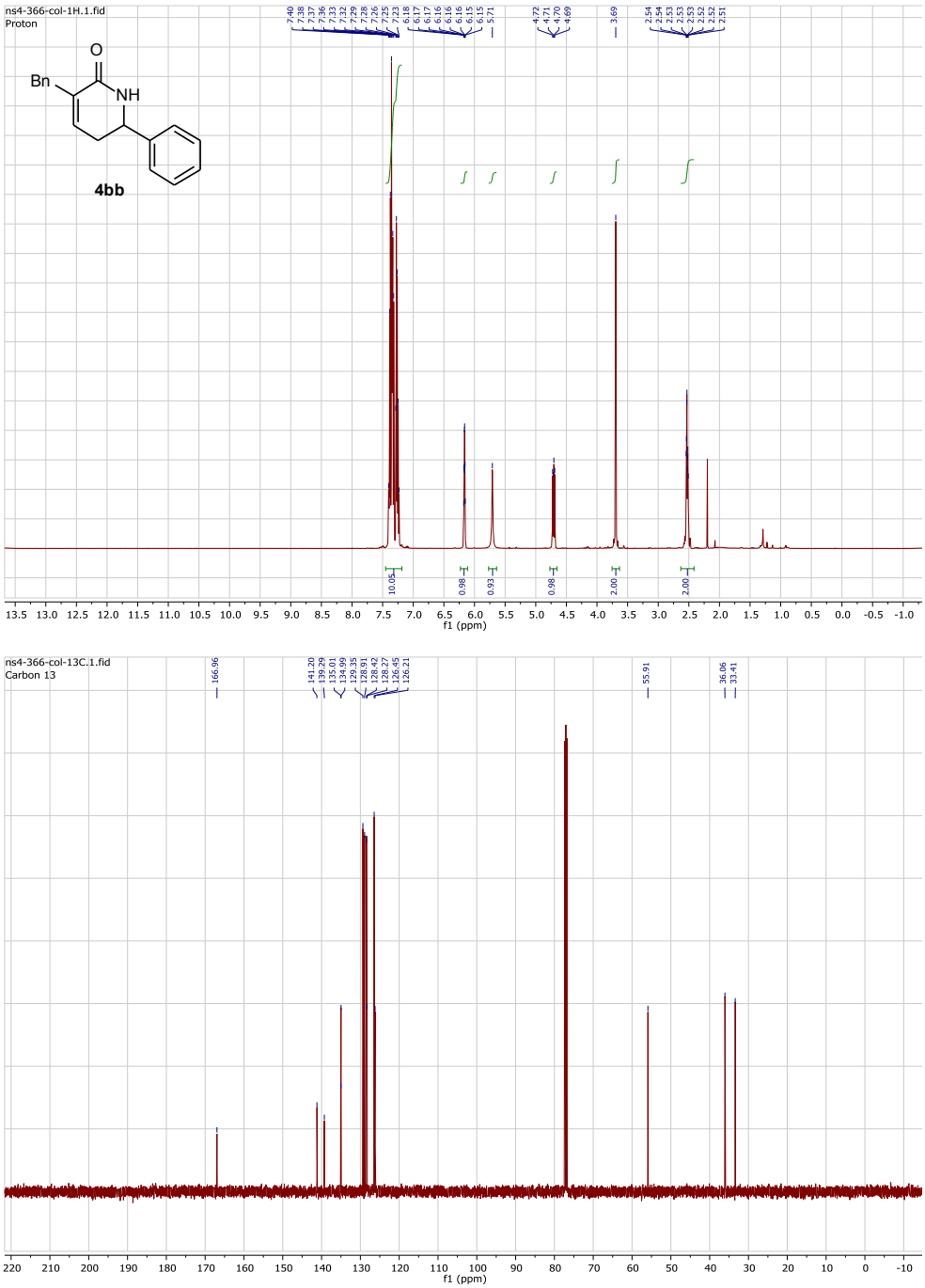

Figure 4.22: 3-Benzyl-6-phenyl-5,6-dihydropyridin-2(1H)-one (4bb) NMR.

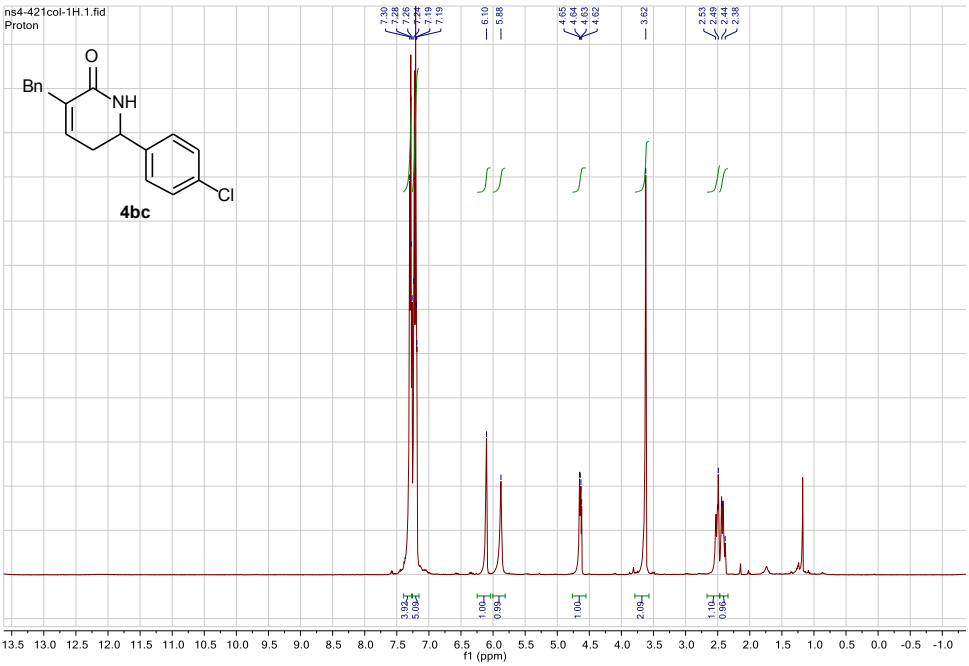

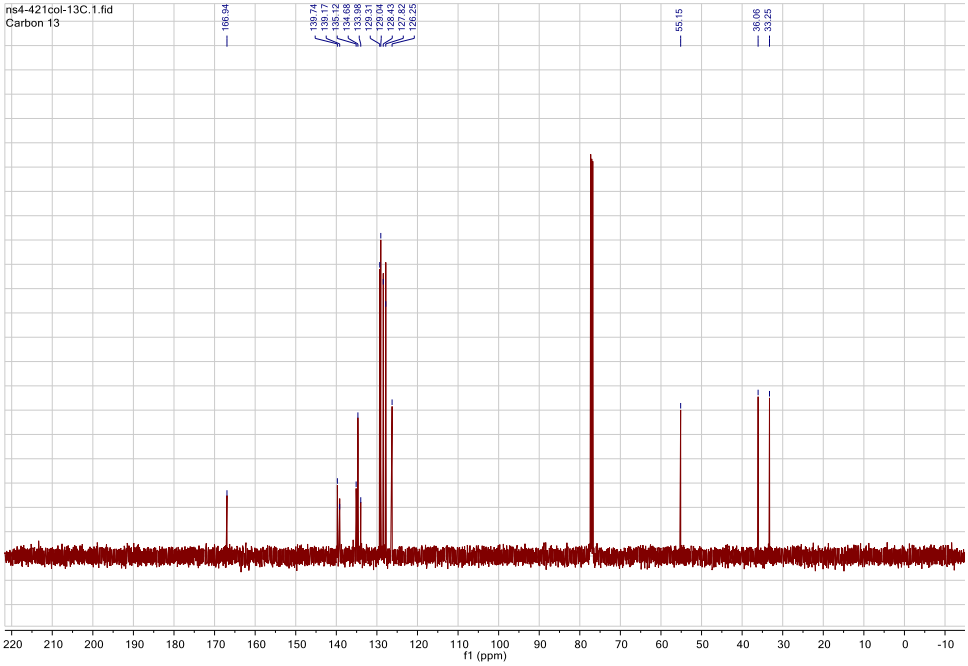

Figure 4.23: 3-Benzyl-6-(4-chlorophenyl)-5,6-dihydropyridin-2(1H)-one (4bc) NMR.

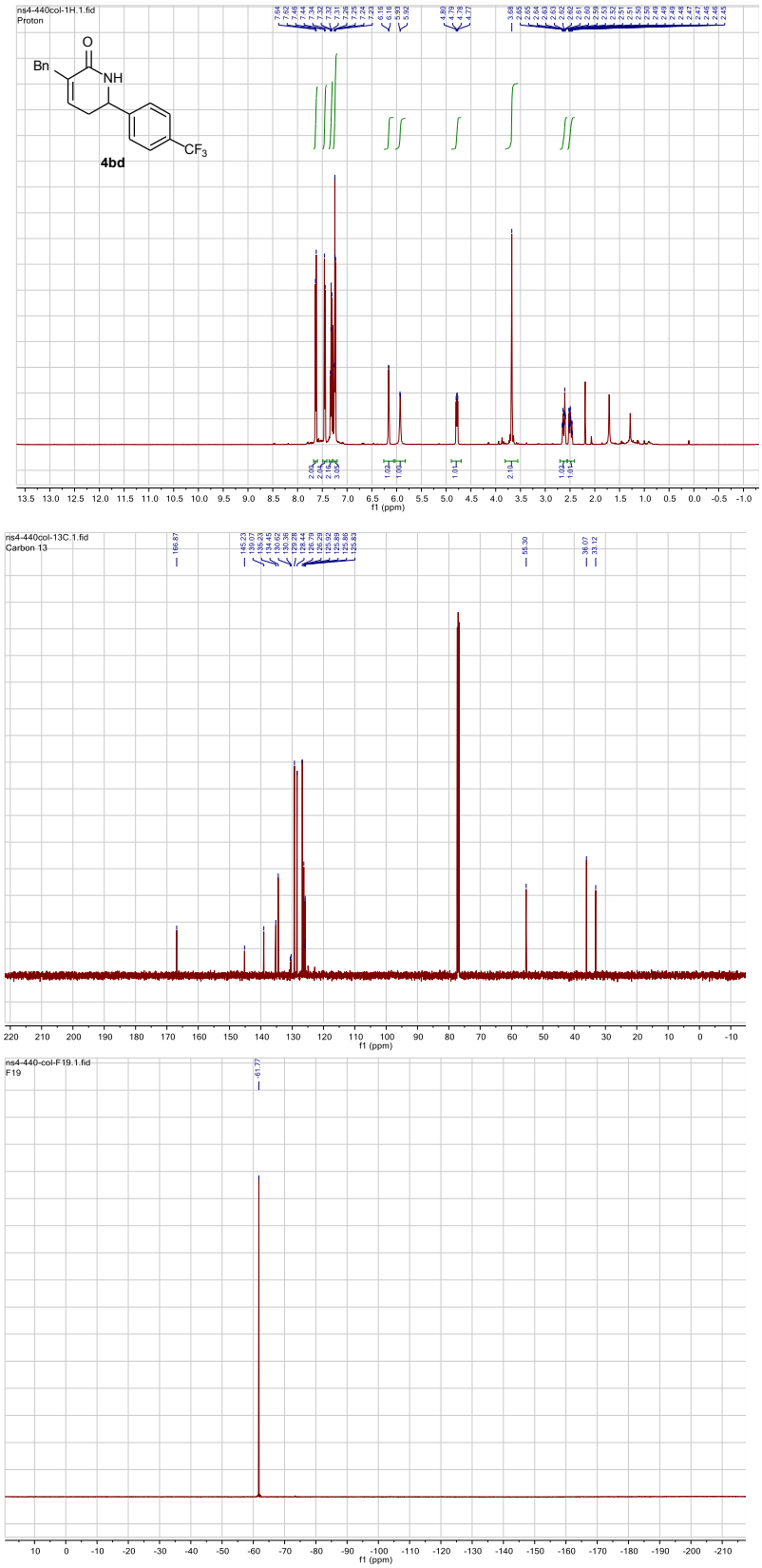

Figure 4.24: 3-Benzyl-6-(4-(trifluoromethyl)phenyl)-5,6-dihydropyridin-2(1H)-one (4bd) NMR.

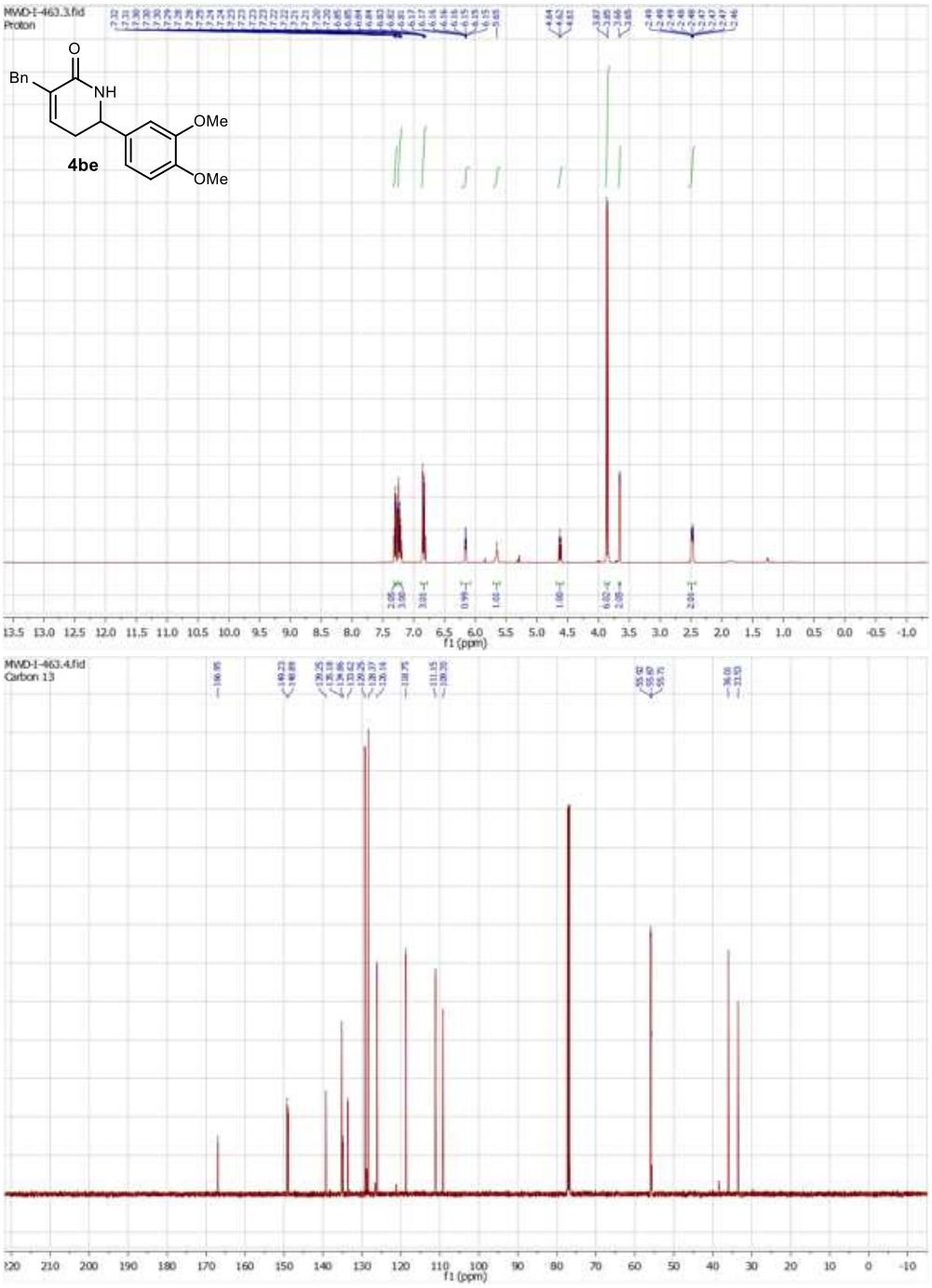

Figure 4.25: 3-Benzyl-6-(3,4-dimethoxyphenyl)-5,6-dihydropyridin-2(1H)-one (4be) NMR.

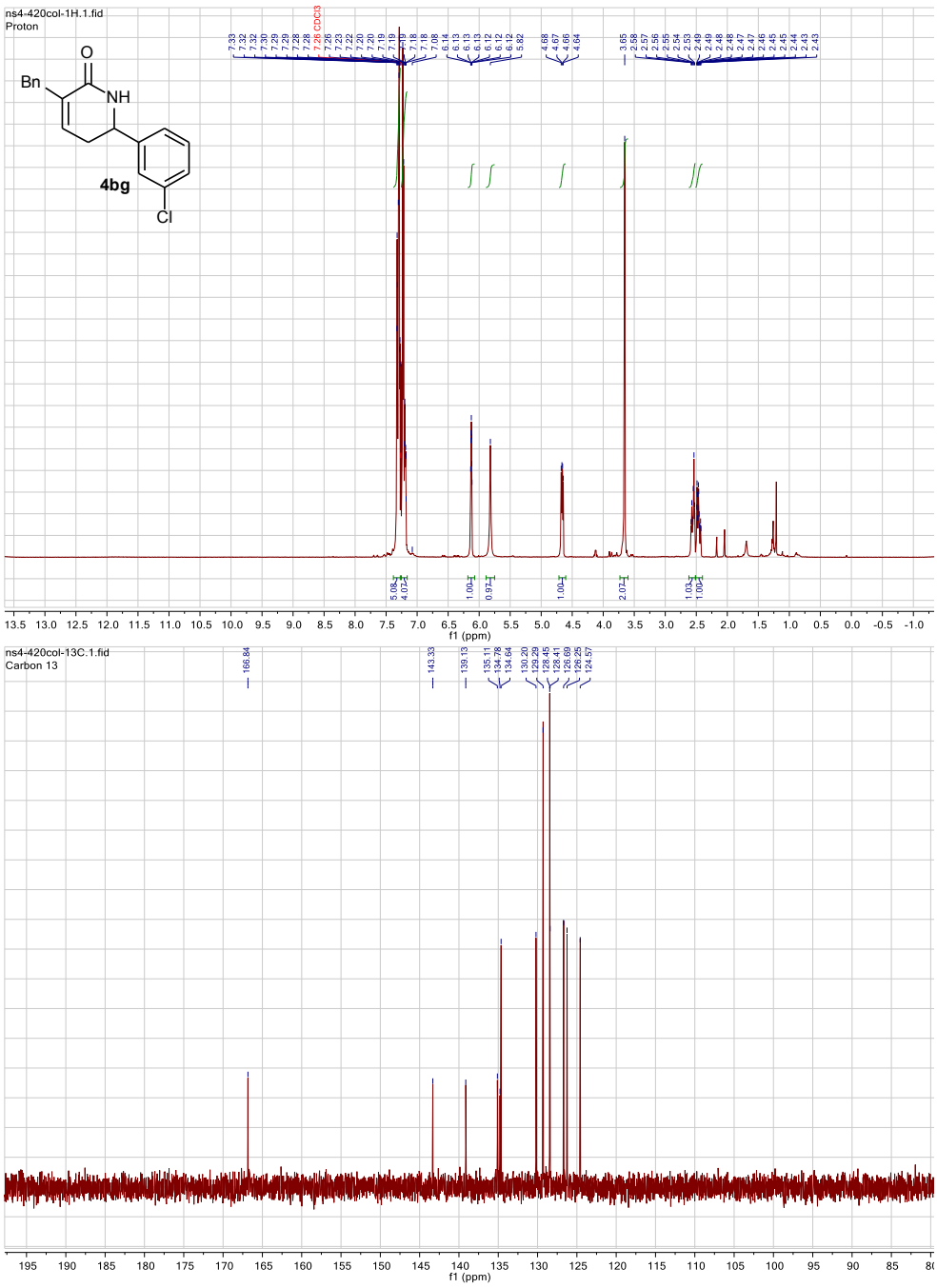

Figure 4.26: 3-Benzyl-6-(3-chlorophenyl)-5,6-dihydropyridin-2(1H)-one (4bg) NMR.

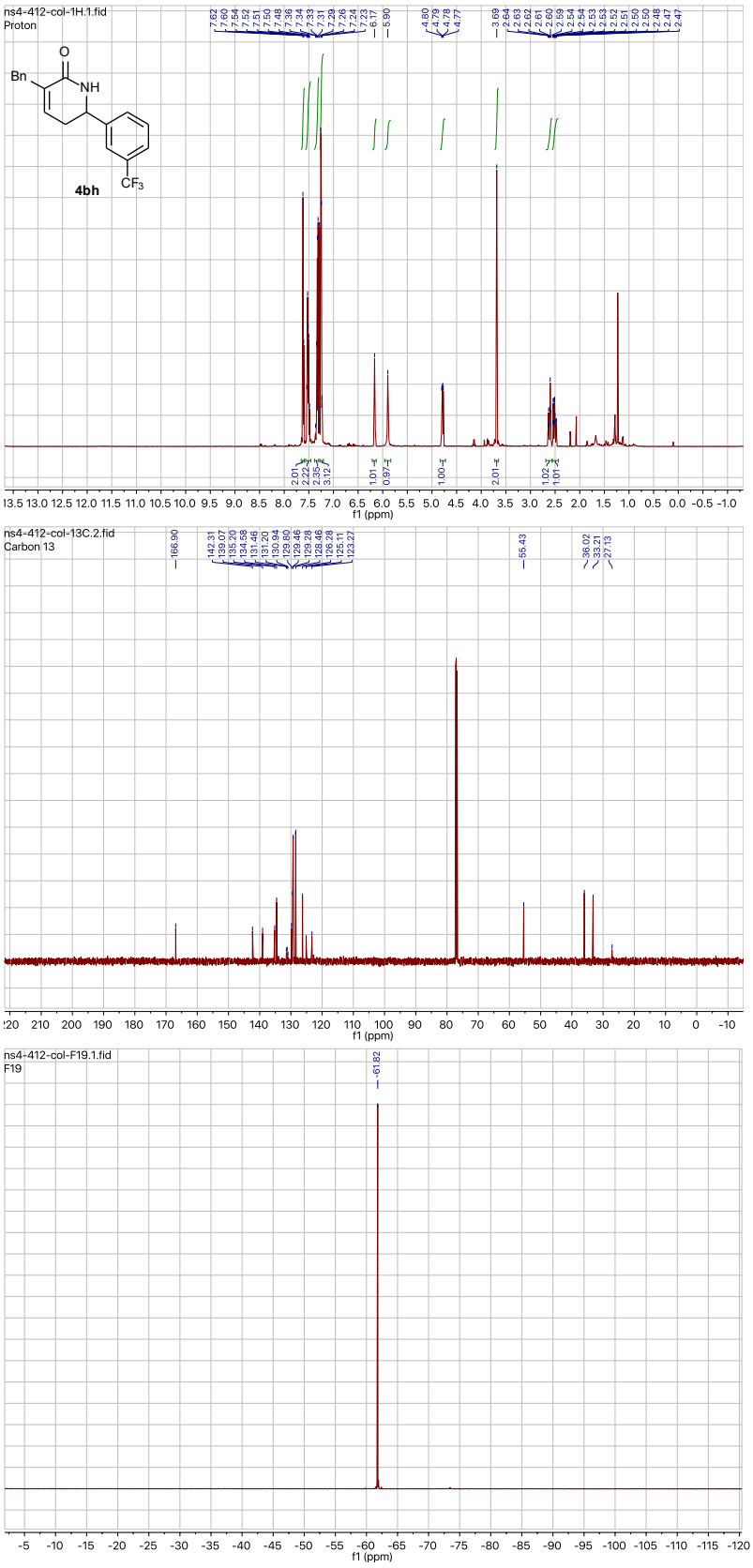

Figure 4.27: 3-Benzyl-6-(3-(trifluoromethyl)phenyl)-5,6-dihydropyridin-2(1H)-one (4bh) NMR.

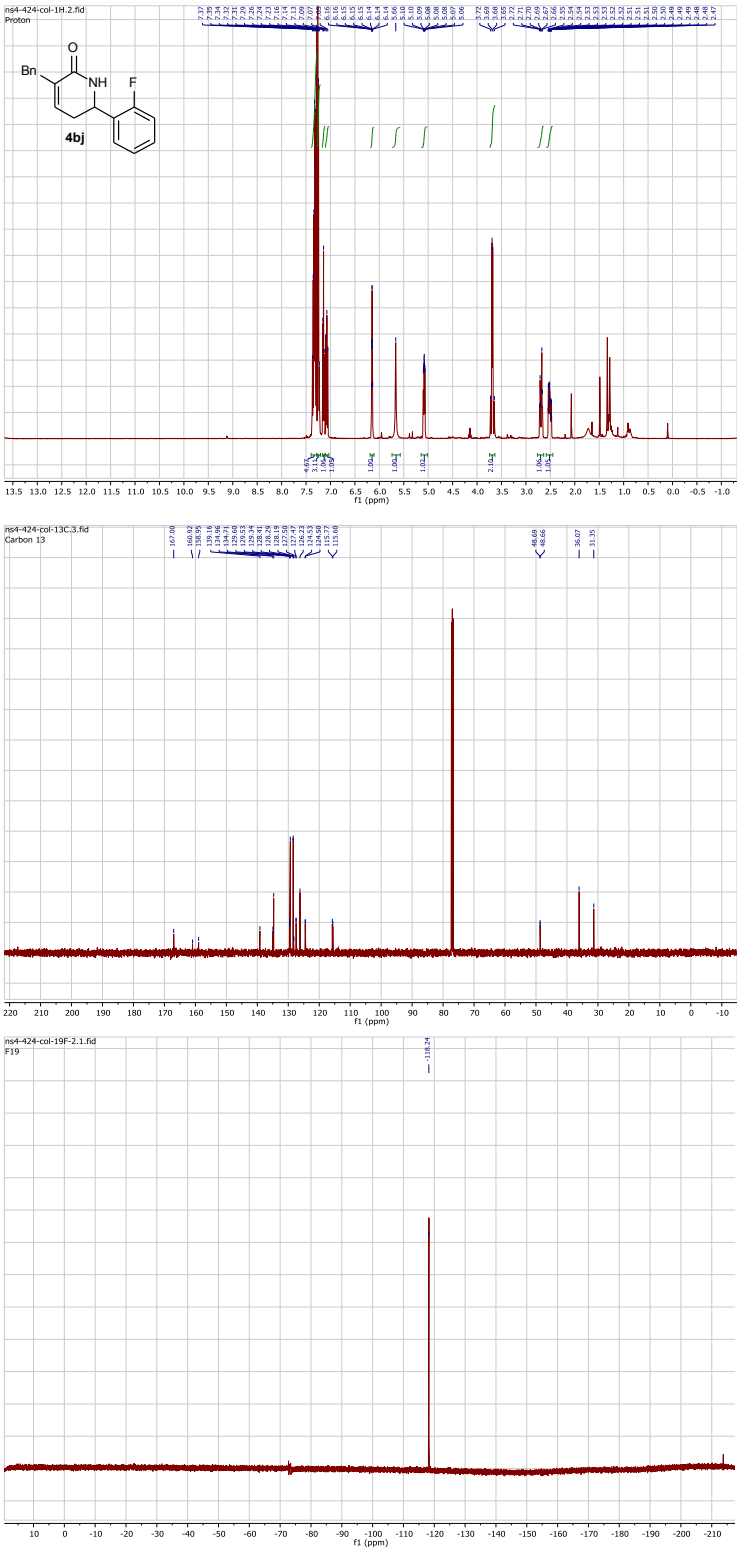

Figure 4.28: 3-Benzyl-6-(3-Benzyl-6-(3-fluorophenyl)-5,6-dihydropyridin-2(1H)-one (4bj) NMR.

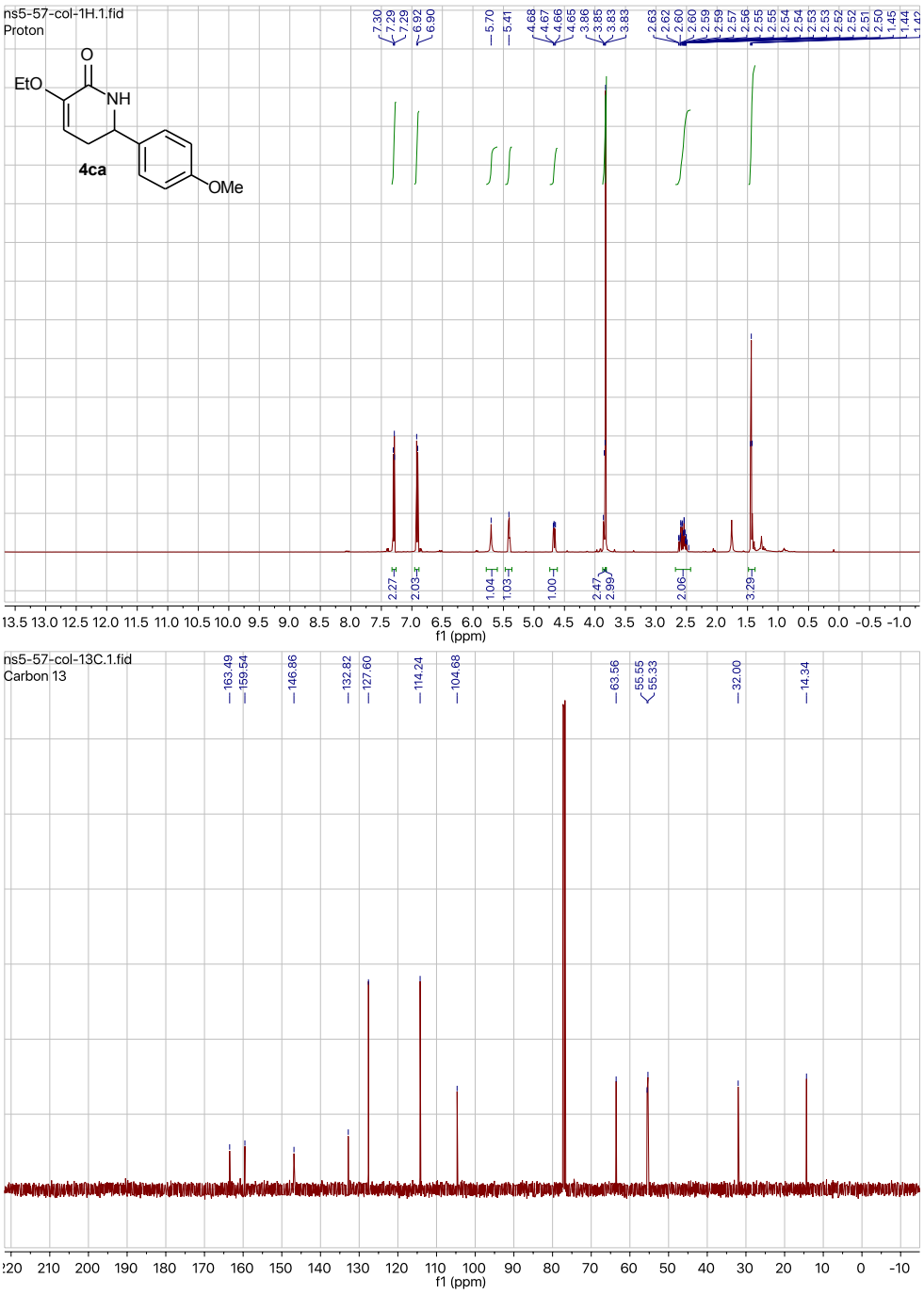

Figure 4.29: 3-Ethoxy-6-(4-methoxyphenyl)-5,6-dihydropyridin-2(1H)-one (4ca) NMR.

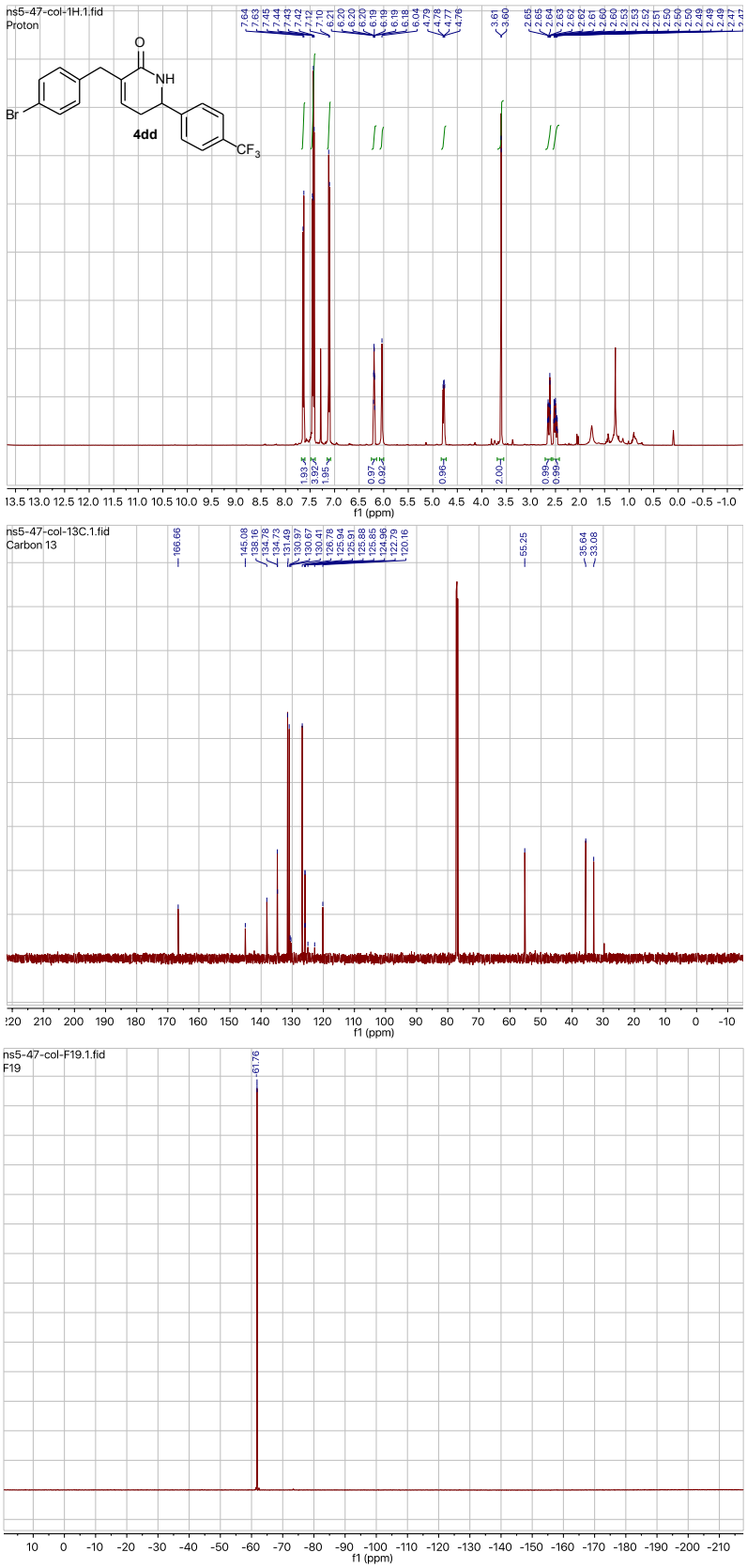

Figure 4.30: 3-(4-Bromobenzyl)-6-(4-(trifluoromethyl)phenyl)-5,6-dihydropyridin-2(1H)-one (4dd) NMR.

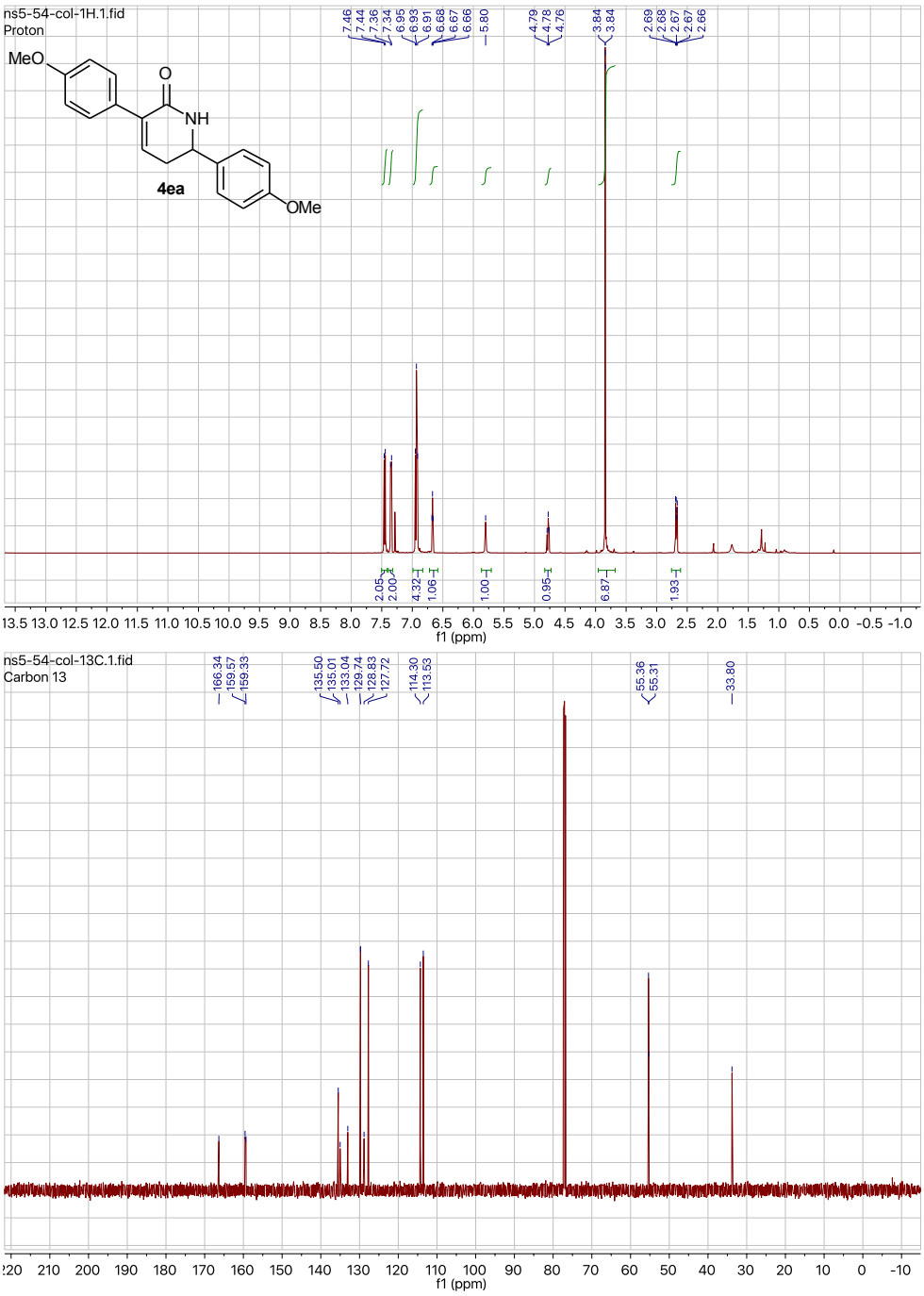

Figure 4.31: 3,6-Bis(4-methoxyphenyl)-5,6-dihydropyridin-2(1H)-one (4ea) NMR.

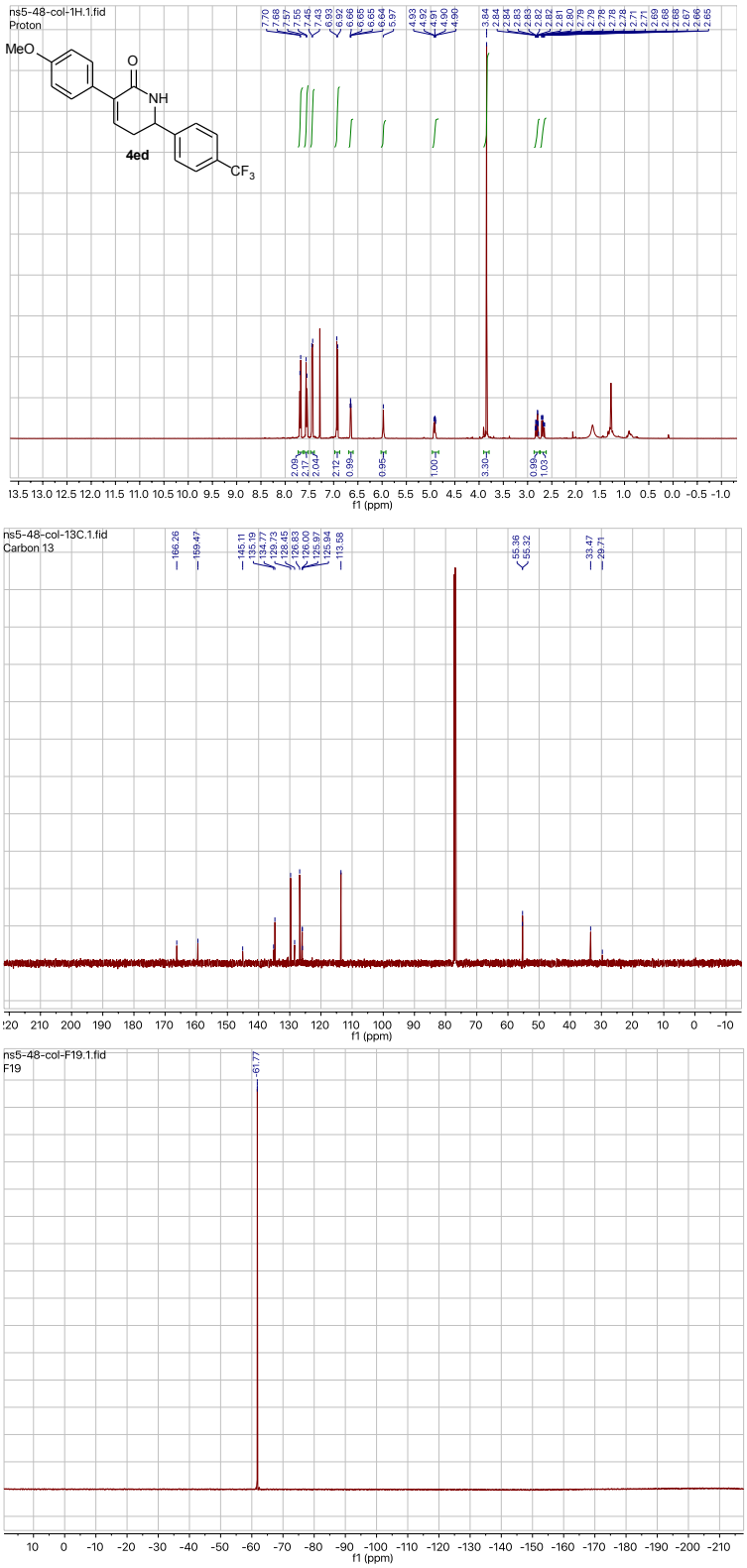

Figure 4.32: 3-(4-Methoxyphenyl)-6-(4-(trifluoromethyl)phenyl)-5,6-dihydropyridin-2(1H)-one (4ed) NMR.

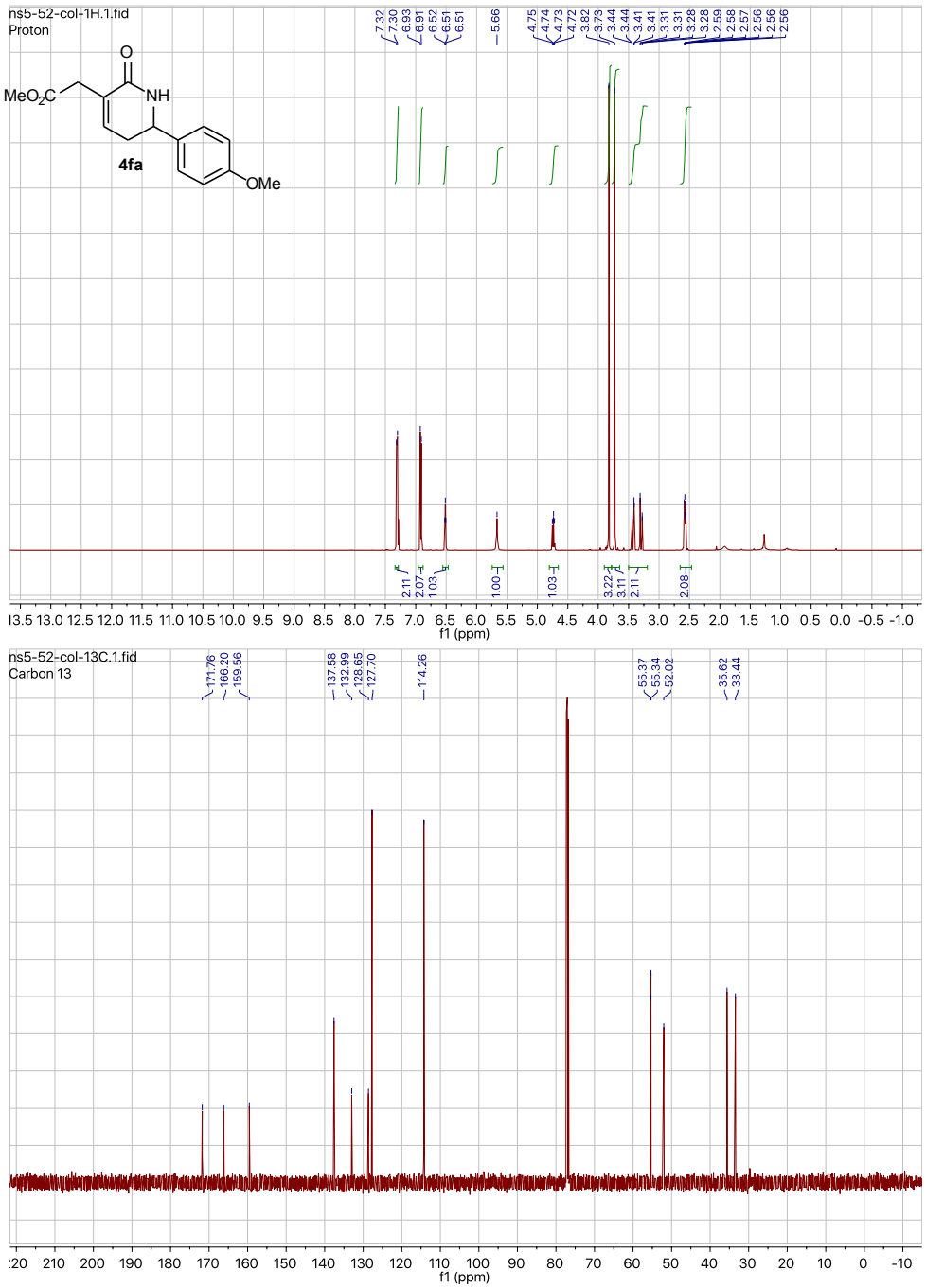

Figure 4.33: Methyl 2-(6-(4-methoxyphenyl)-2-oxo-1,2,5,6-tetrahydropyridin-3-yl)acetate (4fa) NMR.

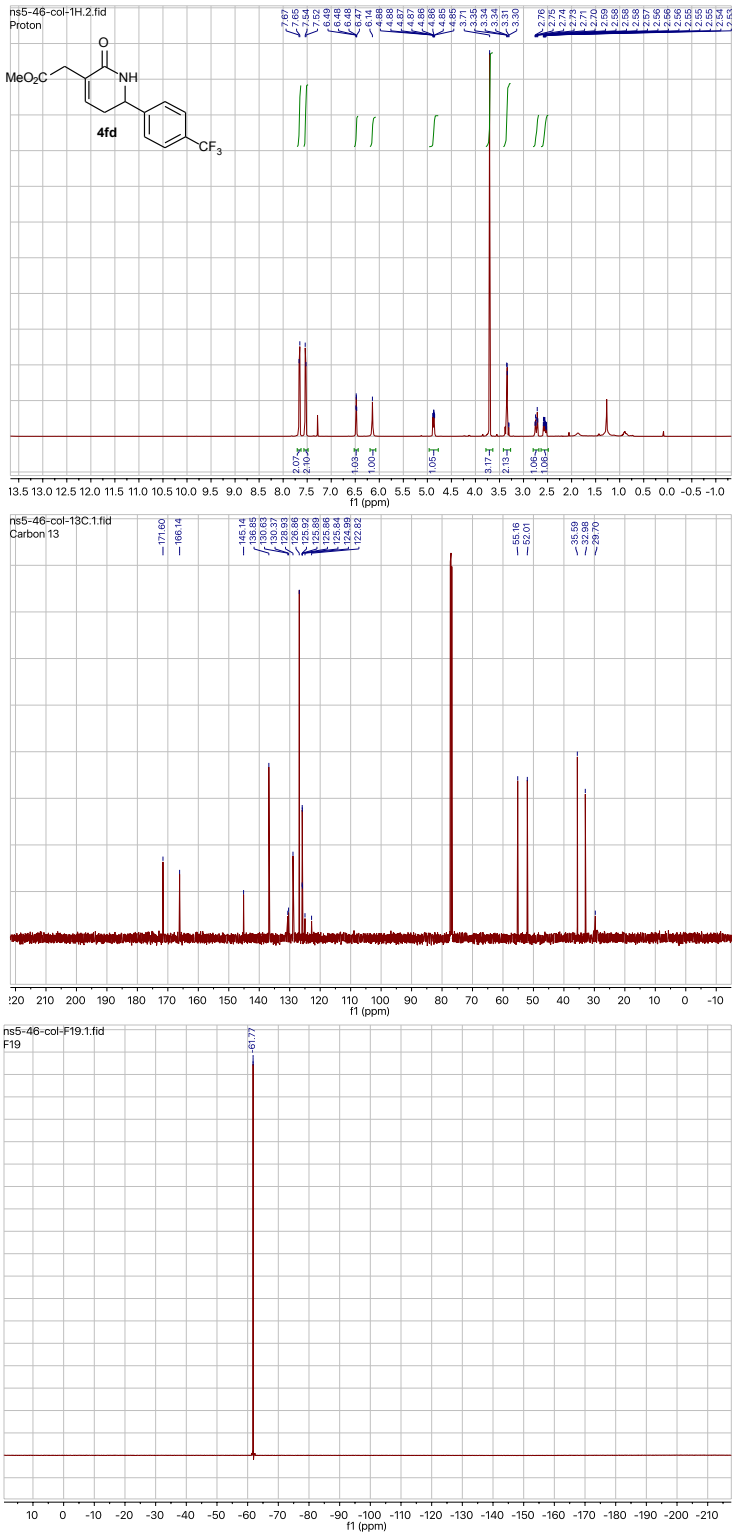

Figure 4.34: Methyl 2-(2-oxo-6-(4-(trifluoromethyl)phenyl)-1,2,5,6-tetrahydropyridin-3-yl)acetate (4fd) NMR.

4.4.6 General procedures for asymmetric dihydropyridone synthesis

General procedure A for asymmetric dihydropyridone synthesis

To a 750 μL clear glass shell vial (8 x 30mm) equipped with a parylene coated stir bar (1.67 x 2.01 x 4.80mm) was added a solution of the acrylamide in MeOH (3.0 μL, 1.0 M, 0.0030 mmol). The alkene (0.0015 mmol) was added followed by 125 μL of acetate buffer (100 mM NaOAc, 100 mM NaCl, pH 7.4). 75 μL of the monomeric streptavidin wild-type metalloenzyme (600 μM, 3 mol%, 0.000045 mmol) in salt water (100 mM NaCl, pH 7.4) was added to the vial achieving the desired reaction mixture (225 μM enzyme, 62.5 mM NaOAc, 100 mM NaCl, pH 7.4). The vial was placed in a 24-well high-throughput experimentation block and the reaction mixture was allowed to stir at 200 rpm at 25 °C. After 72 h the reaction is diluted with ethyl acetate and filtered through a Celite plug into a 20 mL scintillation vial. The reaction vial was washed twice more with ethyl acetate and filtered through the Celite plug into the scintillation vial. The Celite plug was washed an additional three times with ethyl acetate, collecting the filtrate into the scintillation vial. The contents of the scintillation vial were carefully removed via concentration under vacuum. The crude residue of the scintillation vial was dissolved in 600 μL of MeOD. A trimethyl(phenyl)silane internal standard (0.258 μL, 0.0015 mmol) was added to the solution, and mixed thoroughly. The sample was then analyzed by NMR (400 MHz or 500 MHz, MeOD, minimum of 400 scans), and the yield was determined relative to the trimethyl(phenyl)silane internal standard. Enantioselectivity was determined by chiral HPLC. [2]

General procedure B for asymmetric dihydropyridone synthesis

To a 750 μL clear glass shell vial (8 x 30mm) equipped with a parylene coated stir bar (1.67 x 2.01 x 4.80mm) was added a solution of the acrylamide in MeOH (1.5 μL, 1.0 M, 0.0015 mmol). The alkene (0.0030 mmol) was added followed by 25 μL of acetate buffer (100 mM NaOAc, 100 mM NaCl, pH 7.4). 75 μL of the monomeric streptavidin wild-type metalloenzyme (600 μM, 3

[2] All C-H functionalization reactions between acrylamide and styrene coupling partners were repeated independently and in duplicate. HPLC and NMR yields were nearly identical (typically within 5% of each run), and enantioselection was completely identical in duplicate runs. Each data point was the average to two runs, with the exception of the methyl acrylamide and 4-methoxystyrene, which was the average of three runs.

mol%, 0.000045 mmol) in salt water (100 mM NaCl, pH 7.4) was added to the vial achieving the desired reaction mixture (450 μM enzyme, 25 mM NaOAc, 100 mM NaCl, pH 7.4). The vial was placed in a 24-well high-throughput experimentation block and the reaction mixture was allowed to stir at 200 rpm at 25 °C. After 48 h the reaction is diluted with either diethyl ether or ethyl acetate and filtered through a Celite plug into a 20 mL scintillation vial. The reaction vial was washed twice more with diethyl ether or ethyl acetate and filtered through a Celite plug into the scintillation vial. The Celite plug was washed an additional three times with diethyl ether or ethyl acetate, collecting the filtrate into the scintillation vial. The contents of the scintillation vial were carefully removed via concentration under vacuum. Yield was determined either by Chiral HPLC Analysis or NMR Analysis. Enantioselectivity was determined by chiral HPLC.[2]

Chiral HPLC Analysis - The crude residue of the scintillation vial was rediluted with 120 μL of HPLC grade isopropanol and 300 μL of HPLC grade hexanes. 1.5 μL of a 1,3,5-trimethoxybenzene solution (1.0 M in MeOH) was added to the scintillation vial. The contents of the scintillation vial were thoroughly mixed via pipette to ensure uniformity of the solution. 180 μL of the uniform solution were incorporated into at 200 μL vial insert, and the sample was submitted for analysis. Yield was determined by chiral HPLC relative to a 1,3,5-trimethoxybenzene internal standard. Enantioselectivity was also determined by chiral HPLC.

NMR Analysis - The crude residue of the scintillation vial was dissolved in 600 μL of MeOD. A trimethyl(phenyl)silane internal standard (0.258 μL, 0.0015 mmol) was added to the solution, and mixed thoroughly. The sample was then analyzed by NMR (400 MHz or 500 MHz, MeOD, minimum of 400 scans), and the yield was determined relative to the trimethyl(phenyl)silane internal standard. Enantioselectivity was determined by chiral HPLC.

4.4.7 Analytical data for enantioenriched dihydropyridones (NMR/HPLC)

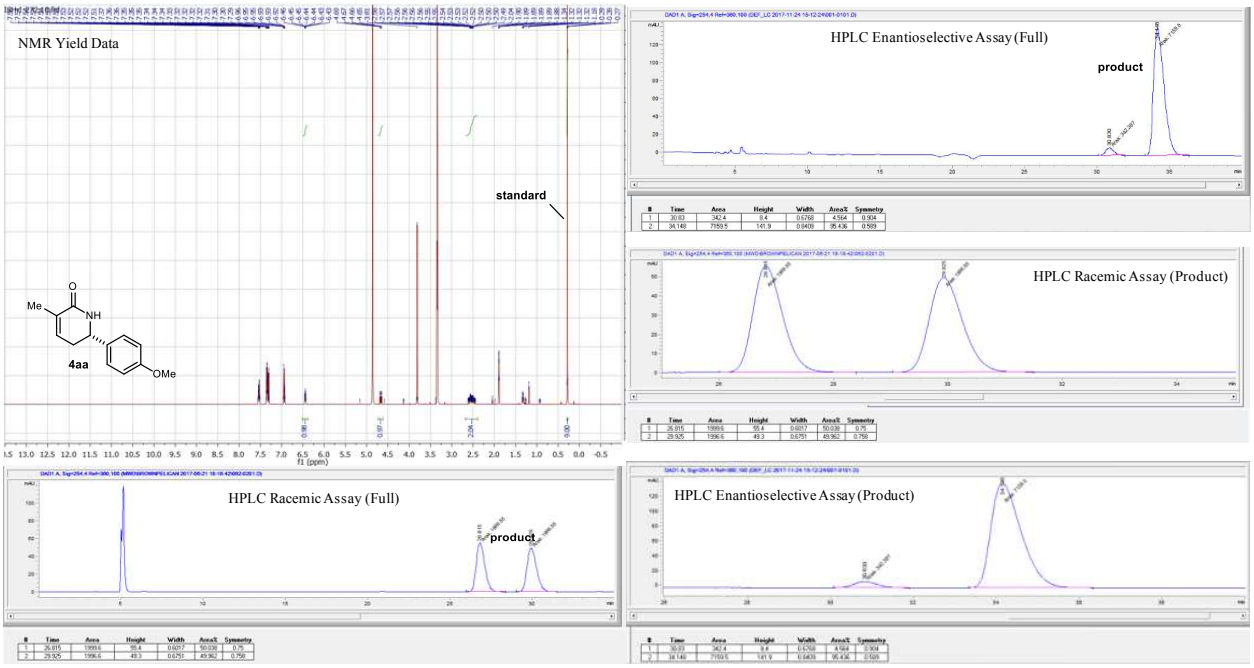

Figure 4.35: 6-(4-Methoxyphenyl)-3-methyl-5,6-dihydropyridin-2(1H)-one (4aa) NMR/HPLC. Product synthesized according to general procedure A. Product yield was determined to be 99% by ^{1}H NMR analysis (400 MHz, MeOD) relative to a trimethyl(phenyl)silane internal standard. The product was determined to be 91% ee by chiral HPLC analysis. (Chiralpak IE, 20% ^{i}PrOH/hexanes, 1 mL/min, $t_r(e_1$, minor) = 30.8 min, $t_r(e_2$, major) = 34.1 min).[3]

[3] The absolute configuration of the δ-lactam products was determined to be the (S)-enantiomer. This was assigned by direct analogy of the configurations previously reported by Cramer and colleagues (Science 2012, 338, 504-506). Cramer furnished the (R)-enantiomer of the reported isoquinolinone products as described in the manuscript and HPLC traces in the supporting information. In our work, we repeated one of Cramer's C-H functionalization reactions (benzhydroxamide and 4-methoxystyrene) with our monomeric streptavidin (mSav) metalloenzymes. Upon using the same HPLC assay and chiral column that Cramer reports, we observed a complete reversal in product enantiosense when utilizing our mSav metalloenzymes, hence the (S)-enantiomer by analogy. Interestingly, when the same reaction is repeated with the tetrameric streptavidin (tSav) metalloenzyme, the (R)-enantiosense is retained in correlation with Cramer's HPLC data. The reversal in enantiosense between mSav and tSav is once again observed when using acrylamide and styrene coupling partners. Based on this evidence, we reported by analogy, that the tSav metalloenzyme give the (R)-enantiomer of our δ-lactam product, whereas the mSav metalloenzyme give the (S)-enantiomer. The inherent assumption is that benzamide and acrylamide binds identically in the mSav pocket but given that they both proceed in similar enantioselectivities and since the enantioselectivities related to the prochiral element (styrene) which is identical in both transformations, we believe this is justified.

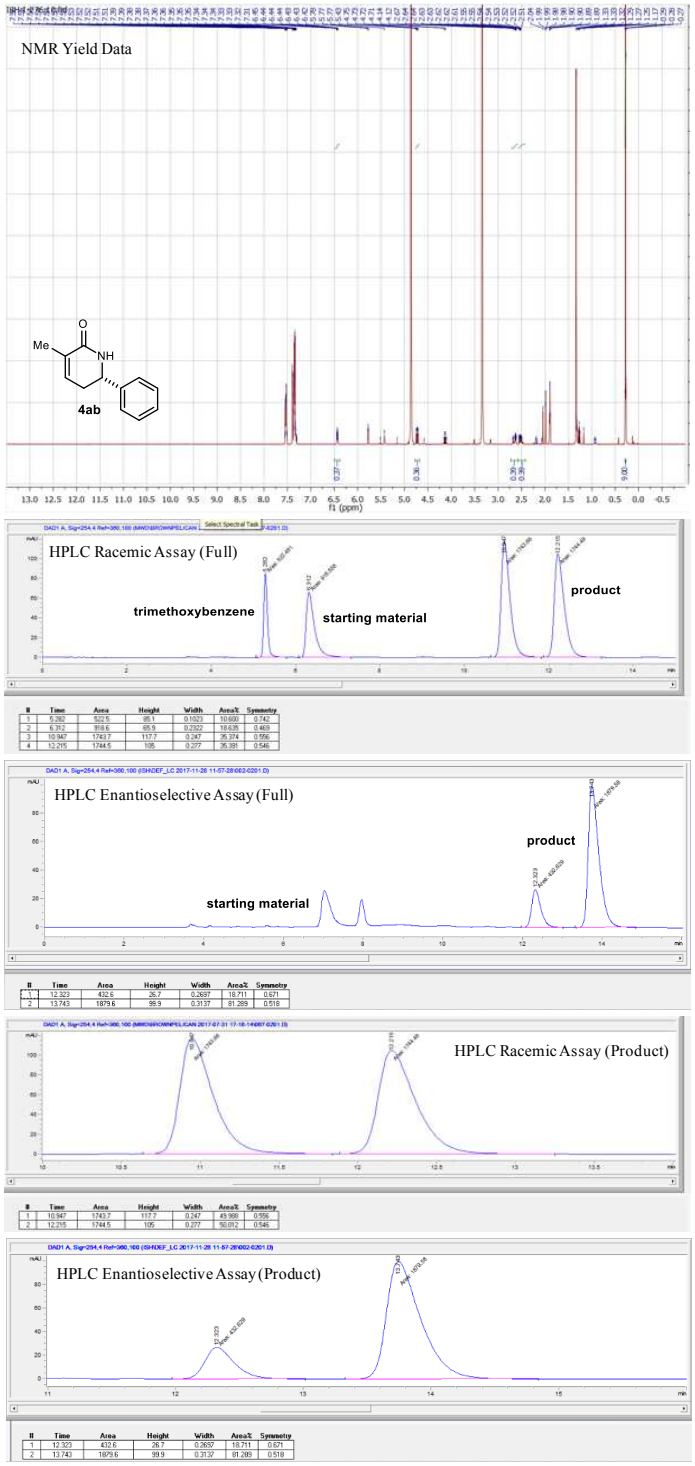

Figure 4.36: 3-Methyl-6-phenyl-5,6-dihydropyridin-2(1H)-one (4ab) NMR/HPLC. Product synthesized according to general procedure A. Product yield was determined to be 39% by ^{1}H NMR analysis (400 MHz, MeOD) relative to a trimethyl(phenyl)silane internal standard. The product was determined to be 63% ee by chiral HPLC analysis. (Chiralpak IB, 10% ^{i}PrOH/hexanes, 1 mL/min,t$_r$(e_1, minor) = 12.3 min, t$_r$(e_2, major) = 13.7 min).

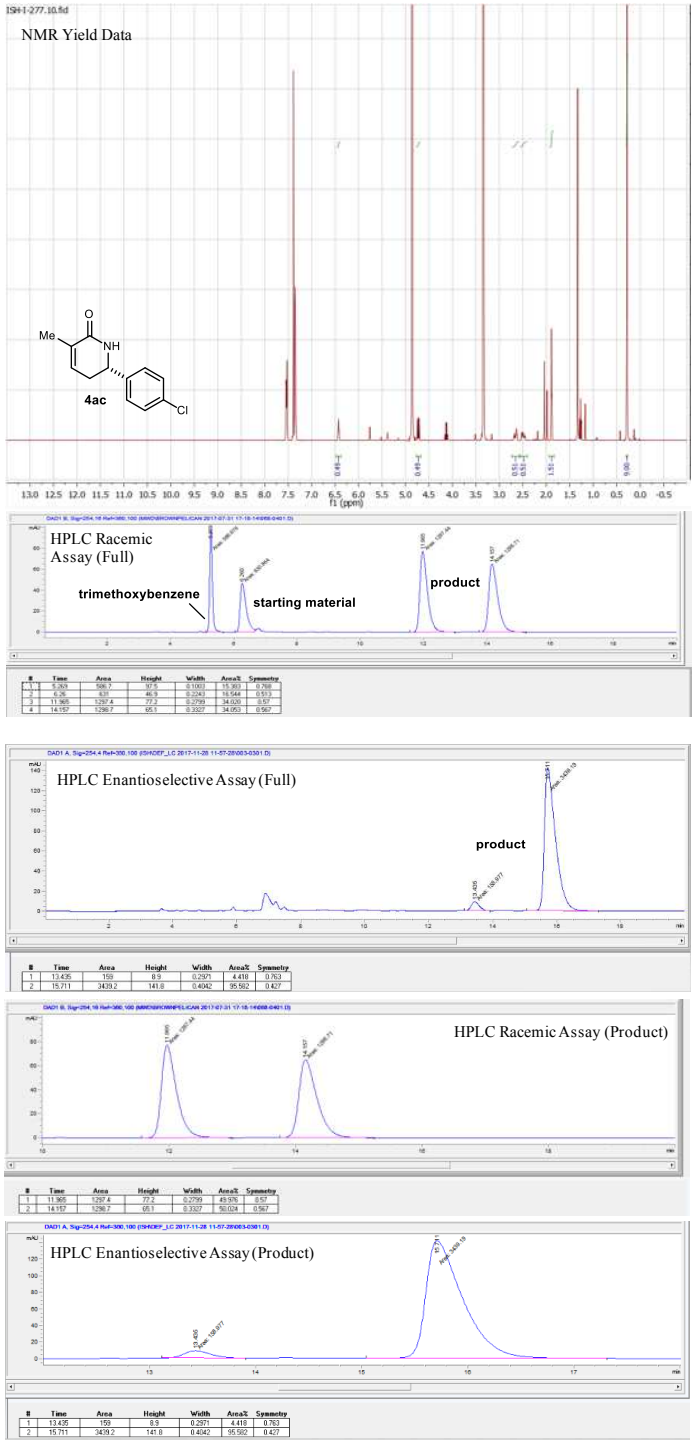

Figure 4.37: 6-(4-Chlorophenyl)-3-methyl-5,6-dihydropyridin-2(1H)-one (4ac) NMR/HPLC. Product synthesized according to general procedure A. Product yield was determined to be 51% by ^{1}H NMR analysis (400 MHz, MeOD) relative to a trimethyl(phenyl)silane internal standard. The product was determined to be 91% ee by chiral HPLC analysis. (Chiralpak IB, 10% ^{i}PrOH/hexanes, 1 mL/min, $t_r(e_1$, minor) = 13.4 min, $t_r(e_2$, major) = 15.7 min).

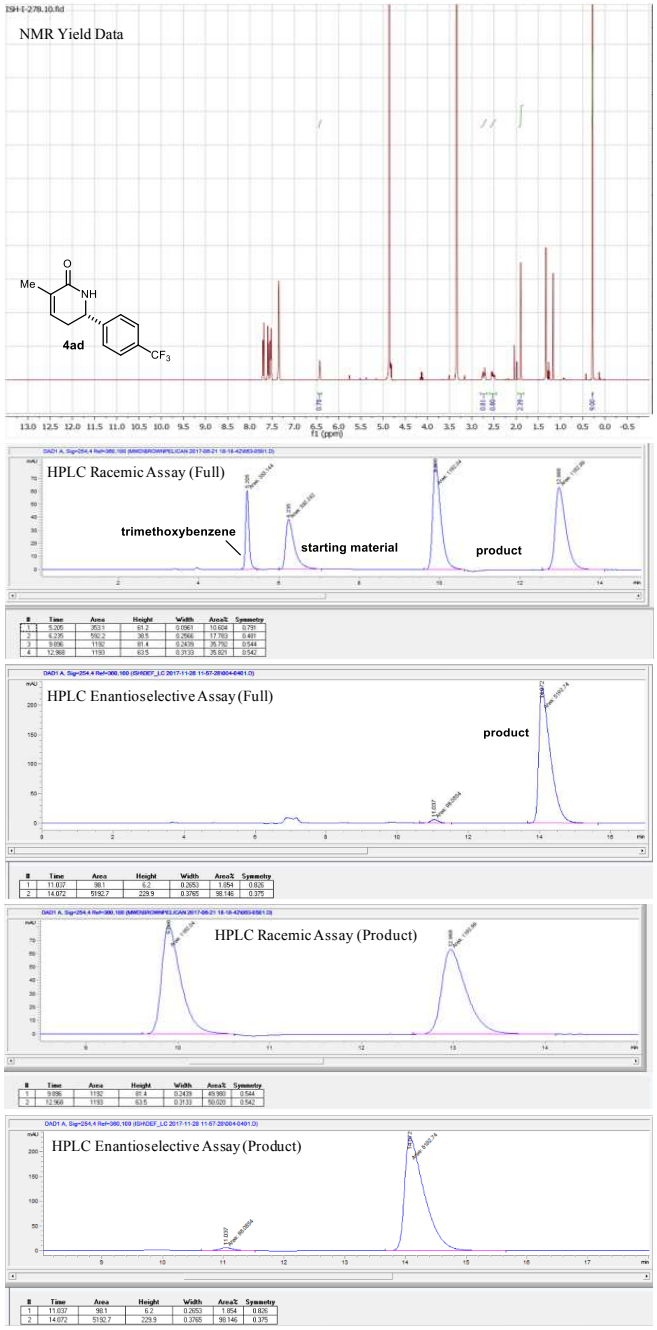

Figure 4.38: 3-Methyl-6-(4-(trifluoromethyl)phenyl)-5,6-dihydropyridin-2(1H)-one (4ad) NMR/HPLC. Product synthesized according to general procedure A. Product yield was determined to be 81% by ^{1}H NMR analysis (400 MHz, MeOD) relative to a trimethyl(phenyl)silane internal standard. The product was determined to be 96% ee by chiral HPLC analysis. (Chiralpak IB, 10% ^{i}PrOH/hexanes, 1 mL/min, $t_r(e_1$, minor) = 11.0 min, $t_r(e_2$, major) = 14.1 min).

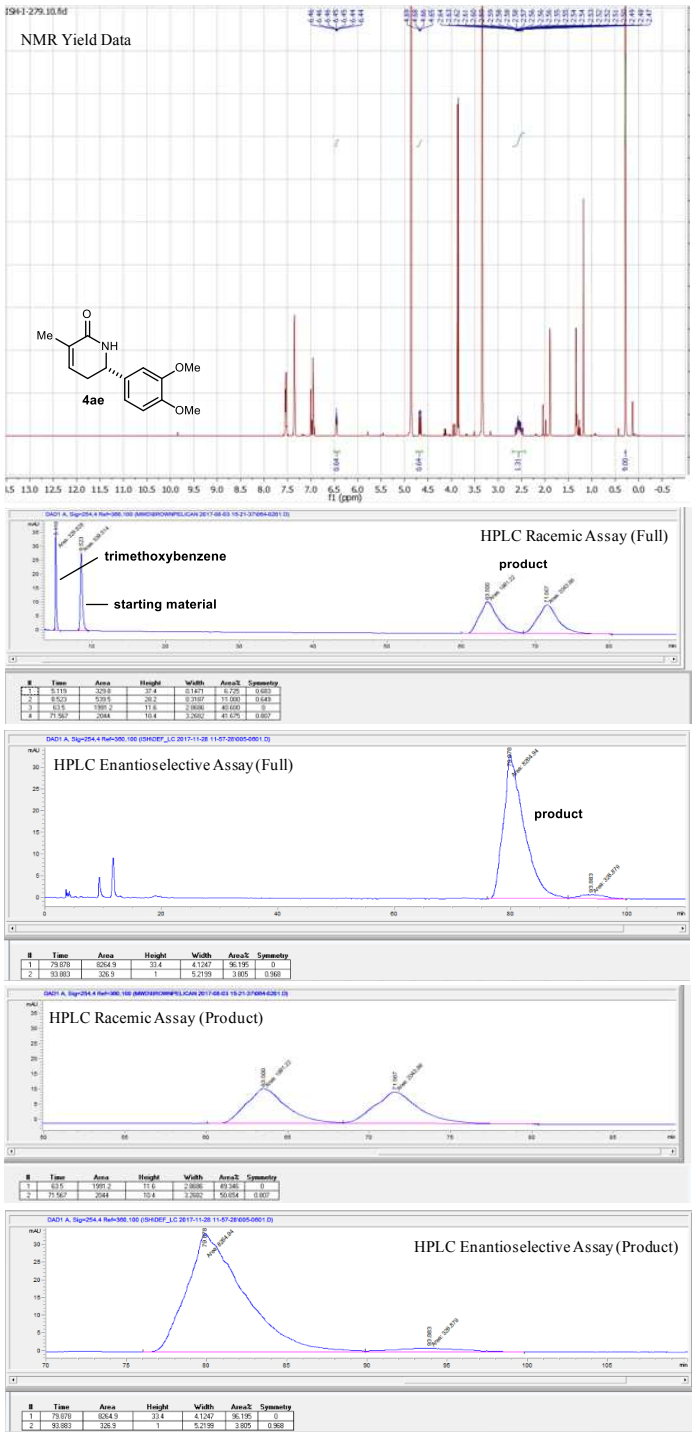

Figure 4.39: 6-(3,4-Dimethoxyphenyl)-3-methyl-5,6-dihydropyridin-2(1H)-one (4ae) NMR/HPLC. Product synthesized according to general procedure A. Product yield was determined to be 65% by ^{1}H NMR analysis (400 MHz, MeOD) relative to a trimethyl(phenyl)silane internal standard. The product was determined to be 92% ee by chiral HPLC analysis. (Chiralpak IA, 5% ^{i}PrOH/hexanes, 1 mL/min, $t_r(e_1$, major) = 79.9 min, $t_r(e_2$, minor) = 93.9 min).

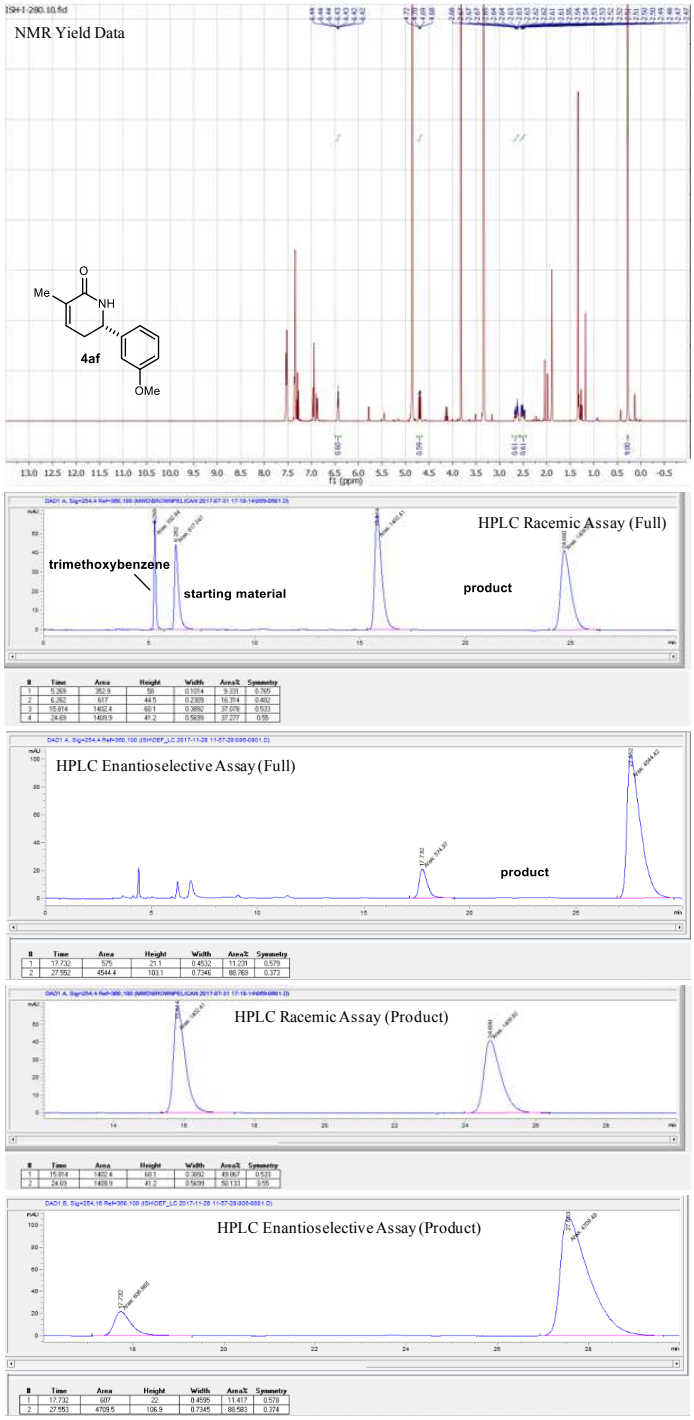

Figure 4.40: 6-(3-Methoxyphenyl)-3-methyl-5,6-dihydropyridin-2(1H)-one (4af) NMR/HPLC. Product synthesized according to general procedure A. Product yield was determined to be 61% by ^{1}H NMR analysis (400 MHz, MeOD) relative to a trimethyl(phenyl)silane internal standard. The product was determined to be 77% ee by chiral HPLC analysis. (Chiralpak IB, 10% ^{i}PrOH/hexanes, 1 mL/min, $t_r(e_1$, minor) = 17.7 min, $t_r(e_2$, major) = 27.6 min).

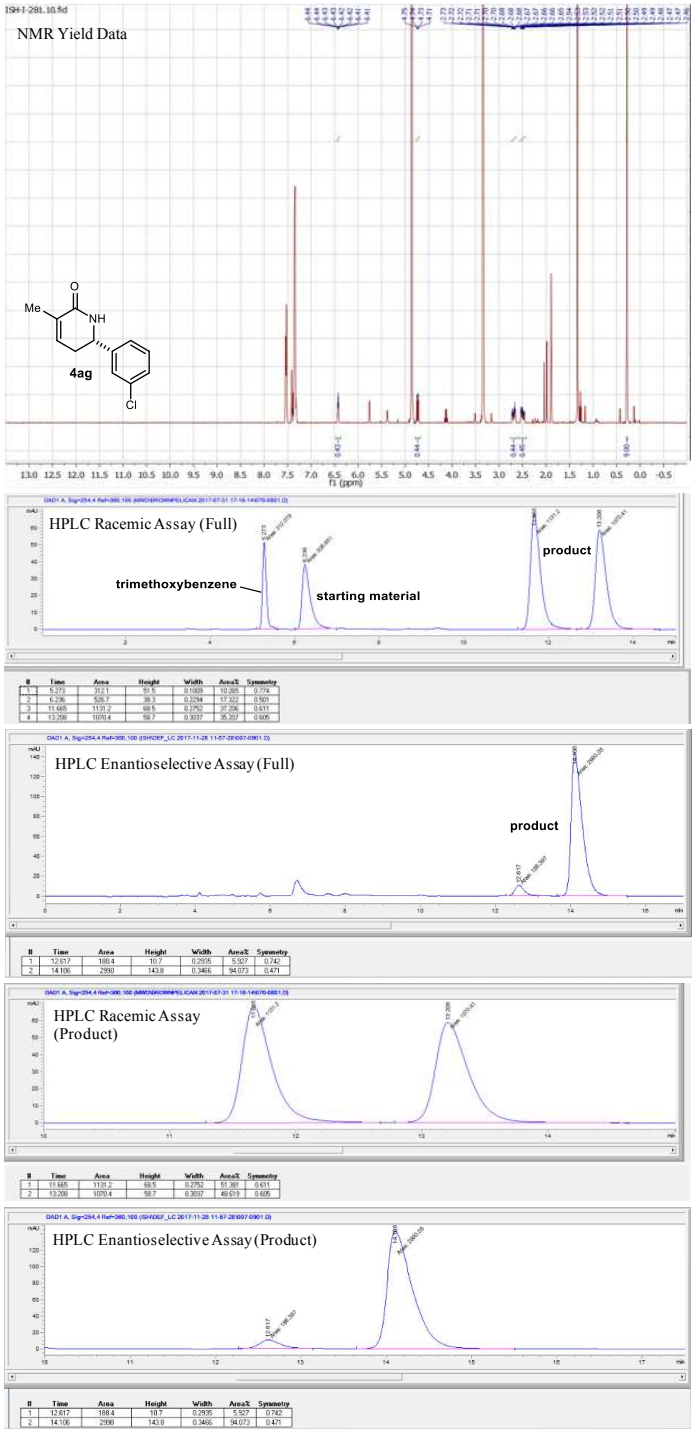

Figure 4.41: 6-(3-Chlorophenyl)-3-methyl-5,6-dihydropyridin-2(1H)-one (4ag) NMR/HPLC. Product synthesized according to general procedure A. Product yield was determined to be 45% by ^{1}H NMR analysis (400 MHz, MeOD) relative to a trimethyl(phenyl)silane internal standard. The product was determined to be 88% ee by chiral HPLC analysis. (Chiralpak IB, 10% ^{i}PrOH/hexanes, 1 mL/min, t$_r$(e_1, minor) = 12.6 min, t$_r$(e_2, major) = 14.1 min).

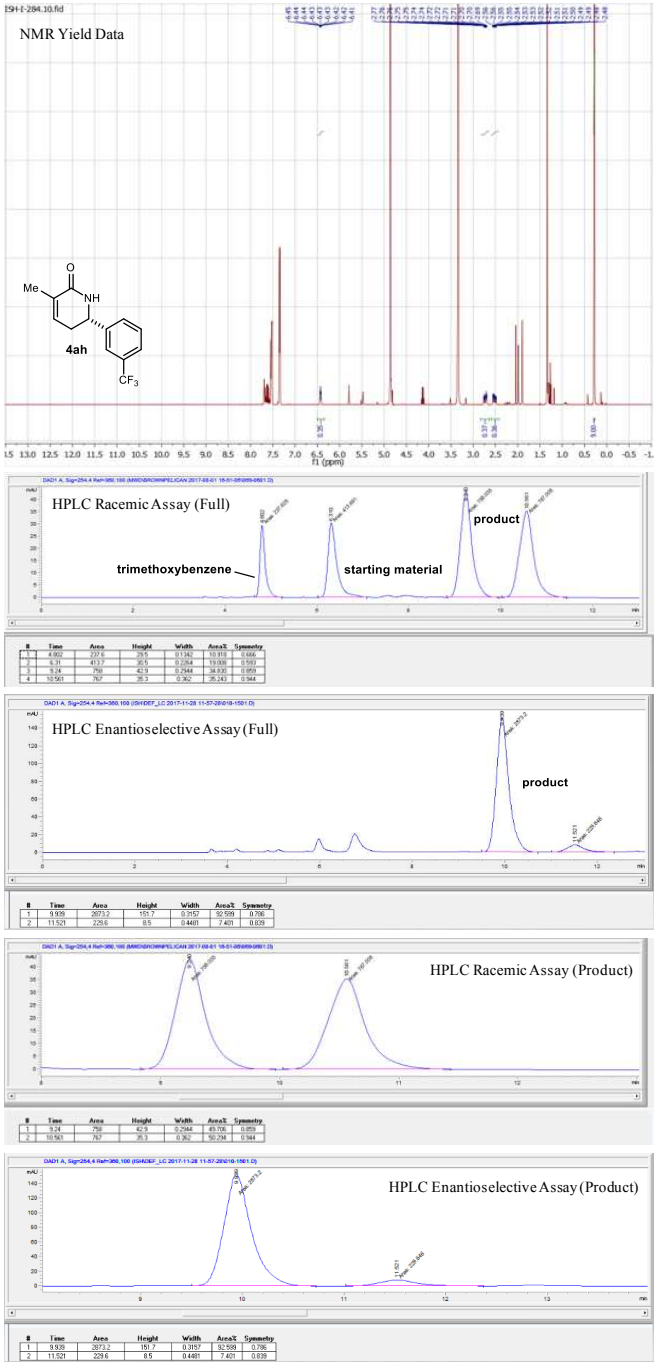

Figure 4.42: 3-Methyl-6-(3-(trifluoromethyl)phenyl)-5,6-dihydropyridin-2(1H)-one (4ah) NMR/HPLC. Product synthesized according to general procedure A. Product yield was determined to be 37% by ^{1}H NMR analysis (400 MHz, MeOD) relative to a trimethyl(phenyl)silane internal standard. The product was determined to be 85% ee by chiral HPLC analysis. (Chiralpak IA, 7% ^{i}PrOH/hexanes, 1 mL/min, $t_r(e_1$, major) = 9.9 min, $t_r(e_2$, minor) = 11.5 min).

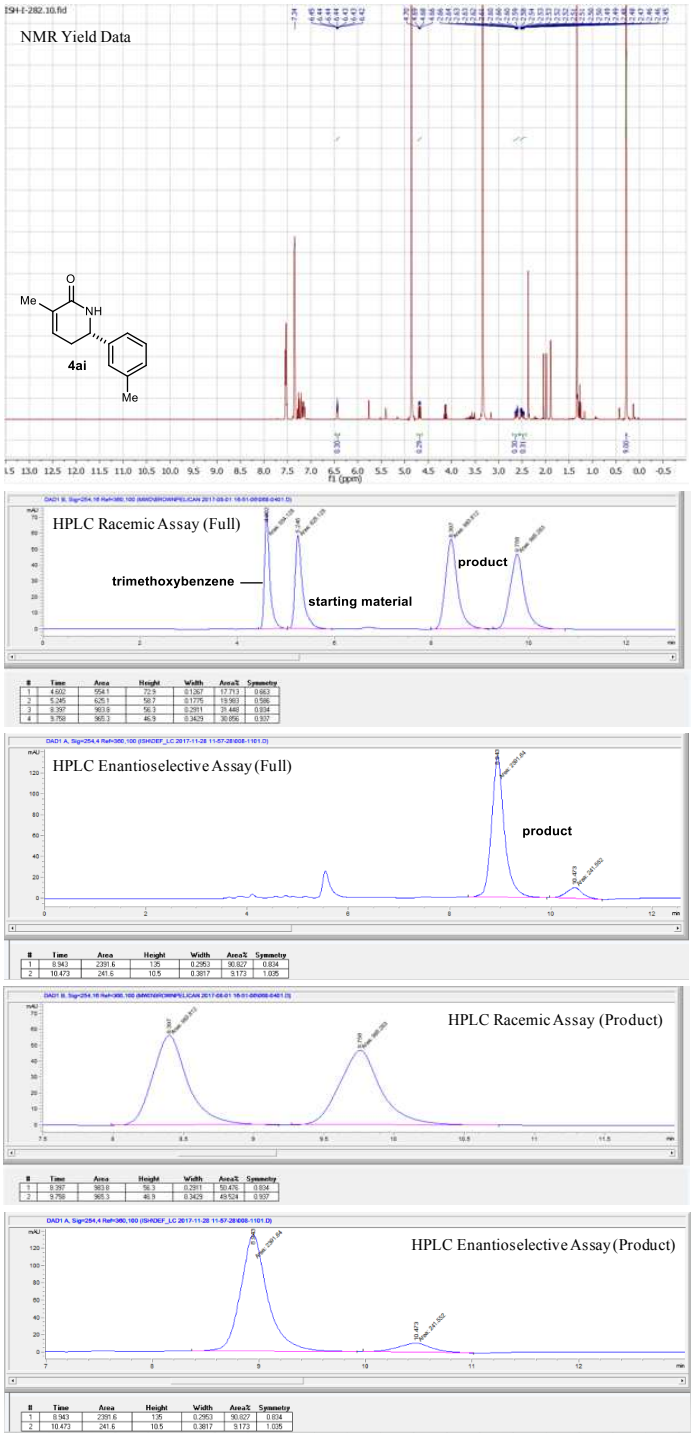

Figure 4.43: 3-Methyl-6-(m-tolyl)-5,6-dihydropyridin-2(1H)-one (4ai) NMR/HPLC. Product synthesized according to general procedure A. Product yield was determined to be 31% by ^{1}H NMR analysis (400 MHz, MeOD) relative to a trimethyl(phenyl)silane internal standard. The product was determined to be 82% ee by chiral HPLC analysis. (Chiralpak IA, 10% ^{i}PrOH/hexanes, 1 mL/min, $t_r(e_1$, major) = 8.9 min, $t_r(e_2$, minor) = 10.5 min).

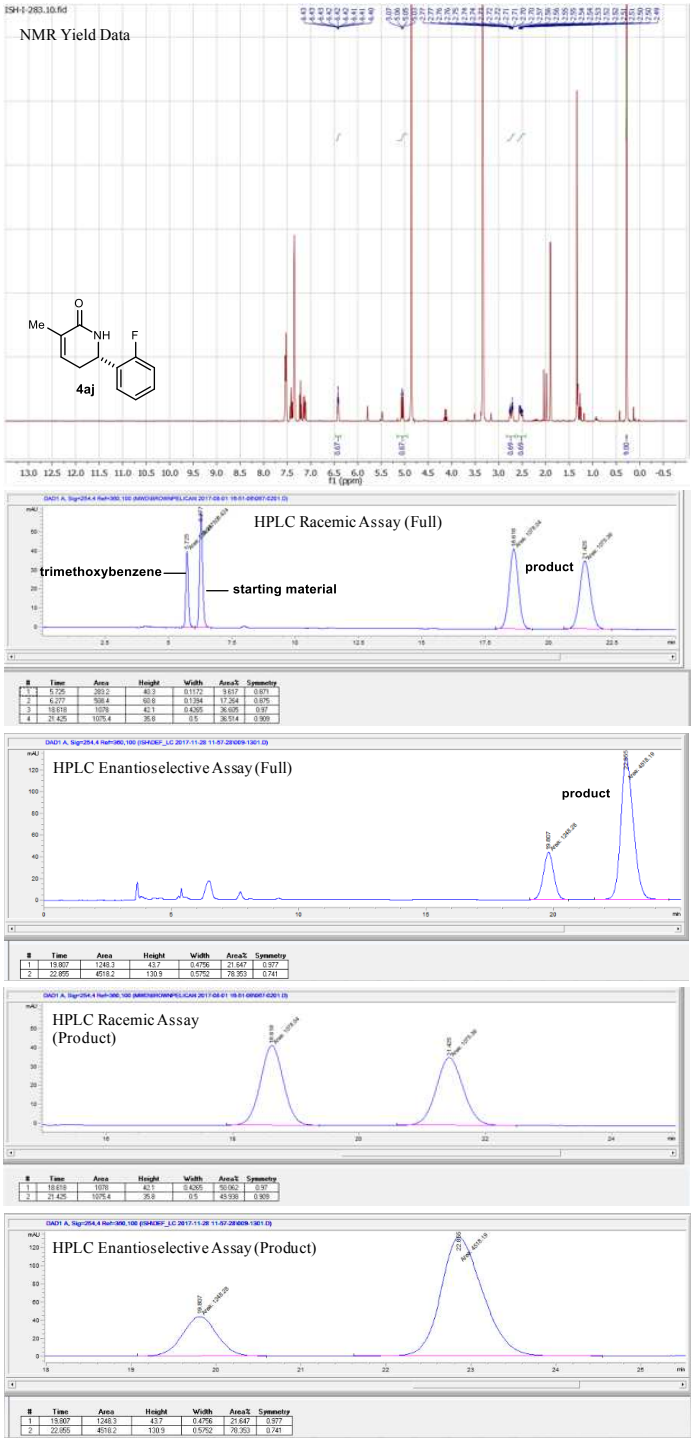

Figure 4.44: 6-(2-Fluorophenyl)-3-methyl-5,6-dihydropyridin-2(1H)-one (4aj) NMR/HPLC. Product synthesized according to general procedure A. Product yield was determined to be 69% by ^{1}H NMR analysis (400 MHz, MeOD) relative to a trimethyl(phenyl)silane internal standard. The product was determined to be 57% ee by chiral HPLC analysis. (Chiralpak IC, 15% ^{i}PrOH/hexanes, 1 mL/min, $t_r(e_1$, minor) = 19.8 min, $t_r(e_2$, major) = 22.9 min).

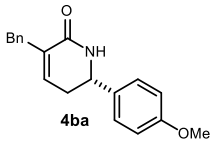

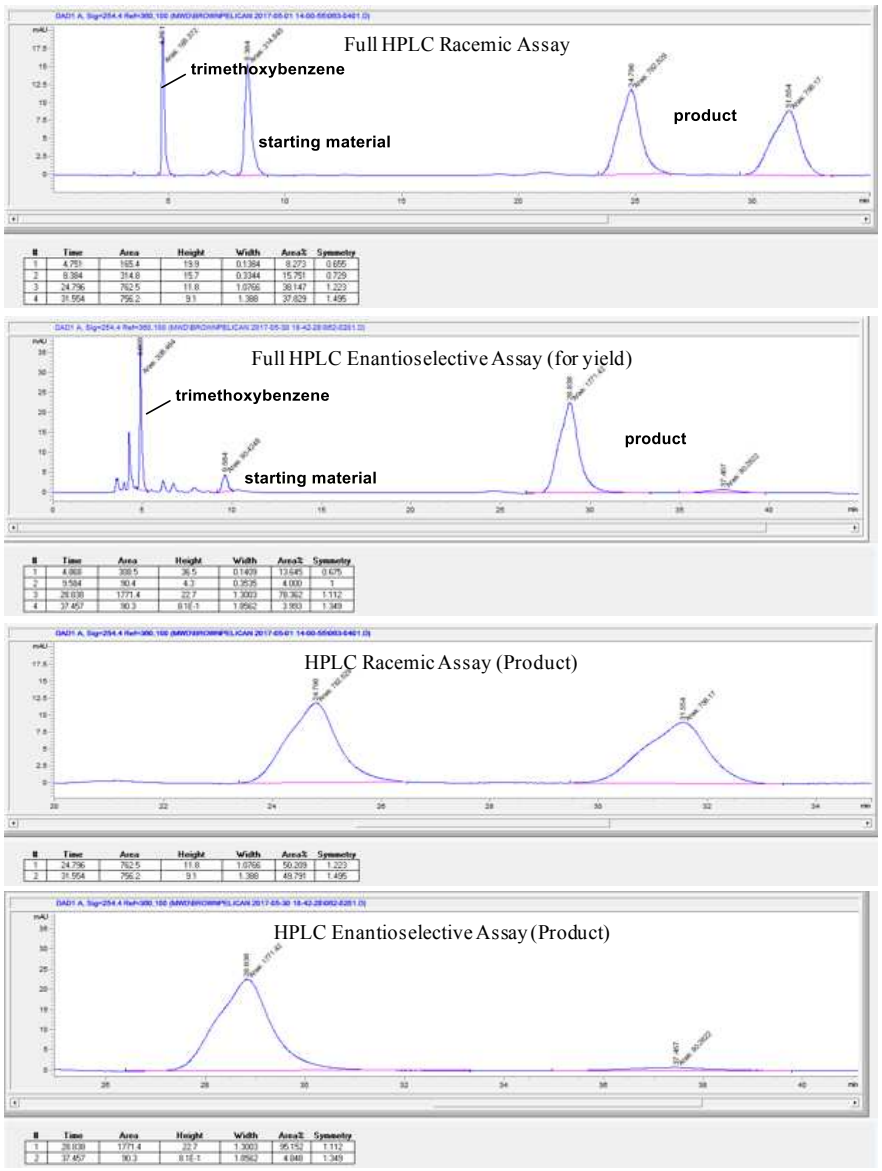

Figure 4.45: 3-Benzyl-6-(4-methoxyphenyl)-5,6-dihydropyridin-2(1H)-one (4ba) HPLC. Product synthesized according to general procedure B, and extracted with diethyl ether. Product yield was determined to be 65% by chiral HPLC analysis relative to a 1,3,5-trimethoxybenzene internal standard. The product was determined to be 90% ee by chiral HPLC analysis. (Chiralpak IA, 7% ^{i}PrOH/hexanes, 1 mL/min, $t_r(e_1$, major) = 28.8 min, $t_r(e_2$, minor) = 37.5 min).

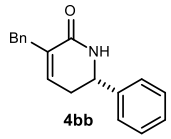

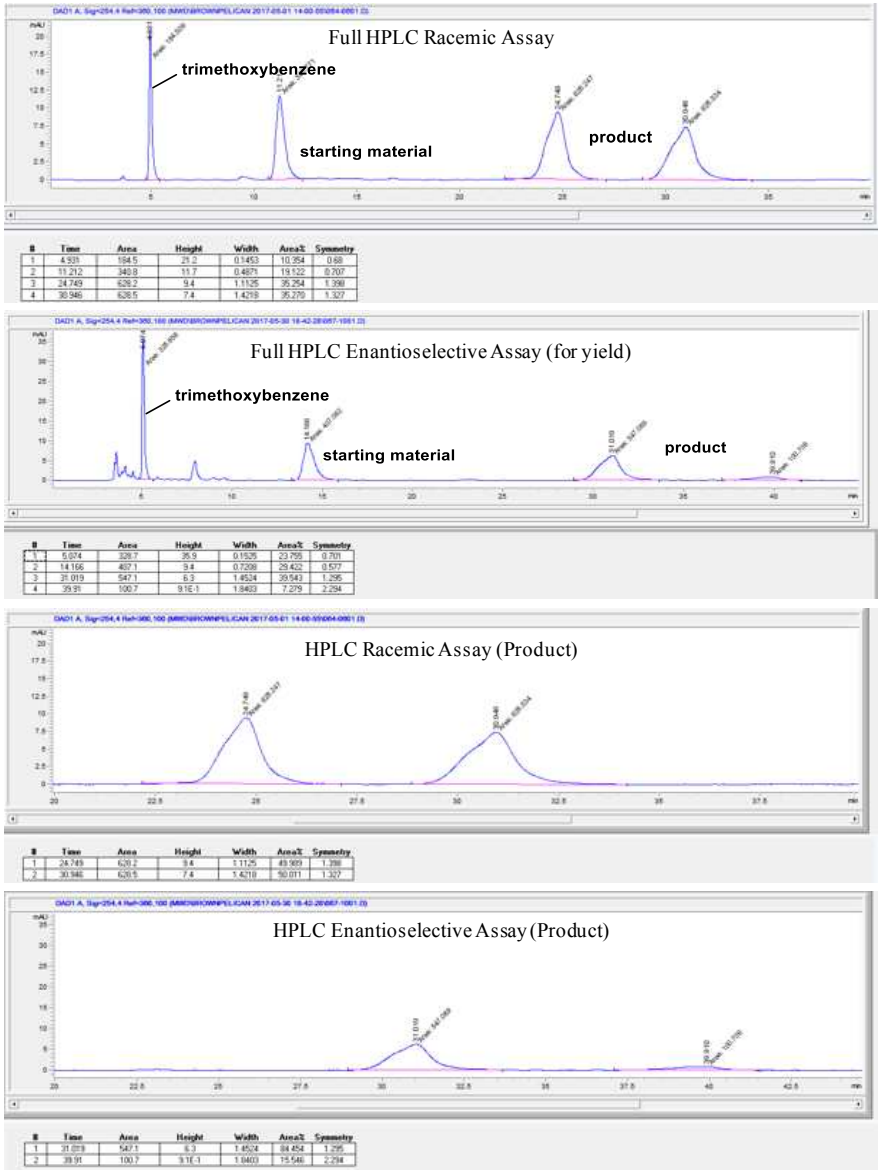

Figure 4.46: 3-Benzyl-6-phenyl-5,6-dihydropyridin-2(1H)-one (4bb) HPLC. Product synthesized according to general procedure B, and extracted with diethyl ether. Product yield was determined to be 29% by chiral HPLC analysis relative to a 1,3,5-trimethoxybenzene internal standard. The product was determined to be 69% ee by chiral HPLC analysis. (Chiralpak IA, 5% ^{i}PrOH/hexanes, 1 mL/min, $t_r(e_1$, major) = 31.0 min, $t_r(e_2$, minor) = 39.9 min).

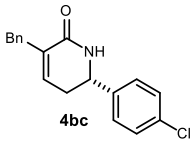

4bc

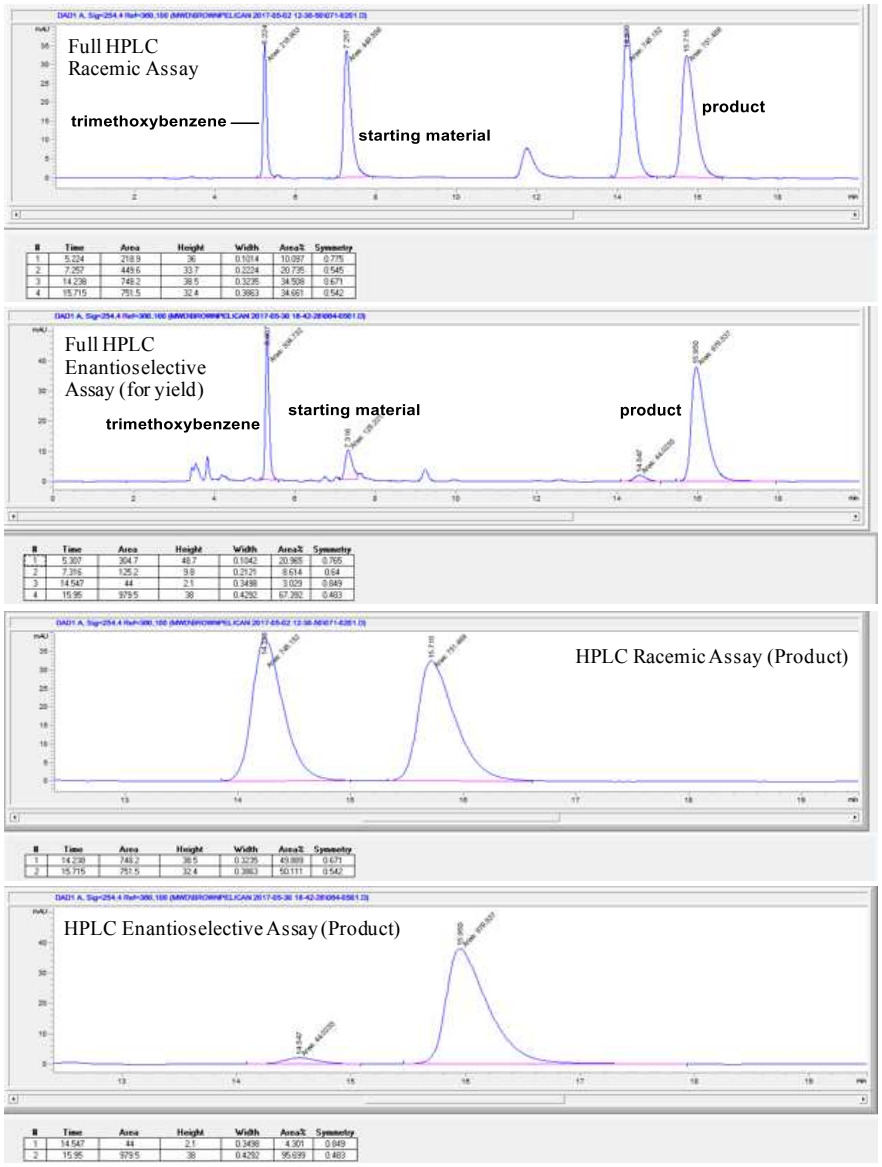

Figure 4.47: 3-Benzyl-6-(4-chlorophenyl)-5,6-dihydropyridin-2(1H)-one (4bc) HPLC. Product synthesized according to general procedure B, and extracted with diethyl ether. Product yield was determined to be 49% by chiral HPLC analysis relative to a 1,3,5-trimethoxybenzene internal standard. The product was determined to be 91% ee by chiral HPLC analysis. (Chiralpak IB, 10% ^{i}PrOH/hexanes, 1 mL/min, $t_r(e_1$, minor) = 14.5 min, $t_r(e_2$, major) = 16.0 min).

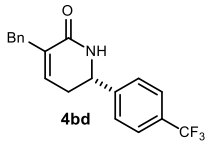

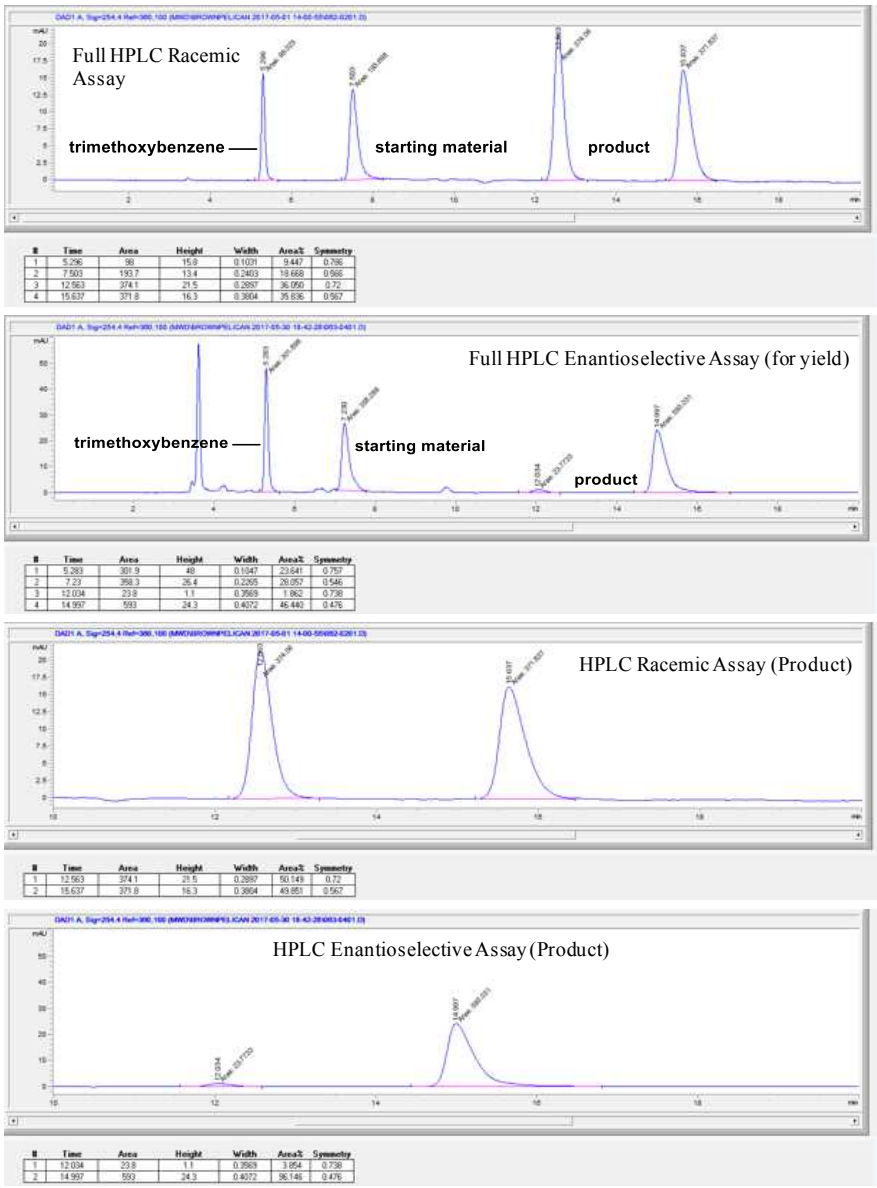

Figure 4.48: 3-Benzyl-6-(4-(trifluoromethyl)phenyl)-5,6-dihydropyridin-2(1H)-one (4bd) HPLC. Product synthesized according to general procedure B, and extracted with diethyl ether. Product yield was determined to be 27% by chiral HPLC analysis relative to a 1,3,5-trimethoxybenzene internal standard. The product was determined to be 92% ee by chiral HPLC analysis. (Chiralpak IB, 10% ^{i}PrOH/hexanes, 1 mL/min, $t_r(e_1$, minor) = 12.0 min, $t_r(e_2$, major) = 15.0 min).

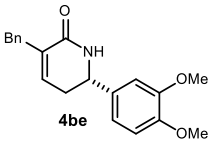

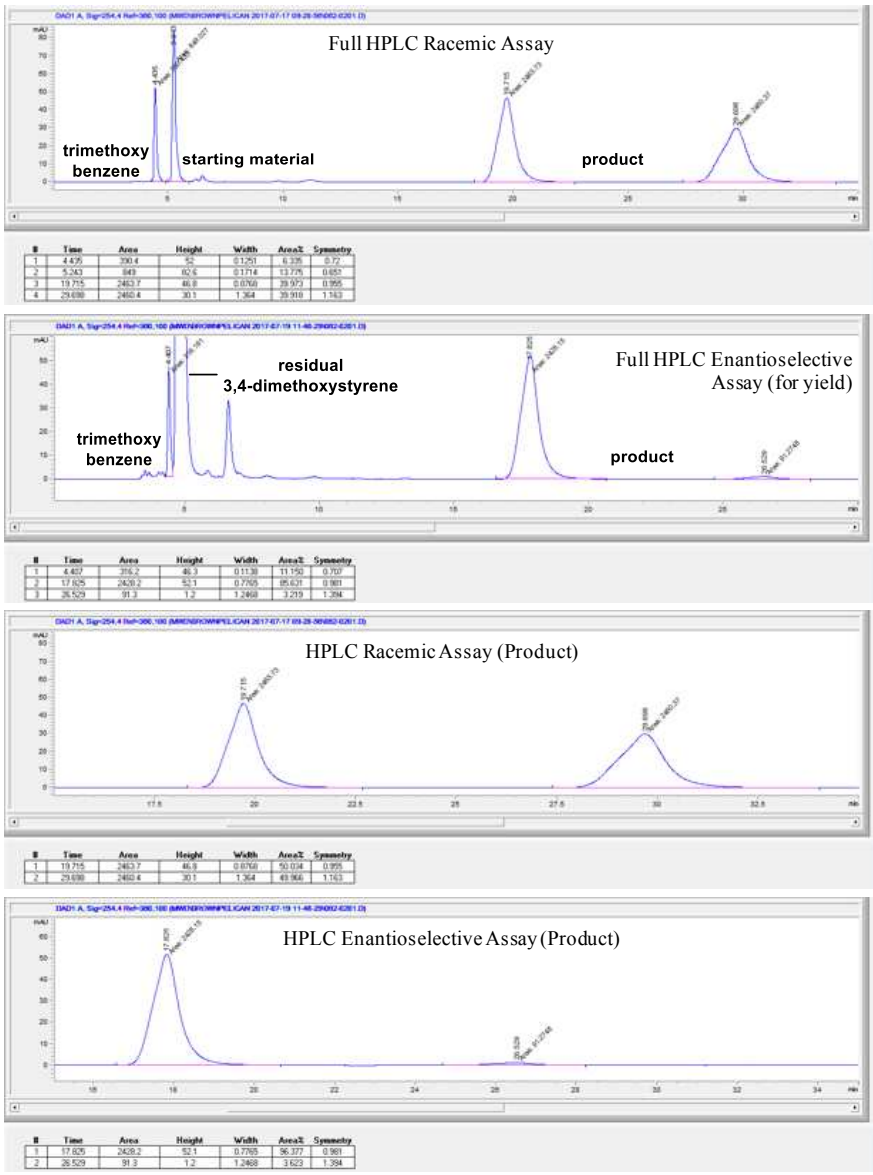

Figure 4.49: 3-Benzyl-6-(3,4-dimethoxyphenyl)-5,6-dihydropyridin-2(1H)-one (4be) HPLC. Product synthesized according to general procedure B, and extracted with diethyl ether. Product yield was determined to be 62% by chiral HPLC analysis relative to a 1,3,5-trimethoxybenzene internal standard. The product was determined to be 93% ee by chiral HPLC analysis. (Chiralpak IA, 15% ^{i}PrOH/hexanes, 1 mL/min, $t_r(e_1$, major) = 17.8 min, $t_r(e_2$, minor) = 26.5 min).

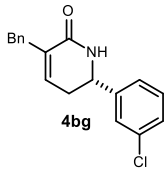

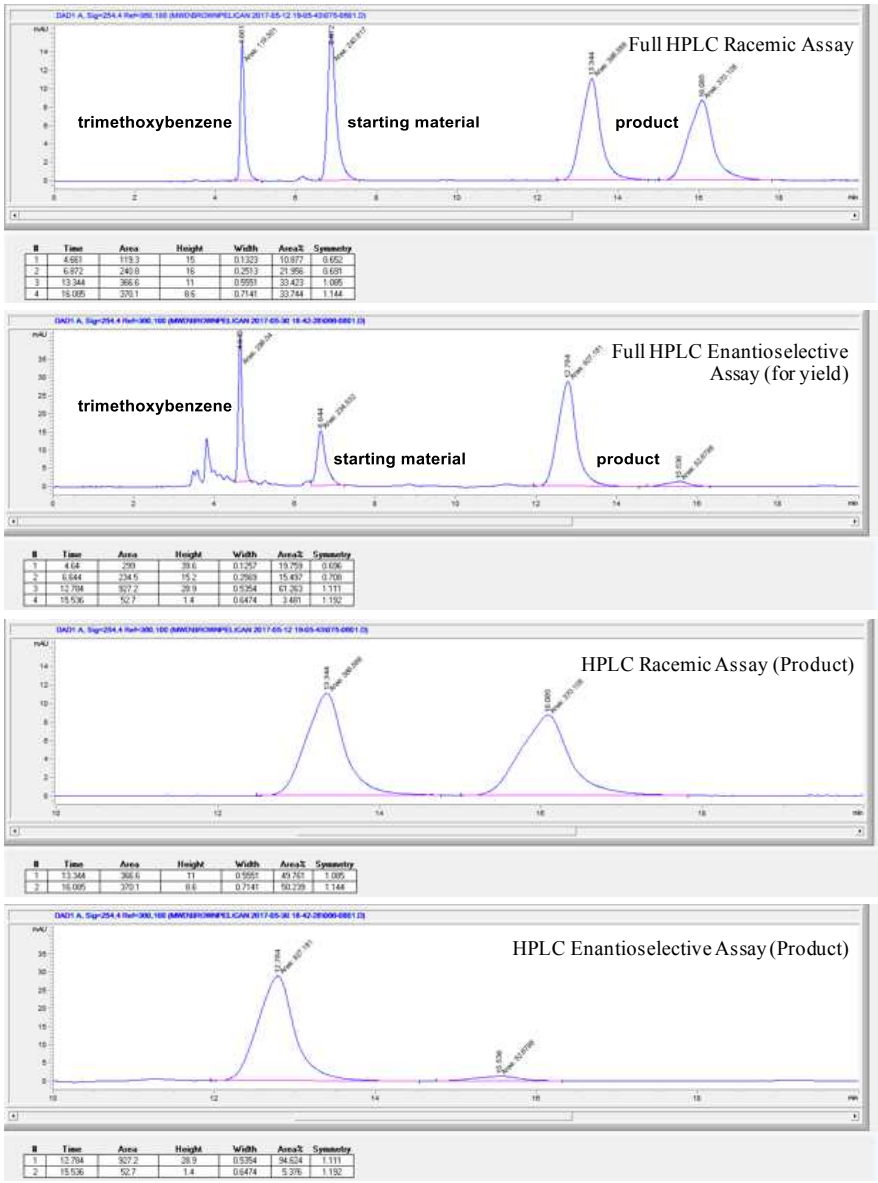

Figure 4.50: 3-Benzyl-6-(3-chlorophenyl)-5,6-dihydropyridin-2(1H)-one (4bg) HPLC. Product synthesized according to general procedure B, and extracted with diethyl ether. Product yield was determined to be 52% by chiral HPLC analysis relative to a 1,3,5-trimethoxybenzene internal standard. The product was determined to be 89% ee by chiral HPLC analysis. (Chiralpak IA, 10% ^{i}PrOH/hexanes, 1 mL/min, $t_r(e_1$, major) = 12.8 min, $t_r(e_2$, minor) = 15.5 min).

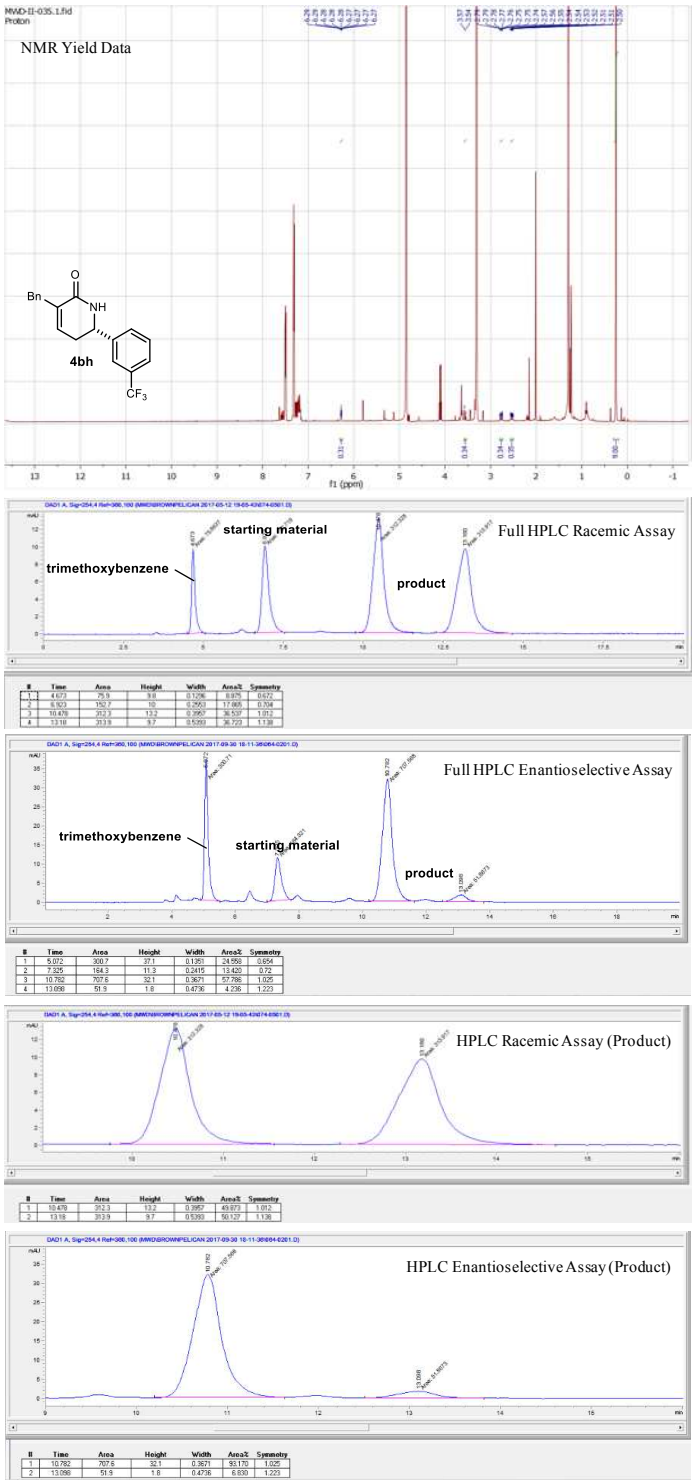

Figure 4.51: 3-Benzyl-6-(3-(trifluoromethyl)phenyl)-5,6-dihydropyridin-2(1H)-one (4bh) NMR/HPLC. Product synthesized according to general procedure B, and extracted with ethyl acetate. Product yield was determined to be 32% by ^{1}H NMR analysis (500 MHz, MeOD) relative to a trimethyl(phenyl)silane internal standard. The product was determined to be 86% ee by chiral HPLC analysis. (Chiralpak IA, 10% ^{i}PrOH/hexanes, 1 mL/min, $t_r(e_1$, major) = 10.8 min, $t_r(e_2$, minor) = 13.1 min).

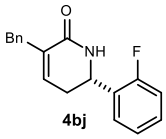

4bj

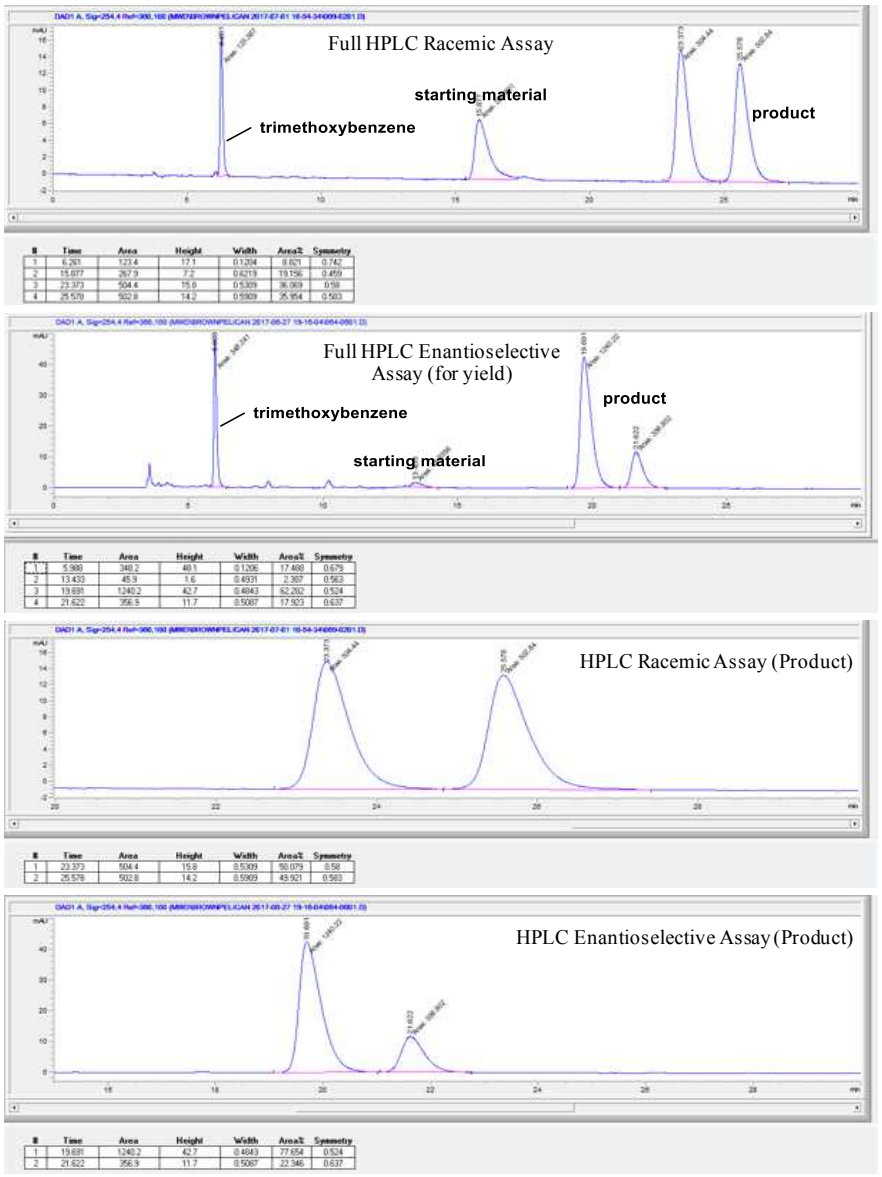

Figure 4.52: 3-Benzyl-6-(3-fluorophenyl)-5,6-dihydropyridin-2(1H)-one (4bj) HPLC. Product synthesized according to general procedure B, and extracted with diethyl ether. Product yield was determined to be 55% by chiral HPLC analysis relative to a 1,3,5-trimethoxybenzene internal standard. The product was determined to be 55% ee by chiral HPLC analysis. (Chiralpak IB, 5% ^{i}PrOH/hexanes, 1 mL/min, $t_r(e_1$, major) = 19.7 min, $t_r(e_2$, minor) = 21.6 min).

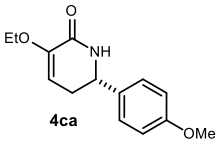

4ca

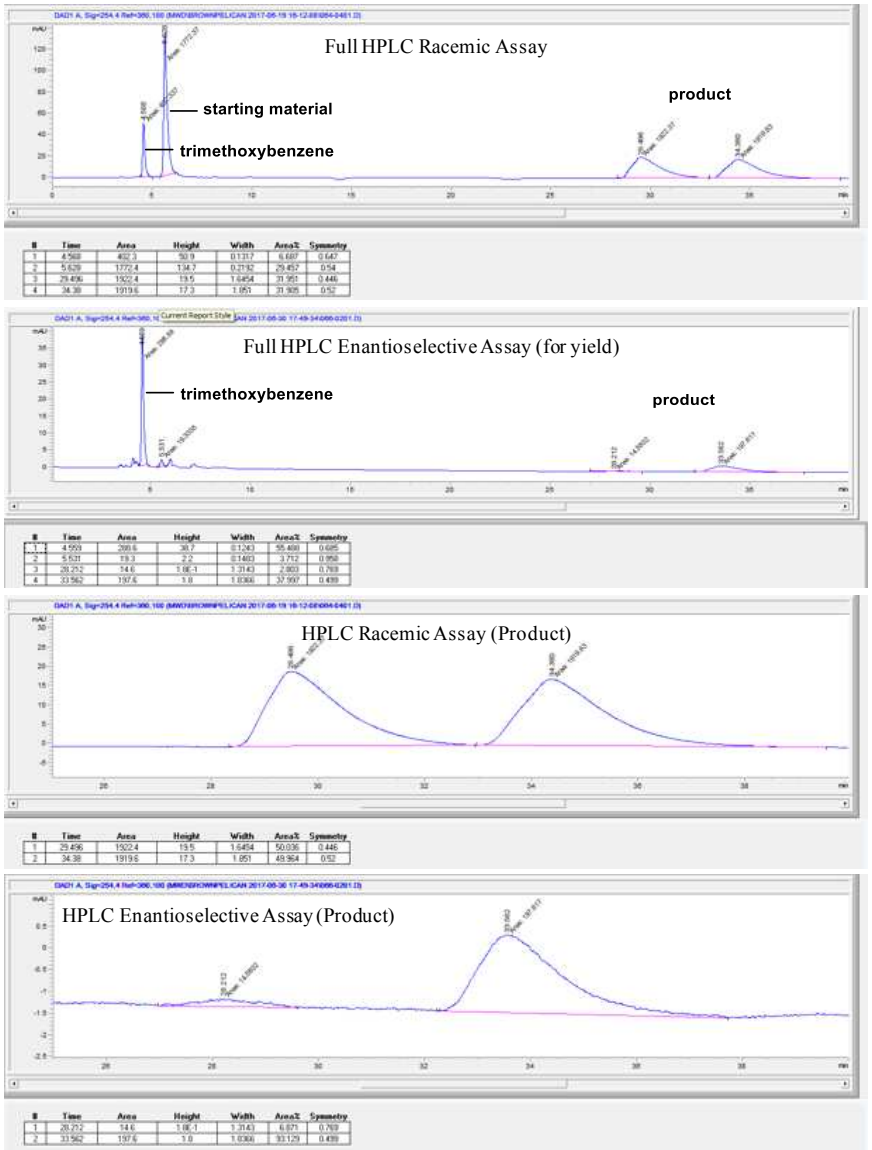

Figure 4.53: 3-Ethoxy-6-(4-methoxyphenyl)-5,6-dihydropyridin-2(1H)-one (4ca) HPLC. Product synthesized according to general procedure B, and extracted with diethyl ether. Product yield was determined to be 8% by chiral HPLC analysis relative to a 1,3,5-trimethoxybenzene internal standard. The product was determined to be 87% ee by chiral HPLC analysis. (Chiralpak IA, 10% ^{i}PrOH/hexanes, 1 mL/min, $t_r(e_1$, minor) = 28.2 min, $t_r(e_2$, major) = 33.6 min).

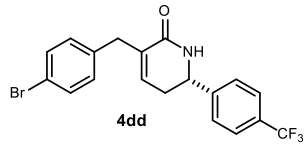

4dd

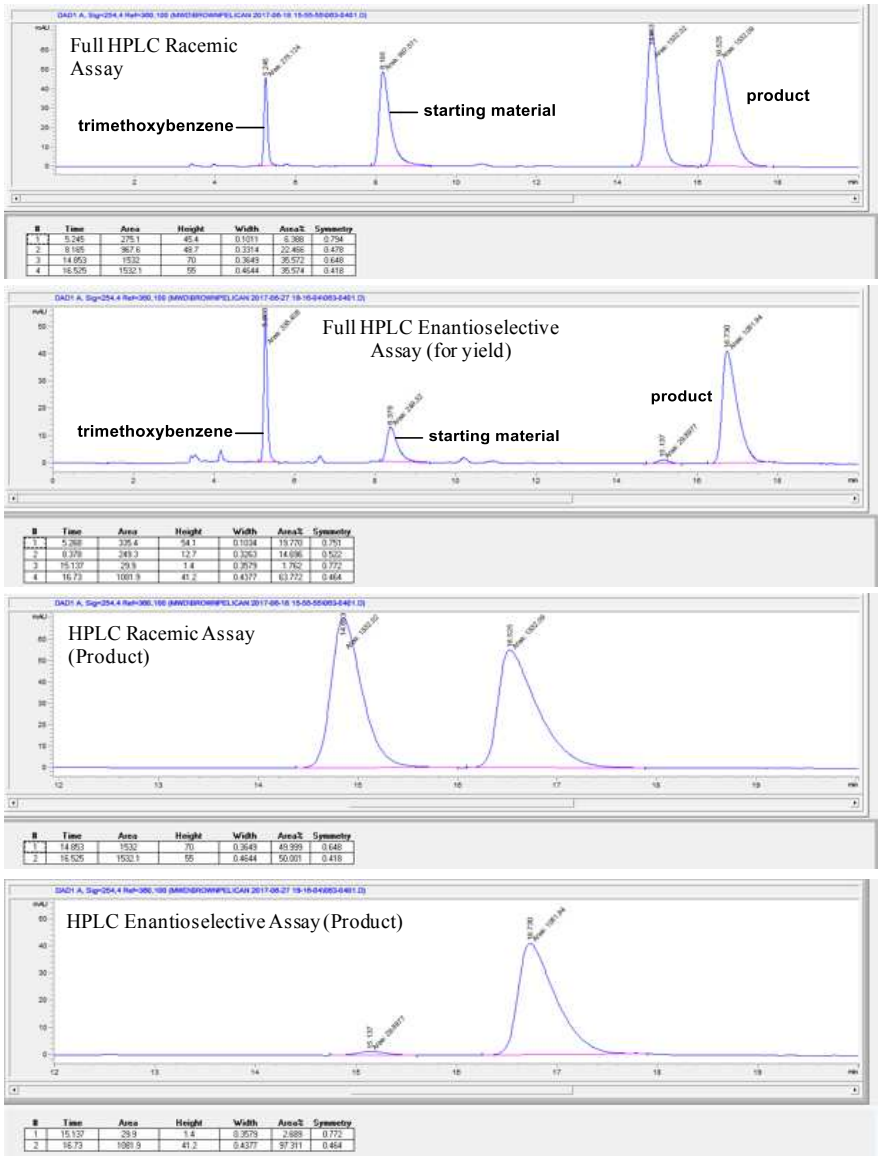

Figure 4.54: 3-(4-Bromobenzyl)-6-(4-(trifluoromethyl)phenyl)-5,6-dihydropyridin-2(1H)-one (4dd) HPLC. Product synthesized according to general procedure B, and extracted with diethyl ether. Product yield was determined to be 30% by chiral HPLC analysis relative to a 1,3,5-trimethoxybenzene internal standard. The product was determined to be 95% ee by chiral HPLC analysis. (Chiralpak IB, 10% ^{i}PrOH/hexanes, 1 mL/min, $t_r(e_1$, minor) = 15.1 min, $t_r(e_2$, major) = 16.7 min).

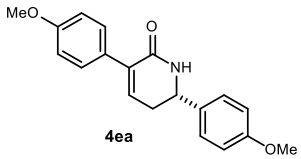

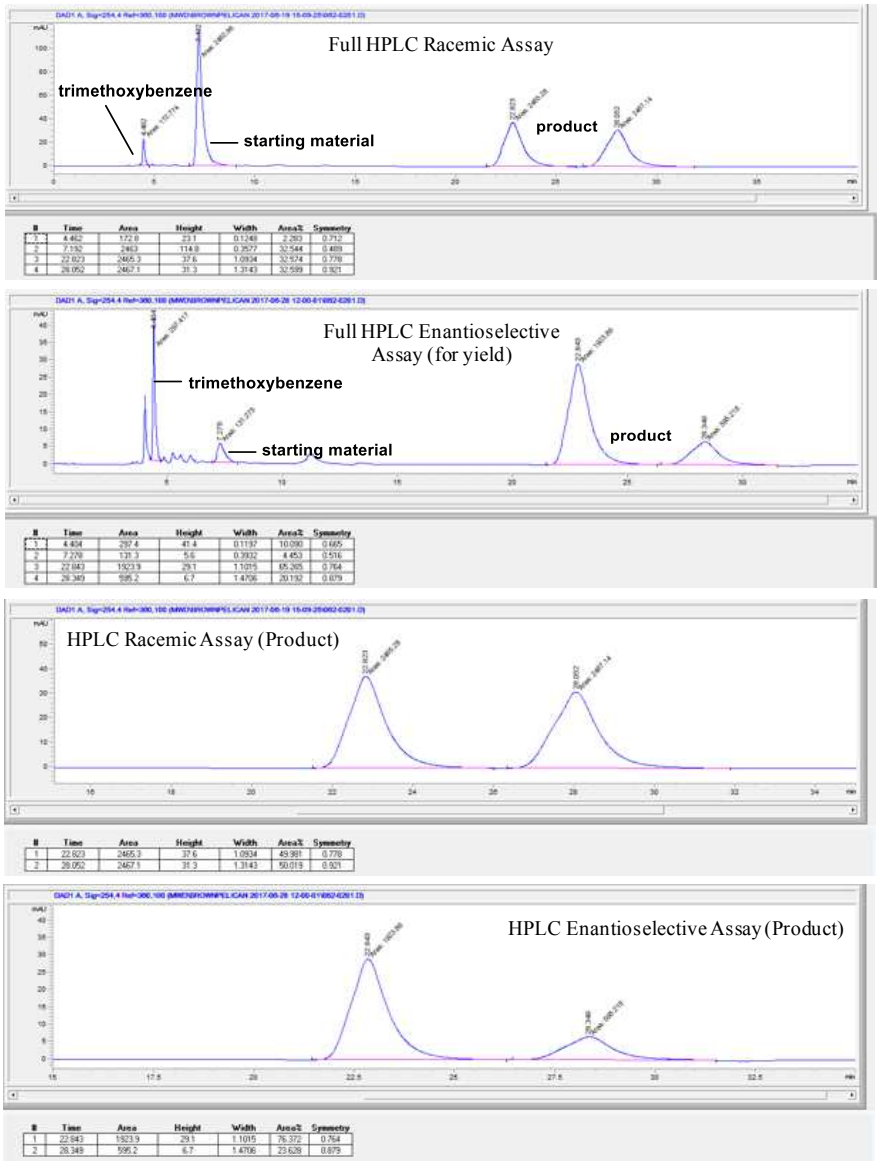

Figure 4.55: 3,6-Bis(4-methoxyphenyl)-5,6-dihydropyridin-2(1H)-one (4ea) HPLC. Product synthesized according to general procedure B, and extracted with diethyl ether. Product yield was determined to be 29% by chiral HPLC analysis relative to a 1,3,5-trimethoxybenzene internal standard. The product was determined to be 53% ee by chiral HPLC analysis. (Chiralpak IA, 15% ^{i}PrOH/hexanes, 1 mL/min, $t_r(e_1$, major) = 22.8 min, $t_r(e_2$, minor) = 28.3 min).

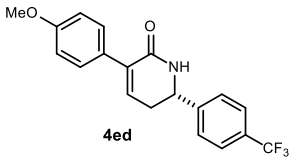

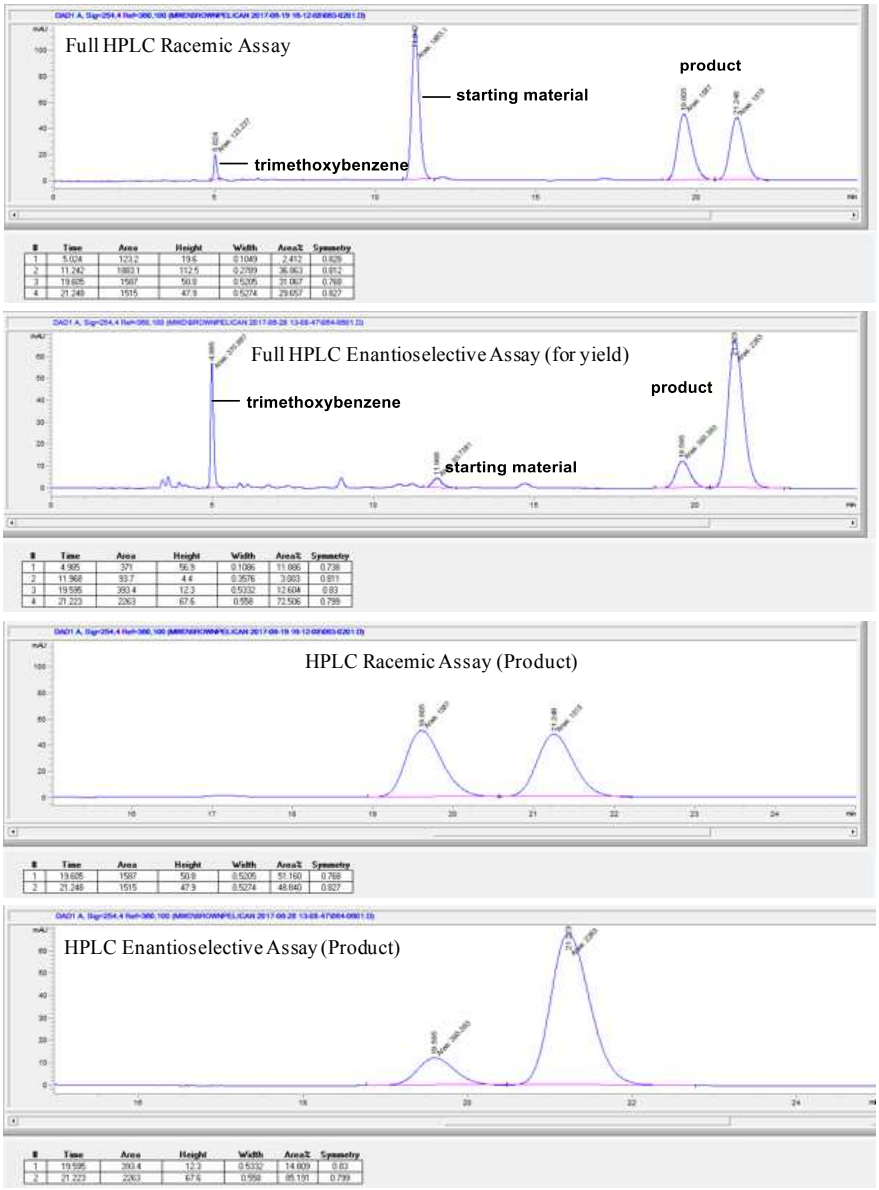

Figure 4.56: 3-(4-Methoxyphenyl)-6-(4-(trifluoromethyl)phenyl)-5,6-dihydropyridin-2(1H)-one (4ed) HPLC. Product synthesized according to general procedure B, and extracted with diethyl ether. Product yield was determined to be 29% by chiral HPLC analysis relative to a 1,3,5-trimethoxybenzene internal standard. The product was determined to be 70% ee by chiral HPLC analysis. (Chiralpak IE, 20% ^{i}PrOH/hexanes, 1 mL/min, $t_r(e_1$, minor) = 19.6 min, $t_r(e_2$, major) = 21.2 min).

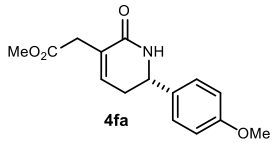

4fa

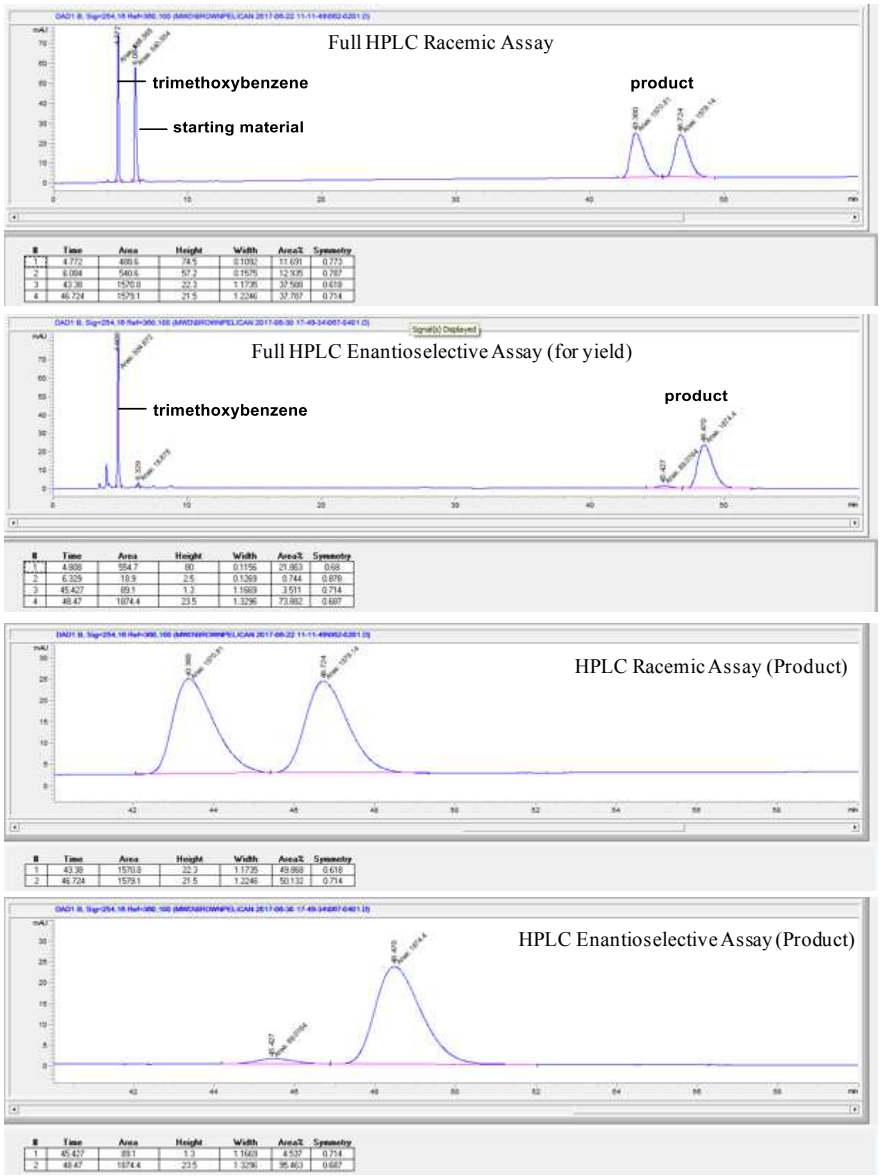

Figure 4.57: Methyl 2-(6-(4-methoxyphenyl)-2-oxo-1,2,5,6-tetrahydropyridin-3-yl)acetate (4fa) HPLC. Product synthesized according to general procedure B, and extracted with diethyl ether. Product yield was determined to be 54% by chiral HPLC analysis relative to a 1,3,5-trimethoxybenzene internal standard. The product was determined to be 91% ee by chiral HPLC analysis. (Chiralpak IE, 30% ^{i}PrOH/hexanes, 1 mL/min, $t_r(e_1$, minor) = 45.4 min, $t_r(e_2$, major) = 48.5 min).

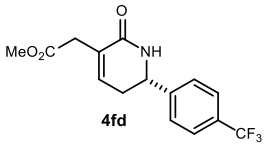

4fd

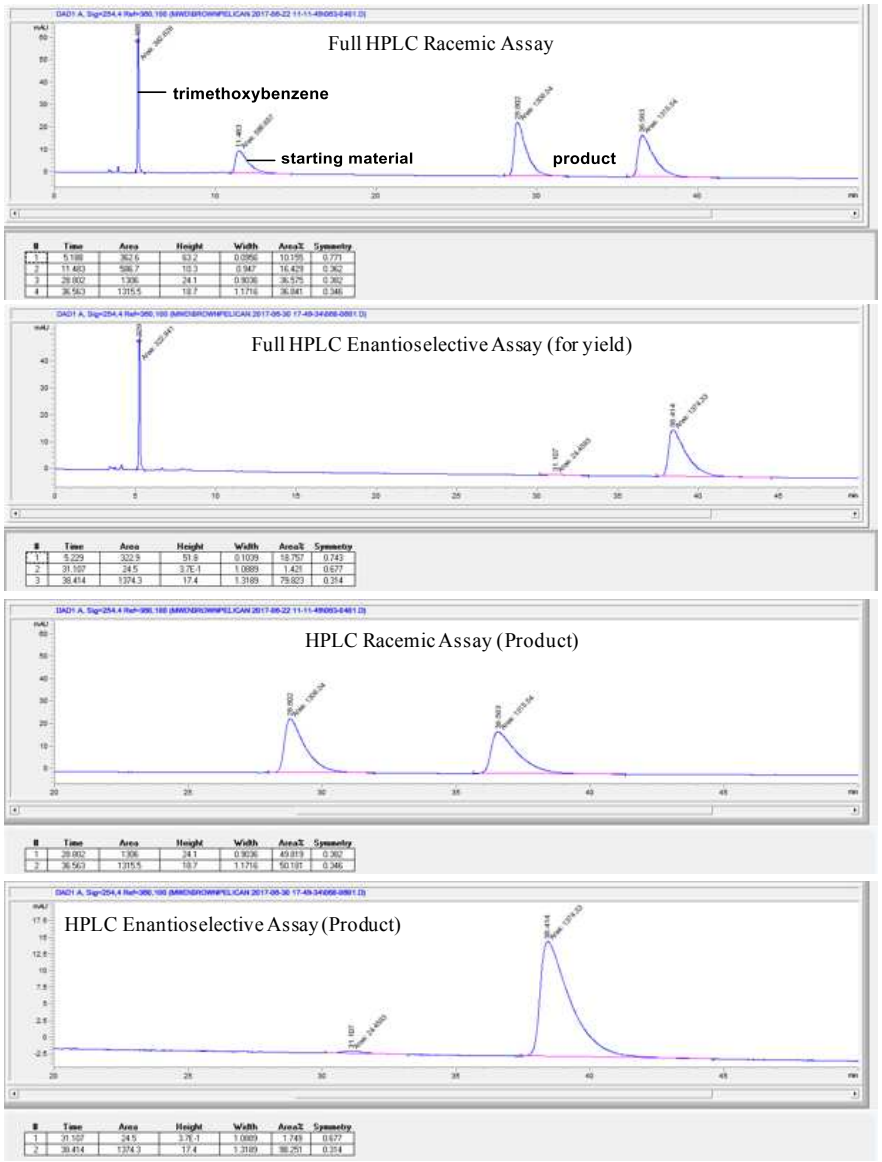

Figure 4.58: Methyl 2-(2-oxo-6-(4-(trifluoromethyl)phenyl)-1,2,5,6-tetrahydropyridin-3-yl)acetate (4fd) HPLC. Product synthesized according to general procedure B, and extracted with diethyl ether. Product yield was determined to be 60% by chiral HPLC analysis relative to a 1,3,5-trimethoxybenzene internal standard. The product was determined to be 97% ee by chiral HPLC analysis. (Chiralpak IB, 10% ^{i}PrOH/hexanes, 1 mL/min, $t_r(e_1$, minor) = 31.1 min, $t_r(e_2$, major) = 38.4 min).

4.4.8 Product derivatization to piperidines (procedure, characterization, and spectra)

Derivatization of enantioenriched substrate

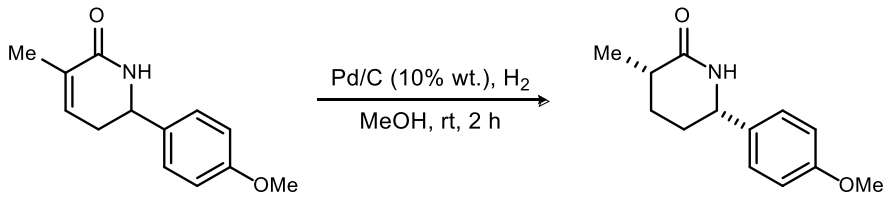

Figure 4.59: 6-(4-methoxyphenyl)-3-methylpiperidin-2-one (6aa).

6-(4-methoxyphenyl)-3-methylpiperidin-2-one (6aa).

A round bottom flask equipped with a stir bar was flame dried under vacuum and purged with N_2. Upon cooling, Pd/C (3.26 mg, 10% by weight) was quickly added, and the flask was evacuated and refilled with N_2 (3x). The piperidone (32.6 mg, 150 μmol) was added to the flask as a solution in MeOH (1.75 mL, 0.1 M), and it was ensured that all Pd/C was properly suspended. The flask was then evacuated once more before being refilled with H_2 (balloon), and the resulting mixture was allowed to stir for 4 h at rt before TLC analysis. The resulting solution was filtered through a Celite plug and washed with EtOAc. The solvent was removed *in vacuo* to afford the desired lactam as a white solid (32.6 mg, 99% yield, 10:1 dr). When this reaction was conducted on enantioenriched 4aa, 6aa was generated in 99% yield, 91% ee and 10:1 dr by chiral HPLC analysis; (Chiralpak AD-H, 5% ^{i}PrOH/hexanes, 1 mL/min, t_r(*anti*, major/minor) = 36.43 min, t_r(*syn*, major/minor) = 38.39 min, t_r(*anti*, minor/major) = 43.05 min, t_r(*syn*, minor/major) = 45.60 min.

^{1}H NMR (for major diastereomer only, 400 MHz, $CDCl_3$) δ 7.18 (d, J = 8.4 Hz, 2H), 6.89 (d, J = 8.8 Hz, 2H), 5.74 (br s, 1H), 4.53 (ddd, J = 7.2, 4.8, 1.6 Hz, 1H), 3.80 (s, 3H), 2.51 (ddq, J = 7.2, 6.0, 6.0 Hz, 1H), 2.07-1.99 (m, 1H), 1.94-1.72 (m, 2H), 1.64-1.55 (m, 1H), 1.32 (d, J = 7.2 Hz, 3H).

^{13}C NMR (for major diastereomer only, 500 MHz, $CDCl_3$) δ 175.89, 159.14, 134.72, 127.17, 114.08, 56.78, 55.31, 35.36, 29.30, 26,19, 18.02.

IR (neat, cm^{-1}) 3281, 3192, 3064, 2957, 2932, 2872, 2838, 1643, 1613, 1587, 1515, 1468, 1404, 1361, 1336, 1302, 1281, 1247, 1175.

HRMS (ASAP) m/z calcd for $C_{13}H_{18}NO_2$ $[M+H]^+$: 220.1338, found: 220.1342.

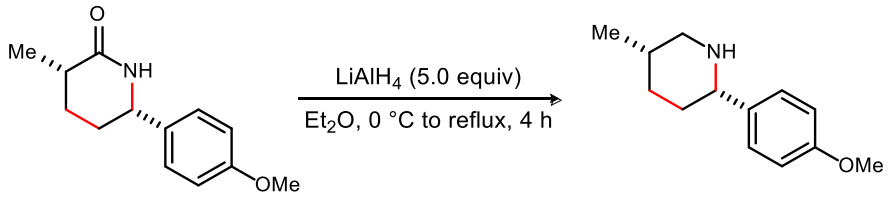

Figure 4.60: 2-(4-methoxyphenyl)-5-methylpiperidine (5aa).

2-(4-methoxyphenyl)-5-methylpiperidine (5aa).

To an oven-dried flask equipped with a stir bar was added $LiAlH_4$ (28.2 mg, 743 μmol) and dry Et_2O (15.0 mL, 0.01 M). The suspension was chilled to 0 °C before the addition of the piperidone (32.9 mg, 148.5 μmol). The solution was refluxed overnight and then chilled back to 0 °C. A 10% sodium hydroxide solution (10 mL/0.1 mol) was added dropwise to the chilled solution and the resulting mixture stirred for another hour at rt. The phases were then separated, and the aqueous layer was extracted with ethyl acetate (3x). The combined organic layers were washed with brine, dried ($MgSO_4$), and concentrated. Flash column chromatography of the residue (SiO_2, 1-2-5-10-20% methanol in dichloromethane) afforded the desired product as a clear viscous oil (24.7 mg, 81% yield, 6:1 dr). The product was determined to be 92% ee and 6:1 dr by chiral HPLC analysis, derivatized as its corresponding NBoc amide; (Chiralpak IE, 5% ^{i}PrOH/hexanes, 1 mL/min, t_r(*syn*, major/minor) = 17.1 min, t_r(*anti*, major/minor) = 18.7 min, t_r(*anti*, minor/major) = 19.4 min, t_r(*syn*, minor/major) = 22.1 min.[4]

^{1}H NMR (for major diastereomer only, 500 MHz, $CDCl_3$) δ 7.51 (d, J = 9.0 Hz, 2H), 6.88 (d, J = 8.5 Hz, 2H), 4.05 (dd, J = 7.5, 4.0 Hz, 1H), 3.72 (s, 3H), 2.94 (dd, J = 13.0, 4.0 Hz, 1H), 2.67 (dd, J = 12.5, 6.5 Hz, 1H), 2.30-2.20 (m, 1H), 2.17-2.02 (m, 2H), 1.80-1.71 (m, 1H), 1.56-1.47 (m, 1H), 1.06 (d, J = 7.0 Hz, 3H).

[4] For HPLC analysis only, a Boc protecting group was installed on the free amine of the piperidine to account for polarity on the chiral column. The retention times reported are associated with the Boc-protected piperidine.

^{13}C NMR (for both diastereomers, 500 MHz, $CDCl_3$) δ 159.92, 159.55, 129.58, 129.36, 128.57, 127.15, 114.16, 114.07, 60.27, 56.81, 55.16, 55.10, 51.44, 47.43, 32.19, 30.05, 29.67, 28.09, 27.96, 26.80, 24.86, 18.69, 17.86.

IR (neat, cm^{-1}) 3404, 2933, 2759, 2701, 2528, 1612, 1585, 1514, 1448, 1301, 1256, 1181. HRMS (ASAP) m/z calcd for $C_{13}H_{20}NO$ $[M+H]^+$: 206.1545, found: 206.1555.

Derivatization of racemic substrates

General procedure is the same as that mentioned above for enantioenriched substrate.

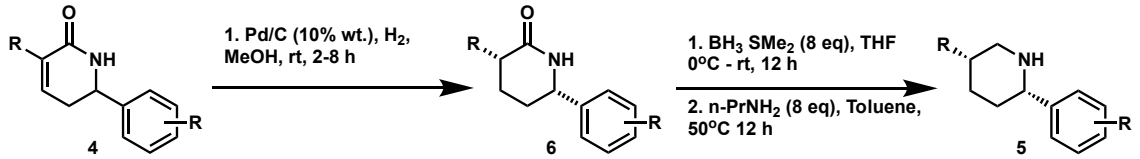

Figure 4.61: General procedure (4, 5, 6).

The stereochemical relationship between the two chiral centers was determined via 2D NOESY for the following substrate:

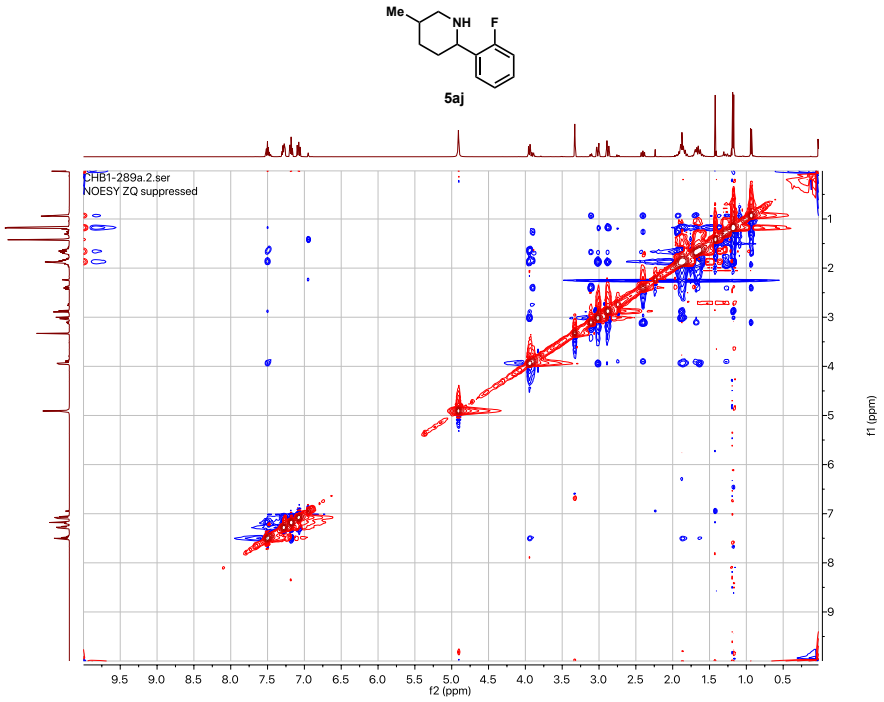

Figure 4.62: 5aj 2D NOESY.

Table 4.32: 6-(4-methoxyphenyl)-3-methylpiperidin-2-one (6aa) characterization.

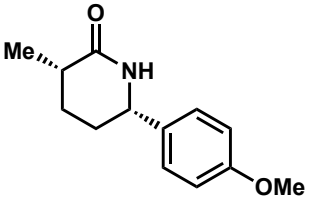

6aa

White solid (29.7 mg, 99% yield, 13:1 dr)

^{1}H NMR (*major diastereomer only,* 400 MHz, $CDCl_3$) δ 7.16 (d, *J* = 8.7 Hz, 2H), 6.87 (d, *J* = 8.7 Hz, 2H), 6.06 (s, 1H), 4.52 (td, *J* = 5.9, 4.8, 1.8 Hz, 1H), 3.79 (s, 3H), 2.58 – 2.34 (m, 1H), 2.02 (m, 1H), 1.93 – 1.69 (m, 2H), 1.64 – 1.45 (m, 1H), 1.30 (d, *J* = 7.3 Hz, 2H).

^{13}C NMR (*major diastereomer only,* 101 MHz, $CDCl_3$)δ 176.29, 159.24, 134.82, 127.28, 114.19, 56.78, 55.42, 35.43, 29.38, 26.23, 18.08.

IR (neat, cm^{-1}) 3205.53, 2932.35, 1655.51, 1512.00, 1464.39, 1406.17, 1336.1, 1247.67, 1176.76, 1112.27, 1031.88, 833.93, 570.23

HRMS (ASAP+) m/z calcd for $C_{13}H_{16}NO_2$ $[M+H]^+$: 218.1181 , found: 218.1175

Table 4.33: 6-(4-chlorophenyl)-3-methylpiperidin-2-one (6ac) characterization.

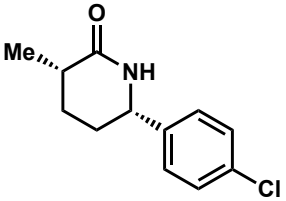

6ac

Light-orange solid (55.9 mg, 99% yield, 19:1 dr)

^{1}H NMR (*major diastereomer only,* 400 MHz, $CDCl_3$)δ 7.18 (d, *J* = 8.7 Hz, 2H), 6.87 (d, *J* = 8.7 Hz, 2H), 6.19 – 6.11 (s, 1H), 4.60 (ddd, *J* = 2.6 Hz, 1H), 3.78 (s, 3H), 2.89 (dd, *J* = 16.1, 4.6 Hz, 1H), 2.80 (m, 1H), 2.55 (dd, *J* = 16.1, 8.2 Hz, 1H), 1.91 – 1.72 (m, 1H).

^{13}C NMR (*both diastereomers,* 101 MHz, $CDCl_3$)δ 172.68, 159.16, 134.69, 127.34, 114.11, 55.39, 51.79, 37.84, 30.00, 22.73.

IR (neat, cm^{-1}) 2950, 1735, 1657, 1512, 1465, 1342, 1248, 1176, 1032, 836.

HRMS (ASAP+) m/z calcd for $C_{12}H_{14}ClNO$ $[M_{deschloro}+H]^+$: 190.1232, found: 190.1229

Table 4.34: 6-(2-fluorophenyl)-3-methylpiperidin-2-one (6aj) characterization.

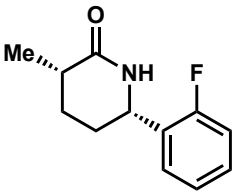

6aj

Off-white solid (28.7 mg, 95% yield, 4:1 dr)

^{1}H NMR (*major diastereomer only,* 400 MHz, $CDCl_3$)δ 7.33 (td, *J* = 7.6, 1.8 Hz, 1H), 7.29 – 7.20 (m, 2H), 7.12 (td, *J* = 7.6, 1.2 Hz, 1H), 7.00 (td, *J* = 10.7, 8.1, 1.2 Hz, 1H), 6.08 (s, 1H), 4.86 (dd, *J* = 9.8, 4.7 Hz, 1H), 2.55 – 2.31 (m, 1H), 2.19 – 2.02 (m, 2H), 1.93 – 1.79 (m, 1H), 1.60 – 1.39 (m, 1H), 1.26 (d, *J* = 7.2 Hz, 2H).

^{13}C NMR (*major diastereomer only* , 101 MHz, $CDCl_3$)δ 176.34, 161.05, 158.60, 129.28 (d, *J* = 8.3 Hz), 127.59 (d, *J* = 4.1 Hz), 124.36 (d, *J* = 3.6 Hz), 115.72 (d, *J* = 21.3 Hz), 50.81 (d, *J* = 3.0 Hz), 35.87, 25.93, 17.73.

IR (neat, cm^{-1}) 2935, 1656, 1485, 758

HRMS (ASAP+) m/z calcd for $C_{12}H_{14}FNO$ $[M+H]^+$: 208.1138, found: 208.1134

Table 4.35: 3-benzyl-6-(4-methoxyphenyl)piperidin-2-one (6ba) characterization.

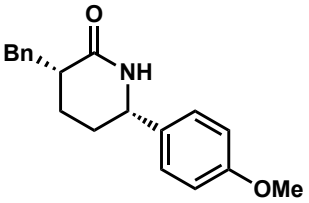

6ba

Light-orange solid (28.7 mg, 99% yield, 10:1 dr)

^{1}H NMR (*major diastereomer only,* 400 MHz, $CDCl_3$)

^{13}C NMR (*both diastereomers,* 101 MHz, $CDCl_3$)δ 174.44, 159.17, 139.57, 134.66, 129.61, 128.5, 127.28, 126.41, 114.12, 56.54, 5v5.42, 42.43, 37.66, 29.49, 21.9

IR (neat, cm^{-1}) 3203.3, 3025.67, 2932.12, 1651.96, 1511.14, 1246.61, 1176.07, 1032.58, 833.89, 1752.84, 702.11

HRMS (ASAP+) m/z calcd for $C_{19}H_{21}NO_2$ $[M+H]^+$: 296.1650, found: 296.1654

Table 4.36: methyl 2-(6-(4-methoxyphenyl)-2-oxopiperidin-3-yl)acetate (6fa) characterization.

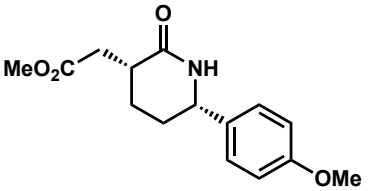

6fa

Off-white solid (4.4 mg, 93% yield, 19:1 dr)

^{1}H NMR (*major diastereomer only,* 500 MHz, $CDCl_3$)δ 7.18 (d, *J* = 8.6 Hz, 2H), 6.87 (d, *J* = 8.7 Hz, 2H), 6.17 (s, 1H), 4.60 (dd, 1H), 3.78 (s, 3H), 3.67 (s, 3H), 2.95 – 2.86 (m, 1H), 2.84 – 2.76 (m, 1H), 2.55 (dd, *J* = 16.2, 8.3 Hz, 1H), 2.19 – 2.06 (m, 1H), 1.88 – 1.75 (m, 2H), 1.70 – 1.56 (m, 1H).

^{13}C NMR (*major diastereomer only,* 126 MHz, $CDCl_3$)δ 173.62, 172.68, 159.12, 134.70, 127.33, 114.08, 55.85, 55.38, 51.79, 37.84, 35.99, 30.00, 22.70.

IR (neat, cm^{-1}) 2952, 1734, 1661, 1511, 1248, 1175, 1034

HRMS (ASAP+) m/z calcd for $C_{15}H_{19}NO_4$ $[M+H]^+$: 278.1392, found: 278.1385.

Table 4.37: 2-(4-methoxyphenyl)-5-methylpiperidine (5aa) characterization.

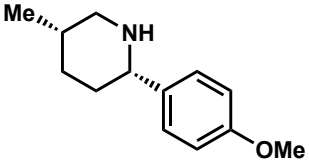

5aa

Pale-yellow oil (20.7 mg, 76% yield, 8:1 dr)

^{1}H NMR (*major diastereomer only,* 400 MHz, $CDCl_3$)δ 7.36 – 7.28 (d, 1H), 6.86 (d, *J* = 8.8 Hz, 1H), 3.65 – 3.53 (d, 1H), 2.99 (dd, *J* = 11.8, 3.4 Hz, 1H), 2.91 – 2.80 (d, 1H), 1.89 – 1.81 (m, 1H), 1.78 – 1.72 (m, 2H), 1.59 (dd, *J* = 9.8, 1.3 Hz, 2H), 1.14 (d, *J* = 7.0 Hz, 3H).

^{13}C NMR (*major diastereomer only,* 101 MHz, $CDCl_3$)δ 158.60, 137.6 8, 113.79, 61.05, 55.38, 52.46, 30.84, 29.63, 27.87, 17.34.

IR (neat, cm^{-1}) 2926.74, 2853.9, 1675.4, 1629.8, 1512.3, 1458.7, 1249.6, 1169.8, 1033, 831.47, 785.85, 732.63, 702.22

HRMS (ASAP+) m/z calcd for $C_{13}H_{20}NO$ $[M+H]^+$: 206.1545, found: 206.1541

Table 4.38: 2-(4-chlorophenyl)-5-methylpiperidine (5ac) characterization.

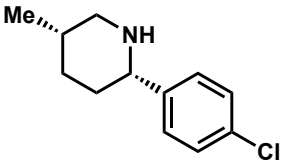

5ac

Clear oil (119.0 mg, 87% yield, 5:1 dr)

^{1}H NMR (*major diastereomer only,* 400 MHz, $CDCl_3$)δ 7.37 – 7.24 (m, 4H), 3.60 (dt, *J* = 7.0, 2.5 Hz, 1H), 2.98 (dd, *J* = 11.8, 3.4 Hz, 1H), 2.85 (ddd, *J* = 11.8, 3.0, 1.5 Hz, 1H), 1.85 (ddd, *J* = 6.7, 4.6, 3.0 Hz, 1H), 1.74 (ddt, *J* = 10.5, 5.9, 2.5 Hz, 2H), 1.63 – 1.55 (m, 2H), 1.15 (d, *J* = 7.0 Hz, 3H).

^{13}C NMR (*major diastereomer only,* 101 MHz, $CDCl_3$)δ 144.07, 132.36, 128.41, 128.07, 60.99, 52.29, 30.68, 29.80, 27.77, 17.21.

IR (neat, cm^{-1}) 2926.74, 2849.87, 2764.63, 1490.43, 1443.67, 1378.61, 1328.54, 1189.01, 1013.35, 813.46, 764.66, 637.65, 531.18, 462.27

HRMS (ASAP+) m/z calcd for $C_{12}H_{17}ClN$ $[M+H]^+$: 210.1049, found: 210.1053.

Table 4.39: 2-(2-fluorophenyl)-5-methylpiperidine (5aj) characterization.

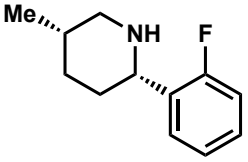

5aj

Clear oil (25.5 mg, 61% yield, 3:1 dr)

^{1}H NMR (*major diastereomer only,* 500 MHz, MeOD)δ 7.51 (d, *J* = 1.8 Hz, 1H), 7.34 – 7.24 (m, 1H), 7.20 (dd, *J* = 7.6, 1.3 Hz, 1H), 7.09 (ddd, *J* = 11.0, 8.2, 1.2 Hz, 1H), 3.96 (dd, *J* = 10.3, 3.1 Hz, 1H), 3.03 (dd, *J* = 12.8, 3.4 Hz, 1H), 2.89 (dt, *J* = 12.7, 2.2 Hz, 1H), 2.03 – 1.79 (m, 3H), 1.79 – 1.53 (m, 2H), 1.19 (d, *J* = 7.2 Hz, 3H).

^{13}C NMR (*major diastereomer only,* 101 MHz, MeOD) δ 160.53, 129.76, 129.13, 125.46, 116.40, 56.31 (d, *J* = 2.7 Hz), 52.84, 35.00, 31.51, 28.46, 17.26.

IR (neat, cm^{-1}) 3372.04, 2925.85, 1584.57, 1489.75, 1451.12, 1829.88, 1331.99, 1281.46, 1225.98, 1121.42, 1116.23, 1089, 1009.78, 754.9, 536.59

HRMS (ASAP+) m/z calcd for $C_{12}H_{17}FN$ $[M+H]^+$: 194.1345, found: 194.1342.

Table 4.40: 5-benzyl-2-(4-methoxyphenyl)piperidine (5ba) characterization.

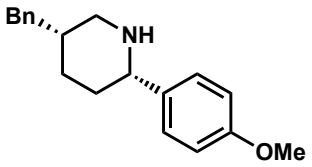

5ba

Clear oil (84.7 mg, 86% yield, 6:1 dr)

^{1}H NMR (*major diastereomer only,* 500 MHz, MeOD)δ 7.38 – 7.33 (d, 2H), 7.31 – 7.23 (m, 3H), 7.21 – 7.15 (m, 2H), 6.92 (d, *J* = 8.7 2H), 3.78 (s, 3H), 3.63 (dd, *J* = 10.2, 2.9 Hz, 1H), 3.47 (ddd, *J* = 22.5, 11.6, 2.6 Hz, 1H), 2.92 (d, *J* = 3.4 Hz, 1H), 2.84 (dd, *J* = 7.8, 4.0 Hz, 1H), 1.96 – 1.85 (m, 1H), 1.79 – 1.57 (m, 5H).

^{13}C NMR (*major diastereomer only,* 101 MHz, $CDCl_3$)δ 158.60, 141.98, 138.00, 129.27, 127.76, 125.73, 113.77, 61.32, 55.33, 50.40, 37.24, 35.42, 30.27, 28.56.

IR (neat, cm^{-1}) 3024.13, 2926.04, 2849.2, 1609.84, 1511.02, 1442.07, 1301.85, 1244.73, 1174.11, 1106.58, 1036.14, 829.06, 771.16, 700.17, 651.50, 542.82

HRMS (ASAP+) m/z calcd for $C_{18}H_{24}NO$ $[M+H]^+$: 282.1858, found: 282.1854 .

Table 4.41: methyl 2-(6-(4-methoxyphenyl)piperidin-3-yl)acetate (5fa) characterization.

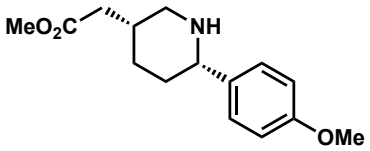

5fa

Clear oil (22.0 mg, 78% yield, 5:1 dr)

^{1}H NMR (*major diastereomer only,* 400 MHz, MeOD) δ 7.31 (d, *J* = 8.7 Hz, 2H), 6.90 (d, *J* = 8.7 Hz, 2H), 3.80 (s, 3H), 3.70 (s, 3H), 2.99 (d, *J* = 3.5 Hz, 2H), 2.70 (dd, *J* = 15.7, 7.5 Hz, 1H), 2.60 (dd, *J* = 15.7, 7.5 Hz, 1H), 2.34 – 2.12 (m, 2H), 1.88 – 1.58 (m, 5H).

^{13}C NMR (*major diastereomer only,* 101 MHz, MeOD)

IR (neat, cm^{-1}) 2928.05, 2834.93, 1732.16, 1610.65, 1532.35, 1511.06, 1437.37, 1276.57, 1169.39, 1035.44, 890.71, 829.59, 772.23, 644.48, 503.09

HRMS (ASAP+) m/z calcd for $C_{15}H_{22}NO_3$ $[M+H]^+$: 264.1600, found: 264.1591.

Table 4.42: methyl 2-(6-(4-methoxyphenyl)piperidin-3-yl)acetate (5fa) characterization.

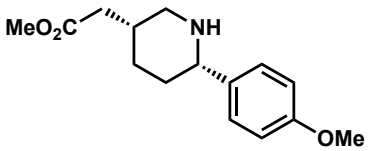

5fa

Clear oil (22.0 mg, 78% yield, 5:1 dr)

^{1}H NMR (*major diastereomer only,* 400 MHz, MeOD) δ 7.31 (d, *J* = 8.7 Hz, 2H), 6.90 (d, *J* = 8.7 Hz, 2H), 3.80 (s, 3H), 3.70 (s, 3H), 2.99 (d, *J* = 3.5 Hz, 2H), 2.70 (dd, *J* = 15.7, 7.5 Hz, 1H), 2.60 (dd, *J* = 15.7, 7.5 Hz, 1H), 2.34 – 2.12 (m, 2H), 1.88 – 1.58 (m, 5H).

^{13}C NMR (*major diastereomer only,* 101 MHz, MeOD)

IR (neat, cm^{-1}) 2928.05, 2834.93, 1732.16, 1610.65, 1532.35, 1511.06, 1437.37, 1276.57, 1169.39, 1035.44, 890.71, 829.59, 772.23, 644.48, 503.09

HRMS (ASAP+) m/z calcd for $C_{15}H_{22}NO_3$ $[M+H]^+$: 264.1600, found: 264.1591.

Copies of NMR spectra

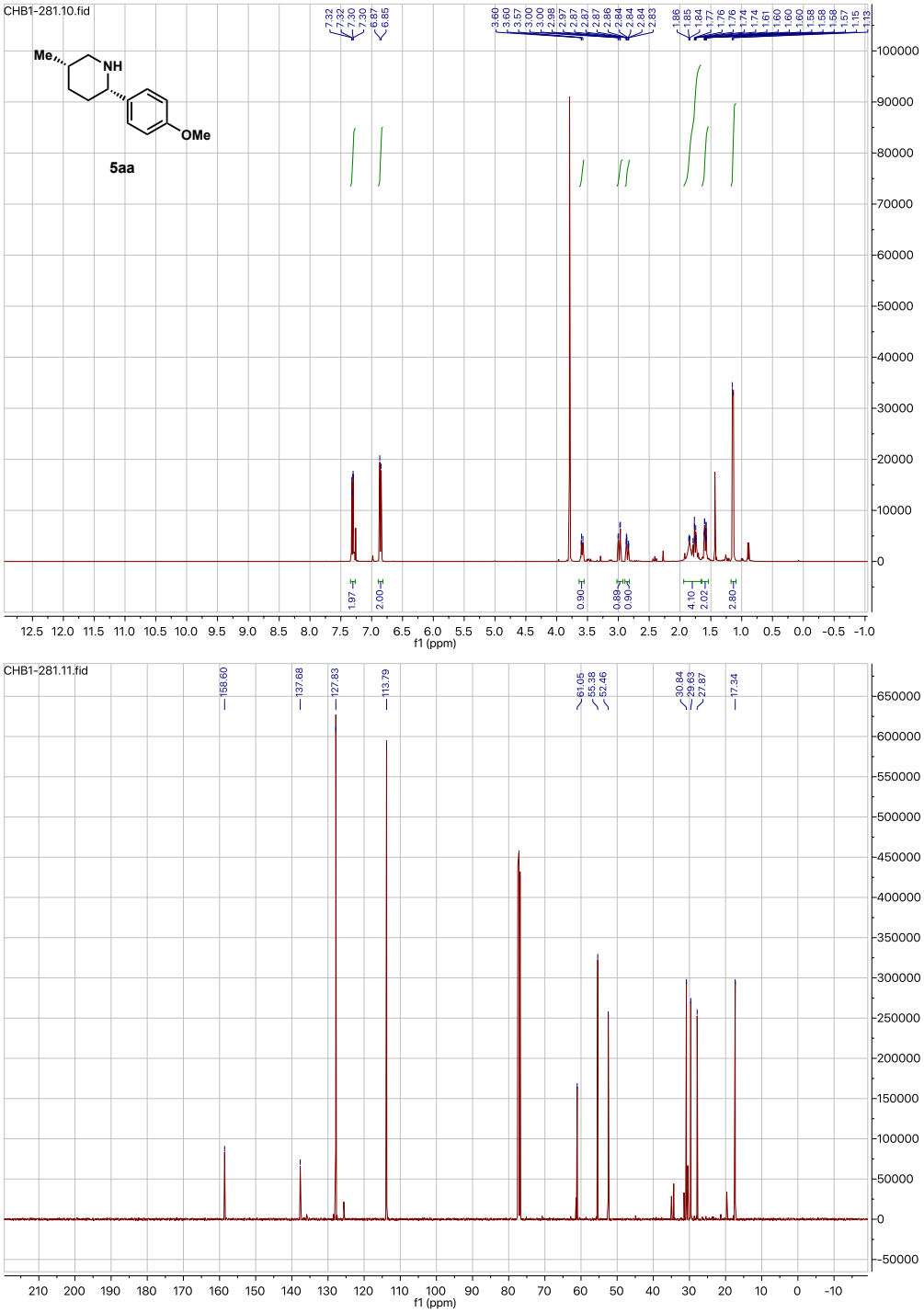

Figure 4.63: 5aa NMR spectra.

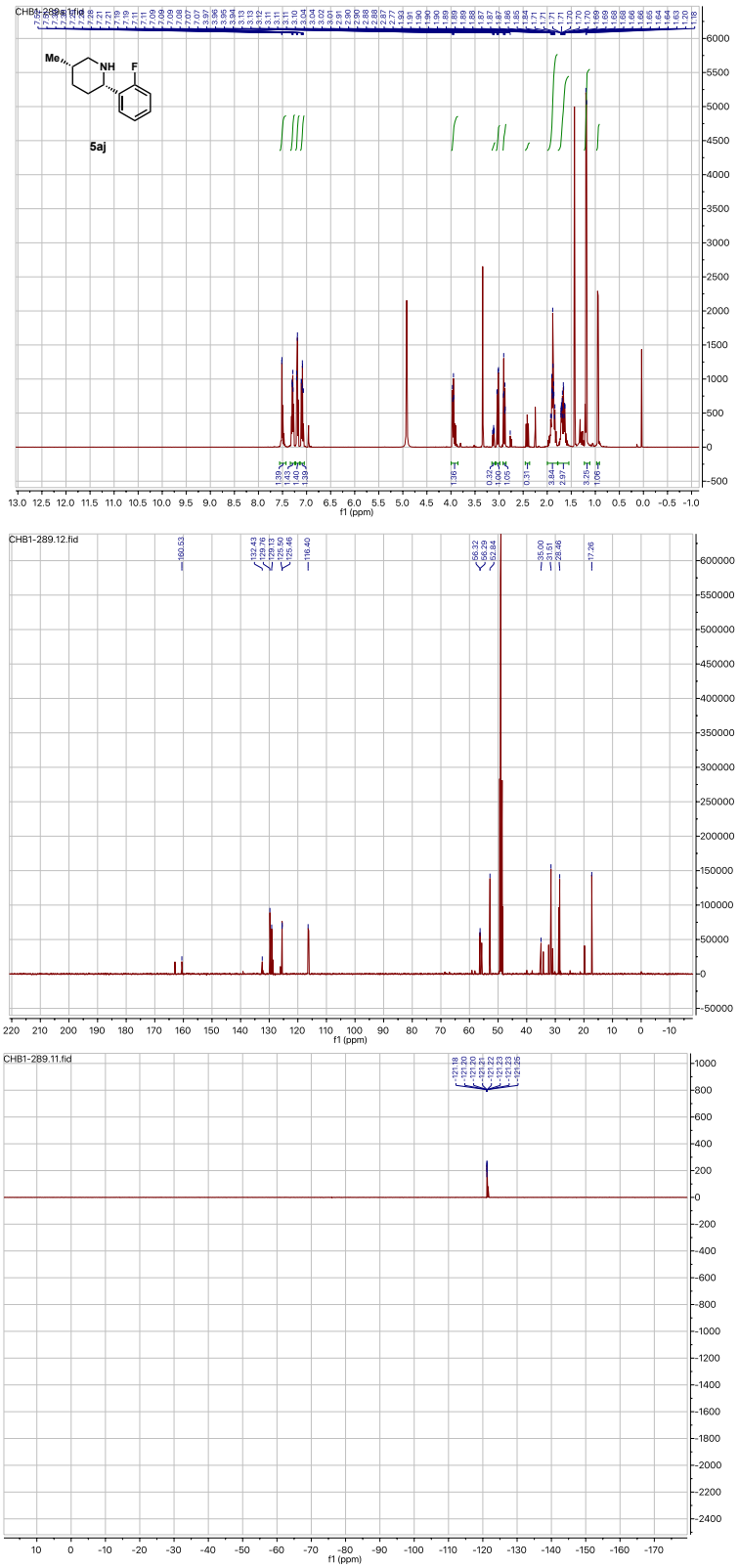

Figure 4.64: 5aj NMR spectra.

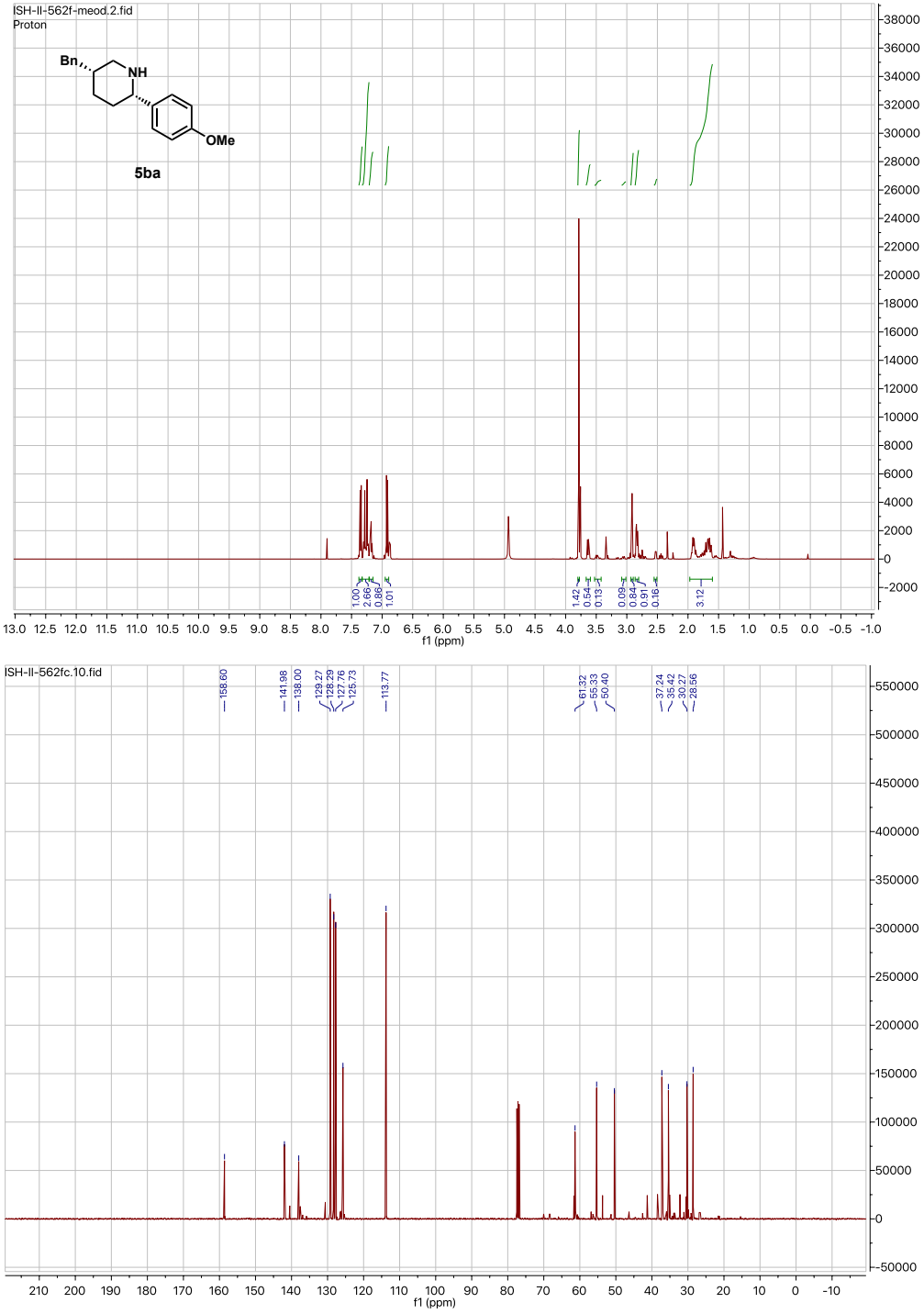

Figure 4.65: 5ba NMR spectra.

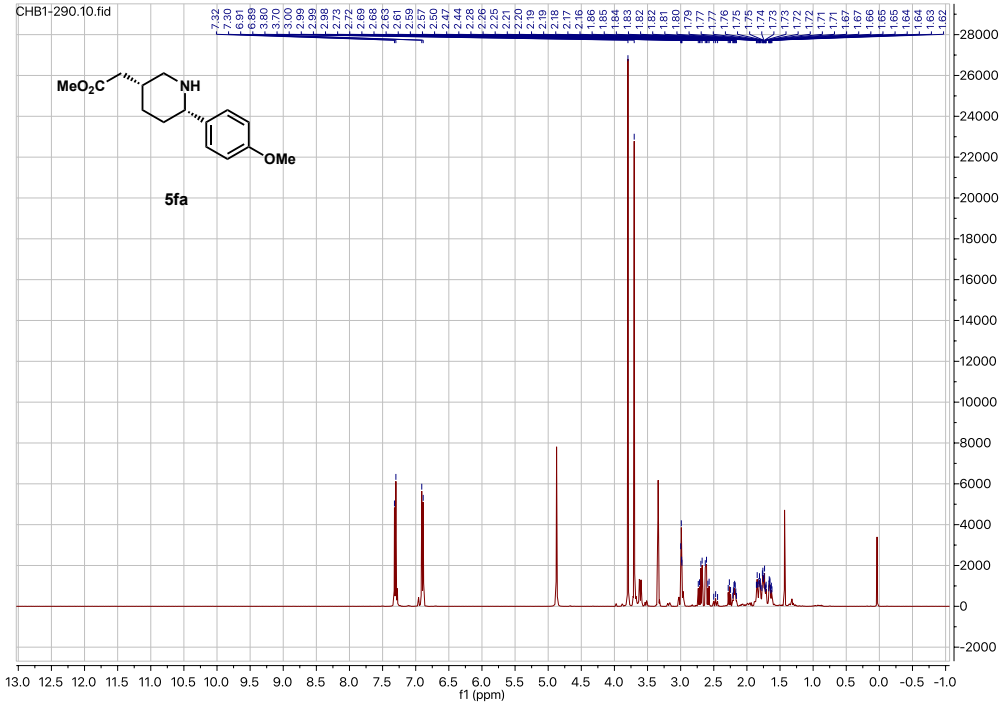

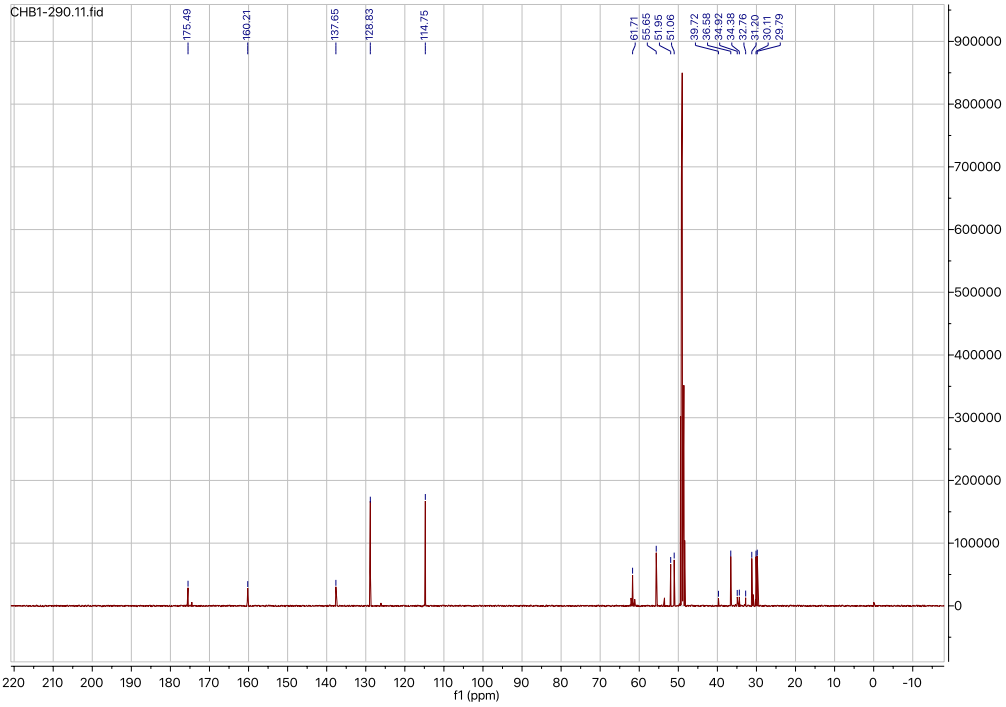

Figure 4.66: 5fa NMR spectra.

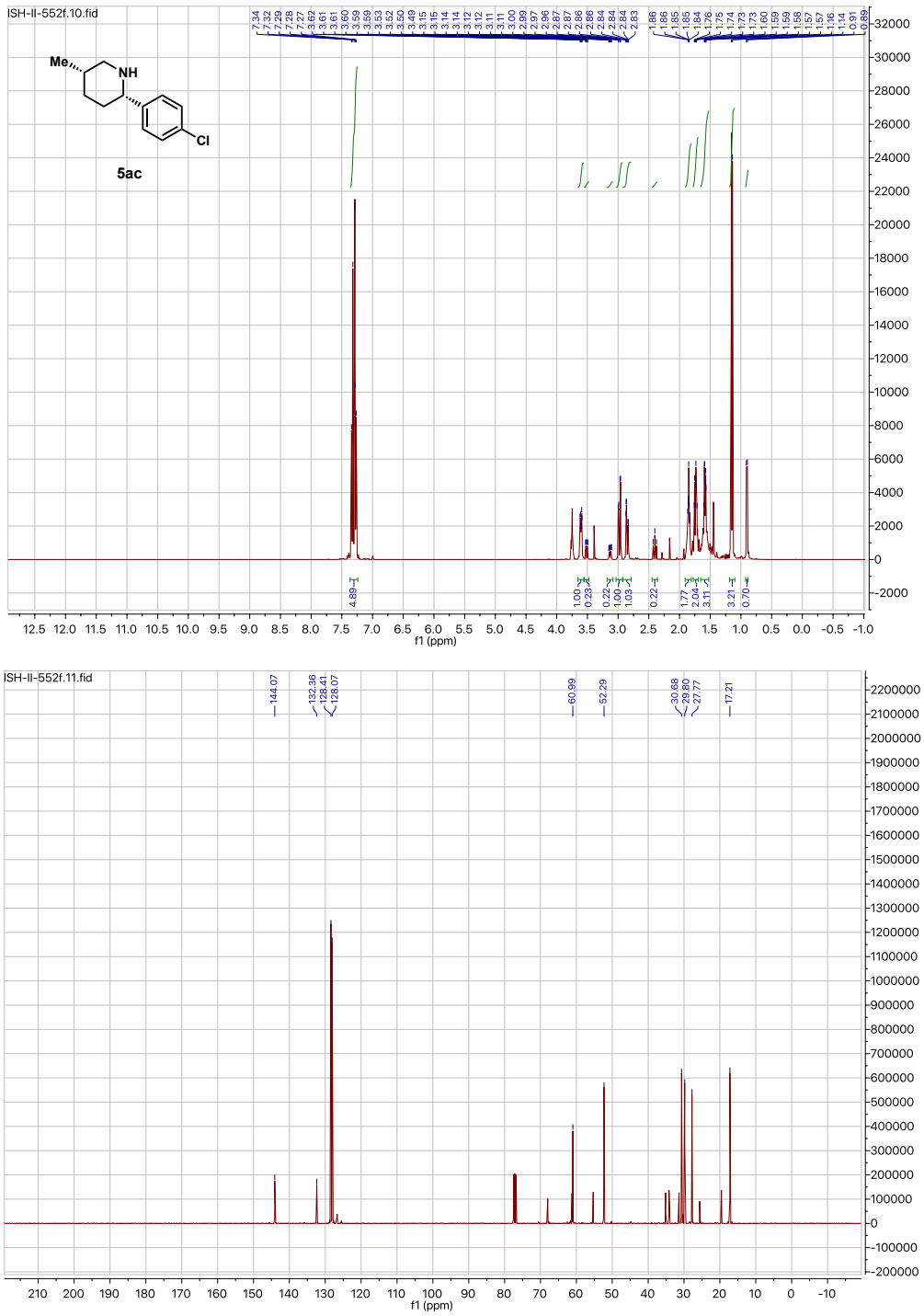

Figure 4.67: 5ac NMR spectra.

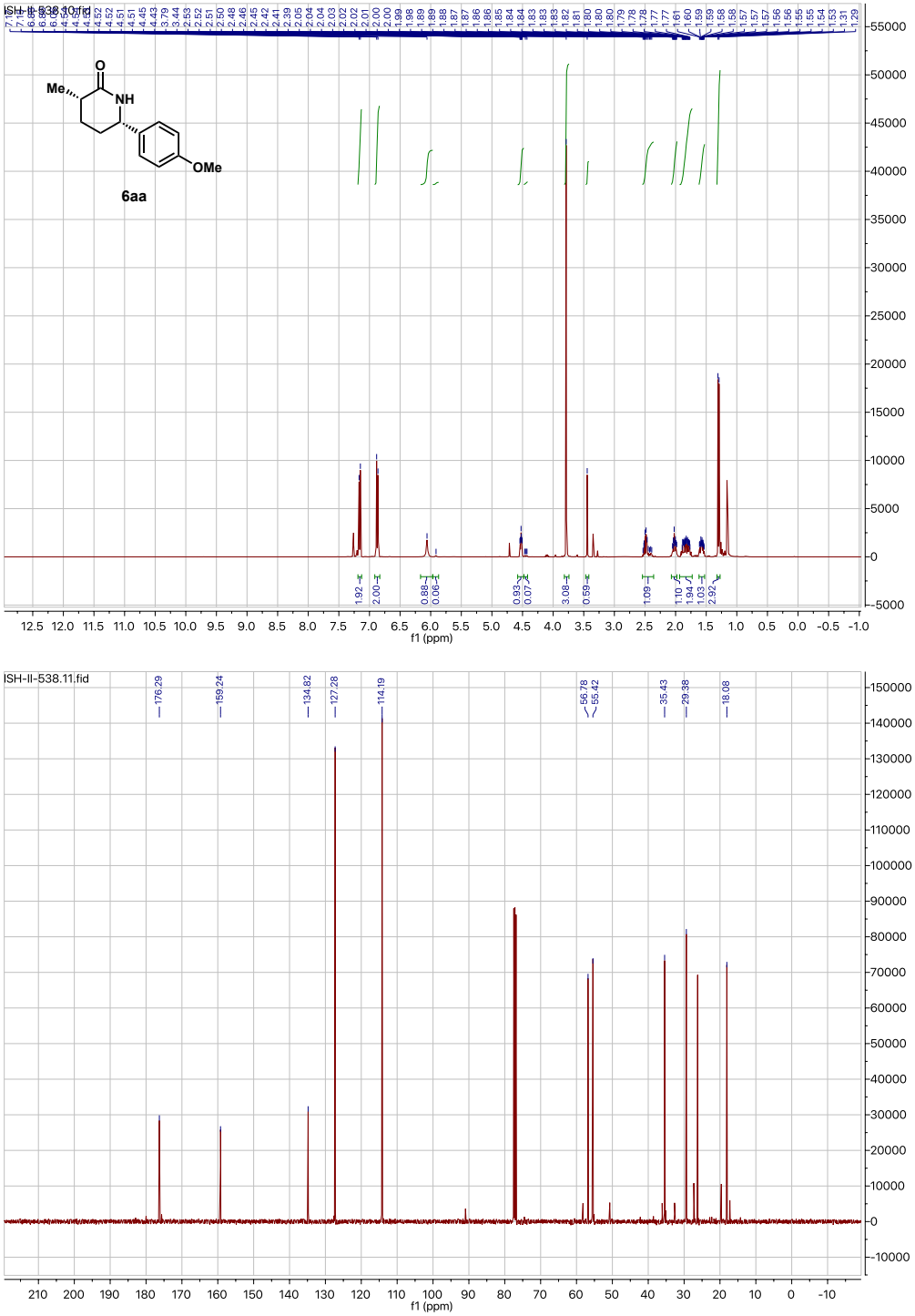

Figure 4.68: 6aa NMR spectra.

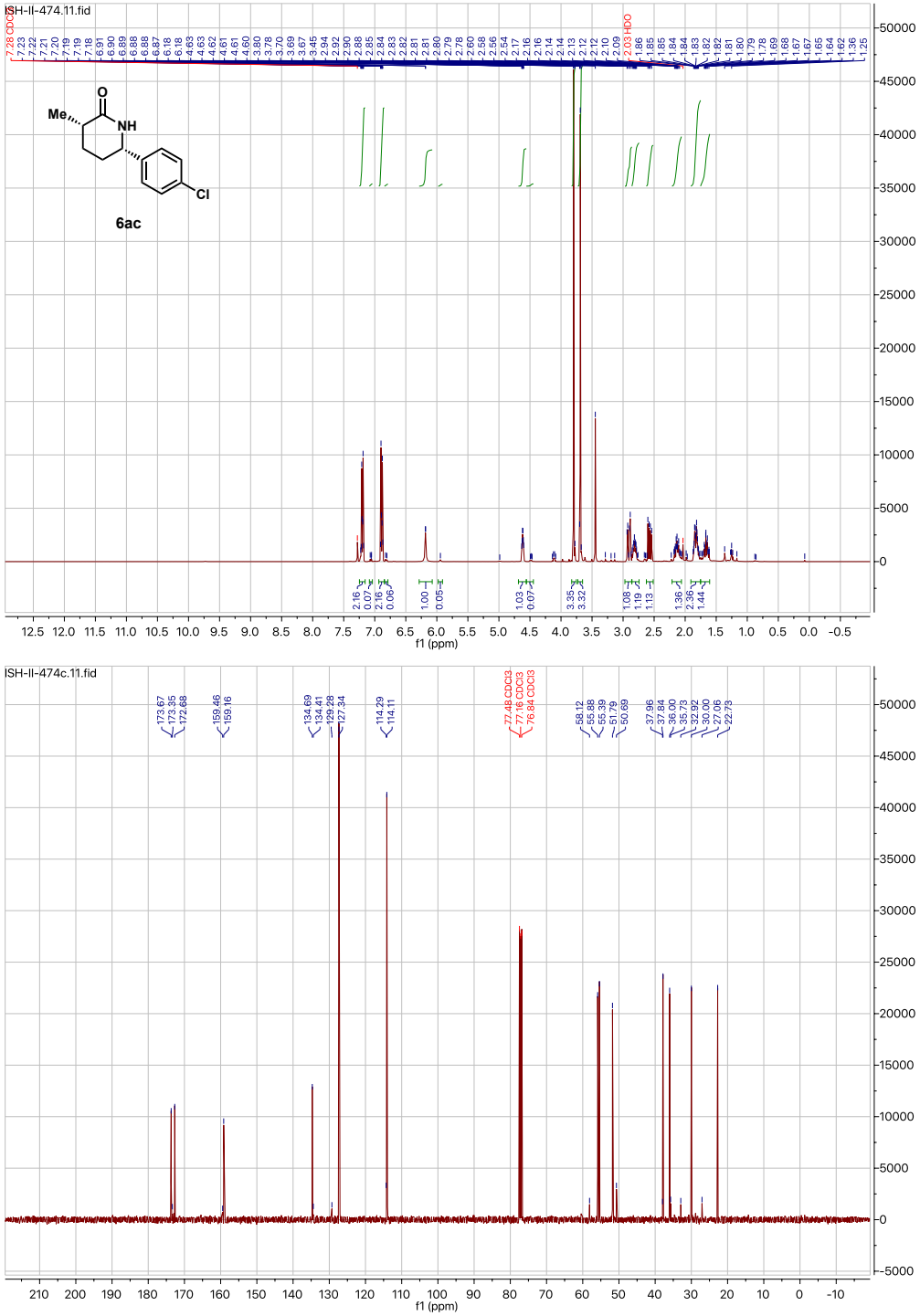

Figure 4.69: 6ac NMR spectra.

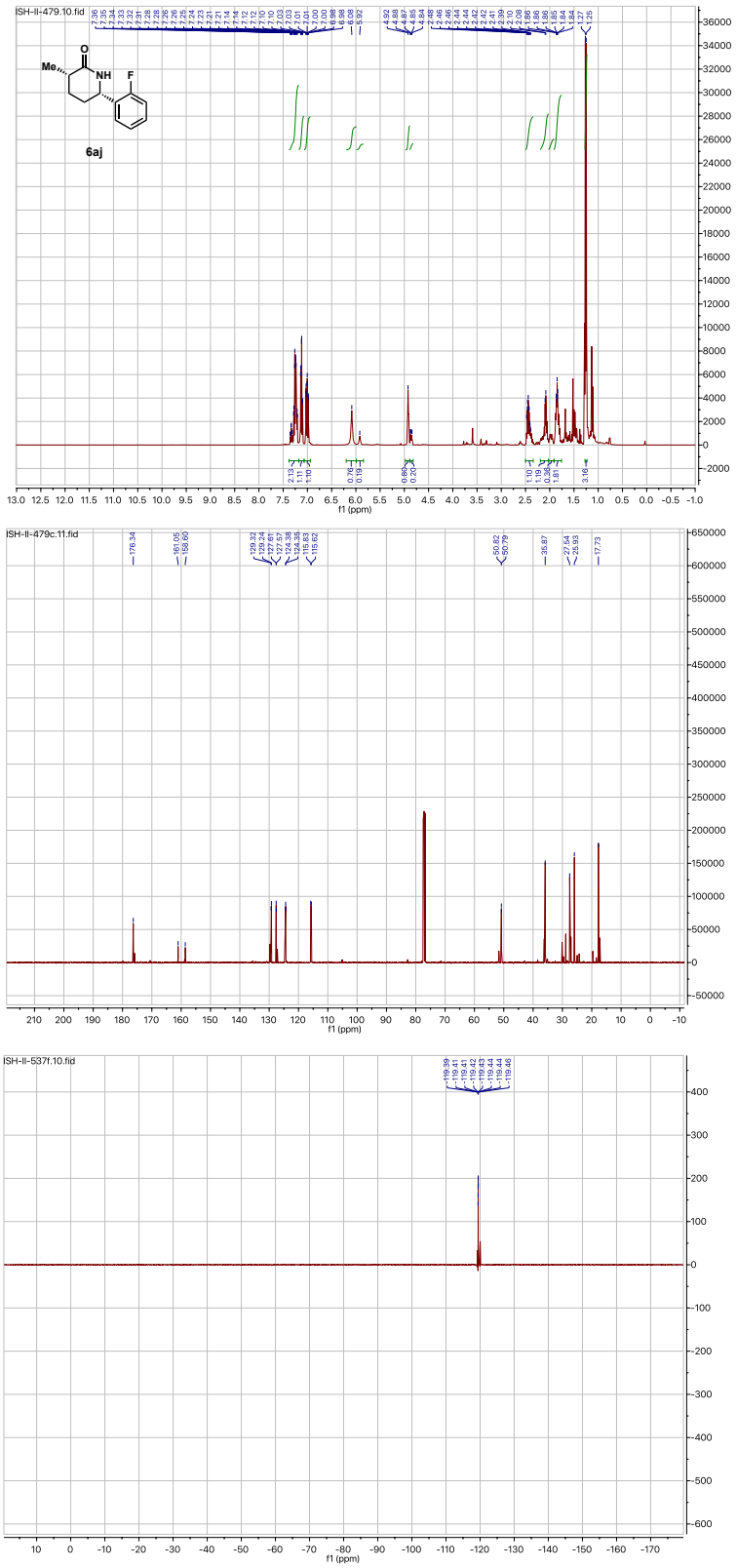

Figure 4.70: 6aj NMR spectra.

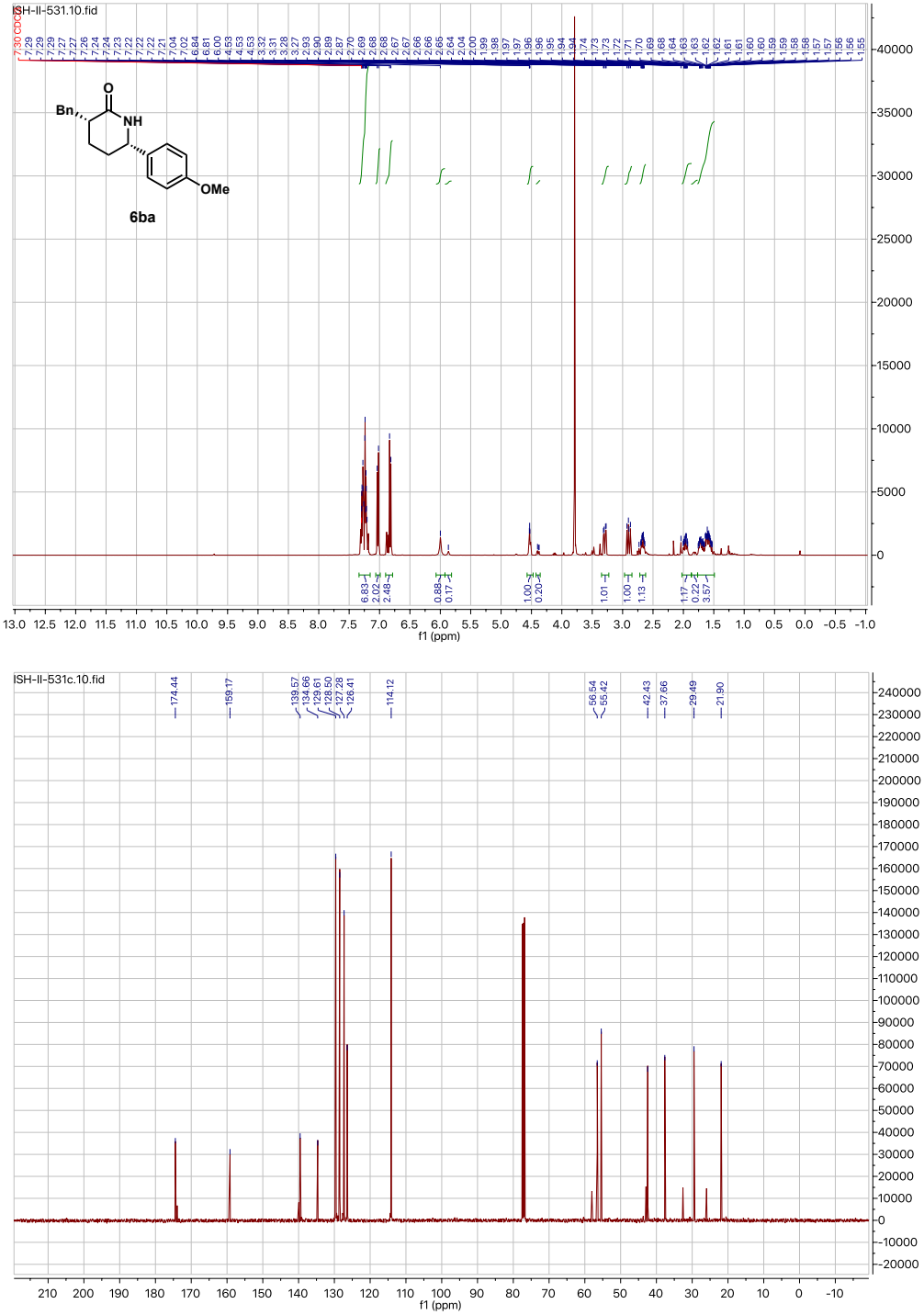

Figure 4.71: 6ba NMR spectra.

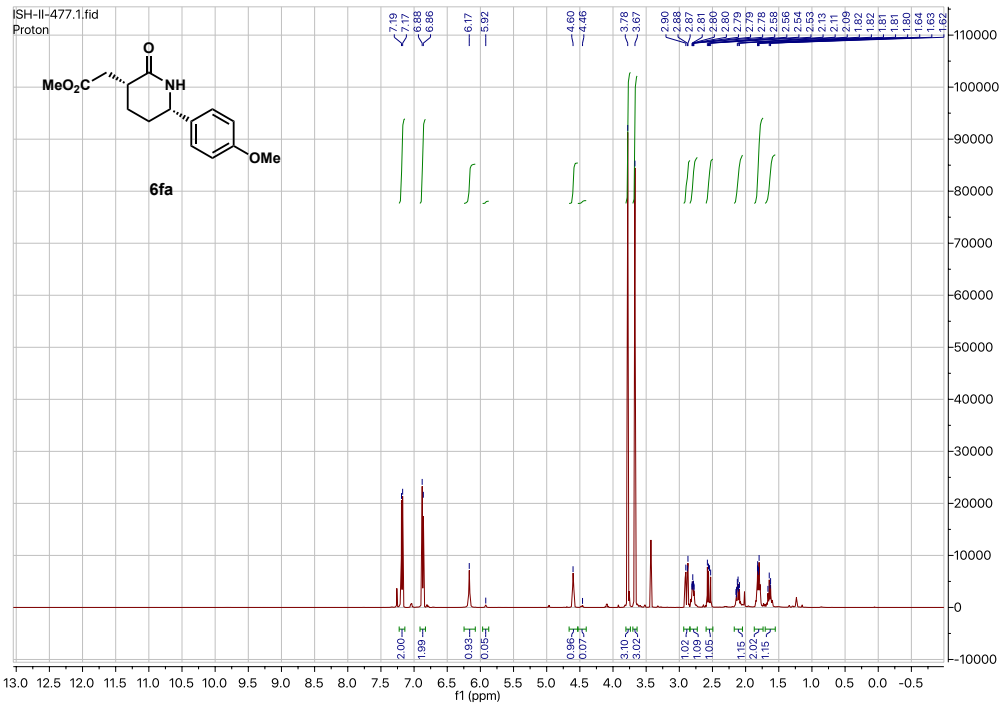

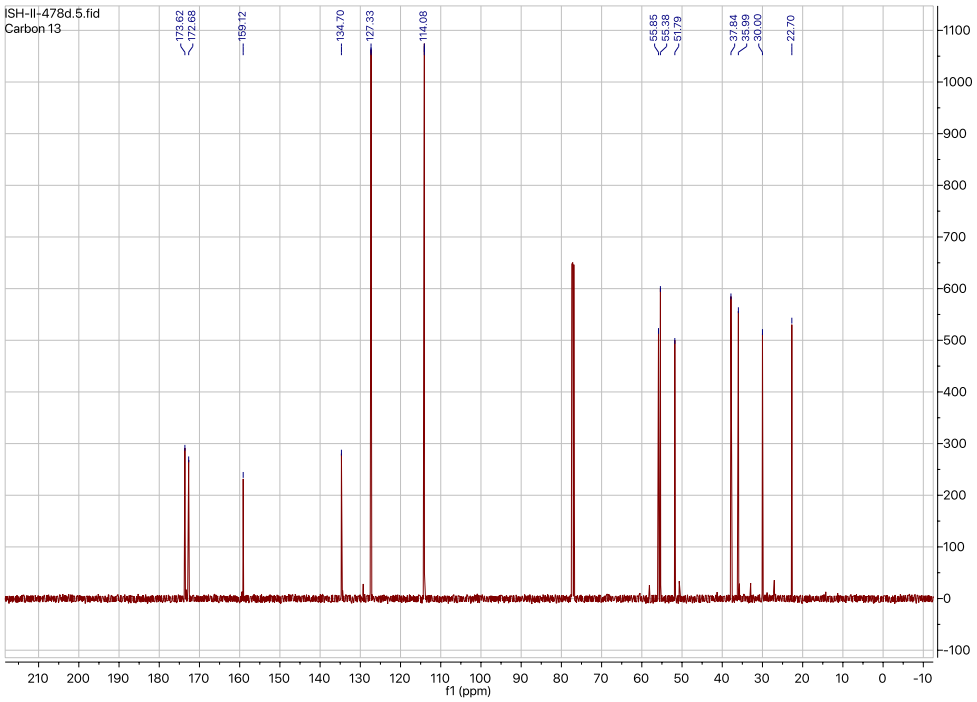

Figure 4.72: 6fa NMR spectra.

4.4.9 Control experiments and mechanistic studies

An experiment was conducted in which deuterated acrylamide d-2a was coupled with 4-methoxystyrene (3a) under enzymatic/aqueous conditions. After a 24 h reaction time (ca. 50% conversion), 32% proton incorporation into d-2a at the C-H bond *cis* to the amide was observed. This result suggest that the C-H activation step is reversible. Additionally, this result suggests that the charge effect from the mSav protein scaffold is not due to concerted metalation deprotonation (CMD) acceleration.

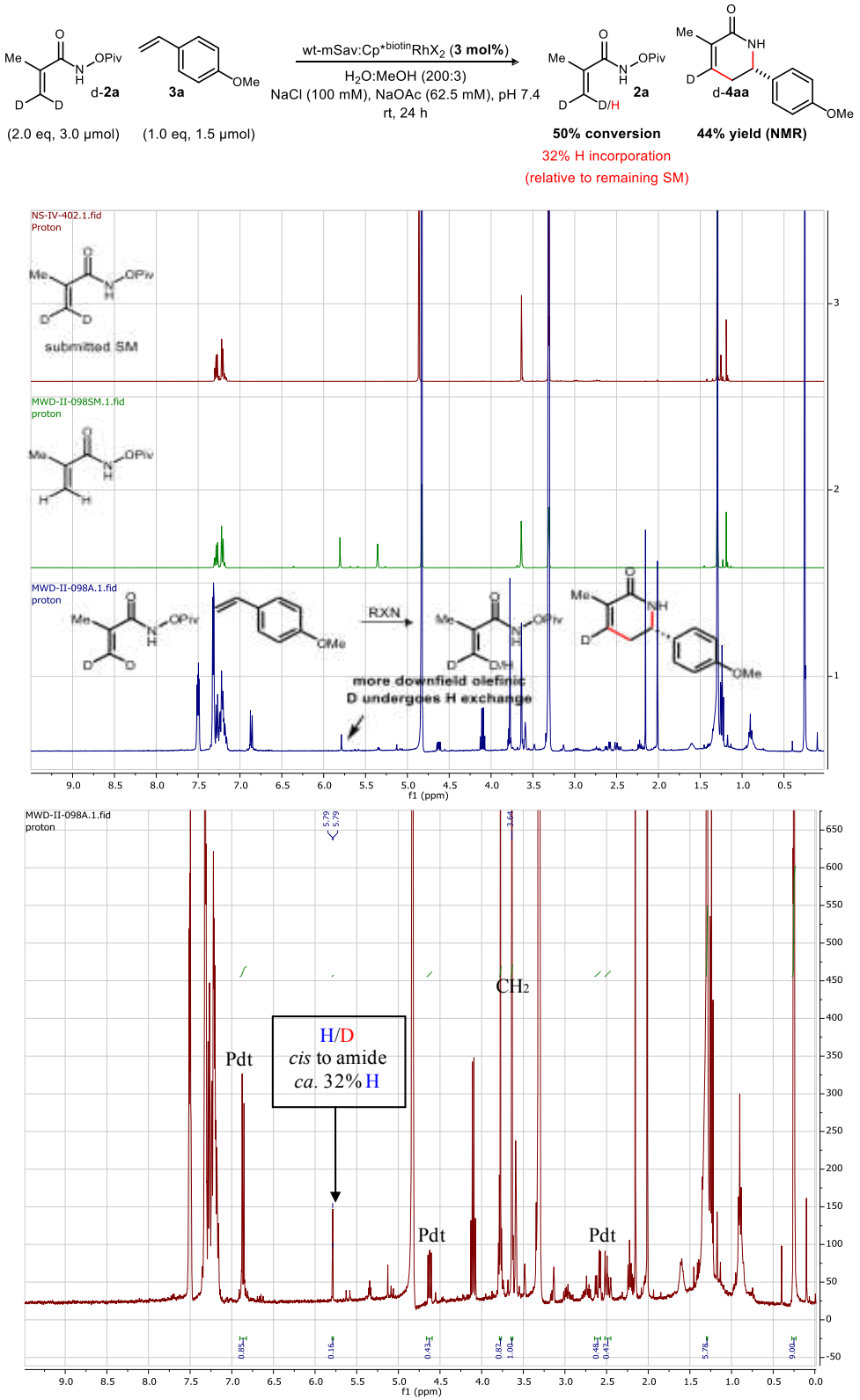

Figure 4.73: Deuterium labeling experiment.

4.4.10 Relative rates of bound and unbound catalyst

The following stock solutions were prepared:

Enzyme in H_2O - (600 μM)

$[Cp^{*biotin}RhCl_2]_2$ in DMSO - (20 mg in 177 μL, 0.1 M)

Methyl acrylamide in MeOH - (0.01 g in 54 μL, 1M)

4-Methoxystyrene in MeOH - (10 μL of styrene in 75 μL 1 M)

Acetate Buffer (100 mM NaCl and 100 mM NaOAc)

Stir bars were added to 7 vials. The first two vials were charged with 1.5 μL of methyl acrylamide solution while the next five were charged with 0.75 μl. The first two vials were then charged with .75 μl of the styrene solution and the next five were charged with .375 μl of the styrene solution. Next, the first two vials were charged with 62.5 μl of acetate buffer and the next five vials were charged with 31.25 μl of acetate buffer. A rhodium solution was added to each vial in various amounts (0 μl, 0.1125 μl, 0.1125 μl, 0.225 μl, 0.335 μl, 0.45 μl, 0.5625 μl, all at 0.1 M). The first two vials were charged with 37.5 μl of the enzyme and the next five were charged with 18.75 μl of metalloenzyme solutions. The vials were sealed and allowed to stir. After 72 h the vials were diluted with ethyl acetate and allowed to stir for an additional 10 minutes. The ethyl acetate phase was transferred to vial and the er was determined by chiral HPLC.

The data was fitted to the following equation:

$$\%(R)_{calculated} = \frac{k_{bound} \cdot \mu_{bound} \cdot \%(R)_{bound} + k_{free} \cdot \mu_{free} \cdot \%(R)_{free}}{k_{bound} \cdot \mu_{bound} + k_{free} \cdot \mu_{free}} \tag{4.1}$$

Where:

k_{bound} = rate constant for reaction with protein

k_{free} = rate constant for reaction without protein

μ_{bound} = % of bound complexes

μ_{free} = % of free complexes

$\%(R)_{bound}$ = % (R) produced by bound complex

$\%(R)_{free}$ = % (R) produced by free complex

The calculated curves represent the percentage major enantiomer if the rate of Rh(III) mSav catalysis is equal to the rate of catalysis due to the cofactor alone.

Equivalents of metal monomer	Observed Major enantiomer
1	0.954
2	0.94775
3	0.93541
5	0.89260
7	0.86253
9	0.83676
11	0.81270

R^2=.9779

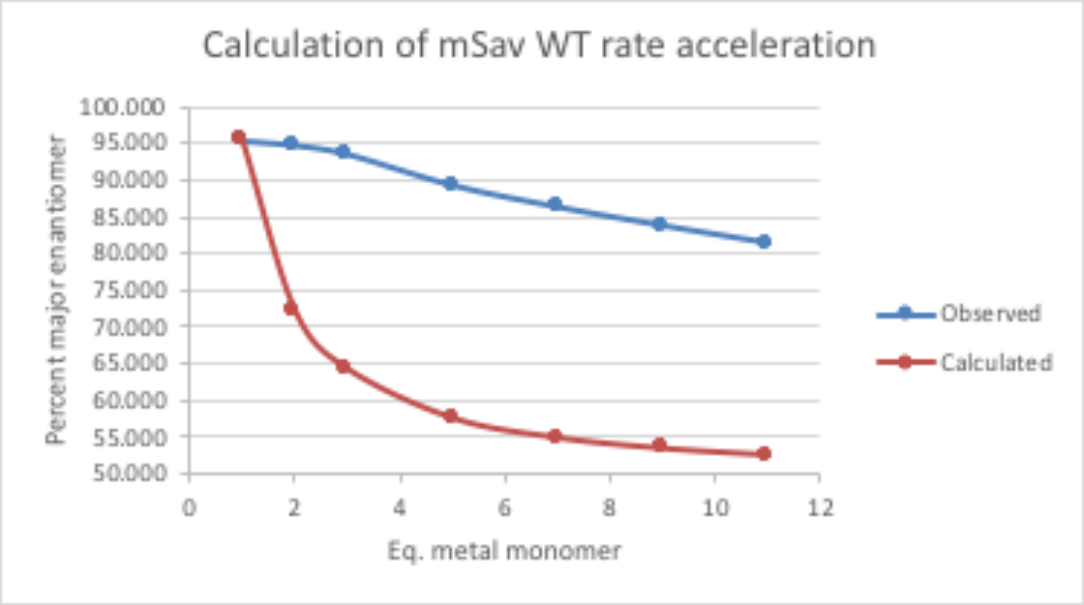

Figure 4.74: Relative rate with WT monomeric streptavidin catalyst.

Equiv of metal monomer	Observed Major enantiomer
1	0.95893
2	0.95595
3	0.94991
5	0.92922
7	0.91085
9	0.88638
11	0.86724

R^2=.9796

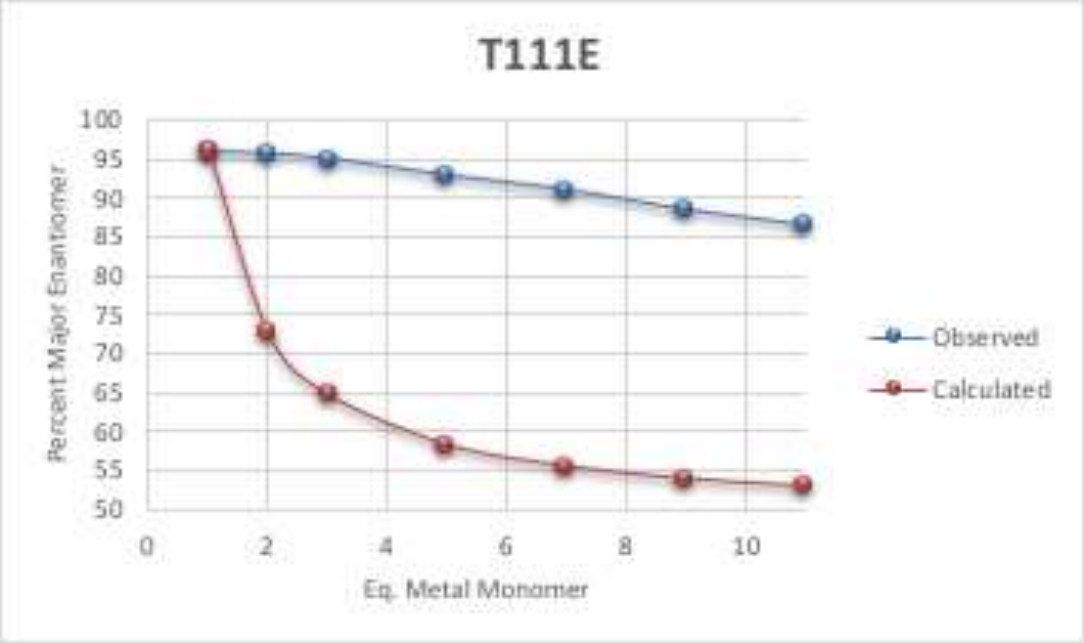

Figure 4.75: Relative rate with T111E monomeric streptavidin catalyst.

Equiv of metal monomer	Observed Major enantiomer
1	0.97138
2	0.96728
3	0.96449
5	0.94618
7	0.93353
9	0.90023
11	0.90932

R^2=.9781

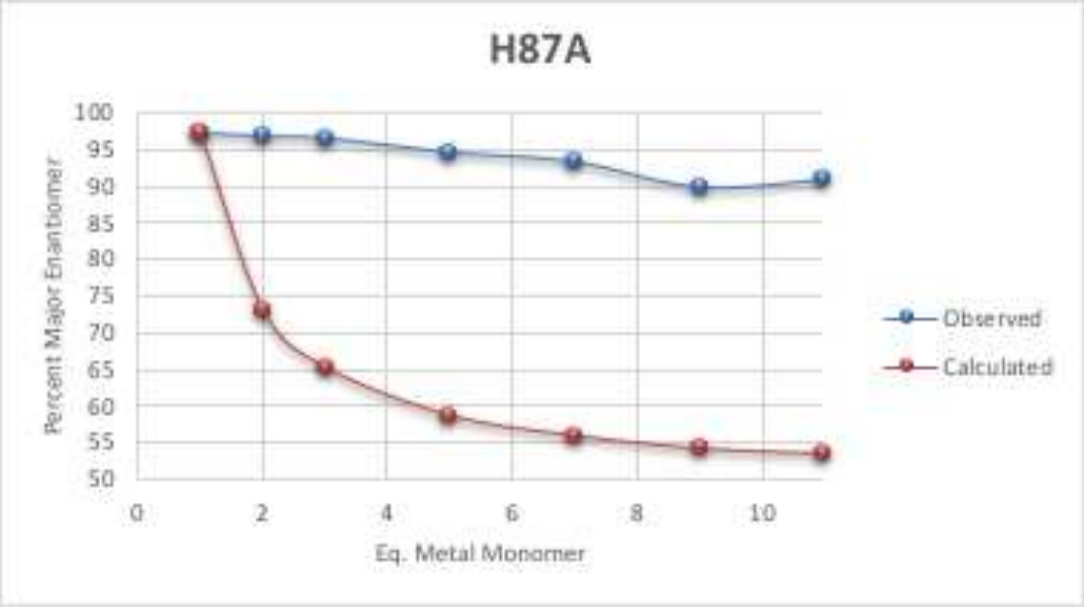

Figure 4.76: Relative rate with H87A monomeric streptavidin catalyst.

Equiv of metal monomer	Observed Major enantiomer
1	0.96897
2	0.94387
3	0.92925
5	0.90037
7	0.86095
9	0.83462
11	0.8262

R^2=.9847

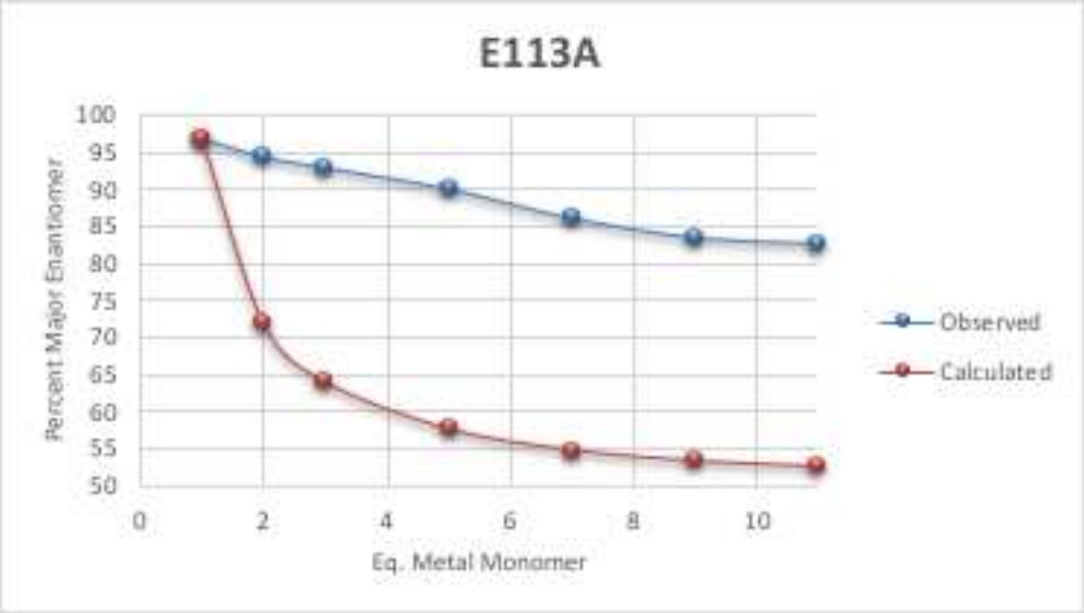

Figure 4.77: Relative rate with E113A monomeric streptavidin catalyst.

Equiv of metal monomer	Observed Major enantiomer
1	0.80647
2	0.77448
3	0.74435
5	0.67515
7	0.63061
9	0.58994
11	0.54548

R^2=.9991

Figure 4.78: Relative rate with Y112A monomeric streptavidin catalyst.

4.4.11 Preparation of artificial metalloenzyme

Protein production and purification:

MBP-mSav was expressed from plasmid pET-MBP-mSav purchased from addgene (plasmid #52319). Plasmid was transformed into BL21 (DE3) *E. coli* for protein production. An overnight culture was grown in LB containing kanamycin at 37 °C shaking at 200 RPM and used to inoculate 1 L (x8) of LB containing kanamycin at 37 °C shaking at 200 RPM for 3.5 hrs to an OD_{600} of 0.6-0.9. Culture was then induced with IPTG (final concentration of 1 mM) and brought to 20 °C shaking at 200 RPM overnight. Cells were harvested by centrifugation (5000 RPM for 10 min

at 4 °C) and resuspended in acetate glycerol lysis buffer (10 mL, 25 mM sodium acetate, 100 mM sodium chloride, 10% glycerol, 0.2% Triton-X-100, pH 7.4) with a protease inhibitor tablet (1/2 tablet, Roche cOmplete ULTRA Tables, Mini, EDTA free, EASYpack). Cell suspension was subject to one freeze-thaw cycle at -20 °C followed by sonication (6 min cycle, 50% amplitude, over ice). Cell lysate was cleared by centrifugation (9500 RPM for 20 min at 4 °C) and the supernatant was incubated with Ni-NTA agarose resin (2 mL) rotating overnight at 4 °C. The resin was collected by centrifugation (4750 RPM for 10 min at 4 °C) and washed with acetate wash buffer (50 mL, 25 mM sodium acetate, 100 mM sodium chloride, 50 mM imidazole, pH 7.4). Protein was then eluted with acetate elution buffer (12 mL, 25 mM sodium acetate, 100 mM sodium chloride, 400 mM imidazole, pH 7.4) and dialyzed in acetate buffer (2 L, 25 mM sodium acetate, 100 mM sodium chloride, pH 7.4) overnight. Purified protein was then observed by SDS-PAGE.

Protein cleavage and re-purification:

Purified MBP-mSav was then subjected to a TEV protease cleavage. TEV protease was expressed from plasmid pRK793 purchased from addgene (plasmid #8827). An overnight culture was grown in LB containing chloramphenicol and carbenicillin at 37 °C shaking at 200 RPM and used to inoculate 1 L (x2) of LB containing chloramphenicol and carbenicillin at 37 °C shaking at 200 RPM for 3 hrs to an OD_{600} of ≈0.5. Culture was then induced with IPTG (final concentration of 1 mM) and brought to 30 °C shaking at 200 RPM overnight. Cells were harvested by centrifugation (5000 RPM for 10 min at 4 °C) and resuspended in acetate glycerol lysis buffer (10 mL, 25 mM sodium acetate, 100 mM sodium chloride, 10% glycerol, 0.2% Triton-X-100, pH 7.4) with a protease inhibitor tablet (1/2 tablet, Roche cOmplete ULTRA Tables, Mini, EDTA free, EASYpack). Cell suspension was subject to one freeze-thaw cycle at -20 °C followed by sonication (2 min cycle, 50% amplitude, over ice). Cell lysate was cleared by centrifugation (9500 RPM for 20 min at 4 °C) and the supernatant was incubated with Ni-NTA agarose resin (1 mL) rotating for 30 min at 4 °C. The resin was collected by centrifugation (4750 RPM for 10 min at 4 °C) and washed with acetate wash buffer (50 mL, 25 mM sodium acetate, 100 mM sodium chloride, 50 mM imida-

zole, pH 7.4). Protein was then eluted with acetate elution buffer (12 mL, 25 mM sodium acetate, 100 mM sodium chloride, 400 mM imidazole, pH 7.4) and dialyzed in acetate buffer (2 L, 25 mM sodium acetate, 100 mM sodium chloride, pH 7.4) overnight. Purified protein was then observed by SDS-PAGE.

Purified TEV protease was then added to purified MBP-mSav (100 mg protein to 1 mg protease) and rotated for 48 hrs at 4 °C. Ni-NTA resin was then added to cleavage mixture and rotated for ≈12 hrs at 4 °C. Supernatant was separated from the resin. Cleaved and re-purified protein was observed by SDS-PAGE.

Metalloenzyme preparation:

The metalloenzyme was prepared by incubating purified mSav with $Cp^{*biotin}Rh$ (30uM protein:60uM biotin) in acetate buffer at RT rotating overnight. Mixtures were then centrifuged to eliminate any precipitation (14000 RPM, 10 min) and transferred to a 10 kDa MWCO ultracentrifugal filter unit for several washes with acetate buffer. Protein solution will now have a yellowish tint due to binding of Rh.

4.4.12 Protein sequences

mSav –

GAEAGITGTWYNQHGSTFTVTAGADGNLTGQYENRAQGTGCQNSPYTLTGRYNGTKL
EWRVEWNNSTENCHSRTEWRGQYQGGAEARINTQWNLTYEGGSGPATEQGQDTFTKVKP
SAASGSDYKDDDDK

mSav H87A –

GAEAGITGTWYNQHGSTFTVTAGADGNLTGQYENRAQGTGCQNSPYTLTGRYNGTKL
EWRVEWNNSTENCASRTEWRGQYQGGAEARINTQWNLTYEGGSGPATEQGQDTFTKVKP
SAASGSDYKDDDDK

mSav T111E –

GAEAGITGTWYNQHGSTFTVTAGADGNLTGQYENRAQGTGCQNSPYTLTGRYNGTKL EWRVEWNNSTENCHSRTEWRGQYQGGAEARINTQWNLEYEGGSGPATEQGQDTFTKVKP SAASGSDYKDDDDK

mSav Y112A –

GAEAGITGTWYNQHGSTFTVTAGADGNLTGQYENRAQGTGCQNSPYTLTGRYNGTKL EWRVEWNNSTENCHSRTEWRGQYQGGAEARINTQWNLTAEGGSGPATEQGQDTFTKVKP SAASGSDYKDDDDK

mSav E113A –

GAEAGITGTWYNQHGSTFTVTAGADGNLTGQYENRAQGTGCQNSPYTLTGRYNGTKL EWRVEWNNSTENCHSRTEWRGQYQGGAEARINTQWNLTYAGGSGPATEQGQDTFTKVKP SAASGSDYKDDDDK

4.4.13 Protein mass spectrometry analysis (TOFMS)

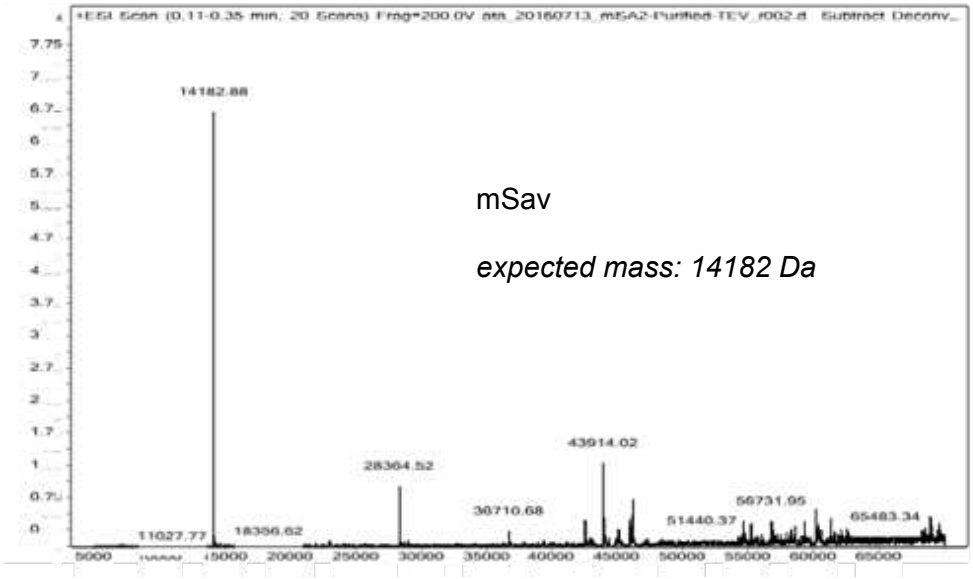

Figure 4.79: WT monomeric streptavidin mass spectrometry data.

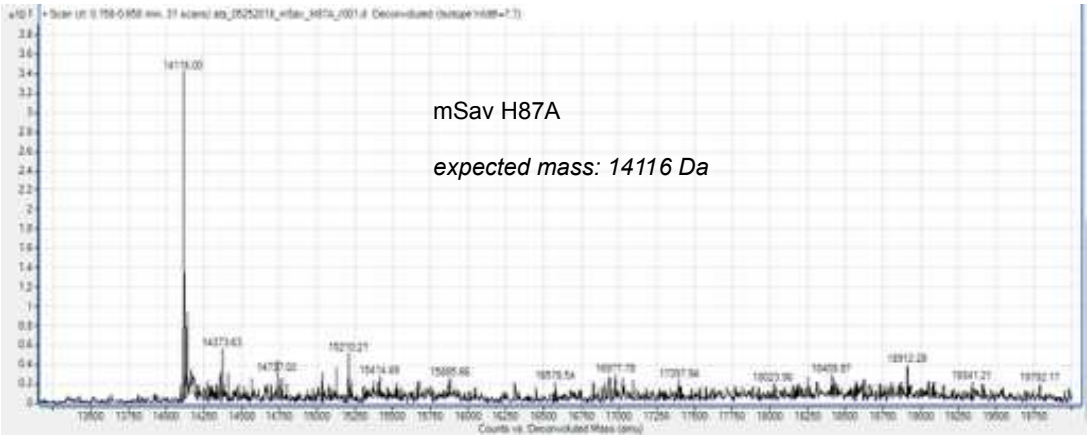

Figure 4.80: H87A monomeric streptavidin mass spectrometry data.

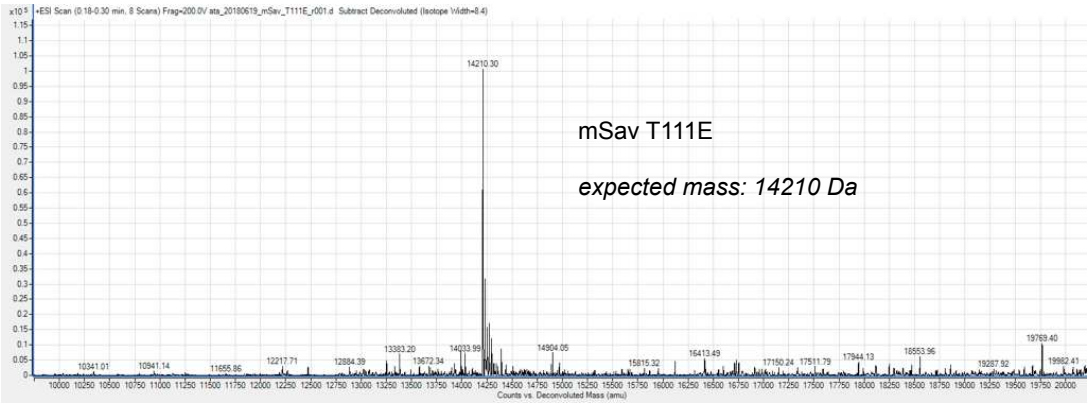

Figure 4.81: T111E monomeric streptavidin mass spectrometry data.

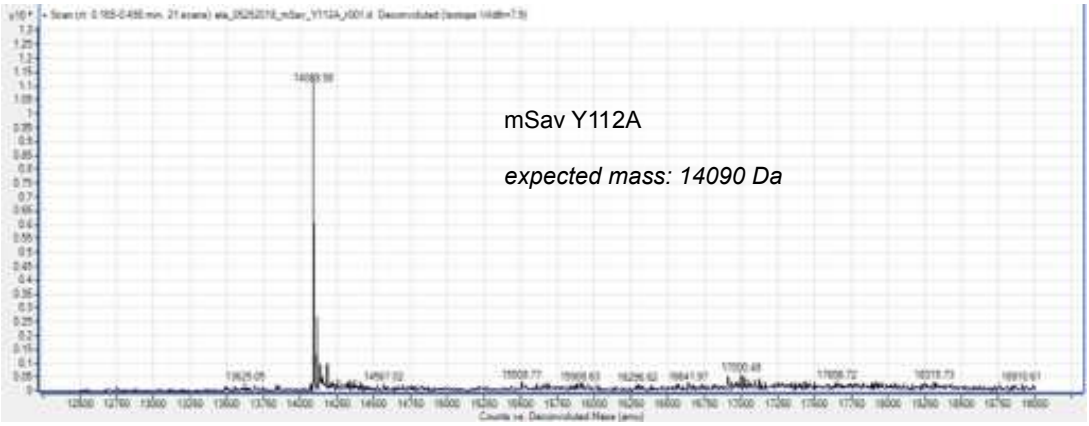

Figure 4.82: Y112A monomeric streptavidin mass spectrometry data.

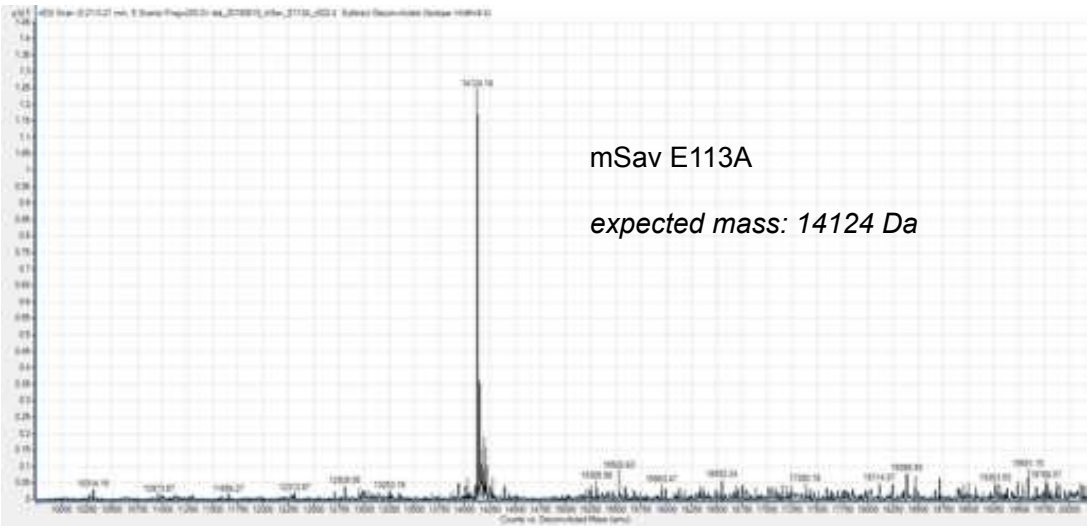

Figure 4.83: E113A monomeric streptavidin mass spectrometry data.

4.4.14 Protein gel

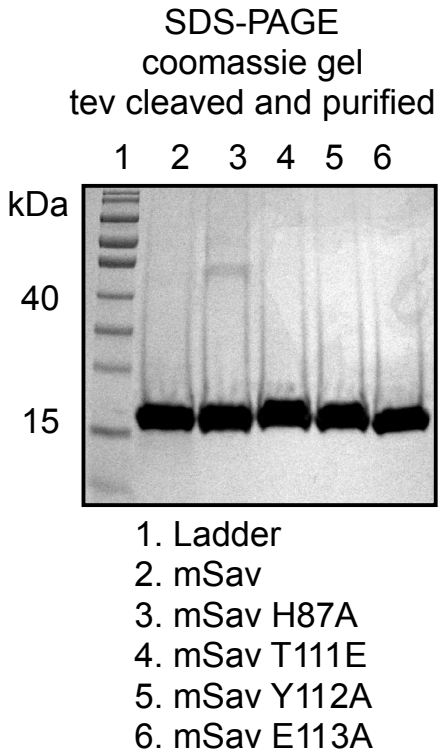

Figure 4.84: SDS-PAGE coomassie gel tev cleaved and purified monomeric streptavidin mutants.

4.4.15 Biotin binding ELISA

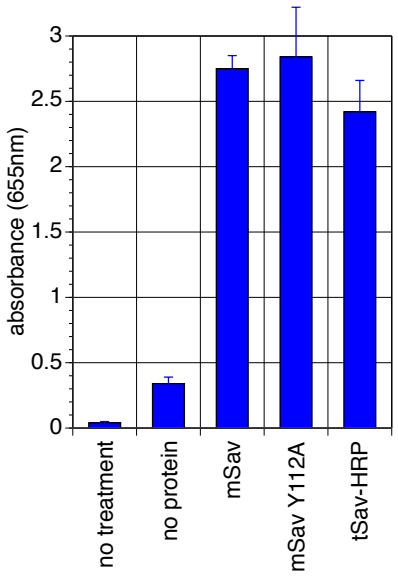

Figure 4.85: Biotin binding ELISA.

4.4.16 Protein data bank

mSav – 4JNJ

tSav – 3RY1

4.4.17 Calculation of initial rates and relative rates

Acrylamide coupling reactions were setup according to the general procedure (section 4.4.6). Varying amounts of acrylamide (1 M in MeOH) and styrene (1 M in MeOH) were added in order to vary substrate concentration and NMR yields were used to calculate reaction velocities. Initial reaction rates were obtained by running the reaction for six hours.

.0045 M		
Mutant	**Initial Rxn Velocity/Rate (umol/hr)**	**Relative rate**
WT	1.50E-02	14285.71
H87A	7.20E-02	68571.43
T111E	4.50E-02	42857.14
E113A	3.63E-02	34609.52
Y112A	7.50E-04	714.29
biot-Rh	1.05E-06	1.00

Figure 4.86: Initial and relative rate calculations at 0.0045M.

.0075 M		
Mutant	**Initial Rxn Velocity/Rate (umol/hr)**	**Relative rate**
WT	4.38E-02	4.95
H87A	1.15E-01	13.01
T111E	8.75E-02	9.90
E113A	6.61E-02	7.48
Y112A	5.00E-03	0.57
biot-Rh	8.84E-03	1.00

Figure 4.87: Initial and relative rate calculations at 0.0075M.

.0105 M		
Mutant	**Initial Rxn Velocity/Rate (umol/hr)**	**Relative rate**
WT	7.00E-02	6.73
H87A	1.50E-01	14.42
T111E	1.26E-01	12.12
E113A	9.503E-02	9.14
Y112A	1.05E-02	1.01
biot-Rh	1.04E-02	1.00

Figure 4.88: Initial and relative rate calculations at 0.0105M.

.0125 M		
Mutant	**Initial Rxn Velocity/Rate (umol/hr)**	**Relative rate**
WT	7.50E-02	6.10
H87A	1.50E-01	12.20
T111E	1.46E-01	11.87
E113A	1.10E-01	8.92
Y112A	1.67E-02	1.36
biot-Rh	1.23E-02	1.00

Figure 4.89: Initial and relative rate calculations at 0.0125M.

.0145 M		
Mutant	**Initial Rxn Velocity/Rate (umol/hr)**	**Relative rate**
WT	7.73E-02	6.72
H87A	1.45E-01	12.61
T111E	1.69E-01	14.70
E113A	1.16E-01	10.12
Y112A	2.42E-02	2.10
biot-Rh	1.15E-02	1.00

Figure 4.90: Initial and relative rate calculations at 0.0145M.

References

[1] Gestur Vidarsson, Gillian Dekkers, and Theo Rispens. Igg subclasses and allotypes: from structure to effector functions. *Frontiers in immunology*, 5:520, 2014.

[2] Hongcheng Liu and Kimberly May. Disulfide bond structures of igg molecules: structural variations, chemical modifications and possible impacts to stability and biological function. In *MAbs*, volume 4, pages 17–23. Taylor & Francis, 2012.

[3] Takuo Suzuki, Akiko Ishii-Watabe, Minoru Tada, Tetsu Kobayashi, Toshie Kanayasu-Toyoda, Toru Kawanishi, and Teruhide Yamaguchi. Importance of neonatal fcr in regulating the serum half-life of therapeutic proteins containing the fc domain of human igg1: a comparative study of the affinity of monoclonal antibodies and fc-fusion proteins to human neonatal fcr. *The journal of immunology*, page ji_0903296, 2010.

[4] Nancy A Goebl, Clifford M Babbey, Amita Datta-Mannan, Derrick R Witcher, Victor J Wroblewski, and Kenneth W Dunn. Neonatal fc receptor mediates internalization of fc in transfected human endothelial cells. *Molecular biology of the cell*, 19(12):5490–5505, 2008.

[5] Derry C Roopenian and Shreeram Akilesh. Fcrn: the neonatal fc receptor comes of age. *Nature reviews immunology*, 7(9):715, 2007.

[6] Wilhelm P Burmeister, Louis N Gastinel, Neil E Simister, Michael L Blum, and Pamela J Bjorkman. Crystal structure at 2.2 å resolution of the mhc-related neonatal fc receptor. *Nature*, 372(6504):336, 1994.

[7] Wilhelm P Burmeister, Andrew H Huber, and Pamela J Bjorkman. Crystal structure of the complex of rat neonatal fc receptor with fc. *Nature*, 372(6504):379, 1994.

[8] Jeffrey V Ravetch and Raphael A Clynes. Divergent roles for fc receptors and complement in vivo. *Annual review of immunology*, 16(1):421–432, 1998.

[9] Ursula Jördis Eva Seidel, Patrick Schlegel, and Peter Lang. Natural killer cell mediated antibody-dependent cellular cytotoxicity in tumor immunotherapy with therapeutic antibodies. *Frontiers in immunology*, 4:76, 2013.

[10] N Prang, S Preithner, K Brischwein, A Wöppel, J Müller, C Steiger, M Peters, PA Baeuerle, and AJ da Silva. Cellular and complement-dependent cytotoxicity of ep-cam-specific monoclonal antibody mt201 against breast cancer cell lines. *British journal of cancer*, 92(2):342, 2005.

[11] Mark J Walport. Complement. *New England Journal of Medicine*, 344(15):1140–1144, 2001.

[12] Sergei Radaev, Shawn Motyka, Wolf-Herman Fridman, Catherine Sautes-Fridman, and Peter D Sun. The structure of a human type iii fcγ receptor in complex with fc. *Journal of Biological Chemistry*, 276(19):16469–16477, 2001.

[13] Falk Nimmerjahn and Jeffrey V Ravetch. Fcγ receptors as regulators of immune responses. *Nature Reviews Immunology*, 8(1):34, 2008.

[14] Puja Sapra and Boris Shor. Monoclonal antibody-based therapies in cancer: advances and challenges. *Pharmacology & therapeutics*, 138(3):452–469, 2013.

[15] Haritha Samaranayake, Thomas Wirth, Diana Schenkwein, Jani K Räty, and Seppo Ylä-Herttuala. Challenges in monoclonal antibody-based therapies. *Annals of medicine*, 41(5):322–331, 2009.

[16] John Löfblom, Fredrik Y Frejd, and Stefan Ståhl. Non-immunoglobulin based protein scaffolds. *Current opinion in biotechnology*, 22(6):843–848, 2011.

[17] Adam P Silverman, Mihalis S Kariolis, and Jennifer R Cochran. Cystine-knot peptides engineered with specificities for αiibβ3 or αiibβ3 and αvβ3 integrins are potent inhibitors of platelet aggregation. *Journal of Molecular Recognition*, 24(1):127–135, 2011.

[18] Michaela Gebauer and Arne Skerra. Engineered protein scaffolds as next-generation antibody therapeutics. *Current opinion in chemical biology*, 13(3):245–255, 2009.

[19] Katja Škrlec, Borut Štrukelj, and Aleš Berlec. Non-immunoglobulin scaffolds: a focus on their targets. *Trends in biotechnology*, 33(7):408–418, 2015.

[20] H Kaspar Binz, Patrick Amstutz, and Andreas Plückthun. Engineering novel binding proteins from nonimmunoglobulin domains. *Nature biotechnology*, 23(10):1257, 2005.

[21] Philipp Holliger and Peter J Hudson. Engineered antibody fragments and the rise of single domains. *Nature biotechnology*, 23(9):1126, 2005.

[22] Takashi Yokota, Diane E Milenic, Marc Whitlow, and Jeffrey Schlom. Rapid tumor penetration of a single-chain fv and comparison with other immunoglobulin forms. *Cancer research*, 52(12):3402–3408, 1992.

[23] Rakesh K Jain. Physiological barriers to delivery of monoclonal antibodies and other macromolecules in tumors. *Cancer research*, 50(3 Supplement):814s–819s, 1990.

[24] Christoph Rader. Overview on concepts and applications of fab antibody fragments. *Current protocols in protein science*, 55(1):6–9, 2009.

[25] Marc Better, C Paul Chang, Randy R Robinson, and Arnold H Horwitz. Escherichia coli secretion of an active chimeric antibody fragment. *Science*, 240(4855):1041–1043, 1988.

[26] Aaron L Nelson and Janice M Reichert. Development trends for therapeutic antibody fragments. *Nature biotechnology*, 27(4):331, 2009.

[27] Aaron L Nelson. Antibody fragments: hope and hype. In *MAbs*, volume 2, pages 77–83. Taylor & Francis, 2010.

[28] Joycelyn Entwistle, Jennifer G Brown, Shilpa Chooniedass, Jeannick Cizeau, and Glen C MacDonald. Preclinical evaluation of vb6-845: an anti-epcam immunotoxin with reduced

immunogenic potential. *Cancer Biotherapy and Radiopharmaceuticals*, 27(9):582–592, 2012.

[29] Tim Eisen, Gunnar Hedlund, Göran Forsberg, and Robert Hawkins. Naptumomab estafenatox: targeted immunotherapy with a novel immunotoxin. *Current oncology reports*, 16(2):370, 2014.

[30] James D Douketis, Jeffrey S Ginsberg, Susan Haley, Jim Julian, Miriam Dwyer, Mark Levine, Paul R Eisenberg, Richard Smart, Wendy Tsui, Richard H White, et al. Accuracy and safety of 99mtc-labeled anti-d-dimer (di-80b3) fab'fragments (thromboview®) in the diagnosis of deep vein thrombosis: A phase ii study. *Thrombosis research*, 130(3):381–389, 2012.

[31] Tatsuya Morisaki, Kenneth Lyon, Keith F DeLuca, Jennifer G DeLuca, Brian P English, Zhengjian Zhang, Luke D Lavis, Jonathan B Grimm, Sarada Viswanathan, Loren L Looger, et al. Real-time quantification of single rna translation dynamics in living cells. *Science*, 352(6292):1425–1429, 2016.

[32] James S Huston, Douglas Levinson, Meredith Mudgett-Hunter, Mei-Sheng Tai, Jiří Novotnỳ, Michael N Margolies, Richard J Ridge, Robert E Bruccoleri, Edgar Haber, and Roberto Crea. Protein engineering of antibody binding sites: recovery of specific activity in an anti-digoxin single-chain fv analogue produced in escherichia coli. *Proceedings of the National Academy of Sciences*, 85(16):5879–5883, 1988.

[33] Cristina FRO Matos, Colin Robinson, Heli I Alanen, Piotr Prus, Yuko Uchida, Lloyd W Ruddock, Robert B Freedman, and Eli Keshavarz-Moore. Efficient export of prefolded, disulfide-bonded recombinant proteins to the periplasm by the tat pathway in escherichia coli cydisco strains. *Biotechnology progress*, 30(2):281–290, 2014.

[34] Nina E Weisser and J Christopher Hall. Applications of single-chain variable fragment antibodies in therapeutics and diagnostics. *Biotechnology advances*, 27(4):502–520, 2009.

[35] Yuko Sato, Masanori Mukai, Jun Ueda, Michiko Muraki, Timothy J Stasevich, Naoki Horikoshi, Tomoya Kujirai, Hiroaki Kita, Taisuke Kimura, Seiji Hira, et al. Genetically encoded system to track histone modification in vivo. *Scientific reports*, 3:2436, 2013.

[36] Marvin E Tanenbaum, Luke A Gilbert, Lei S Qi, Jonathan S Weissman, and Ronald D Vale. A protein-tagging system for signal amplification in gene expression and fluorescence imaging. *Cell*, 159(3):635–646, 2014.

[37] Shi-zhen Hu, Louise Shively, Andrew Raubitschek, Mark Sherman, Lawrence E Williams, Jeffrey YC Wong, John E Shively, and Anna M Wu. Minibody: a novel engineered anti-carcinoembryonic antigen antibody fragment (single-chain fv-ch3) which exhibits rapid, high-level targeting of xenografts. *Cancer research*, 56(13):3055–3061, 1996.

[38] Lillian S Shahied, Yong Tang, R Katherine Alpaugh, Robert Somer, Dana Greenspon, and Louis M Weiner. Bispecific minibodies targeting her2/neu and cd16 exhibit improved tumor lysis when placed in a divalent tumor antigen-binding format. *Journal of Biological Chemistry*, 2004.

[39] Eric J Lepin, Jeffrey V Leyton, Yu Zhou, Tove Olafsen, Felix B Salazar, Katelyn E McCabe, Scott Hahm, James D Marks, Robert E Reiter, and Anna M Wu. An affinity matured minibody for pet imaging of prostate stem cell antigen (psca)-expressing tumors. *European journal of nuclear medicine and molecular imaging*, 37(8):1529–1538, 2010.

[40] Scott M Knowles, Kirstin A Zettlitz, Richard Tavaré, Matthew M Rochefort, Felix B Salazar, David B Stout, Paul J Yazaki, Robert E Reiter, and Anna M Wu. Quantitative immunopet of prostate cancer xenografts with 89zr-and 124i-labeled anti-psca a11 minibody. *Journal of nuclear medicine: official publication, Society of Nuclear Medicine*, 55(3):452, 2014.

[41] Thomas Han, Ussama M Abdel-Motal, De-Kuan Chang, Jianhua Sui, Asli Muvaffak, James Campbell, Quan Zhu, Thomas S Kupper, and Wayne A Marasco. Human anti-ccr4 minibody gene transfer for the treatment of cutaneous t-cell lymphoma. *PloS one*, 7(9):e44455, 2012.

[42] Yeon Kyung Lee, Keun Sik Kim, Jung Seok Kim, Jin Ee Baek, Sang Il Park, Hwa Yeon Jeong, Sang Soon Yoon, Kyeong Cheon Jung, Hyung Geun Song, and Yong Serk Park. Leukemia-specific sirna delivery by immunonanoplexes consisting of anti-jl1 minibody conjugated to oligo-9 arg-peptides. *Molecules and cells*, 29(5):457–462, 2010.

[43] Ussama M Abdel-Motal, Phuong TN Sarkis, Thomas Han, Jeffery Pudney, Deborah J Anderson, Quan Zhu, and Wayne A Marasco. Anti-gp120 minibody gene transfer to female genital epithelial cells protects against hiv-1 virus challenge in vitro. *PloS one*, 6(10):e26473, 2011.

[44] Philipp Holliger, Terence Prospero, and Greg Winter. " diabodies": small bivalent and bispecific antibody fragments. *Proceedings of the National Academy of Sciences*, 90(14):6444–6448, 1993.

[45] Olga Perisic, Philip A Webb, Philipp Holliger, Greg Winter, and Roger L Williams. Crystal structure of a diabody, a bivalent antibody fragment. *Structure*, 2(12):1217–1226, 1994.

[46] Ruth Muchekehu, Dingguo Liu, Mark Horn, Lioudmila Campbell, Joselyn Del Rosario, Michael Bacica, Haim Moskowitz, Trina Osothprarop, Anouk Dirksen, Venkata Doppalapudi, et al. The effect of molecular weight, pk, and valency on tumor biodistribution and efficacy of antibody-based drugs. *Translational oncology*, 6(5):562–572, 2013.

[47] Aneta Todorovska, Rob C Roovers, Olan Dolezal, Alexander A Kortt, Hennie R Hoogenboom, and Peter J Hudson. Design and application of diabodies, triabodies and tetrabodies for cancer targeting. *Journal of immunological methods*, 248(1-2):47–66, 2001.

[48] Mark D Girgis, Vania Kenanova, Tove Olafsen, Katelyn E McCabe, Anna M Wu, and James S Tomlinson. Anti-ca19-9 diabody as a pet imaging probe for pancreas cancer. *Journal of Surgical Research*, 170(2):169–178, 2011.

[49] Katelyn E McCabe, Bin Liu, James D Marks, James S Tomlinson, Hong Wu, and Anna M Wu. An engineered cysteine-modified diabody for imaging activated leukocyte cell adhesion molecule (alcam)-positive tumors. *Molecular Imaging and Biology*, 14(3):336–347, 2012.

[50] Smitha Reddy, Calvin C Shaller, Mohan Doss, Irina Shchaveleva, James D Marks, Q Yu Jian, and Matthew K Robinson. Evaluation of the anti-her2 c6. 5 diabody as a pet radiotracer to monitor her2 status and predict response to trastuzumab treatment. *Clinical Cancer Research*, 17(6):1509–1520, 2011.

[51] Gregory P Adams, Calvin C Shaller, Ekaterina Dadachova, Heidi H Simmons, Eva M Horak, Abohawariat Tesfaye, Andres JP Klein-Szanto, James D Marks, Martin W Brechbiel, and Louis M Weiner. A single treatment of yttrium-90-labeled chx-a"–c6. 5 diabody inhibits the growth of established human tumor xenografts in immunodeficient mice. *Cancer research*, 64(17):6200–6206, 2004.

[52] Christina Ebbinghaus, Roberto Ronca, Manuela Kaspar, Dragan Grabulovski, Alexander Berndt, Hartwig Kosmehl, Luciano Zardi, and Dario Neri. Engineered vascular-targeting antibody-interferon-γ fusion protein for cancer therapy. *International journal of cancer*, 116(2):304–313, 2005.

[53] Tove Olafsen, Chia-wei Cheung, Paul J Yazaki, Lin Li, Gobalakrishnan Sundaresan, Sanjiv S Gambhir, Mark A Sherman, Lawrence E Williams, John E Shively, Andrew A Raubitschek, et al. Covalent disulfide-linked anti-cea diabody allows site-specific conjugation and radiolabeling for tumor targeting applications. *Protein Engineering Design and Selection*, 17(1):21–27, 2004.

[54] Mireille Dumoulin, Katja Conrath, Annemie Van Meirhaeghe, Filip Meersman, Karel Heremans, Leon GJ Frenken, Serge Muyldermans, Lode Wyns, and Andre Matagne. Single-domain antibody fragments with high conformational stability. *Protein Science*, 11(3):500–515, 2002.

[55] Coralie Pain, Janice Dumont, and Mireille Dumoulin. Camelid single-domain antibody fragments: Uses and prospects to investigate protein misfolding and aggregation, and to treat diseases associated with these phenomena. *Biochimie*, 111:82–106, 2015.

[56] Serge Muyldermans. Nanobodies: natural single-domain antibodies. *Annual review of biochemistry*, 82:775–797, 2013.

[57] Jonas Helma, M Cristina Cardoso, Serge Muyldermans, and Heinrich Leonhardt. Nanobodies and recombinant binders in cell biology. *J Cell Biol*, 209(5):633–644, 2015.

[58] Aroop Sircar, Kayode A Sanni, Jiye Shi, and Jeffrey J Gray. Analysis and modeling of the variable region of camelid single-domain antibodies. *The Journal of Immunology*, page 1100116, 2011.

[59] Erwin De Genst, Karen Silence, Klaas Decanniere, Katja Conrath, Remy Loris, Jörg Kinne, Serge Muyldermans, and Lode Wyns. Molecular basis for the preferential cleft recognition by dromedary heavy-chain antibodies. *Proceedings of the National Academy of Sciences*, 103(12):4586–4591, 2006.

[60] Carolina Gutierrez and Rachel Schiff. Her2: biology, detection, and clinical implications. *Archives of pathology & laboratory medicine*, 135(1):55–62, 2011.

[61] Min Yan, Maria Schwaederle, David Arguello, Sherri Z Millis, Zoran Gatalica, and Razelle Kurzrock. Her2 expression status in diverse cancers: review of results from 37,992 patients. *Cancer and Metastasis Reviews*, 34(1):157–164, 2015.

[62] Ilse Vaneycken, Nick Devoogdt, Naomi Van Gassen, Cécile Vincke, Catarina Xavier, Ulrich Wernery, Serge Muyldermans, Tony Lahoutte, and Vicky Caveliers. Preclinical screening of anti-her2 nanobodies for molecular imaging of breast cancer. *The FASEB Journal*, 25(7):2433–2446, 2011.

[63] Marta M Kijanka, Aram SA van Brussel, Elsken van der Wall, Willem PTM Mali, Paul J van Diest, Paul MP van Bergen en Henegouwen, and Sabrina Oliveira. Optical imaging of pre-invasive breast cancer with a combination of vhhs targeting caix and her2 increases contrast and facilitates tumour characterization. *EJNMMI research*, 6(1):14, 2016.

[64] Melissa A Gray, Ran N Tao, Sandra M DePorter, David A Spiegel, and Brian R McNaughton. A nanobody activation immunotherapeutic that selectively destroys her2-positive breast cancer cells. *ChemBioChem*, 17(2):155–158, 2016.

[65] Marek Pruszynski, Eftychia Koumarianou, Ganesan Vaidyanathan, Hilde Revets, Nick Devoogdt, Tony Lahoutte, and Michael R Zalutsky. Targeting breast carcinoma with radioiodinated anti-her2 nanobody. *Nuclear medicine and biology*, 40(1):52–59, 2013.

[66] K Karjalaninen and O Mäkelä. Concentrations of three hapten-binding immunoglobulins in pooled normal human serum. *European journal of immunology*, 6(2):88–93, 1976.

[67] FS Farah. Natural antibodies specific to the 2, 4-dinitrophenyl group. *Immunology*, 25(2):217, 1973.

[68] Christopher G Parker, Robert A Domaoal, Karen S Anderson, and David A Spiegel. An antibody-recruiting small molecule that targets hiv gp120. *Journal of the American Chemical Society*, 131(45):16392–16394, 2009.

[69] Patrick J McEnaney, Christopher G Parker, Andrew X Zhang, and David A Spiegel. Antibody-recruiting molecules: an emerging paradigm for engaging immune function in treating human disease. *ACS chemical biology*, 7(7):1139–1151, 2012.

[70] Ulrich Rothbauer, Kourosh Zolghadr, Sergei Tillib, Danny Nowak, Lothar Schermelleh, Anja Gahl, Natalija Backmann, Katja Conrath, Serge Muyldermans, M Cristina Cardoso, et al. Targeting and tracing antigens in live cells with fluorescent nanobodies. *Nature methods*, 3(11):887, 2006.

[71] Marta H Kubala, Oleksiy Kovtun, Kirill Alexandrov, and Brett M Collins. Structural and thermodynamic analysis of the gfp: Gfp-nanobody complex. *Protein Science*, 19(12):2389–2401, 2010.

[72] Axel Kirchhofer, Jonas Helma, Katrin Schmidthals, Carina Frauer, Sheng Cui, Annette Karcher, Mireille Pellis, Serge Muyldermans, Corella S Casas-Delucchi, M Cristina Cardoso, et al. Modulation of protein properties in living cells using nanobodies. *Nature structural & molecular biology*, 17(1):133, 2010.

[73] Virginia J Bruce, Monica Lopez-Islas, and Brian R McNaughton. Resurfaced cell-penetrating nanobodies: A potentially general scaffold for intracellularly targeted protein discovery. *Protein Science*, 25(6):1129–1137, 2016.

[74] Michael B Braun, Bjoern Traenkle, Philipp A Koch, Felix Emele, Frederik Weiss, Oliver Poetz, Thilo Stehle, and Ulrich Rothbauer. Peptides in headlock–a novel high-affinity and versatile peptide-binding nanobody for proteomics and microscopy. *Scientific reports*, 6:19211, 2016.

[75] Akiko Koide, Charles W Bailey, Xiaolin Huang, and Shohei Koide. The fibronectin type iii domain as a scaffold for novel binding proteins1. *Journal of molecular biology*, 284(4):1141–1151, 1998.

[76] Randy B Stockbridge, Akiko Koide, Christopher Miller, and Shohei Koide. Proof of dual-topology architecture of fluc f- channels with monobody blockers. *Nature communications*, 5:5120, 2014.

[77] Daniel L Turman, Jacob T Nathanson, Randy B Stockbridge, Timothy O Street, and Christopher Miller. Two-sided block of a dual-topology f- channel. *Proceedings of the National Academy of Sciences*, page 201505301, 2015.

[78] Randy B Stockbridge, Ludmila Kolmakova-Partensky, Tania Shane, Akiko Koide, Shohei Koide, Christopher Miller, and Simon Newstead. Crystal structures of a double-barrelled fluoride ion channel. *Nature*, 525(7570):548, 2015.

[79] Gurkan Guntas, Steven M Lewis, Kathleen M Mulvaney, Erica W Cloer, Ashutosh Tripathy, Thomas R Lane, Michael B Major, and Brian Kuhlman. Engineering a genetically encoded competitive inhibitor of the keap1–nrf2 interaction via structure-based design and phage display. *Protein Engineering, Design & Selection*, 29(1):1–9, 2015.

[80] Seung-Hwan Park, Sukho Park, Dong-Yeon Kim, Ayoung Pyo, Richard H Kimura, Ataya Sathirachinda, Hyon E Choy, Jung-Joon Min, Sanjiv Sam Gambhir, and Yeongjin Hong. Isolation and characterization of a monobody with a fibronectin domain iii scaffold that specifically binds epha2. *PLoS One*, 10(7):e0132976, 2015.

[81] Shun-ichi Tanaka, Tetsuya Takahashi, Akiko Koide, Satoru Ishihara, Satoshi Koikeda, and Shohei Koide. Monobody-mediated alteration of enzyme specificity. *Nature chemical biology*, 11(10):762, 2015.

[82] Kevin M Esvelt, Jacob C Carlson, and David R Liu. A system for the continuous directed evolution of biomolecules. *Nature*, 472(7344):499, 2011.

[83] Ahmed H Badran, Victor M Guzov, Qing Huai, Melissa M Kemp, Prashanth Vishwanath, Wendy Kain, Autumn M Nance, Artem Evdokimov, Farhad Moshiri, Keith H Turner, et al. Continuous evolution of bacillus thuringiensis toxins overcomes insect resistance. *Nature*, 533(7601):58, 2016.

[84] Ingrid Sassoon and Veronique Blanc. Antibody–drug conjugate (adc) clinical pipeline: a review. In *Antibody-Drug Conjugates*, pages 1–27. Springer, 2013.

[85] Pharma Compass. Top drugs by sales revenue in 2015: Who sold the biggest blockbuster drugs? 2016.

[86] Virginia J Bruce, Angeline N Ta, and Brian R McNaughton. Minimalist antibodies and mimetics: an update and recent applications. *Chembiochem*, 17(20):1892–1899, 2016.

[87] Alan Menter, Stephen K Tyring, Kenneth Gordon, Alexa B Kimball, Craig L Leonardi, Richard G Langley, Bruce E Strober, Martin Kaul, Yihua Gu, Martin Okun, et al. Adalimumab therapy for moderate to severe psoriasis: a randomized, controlled phase iii trial. *Journal of the American Academy of Dermatology*, 58(1):106–115, 2008.

[88] Joseph Keane, Sharon Gershon, Robert P Wise, Elizabeth Mirabile-Levens, John Kasznica, William D Schwieterman, Jeffrey N Siegel, and M Miles Braun. Tuberculosis associated with infliximab, a tumor necrosis factor α–neutralizing agent. *New England Journal of Medicine*, 345(15):1098–1104, 2001.

[89] Clifford A Hudis. Trastuzumab—mechanism of action and use in clinical practice. *New England Journal of Medicine*, 357(1):39–51, 2007.

[90] Jonathan CW Edwards, Leszek Szczepański, Jacek Szechiński, Anna Filipowicz-Sosnowska, Paul Emery, David R Close, Randall M Stevens, and Tim Shaw. Efficacy of b-cell–targeted therapy with rituximab in patients with rheumatoid arthritis. *New England Journal of Medicine*, 350(25):2572–2581, 2004.

[91] Robbie Woodman, Johannes T-H Yeh, Sophie Laurenson, and Paul Ko Ferrigno. Design and validation of a neutral protein scaffold for the presentation of peptide aptamers. *Journal of molecular biology*, 352(5):1118–1133, 2005.

[92] Rodrigo Vazquez-Lombardi, Tri Giang Phan, Carsten Zimmermann, David Lowe, Lutz Jermutus, and Daniel Christ. Challenges and opportunities for non-antibody scaffold drugs. *Drug discovery today*, 20(10):1271–1283, 2015.

[93] Maarten Van Roy, Cedric Ververken, Els Beirnaert, Sven Hoefman, Joost Kolkman, Michel Vierboom, Elia Breedveld, Sofie Poelmans, Lieselot Bontinck, Alex Hemeryck, et al. The preclinical pharmacology of the high affinity anti-il-6r nanobody® alx-0061 supports its clinical development in rheumatoid arthritis. *Arthritis research & therapy*, 17(1):135, 2015.

[94] Katrien Vanheusden, Laurent Detalle, Alex Hemeryck, Alain Vicari, Roland Grenningloh, Sofie Poelmans, Heidi Wouters, and Thomas Stöhr. Pre-clinical proof-of-concept of alx-0761, a nanobody® neutralizing both il-17a and f in a cynomolgus monkey collagen induced arthritis model. *ACR/ARHP Annual Meeting.*, 1287, 2013.

[95] A Philippidis. The top 15 best-selling drugs of 2017. *Genetic Engineering News*, 2018.

[96] Tak W Mak and Mary E Saunders. *The immune response: basic and clinical principles*. Academic Press, 2005.

[97] David Zahavi, Dalal AlDeghaither, Allison O'Connell, and Louis M Weiner. Enhancing antibody-dependent cell-mediated cytotoxicity: a strategy for improving antibody-based immunotherapy. *Antibody Therapeutics*, 1(1):7–12, 2018.

[98] Gunter von Minckwitz, Marion Procter, Evandro de Azambuja, Dimitrios Zardavas, Mark Benyunes, Giuseppe Viale, Thomas Suter, Amal Arahmani, Nathalie Rouchet, Emma Clark, et al. Adjuvant pertuzumab and trastuzumab in early her2-positive breast cancer. *New England Journal of Medicine*, 377(2):122–131, 2017.

[99] I Rubin and Y Yarden. The basic biology of her2. *Annals of oncology*, 12(suppl_1):S3–S8, 2001.

[100] Gábor Tóth, Árpád Szöőr, László Simon, Yosef Yarden, János Szöllősi, and György Vereb. The combination of trastuzumab and pertuzumab administered at approved doses may delay development of trastuzumab resistance by additively enhancing antibody-dependent cell-mediated cytotoxicity. In *MAbs*, volume 8, pages 1361–1370. Taylor & Francis, 2016.

[101] Joachim Diessner, Valentin Bruttel, Kathrin Becker, Miriam Pawlik, Roland Stein, Sebastian Häusler, Johannes Dietl, Jörg Wischhusen, and Arnd Hönig. Targeting breast cancer stem cells with her2-specific antibodies and natural killer cells. *American journal of cancer research*, 3(2):211, 2013.

[102] Zhengyuan Zhou, Ganesan Vaidyanathan, Darryl McDougald, Choong Mo Kang, Irina Balyasnikova, Nick Devoogdt, Angeline N Ta, Brian R McNaughton, and Michael R Zalutsky. Fluorine-18 labeling of the her2-targeting single-domain antibody 2rs15d using a residualizing label and preclinical evaluation. *Molecular Imaging and Biology*, 19(6):867–877, 2017.

[103] Charles Eigenbrot, Mark Ultsch, Anatoly Dubnovitsky, Lars Abrahmsén, and Torleif Härd. Structural basis for high-affinity her2 receptor binding by an engineered protein. *Proceedings of the National Academy of Sciences*, 107(34):15039–15044, 2010.

[104] Matthias D'Huyvetter, Jens De Vos, Catarina Xavier, Marek Pruszynski, Yann GJ Sterckx, Sam Massa, Geert Raes, Vicky Caveliers, Michael Zalutsky, Tony Lahoutte, et al. 131i-labeled anti-her2 camelid sdab as a theranostic tool in cancer treatment. *Clinical Cancer Research*, pages clincanres–0310, 2017.

[105] Eugene F Douglass Jr, Chad J Miller, Gerson Sparer, Harold Shapiro, and David A Spiegel. A comprehensive mathematical model for three-body binding equilibria. *Journal of the American Chemical Society*, 135(16):6092–6099, 2013.

[106] Pierre Bruhns, Bruno Iannascoli, Patrick England, David A Mancardi, Nadine Fernandez, Sylvie Jorieux, and Marc Daëron. Specificity and affinity of human fcγ receptors and their polymorphic variants for human igg subclasses. *Blood*, 113(16):3716–3725, 2009.

[107] Josée Golay, Manuela Lazzari, Valeria Facchinetti, Sergio Bernasconi, Gianmaria Borleri, Tiziano Barbui, Alessandro Rambaldi, and Martino Introna. Cd20 levels determine the in

vitro susceptibility to rituximab and complement of b-cell chronic lymphocytic leukemia: further regulation by cd55 and cd59. *Blood*, 98(12):3383–3389, 2001.

[108] Stefanie Derer, Philip Bauer, Stefan Lohse, Andreas H Scheel, Sven Berger, Christian Kellner, Matthias Peipp, and Thomas Valerius. Impact of epidermal growth factor receptor (egfr) cell surface expression levels on effector mechanisms of egfr antibodies. *The Journal of Immunology*, page 1202037, 2012.

[109] Kirstie LS Cleary, HT Claude Chan, Sonja James, Martin J Glennie, and Mark S Cragg. Antibody distance from the cell membrane regulates antibody effector mechanisms. *The Journal of Immunology*, page 1601473, 2017.

[110] Richard Cowan and P Anne Underwood. Steric effects in antibody reactions with polyvalent antigen. *Journal of theoretical biology*, 132(3):319–335, 1988.

[111] William S Hlavacek, Richard G Posner, and Alan S Perelson. Steric effects on multivalent ligand-receptor binding: exclusion of ligand sites by bound cell surface receptors. *Biophysical Journal*, 76(6):3031–3043, 1999.

[112] Bart S Hendriks, Stephan G Klinz, Joseph G Reynolds, Christopher W Espelin, Daniel F Gaddy, and Thomas J Wickham. Impact of tumor her2/erbb2 expression level on her2-targeted liposomal doxorubicin-mediated drug delivery: multiple low-affinity interactions lead to a threshold effect. *Molecular cancer therapeutics*, pages molcanther–0180, 2013.

[113] Fiora Rosati and Gerard Roelfes. Artificial metalloenzymes. *ChemCatChem*, 2(8):916–927, 2010.

[114] Kazuo Yamamura and Emil Thomas Kaiser. Studies on the oxidase activity of copper (ii) carboxypeptidase a. *Journal of the Chemical Society, Chemical Communications*, (20):830–831, 1976.

[115] Michael E Wilson and George M Whitesides. Conversion of a protein to a homogeneous asymmetric hydrogenation catalyst by site-specific modification with a diphosphinerhodium (i) moiety. *Journal of the American Chemical Society*, 100(1):306–307, 1978.

[116] A Schmid, JS Dordick, B Hauer, Al Kiener, M Wubbolts, and B Witholt. Industrial biocatalysis today and tomorrow. *nature*, 409(6817):258, 2001.

[117] Jeffrey Bos and Gerard Roelfes. Artificial metalloenzymes for enantioselective catalysis. *Current opinion in chemical biology*, 19:135–143, 2014.

[118] Christian Trindler and Thomas R Ward. Artificial metalloenzymes. In *Effects of Nanoconfinement on Catalysis*, pages 49–82. Springer, 2017.

[119] Jared C Lewis. Artificial metalloenzymes and metallopeptide catalysts for organic synthesis. *Acs Catalysis*, 3(12):2954–2975, 2013.

[120] Takafumi Ueno, Hiroyasu Tabe, and Yuya Tanaka. Artificial metalloenzymes constructed from hierarchically-assembled proteins. *Chemistry–An Asian Journal*, 8(8):1646–1660, 2013.

[121] Markus Jeschek, Sven Panke, and Thomas R Ward. Artificial metalloenzymes on the verge of new-to-nature metabolism. *Trends in biotechnology*, 2017.

[122] Fabian Schwizer, Yasunori Okamoto, Tillmann Heinisch, Yifan Gu, Michela M Pellizzoni, Vincent Lebrun, Raphael Reuter, Valentin Kohler, Jared C Lewis, and Thomas R Ward. Artificial metalloenzymes: reaction scope and optimization strategies. *Chemical reviews*, 118(1):142–231, 2017.

[123] Shun Hirota and Ying-Wu Lin. Design of artificial metalloproteins/metalloenzymes by tuning noncovalent interactions. *JBIC Journal of Biological Inorganic Chemistry*, 23(1):7–25, 2018.

[124] Melanie Bordeaux, Vikas Tyagi, and Rudi Fasan. Highly diastereoselective and enantioselective olefin cyclopropanation using engineered myoglobin-based catalysts. *Angewandte Chemie*, 127(6):1764–1768, 2015.

[125] Priyanka Bajaj, Gopeekrishnan Sreenilayam, Vikas Tyagi, and Rudi Fasan. Gram-scale synthesis of chiral cyclopropane-containing drugs and drug precursors with engineered myoglobin catalysts featuring complementary stereoselectivity. *Angewandte Chemie International Edition*, 55(52):16110–16114, 2016.

[126] Melanie Bordeaux, Ritesh Singh, and Rudi Fasan. Intramolecular c (sp3) h amination of arylsulfonyl azides with engineered and artificial myoglobin-based catalysts. *Bioorganic & medicinal chemistry*, 22(20):5697–5704, 2014.

[127] John A McIntosh, Pedro S Coelho, Christopher C Farwell, Z Jane Wang, Jared C Lewis, Tristan R Brown, and Frances H Arnold. Enantioselective intramolecular c h amination catalyzed by engineered cytochrome p450 enzymes in vitro and in vivo. *Angewandte Chemie*, 125(35):9479–9482, 2013.

[128] Todd K Hyster, Christopher C Farwell, Andrew R Buller, John A McIntosh, and Frances H Arnold. Enzyme-controlled nitrogen-atom transfer enables regiodivergent c–h amination. *Journal of the American Chemical Society*, 136(44):15505–15508, 2014.

[129] Christopher K Prier, Ruijie K Zhang, Andrew R Buller, Sabine Brinkmann-Chen, and Frances H Arnold. Enantioselective, intermolecular benzylic c–h amination catalysed by an engineered iron-haem enzyme. *Nature chemistry*, 9(7):629, 2017.

[130] Christopher C Farwell, John A McIntosh, Todd K Hyster, Z Jane Wang, and Frances H Arnold. Enantioselective imidation of sulfides via enzyme-catalyzed intermolecular nitrogen-atom transfer. *Journal of the American Chemical Society*, 136(24):8766–8771, 2014.

[131] Christopher K Prier, Todd K Hyster, Christopher C Farwell, Audrey Huang, and Frances H Arnold. Asymmetric enzymatic synthesis of allylic amines: a sigmatropic rearrangement strategy. *Angewandte Chemie International Edition*, 55(15):4711–4715, 2016.

[132] Z Jane Wang, Nicole E Peck, Hans Renata, and Frances H Arnold. Cytochrome p450-catalyzed insertion of carbenoids into n–h bonds. *Chemical science*, 5(2):598–601, 2014.

[133] Gopeekrishnan Sreenilayam and Rudi Fasan. Myoglobin-catalyzed intermolecular carbene n–h insertion with arylamine substrates. *Chemical Communications*, 51(8):1532–1534, 2015.

[134] Vikas Tyagi, Rachel B Bonn, and Rudi Fasan. Intermolecular carbene s–h insertion catalysed by engineered myoglobin-based catalysts. *Chemical science*, 6(4):2488–2494, 2015.

[135] Frank Hannemann, Andreas Bichet, Kerstin M Ewen, and Rita Bernhardt. Cytochrome p450 systems—biological variations of electron transport chains. *Biochimica et Biophysica Acta (BBA)-General Subjects*, 1770(3):330–344, 2007.

[136] Antonio Tinoco, Viktoria Steck, Vikas Tyagi, and Rudi Fasan. Highly diastereo-and enantioselective synthesis of trifluoromethyl-substituted cyclopropanes via myoglobin-catalyzed transfer of trifluoromethylcarbene. *Journal of the American Chemical Society*, 139(15):5293–5296, 2017.

[137] SB Jennifer Kan, Russell D Lewis, Kai Chen, and Frances H Arnold. Directed evolution of cytochrome c for carbon–silicon bond formation: Bringing silicon to life. *Science*, 354(6315):1048–1051, 2016.

[138] Osami Shoji and Yoshihito Watanabe. Monooxygenation of nonnative substrates catalyzed by bacterial cytochrome p450s facilitated by decoy molecules. *Chemistry Letters*, 46(3):278–288, 2016.

[139] Koji Oohora, Yushi Kihira, Eiichi Mizohata, Tsuyoshi Inoue, and Takashi Hayashi. C (sp3)–h bond hydroxylation catalyzed by myoglobin reconstituted with manganese porphycene. *Journal of the American Chemical Society*, 135(46):17282–17285, 2013.

[140] Paweł Dydio, Hanna M Key, Hiroki Hayashi, Douglas S Clark, and John F Hartwig. Chemoselective, enzymatic c–h bond amination catalyzed by a cytochrome p450 containing an ir (me)-pix cofactor. *Journal of the American Chemical Society*, 139(5):1750–1753, 2017.

[141] Hanna M Key, Paweł Dydio, Douglas S Clark, and John F Hartwig. Abiological catalysis by artificial haem proteins containing noble metals in place of iron. *Nature*, 534(7608):534, 2016.

[142] P Dydio, HM Key, A Nazarenko, JY-E Rha, V Seyedkazemi, DS Clark, and JF Hartwig. An artificial metalloenzyme with the kinetics of native enzymes. *Science*, 354(6308):102–106, 2016.

[143] Sagar D Khare, Yakov Kipnis, Ryo Takeuchi, Yacov Ashani, Moshe Goldsmith, Yifan Song, Jasmine L Gallaher, Israel Silman, Haim Leader, Joel L Sussman, et al. Computational redesign of a mononuclear zinc metalloenzyme for organophosphate hydrolysis. *Nature chemical biology*, 8(3):294, 2012.

[144] Hao Yang, Poonam Srivastava, Chen Zhang, and Jared C Lewis. A general method for artificial metalloenzyme formation through strain-promoted azide–alkyne cycloaddition. *ChemBioChem*, 15(2):223–227, 2014.

[145] Poonam Srivastava, Hao Yang, Ken Ellis-Guardiola, and Jared C Lewis. Engineering a dirhodium artificial metalloenzyme for selective olefin cyclopropanation. *Nature communications*, 6:7789, 2015.

[146] Nathalie Madern, Barisa Talbi, and Michèle Salmain. Aqueous phase transfer hydrogenation of aryl ketones catalysed by achiral ruthenium (ii) and rhodium (iii) complexes and their papain conjugates. *Applied Organometallic Chemistry*, 27(1):6–12, 2013.

[147] Nathalie Madern, Nicolas Queyriaux, Alice Chevalley, Mahsa Ghasemi, Orazio Nicolotti, Ilaria Ciofini, Giuseppe Felice Mangiatordi, and Michèle Salmain. Piano-stool d6-rhodium (iii) complexes of chelating pyridine-based ligands and their papain bioconjugates for the catalysis of transfer hydrogenation of aryl ketones in aqueous medium. *Journal of Molecular Catalysis B: Enzymatic*, 122:314–322, 2015.

[148] Takashi Matsuo, Chie Imai, Takefumi Yoshida, Takashi Saito, Takashi Hayashi, and Shun Hirota. Creation of an artificial metalloprotein with a hoveyda–grubbs catalyst moiety through the intrinsic inhibition mechanism of α-chymotrypsin. *Chemical Communications*, 48(11):1662–1664, 2012.

[149] Manuel Basauri-Molina, Dide GA Verhoeven, Arnoldus J Van Schaik, Henk Kleijn, and Robertus JM Klein Gebbink. Ring-closing and cross-metathesis with artificial metalloenzymes created by covalent active site-directed hybridization of a lipase. *Chemistry–A European Journal*, 21(44):15676–15685, 2015.

[150] M Basauri-Molina, CF Riemersma, MA Würdemann, H Kleijn, and RJM Klein Gebbink. Lipase active site covalent anchoring of rh (nhc) catalysts: towards chemoselective artificial metalloenzymes. *Chemical Communications*, 51(31):6792–6795, 2015.

[151] Marco Filice, Oscar Romero, Antonio Aires, Jose M Guisan, Angel Rumbero, and Jose M Palomo. Preparation of an immobilized lipase-palladium artificial metalloenzyme as catalyst in the heck reaction: role of the solid phase. *Advanced Synthesis & Catalysis*, 357(12):2687–2696, 2015.

[152] Tillmann Heinisch and Thomas R Ward. Artificial metalloenzymes based on the biotin–streptavidin technology: challenges and opportunities. *Accounts of chemical research*, 49(9):1711–1721, 2016.

[153] Thomas R Ward. Artificial metalloenzymes based on the biotin- avidin technology: enantioselective catalysis and beyond. *Accounts of Chemical Research*, 44(1):47–57, 2010.

[154] Anamitra Chatterjee, Hendrik Mallin, Juliane Klehr, Jaicy Vallapurackal, Aaron D Finke, Laura Vera, May Marsh, and Thomas R Ward. An enantioselective artificial suzukiase based on the biotin–streptavidin technology. *Chemical science*, 7(1):673–677, 2016.

[155] Julien Pierron, Christophe Malan, Marc Creus, Julieta Gradinaru, Ines Hafner, Anita Ivanova, Alessia Sardo, and Thomas R Ward. Artificial metalloenzymes for asymmetric allylic alkylation on the basis of the biotin–avidin technology. *Angewandte Chemie*, 120(4):713–717, 2008.

[156] A Pordea, D Mathis, and Thomas R Ward. Incorporation of biotinylated manganese-salen complexes into streptavidin: new artificial metalloenzymes for enantioselective sulfoxidation. *Journal of Organometallic Chemistry*, 694(6):930–936, 2009.

[157] Anca Pordea, Marc Creus, Jaroslaw Panek, Carole Duboc, Déborah Mathis, Marjana Novic, and Thomas R Ward. Artificial metalloenzyme for enantioselective sulfoxidation based on vanadyl-loaded streptavidin. *Journal of the American Chemical Society*, 130(25):8085–8088, 2008.

[158] Myriem Skander, Christophe Malan, Anita Ivanova, and Thomas R Ward. Chemical optimization of artificial metalloenzymes based on the biotin-avidin technology:(s)-selective and solvent-tolerant hydrogenation catalysts via the introduction of chiral amino acid spacers. *Chemical Communications*, (38):4815–4817, 2005.

[159] Untung E Rusbandi, Cheikh Lo, Myriem Skander, Anita Ivanova, Marc Creus, Nicolas Humbert, and Thomas R Ward. Second generation artificial hydrogenases based on the

biotin-avidin technology: Improving activity, stability and selectivity by introduction of enantiopure amino acid spacers. *Advanced Synthesis & Catalysis*, 349(11-12):1923–1930, 2007.

[160] Myriem Skander, Nicolas Humbert, Jérôme Collot, Julieta Gradinaru, Gérard Klein, Andreas Loosli, Jérôme Sauser, Andrea Zocchi, François Gilardoni, and Thomas R Ward. Artificial metalloenzymes:(strept) avidin as host for enantioselective hydrogenation by achiral biotinylated rhodium- diphosphine complexes. *Journal of the American Chemical Society*, 126(44):14411–14418, 2004.

[161] Tommaso Quinto, Daniel Häussinger, Valentin Köhler, and Thomas R Ward. Artificial metalloenzymes for the diastereoselective reduction of nad+ to nad 2 h. *Organic & biomolecular chemistry*, 13(2):357–360, 2015.

[162] Tillmann Heinisch, Karolina Langowska, Pascal Tanner, Jean-Louis Reymond, Wolfgang Meier, Cornelia Palivan, and Thomas R Ward. Fluorescence-based assay for the optimization of the activity of artificial transfer hydrogenase within a biocompatible compartment. *ChemCatChem*, 5(3):720–723, 2013.

[163] Anca Pordea, Marc Creus, Christophe Letondor, Anita Ivanova, and Thomas R Ward. Improving the enantioselectivity of artificial transfer hydrogenases based on the biotin–streptavidin technology by combinations of point mutations. *Inorganica Chimica Acta*, 363(3):601–604, 2010.

[164] Marc Dürrenberger, Tillmann Heinisch, Yvonne M Wilson, Thibaud Rossel, Elisa Nogueira, Livia Knörr, Annette Mutschler, Karoline Kersten, Malcolm Jeremy Zimbron, Julien Pierron, et al. Artificial transfer hydrogenases for the enantioselective reduction of cyclic imines. *Angewandte Chemie International Edition*, 50(13):3026–3029, 2011.

[165] Christophe Letondor, Anca Pordea, Nicolas Humbert, Anita Ivanova, Sylwester Mazurek, Marjana Novic, and Thomas R Ward. Artificial transfer hydrogenases based on the biotin-

(strept) avidin technology: fine tuning the selectivity by saturation mutagenesis of the host protein. *Journal of the American Chemical Society*, 128(25):8320–8328, 2006.

[166] Christophe Letondor, Nicolas Humbert, and Thomas R Ward. Artificial metalloenzymes based on biotin-avidin technology for the enantioselective reduction of ketones by transfer hydrogenation. *Proceedings of the National Academy of Sciences*, 102(13):4683–4687, 2005.

[167] Yvonne M Wilson, Marc Durrenberger, Elisa S Nogueira, and Thomas R Ward. Neutralizing the detrimental effect of glutathione on precious metal catalysts. *Journal of the American Chemical Society*, 136(25):8928–8932, 2014.

[168] Jeremy M Zimbron, Tillmann Heinisch, Maurus Schmid, Didier Hamels, Elisa S Nogueira, Tilman Schirmer, and Thomas R Ward. A dual anchoring strategy for the localization and activation of artificial metalloenzymes based on the biotin–streptavidin technology. *Journal of the American Chemical Society*, 135(14):5384–5388, 2013.

[169] V Köhler, YM Wilson, M Dürrenberger, D Ghislieri, E Churakova, T Quinto, L Knörr, D Häussinger, F Hollmann, NJ Turner, et al. Synthetic cascades are enabled by combining biocatalysts with artificial metalloenzymes. *Nature Chemistry*, 5(2):93, 2013.

[170] Fabian Schwizer, Valentin Kohler, Marc Durrenberger, Livia Knorr, and Thomas R Ward. Genetic optimization of the catalytic efficiency of artificial imine reductases based on biotin–streptavidin technology. *ACS Catalysis*, 3(8):1752–1755, 2013.

[171] Victor Munoz Robles, Marc Durrenberger, Tillmann Heinisch, Agusti Lledos, Tilman Schirmer, Thomas R Ward, and Jean-Didier Marechal. Structural, kinetic, and docking studies of artificial imine reductases based on biotin–streptavidin technology: an induced lock-and-key hypothesis. *Journal of the American Chemical Society*, 136(44):15676–15683, 2014.

[172] Cheikh Lo, Mark R Ringenberg, David Gnandt, Yvonne Wilson, and Thomas R Ward. Artificial metalloenzymes for olefin metathesis based on the biotin-(strept) avidin technology. *Chemical Communications*, 47(44):12065–12067, 2011.

[173] Todd K Hyster, Livia Knörr, Thomas R Ward, and Tomislav Rovis. Biotinylated rh (iii) complexes in engineered streptavidin for accelerated asymmetric c–h activation. *Science*, 338(6106):500–503, 2012.

[174] Megan A Emmanuel, Norman R Greenberg, Daniel G Oblinsky, and Todd K Hyster. Accessing non-natural reactivity by irradiating nicotinamide-dependent enzymes with light. *Nature*, 540(7633):414, 2016.

[175] SB Jennifer Kan, Xiongyi Huang, Yosephine Gumulya, Kai Chen, and Frances H Arnold. Genetically programmed chiral organoborane synthesis. *Nature*, 552(7683):132, 2017.

[176] Frances H Arnold. Directed evolution: bringing new chemistry to life. *Angewandte Chemie International Edition*, 57(16):4143–4148, 2018.

[177] Stephan C Hammer, Grzegorz Kubik, Ella Watkins, Shan Huang, Hannah Minges, and Frances H Arnold. Anti-markovnikov alkene oxidation by metal-oxo–mediated enzyme catalysis. *Science*, 358(6360):215–218, 2017.

[178] Hao Yang, Alan M Swartz, Hyun June Park, Poonam Srivastava, Ken Ellis-Guardiola, David M Upp, Gihoon Lee, Ketaki Belsare, Yifan Gu, Chen Zhang, et al. Evolving artificial metalloenzymes via random mutagenesis. *Nature chemistry*, 10(3):318, 2018.

[179] David A Vargas, Antonio Tinoco, Vikas Tyagi, and Rudi Fasan. Myoglobin-catalyzed c- h functionalization of unprotected indoles. *Angewandte Chemie International Edition*, 57(31):9911–9915, 2018.

[180] Koji Oohora, Hiroyuki Meichin, Yushi Kihira, Hiroshi Sugimoto, Yoshitsugu Shiro, and Takashi Hayashi. Manganese (v) porphycene complex responsible for inert c–h

bond hydroxylation in a myoglobin matrix. *Journal of the American Chemical Society*, 139(51):18460–18463, 2017.

[181] Markus Jeschek, Raphael Reuter, Tillmann Heinisch, Christian Trindler, Juliane Klehr, Sven Panke, and Thomas R Ward. Directed evolution of artificial metalloenzymes for in vivo metathesis. *Nature*, 537(7622):661, 2016.

[182] Jérôme Collot, Julieta Gradinaru, Nicolas Humbert, Myriem Skander, Andrea Zocchi, and Thomas R Ward. Artificial metalloenzymes for enantioselective catalysis based on biotin-avidin. *Journal of the American Chemical Society*, 125(30):9030–9031, 2003.

[183] Edon Vitaku, David T Smith, and Jon T Njardarson. Analysis of the structural diversity, substitution patterns, and frequency of nitrogen heterocycles among us fda approved pharmaceuticals: miniperspective. *Journal of medicinal chemistry*, 57(24):10257–10274, 2014.

[184] Simon Duttwyler, Shuming Chen, Michael K Takase, Kenneth B Wiberg, Robert G Bergman, and Jonathan A Ellman. Proton donor acidity controls selectivity in nonaromatic nitrogen heterocycle synthesis. *Science*, 339(6120):678–682, 2013.

[185] Souvik Rakshit, Christoph Grohmann, Tatiana Besset, and Frank Glorius. Rh (iii)-catalyzed directed c- h olefination using an oxidizing directing group: Mild, efficient, and versatile. *Journal of the American Chemical Society*, 133(8):2350–2353, 2011.

[186] Nicolas Guimond, Serge I Gorelsky, and Keith Fagnou. Rhodium (iii)-catalyzed heterocycle synthesis using an internal oxidant: improved reactivity and mechanistic studies. *Journal of the American Chemical Society*, 133(16):6449–6457, 2011.

[187] Daniel Demonte, Christopher M Dundas, and Sheldon Park. Expression and purification of soluble monomeric streptavidin in escherichia coli. *Applied microbiology and biotechnology*, 98(14):6285–6295, 2014.

[188] Sau-Ching Wu and Sui-Lam Wong. Engineering soluble monomeric streptavidin with reversible biotin binding capability. *Journal of Biological Chemistry*, 280(24):23225–23231, 2005.

[189] Mohammad Hassan Qureshi and Sui-Lam Wong. Design, production, and characterization of a monomeric streptavidin and its application for affinity purification of biotinylated proteins. *Protein expression and purification*, 25(3):409–415, 2002.

[190] Kok Hong Lim, Heng Huang, Arnd Pralle, and Sheldon Park. Stable, high-affinity streptavidin monomer for protein labeling and monovalent biotin detection. *Biotechnology and bioengineering*, 110(1):57–67, 2013.

[191] Daniel DeMonte, Eric J Drake, Kok Hong Lim, Andrew M Gulick, and Sheldon Park. Structure-based engineering of streptavidin monomer with a reduced biotin dissociation rate. *Proteins: Structure, Function, and Bioinformatics*, 81(9):1621–1633, 2013.

[192] Tiffany Piou and Tomislav Rovis. Electronic and steric tuning of a prototypical piano stool complex: Rh (iii) catalysis for c–h functionalization. *Accounts of chemical research*, 51(1):170–180, 2017.

[193] Yecai Lai, Lijie Sun, Man Ki Sit, Yan Wang, and Wei-Min Dai. Diastereoselective synthesis of trans-3, 5-disubstituted dihydrofuran-2 (3h)-ones via smi2-mediated reductive coupling of 2-alkylacrylates of n, n-diisopropyl-2-hydroxybenzamide with aldehydes. *Tetrahedron*, 72(5):664–673, 2016.

[194] Christian Gloegaard and Tom Christian Berg. Method for the production of pyruvic acid, December 30 2008. US Patent 7,470,813.

[195] François-Xavier Felpin, Karinne Miqueu, Jean-Marc Sotiropoulos, Eric Fouquet, Oier Ibarguren, and Julia Laudien. Room-temperature, ligand-and base-free heck reactions of aryl diazonium salts at low palladium loading: Sustainable preparation of substituted stilbene derivatives. *Chemistry–A European Journal*, 16(17):5191–5204, 2010.

[196] Ravikumar R Gowda and Eugene Y-X Chen. Synthesis of β-methyl-α-methylene-γ-butyrolactone from biorenewable itaconic acid. *Organic Chemistry Frontiers*, 1(3):230–234, 2014.